Investigation of External Oil Flow from a Journal Bearing in an Epicyclic Gearbox

Martin Berthold, Dipl.-Ing.

A dissertation submitted to the University of Nottingham

for the degree of Doctor of Philosophy

September 2020

Abstract

High loads and bearing life requirements make journal bearings the preferred choice for use in planetary gearboxes in aero-engines. Due to the high power being transmitted, large oil quantities are required for cooling and lubrication purposes. A significant part of the total gear box oil flow rate is directed to the journal bearings, which are therefore potentially a major source for load-independent power losses.

Journal bearing oil outflow has not yet been comprehensively reviewed. The research work presented in this thesis aims to close this knowledge gap by developing a validated methodology to analyse and evaluate external oil flow from a journal bearing. Thus, new design rules and guidelines to improve epicyclic gearbox performance shall be facilitated.

This is achieved by a combination of transient multiphase computational fluid dynamics (CFD) analyses of non-orbiting and orbiting journal bearings using the Volume of Fluid (VOF) method and experimental rig testing with a simplified journal bearing geometry.

For numerical fluid flow investigations, the application of representative boundary conditions is imperative. Therefore, an inlet boundary condition was developed to allow the modelling of external oil flow without the need to determine the flow characteristics inside the journal bearing's lubricating gap by CFD analyses.

Numerical analyses showed that, depending on the liquid properties and the operating conditions, two fundamentally different outflow directions and different liquid disintegration regimes occur. Validation of these results was performed through analytical considerations and by experiments. Rig testing was focused on confirming both the outflow direction and the liquid disintegration regimes. An additional outcome was the generation of flow maps, which allow the flow path direction and the liquid disintegration regime to be predicted empirically based on the liquid properties and the operating conditions.

Establishing a validated methodology for investigating external oil flow from a journal bearing allowed recommendations for design improvements to be made. These help to maximise gearbox efficiency by minimising the load-independent power losses caused by oil emerging from the journal bearings.

Preface

The research work presented in this thesis was carried out at the University of Nottingham's Gas Turbine and Transmissions Research Centre (G2TRC), which is also home to the Rolls-Royce University Technology Centre (UTC) in gas turbine transmission systems, between October 2014 and September 2020. As a former Rolls-Royce employee and part-time PhD student, I am very grateful to have been given the opportunity to pursue these studies. Without the support and commitment from the Structures and Transmissions (S&T) Supply Chain Unit (SCU) of Rolls-Royce plc, Rolls-Royce Deutschland Ltd and Co KG (RRD) and the University of Nottingham's G2TRC, this would not have been possible.

Being able to conduct research on a key subsystem for a new aero-engine architecture is a privilege, especially in the working environment that I was fortunate enough to be a part of. This did not only include having access to top-class research facilities and resources, but, more importantly, relates to the people I studied with, worked with and worked for. I will treasure the experiences I made on a professional and personal level whilst working on this project forever.

I hereby confirm that this dissertation is my own work and contains nothing which is the outcome of work carried out in collaboration with others, except as specified in the text and acknowledgements. Whenever information from other authors was used, an appropriate reference was made. No parts of this work have been submitted to any other University or Institution for any other qualification.

Martin Berthold

September 2020

Kongsberg, Norway

Acknowledgements

This research project would not have been possible without the support of a number of people. First and foremost, I would like to thank my academic supervisors, Dr. Richard Jefferson-Loveday, Prof. Hervé Morvan, Dr. Carol Eastwick and Prof. Seamus Garvey. Additionally, I would like to thank Dr. Stephen Ambrose, Dr. Benjamin C Rothwell and Dr. Kathy Johnson. I wish to extend my gratitude to my industrial supervisor, Dr. Colin Young, from Rolls-Royce plc. I could not have imagined any better support and guidance.

There are a number of people from the Gas Turbine and Transmissions Research Centre (G2TRC) who deserve special acknowledgements. I would like to thank my colleagues and ex-colleagues who are and were involved with numerical analyses of two-phase flows in gearboxes and bearing chambers, namely Dr. Arun Prabhakar, Dr. Kiran Kumar Palla Venkata Satya, Dr. Kuldeep Singh and Dr. Bruce Kakimpa. From the G2TRC technical team, I would like to express my gratitude to Dr. Graham Johnson, Dr. Stephen Pearson, Dr. Aliyu Aliyu, Dr. Rajab Omar, Dr. Paloma Paleo Cageao, James Garvey, Robert Stables, Terry Alvey, Berry Hatch and Richard Thompson. Without them, experimental testing would not have been possible.

As I remained an employee of Rolls-Royce plc during the majority of my studies, this work was carried out in close cooperation with the company. I would like to thank Mike Walsh, Adrian Jacobs, Steve Curzons, Dr. Vincenzo Fico and Dr. Andrea Bristot, whose advice and feedback helped me to resolve a number of issues.

The Structures and Transmissions (S&T) department of Rolls-Royce plc played a key role in the early stages of the project, particularly when agreeing funding. Without the help and support of my S&T team leaders, line managers and the senior leadership team, I would not have been able to pursue my dream of doing a PhD. I would like to express my special thanks to Ian Burrows, John Hunter, Mike Mountney, Dr. John Schofield, Dr. Chris Lobley, Luke Logan, Julie Hoar, Andrew Nicholls, Will Dickinson and Lewis Fisher.

This project was carried out as part of the Rolls-Royce UltraFan® research activities, which were partly coordinated by Rolls-Royce Deutschland Ltd & Co KG (RRD). I would like to thank Wolfram Kurz-Hardjosoekatmo, Dr. Michael Klingsporn, Jens Klostermann, Paul Gorenz and Dr. Stephan Uhkötter for the excellent support.

Last but not least I would like to thank my friends and my family, especially Elisabeth and Olav, for their continued support and for helping me to put CFD convergence issues and experimental rig break-downs into perspective.

Contents

List of Figures

List of Tables

Nomenclature

Unless stated otherwise, the following units apply to Latin and Greek symbols.

Latin symbols

Symbol	Unit	Description
a	m	Radial extent of liquid sheet
a	m/s^2	Acceleration
a_{nb}	-	Linearised coefficient for ϕ_{nb}
a_{P}	-	Linearised coefficient for ϕ
A	m^2	Area
c_m	-	Dimensionless moment coefficient
c_{p}	J/(kg K)	Specific heat capacity at constant pressure
C	m	Radial clearance
C	-	Courant number
C_{i}	-	Constant
C_μ	-	Constant
d	m	Diameter
e	-	Eccentricity
f	-	Face
F	N	Force
F_{slip}	-	Slip factor
g	m/s^2	Gravitational acceleration
h	m	Gap height
$I_{\dot{m}}$	-	Normalised mass flow imbalance
k		Thermal conductivity
k	m^2/s^2	Turbulent kinetic energy
l	m	Length
ℓ	m	Length scale

ℓ_m	m	Mixing length
m	-	Counter variable
m	kg	Mass
$\dot{m}$	kg/s	Mass flow rate
M	Nm	Torque
n	1/s	Rotational speed
$\boldsymbol{n}$	°	Normal vector
n	-	Counter variable
Oh	-	Ohnesorge number
p	Pa	Pressure
P	W	Power
r	m	Radius
Re	-	Reynolds number
s	m	Axial gap
s_{ij}	1/s	Deformation rate
S_R	-	Swirl ratio
S_α	kg/s	Source term for phase mass flow
S_ϕ	[ ]	Source term for ϕ
St	-	Stability number
t	s	Time
t_S	m	Sheet thickness
t_F	m	Film thickness
T	°C	Temperature
ΔT	K	Temperature difference
T_{i}	-	Base function for Chebyshev polynomial
T^+	-	Non-dimensional temperature
Ta	-	Taylor number
u	m/s	Velocity in the x-direction
u^+	-	Non-dimensional velocity
u_τ	m/s	Shear velocity
$\boldsymbol{u}$	m/s, °	Flow velocity vector composed of u, v and w
$\boldsymbol{u}^*$	m/s, °	Flow velocity vector composed of v and w
$\boldsymbol{u}'$	m/s, °	Flow velocity vector composed of u and w
U	m/s	Surface velocity in the x-direction
v	m/s	Velocity in the y-direction

$\mathscr{v}$	m/s	Velocity scale
V	m^3	Volume
$\dot{V}$	m^3/s	Volumetric flow rate
$\dot{V}^+$	-	Non-dimensional volumetric flow rate
w	m/s	Velocity in the z-direction
W	m/s	Surface velocity in the z-direction
We	-	Weber number
We^*	-	Modified Weber number
x	m	Circumferential Cartesian coordinate
$\boldsymbol{x}$	m, °	Position vector
$\boldsymbol{x}_0$	m, °	Initial position vector
y	m	Axial Cartesian coordinate
y	m	Wall distance
y^+	-	Non-dimensional wall distance
z	m	Radial Cartesian coordinate

Greek symbols

Symbol	Unit	Description
α	-	Phase volume fraction value
β	-	Slope limiter
γ	°	Angle between liquid sheet and vertical face of planet gear base
Γ	-	Coefficient of Diffusion
δ	m	Boundary layer thickness
δ_{ij}	-	Kronecker delta
Δ	-	Difference
ε	m^2/s^3	Rate of dissipation of turbulent kinetic energy
ϵ	-	Error
ζ	-	Non-dimensional wall distance
θ	°	Circumferential polar coordinate
κ	-	Von Kármán constant
λ	°	Flow deflection angle
μ	kg/(ms)	Dynamic viscosity
μ_t	kg/(ms)	Dynamic turbulent (eddy) viscosity

ν	m^2/s	Kinematic viscosity
ν_t	m^2/s	Kinematic turbulent (eddy) viscosity
ν_R	-	Kinematic viscosity ratio
ξ	°	Gear chamfer angle
o	°	Contact angle
ρ	kg/m^3	Density
σ	N/m	Surface tension
τ	N/m^2	Shear stress
τ_w	N/m^2	Wall shear stress
ϕ	[ ]	General flow variable
ω	1/s	Angular velocity
ω	1/s	Turbulence frequency

Indices

Index	Description
0	At constant gap height
amb	Ambient
b	Break-up
B	Body
c	Centrifugal
C	Carrier
cav	Cavitation
cool	Coolant
crit	critical
d	Donor cell
D	Disc
ent	Entrance
ext	External
f	Face value
flux	Flux
g	Gas
G	Gear
in	Inlet
int	Internal

l	Loss
lq	Liquid
L	Lip
man	Manifold
max	Maximum
max load	Maximum load
mean	Mean
min	Minimum
min load	Minimum load
nb	Neighbouring cells
net	Net
out	Outlet
O	Orbit
P	Pin
Pl	Plenum
rad	Radial
rq	required
ref	Reference
res	Resultant
rw	Combined rim and wave disintegration
S	Scavenge
sat	Saturation
St	Stator
sup	Supplied
T	Tank
tan	Tangential
vap	Vapour
w	Wave disintegration

Acronyms

Acronym	Description
ACARE	Advisory Council for Aviation Research and Innovation in Europe
ASM	Algebraic Stress Model
CAD	Computer Aided Design
CFD	Computational Fluid Dynamics

CICSAM	Compressive Interface Construction Scheme for Arbitrary Meshes
CV	Control Volume
DC	Direct Current
DNS	Direct numerical simulation
DPM	Discrete Phase Model
EHL	Elasto-Hydrodynamic Lubrication
ETFM	Eulerian Thin Film Model
FDS	Facility Drive System
FOS	Facility Oil System
GTF	Geared Turbofan
G2TRC	Gas Turbine and Transmissions Research Centre
GUI	Graphical User Interface
HPC	High Performance Computing
HRIC	High Resolution Interface Capturing
LBM	Lattice Boltzmann Method
LES	Large Eddy Simulation
NITA	Non-Iterative Time Advancement
PDE	Partial Differential Equation
PGB	Power Gearbox
PISO	Pressure-Implicit with Splitting of Operators
PLIC	Piecewise Linear Interface Construction
RANS	Reynolds-Averaged Navier-Stokes
RNG	Renormalisation group
RRD	Rolls-Royce Deutschland
RSM	Reynolds Stress Model
SCADA	Supervisory Control and Data Acquisition
SCU	Supply Chain Unit
SFC	Specific Fuel Consumption
SGS	Sub-Grid Stresses
SIMPLE	Semi-implicit method for pressure-linked equations
SIMPLEC	SIMPLE-consistent
SOP	Safe Operating Procedure
SPH	Smoothed Particle Hydrodynamics
SRA	Strategic Research Agenda
SST	Shear Stress Transport

S&T	Structures and Transmissions
UDF	User-Defined Function
UTC	University Technology Centre
UUT	Unit Under Test
VOF	Volume of Fluid
XWB	Extra Wide Body

1 Introduction

Aviation has dramatically transformed society over the past 40 years. In order to best serve society's needs with regard to efficient and fast transportation of people and goods around the planet, the Advisory Council for Aviation Research and Innovation in Europe (ACARE) was founded in 2001. ACARE's main focus is to follow and maintain a Strategic Research Agenda (SRA) with the aim to meet the goals set out for 2020 and 2050. The environmental goals for 2050, for example, are to reduce CO_2 emissions by 75%, NO_x emissions by 90% and the perceived noise emission of flying aircraft by 65% compared to the levels of the year 2000 [1].

A major share of the targeted improvements will have to be contributed through advances in aero-engine technology. In order to meet the ACARE goals, and thus be competitive in the global market place, manufacturers continuously drive to reduce emissions. Therefore, lowering the specific fuel consumption (SFC) is one of the main objectives when developing new aero-engines. As it is increasingly difficult to achieve the targeted improvements through advances in conventional two and three-shaft architectures, aero-engine manufacturers need to develop new technologies and concepts.

One approach to reducing SFC is to increase aero-engine efficiency by operating the fan and its driving turbine at their respective optimal rotational speeds. Operating the turbine at higher rotational speeds is particularly attractive. As more power can be extracted from the main gas path [2], fewer turbine stages are required to drive the fan. Consequently, a more compact turbine can be designed, which will also have beneficial effects on weight.

The key technology to enable the decoupling of the fan and its associated turbine is an epicyclic reduction gearbox. Based on their achievable gear ratios, for use in turbofan aero-engines, both the star and the planetary gearbox configurations are viable options (Figure 1.1, Figure 1.2). In both configurations, the sun gear is driven by the turbine shaft. In a planetary gearbox configuration, the fan is driven by the rotating planet carrier (Figure 1.1), whereas in a star gearbox configuration, the fan is driven by the rotating annulus gear (Figure 1.2).

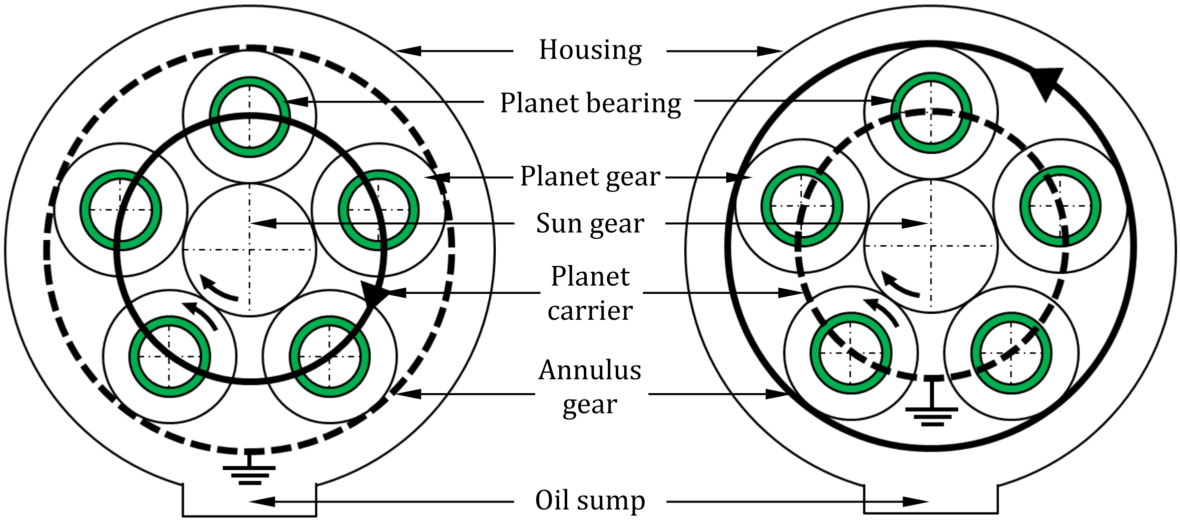

Figure 1.1: Epicyclic gearbox in planetary configuration

Figure 1.2: Epicyclic gearbox in star configuration

For turbofan aero-engines, using an epicyclic gear train rather than a fixed parallel axis arrangement is practical for a number of reasons. For an equivalent power transmission over a fixed gear ratio, epicyclic gear trains are lighter, require less space and are more efficient [3, 4]. Hence, epicyclic gearboxes can achieve higher power densities compared to fixed parallel axis gear trains [4].

Designing an epicyclic gearbox capable of transmitting the power generated by a large aero-engine, whilst meeting very stringent requirements with respect to gearbox efficiency, reliability, safety and weight, presents a number of challenges, which are discussed in section 1.2. One of these challenges is to manage the heat generated by the gearbox due to inevitable power losses by providing adequate lubrication and cooling oil flows. The lubricant and coolant flows themselves will cause power losses as they interact with the different gearbox components.

The need to investigate oil outflow from a non-orbiting rolling-element bearing in an aero-engine bearing chamber was identified by Adeniyi et al [5]. The authors' aim was to characterise the oil's disintegration behaviour as it exits the bearing. The need for similar investigations on external oil flow from a journal bearing, particularly in high-power epicyclic gearboxes, is evident and the research work presented in this thesis has been undertaken to address this need.

According to Townsend [4], for preliminary design considerations, it can be assumed that approximately 50% of the total oil flow supplied to the gearbox will have to be directed to the journal bearings for lubrication and cooling purposes. Therefore, it is important to develop the capability to analyse and evaluate journal bearing oil outflow, gain insight into the external oil flow field behaviour, and use the acquired knowledge to inform and influence the design of the domain under investigation.

Acquiring these capabilities and knowledge is crucial in order to ensure reliable and efficient gearbox operation, and support decision making processes during the design phase, risk mitigation strategies or failure root cause investigations later in the gearbox's life cycle. The rapid development of both multiphase CFD capability and high performance computing (HPC) resources means that this type of analysis is now feasible in an industrial context.

1.1 Aim

The aim of the research work presented in this thesis is twofold. Firstly, a validated methodology shall be developed to analyse and evaluate external oil flow from a journal bearing in an epicyclic gearbox, and, secondly, the developed methodology shall be used to facilitate design rules and guidelines to improve epicyclic gearbox performance.

1.2 Background

Epicyclic gear trains are already widely used in the aerospace industry. All modern turboprop engines, for example, use this technology. Compared to turbofan aero-engines, however, the transmitted power is significantly less. In order to meet future market demands with respect to SFC, epicyclic gearboxes will also be used in aero-engines which power large widebody aircraft. The Rolls-Royce UltraFan® (Figure 1.3), for instance, is designed to provide a thrust of up to 100,000 lbf with a power output of up to approximately 75 MW.

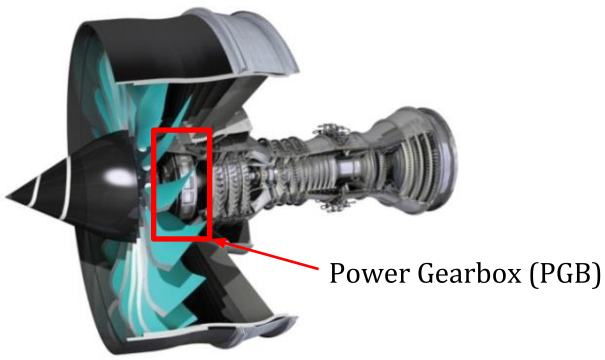

Figure 1.3: Rolls-Royce UltraFan® engine with PGB

In order to be a viable alternative to a conventional engine architecture, the epicyclic gearbox must transmit power reliably and efficiently with an unprecedented power density. For high-power applications, planet bearing design (section 1.2.1), the management of power losses (section 1.2.2), heat rejection (section 1.2.3), and lubricant and coolant flow path management (section 1.2.4) present major challenges, all of which are discussed in more detail in the following sections.

In order to address currently existing knowledge gaps related to fluid flow path management and the oil flow behaviour in epicyclic gearboxes (section 1.2.4 and section 1.2.5), Rolls-Royce and its University Technology Centre in Nottingham, United Kingdom, chose a parallel two-way approach of rig testing and multiphase Computational Fluid Dynamics (CFD) analysis.

Industrial requirements with regard to computing time and currently available CFD methods do not allow the air and oil flow behaviour to be investigated in an epicyclic gearbox as a whole. Limitations arise due to a number of reasons: the physical length scales inside the gearbox, for example, vary between micrometres inside the journal bearings and the gear tooth contacts to one metre for the diameter of the gearbox housing (Figure 1.1, Figure 1.2). The presence of multiple frames of reference and the symmetric arrangement of the planet gears allow some parts of the gearbox to be investigated by sector analysis. This can significantly reduce the required computational effort for CFD simulations. Furthermore, different areas of the gearbox exhibit different oil flow regimes [6]. Whilst the oil forms a film on the housing wall, the oil flow regime in the space between the planet gears is dominated by droplets. Different flow regimes, in turn, require the use of different numerical modelling techniques (section 2.8). For these reasons, it is more efficient to decompose and sub-divide an epicyclic gearbox into sub-models to assess specific areas of interest. One area of interest is the behaviour of the external oil flow from the journal bearings, which is addressed by the research work presented in this thesis.

1.2.1 Planet Bearings in Epicyclic Gearboxes

Based on the available design space and requirements for load-carrying capacity and life, two types of bearings are feasible for use in epicyclic gearboxes: rolling-element bearings and journal bearings. Due to their higher load-carrying capacity and longer life, for large geared turbofan aero-engines, journal bearings are preferred over rolling-element bearings.

Specifically for an epicyclic gearbox in planetary configuration (Figure 1.1), planet bearing design has unique challenges. Due to the superposed rotation of the planet gear about its own axis and the gear’s orbiting motion around the centre of the sun gear, the kinematic conditions are complex. The planet bearing has to reliably withstand the centrifugal force, F_c, and tangential gear forces, $F_{tan, 1}$ and $F_{tan, 2}$ (Figure 1.4).

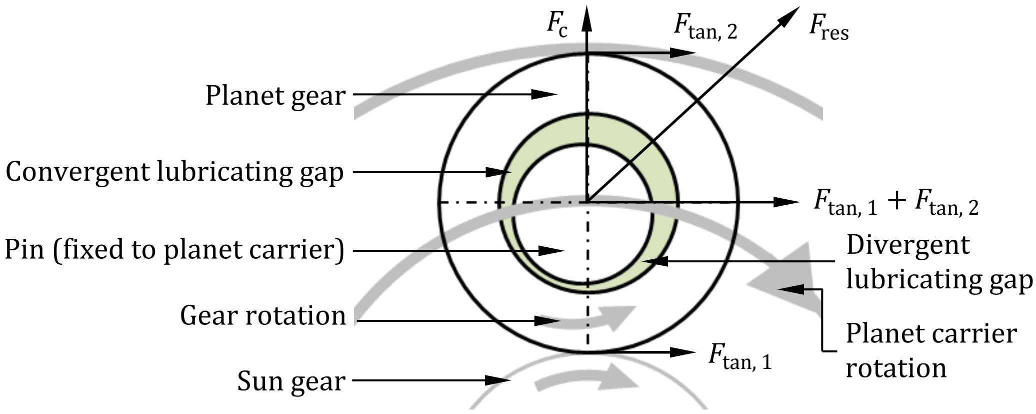

Figure 1.4: Forces acting on a planet bearing

In terms of general arrangement, journal bearings are very simple. They consist of a bushing, which, in an epicyclic gearbox, is formed by the planet gear (Figure 1.4) and a journal, which is formed by the pin (Figure 1.4). Both components move relative to each other. The diameter of the journal is slightly smaller than the diameter of the bushing. Thus, when fitted, there is a gap between the sliding surfaces. Under load, when operating in a hydrodynamic lubrication regime, the gap is convergent-divergent. The journal and the bushing are eccentric relative to one another. Assuming that a sufficient amount of liquid is supplied, due to the relative movement between the journal and the bushing, the lubricant will be drawn into the converging part of the gap and a fluid wedge will be formed. Providing that the rotational speed is sufficiently high, the fluid wedge will be able to fully separate the two sliding surfaces. The journal bearing load is then carried by the hydrodynamically generated fluid pressure in the converging part of the lubricating gap. This is the most desirable operating regime for a journal bearing with no wear taking place [7].

Particularly in highly-loaded journal bearings, the fluid pressure in the lubricating gap is large enough to deform the bearing surfaces significantly compared to the size of the minimum gap height, h_{min}. This type of hydrodynamic lubrication is known as elasto-hydrodynamic lubrication (EHL) [8]. Careful consideration must be given to minimise or, if required, counteract bearing surface deformation, as it can affect the load-carrying capacity of the bearing. Moreover, there is a strong coupling between the fluid pressure, fluid temperature and other fluid properties, and surface deformations. Contact between the sliding surfaces must be avoided in order to ensure reliable operation.

1.2.2 Power Losses in Epicyclic Gearboxes

Well-designed gearboxes can have a very high efficiency. In 1990, for instance, Krantz and Handschuh [9] carried out a systematic efficiency study on epicyclic helicopter gearboxes with a transmission ratio of 4.67. For a stage with four planets, while testing at full power, the measured efficiencies ranged from 99.44% to 99.60%, depending on the lubrication parameters. Although the overall gearbox efficiency appears to be very high, power losses can still be very large, especially in high-power applications. These losses need to be investigated in detail, particularly in the context of hard-won SFC reductions, where tenths and even hundredths of a percent are critical to economic and commercial engine viability.

To date, a large amount of research has been dedicated to investigating the relative magnitudes of the losses caused by different mechanisms. This understanding is crucial in order to address and minimise gearbox losses in a focused and systematic fashion. In general, gearbox power losses are primarily caused by gears and bearings. They can be divided into load-dependent and load-independent contributors. The load-dependent power loss of a gear pair is mainly caused by friction in the tooth contact and in the bearings, and the load-independent power losses are caused by the interaction of the oil and the surrounding air with the gearbox components. All losses attributed to the interaction of gearbox components with the oil are referred to as hydraulic losses. Especially in fast rotating systems, load-independent power losses can contribute a major part to the total power loss. In general, the contribution of load independent power losses to the total power loss will rise with increasing rotational speed [9, 10, 11].

From the above investigations, it can be concluded that load-independent bearing losses and hydraulic losses can contribute significantly to the total power loss. It is therefore necessary to understand the mechanisms that cause these losses in order to address and minimise them.

1.2.3 Heat Management in Epicyclic Gearboxes

Even with a very high efficiency of 99.5% or more, high-power gearboxes can still generate correspondingly large amounts of power loss. The generated heat must be removed by supplying sufficient quantities of coolant. Thus, efficient and effective heat management of the gearbox becomes a major challenge. Particularly in high-power applications, lubrication and cooling is often performed by separate oil jets. Whilst the lubricating oil jet targets the into-mesh zone, the cooling oil jet targets the out-of-mesh region (Figure 1.5).

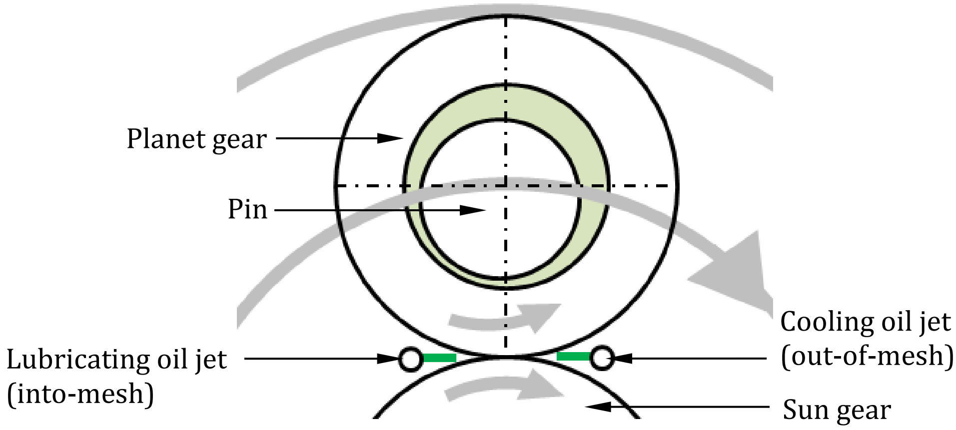

Figure 1.5: Cooling and lubricating oil jet arrangement

A simple calculation helps to better appreciate the amount of lubricant and coolant required to operate a high-power gearbox.

As part of Rolls-Royce's epicyclic gearbox development programme for large turbofan aero-engines, a demonstrator gearbox was designed which transmitted a power of 52 MW [12]. With an assumed efficiency of 99.5% (section 1.2.2), the generated power loss is 260 kW. In order to determine the required lubrication and cooling oil mass flow rate, it is further assumed that the heat will be completely dissipated by the coolant. This simplistic approach neglects heat dissipation into the surrounding components and the environment. The cooling oil mass flow rate can be calculated by

$$\dot{m}_{\mathrm{cool}} = \frac{P_{\mathrm{l}}}{c_{\mathrm{p,cool}} \cdot \Delta T_{\mathrm{cool}}}. \tag{1.1}$$

In the equation above, $\dot{m}_{\mathrm{cool}}$ is the cooling oil mass flow rate, P_{l} is the power loss, $c_{\mathrm{p,cool}}$ is the specific heat capacity of the coolant at constant pressure and ΔT_{cool} is the temperature difference of the coolant before and after heat absorption. Assuming a permissible coolant temperature rise of $\Delta T_{\mathrm{cool}} = 30\ \mathrm{K}$ [4] and a specific heat capacity at constant pressure of $c_{\mathrm{p,cool}} = 2{,}050\ \mathrm{J/(kg\ K)}$ [13], the required cooling oil mass flow rate is 4 kg/s. It should be noted that this flow rate does not include the lubricating oil mass flow required to justify the assumption of an efficiency of 99.5% in the first place. According to Smith [14], when oil is sprayed into-mesh and out-of-mesh, approximately 20% of the total oil flow rate is supplied to the into-mesh region. The remaining 80% is supplied to the out-of-mesh region. Thus, the total oil mass flow rate required by the gearbox is 5 kg/s, 1 kg/s (20%) of which is for lubrication and 4 kg/s (80%) of which is for cooling. For comparison, this means that this gearbox alone requires approximately twice the amount of oil that is supplied to an entire large modern turbofan aero-engine, like the Rolls-Royce Trent XWB. In this context, the need for an ultra-high efficiency gearbox is evident as lower losses require less cooling oil to be supplied. Thus, the overall oil inventory can be reduced. This also has a knock-on effect on other oil system components, which can be designed to be more compact and smaller. Examples include the oil tank and oil pumps, pipes and heat exchangers needed to cool the oil.

The method described above can be used to estimate the amount of lubricant and coolant required by the gearbox. Due to the uncertainties associated with gear train efficiency and permissible oil temperature rise, the actual value can vary significantly. As approximately 50% of the total oil mass flow rate will be required to lubricate and cool the bearings [4], fluid flow path management becomes a necessity in order to avoid excessive load-independent power losses (section 1.2.2).

1.2.4 Fluid Flow Path Management in Epicyclic Gearboxes

Due to the large oil flow rates involved, it is important to understand the oil flow behaviour inside the gearbox and manage the flow path. It is important to adequately condition and deliver the oil to the gear meshes and the journal bearings. Failing to do so can cause the oil to atomise and generate large numbers of fine droplets. This will increase the mean fluid density inside the gearbox, leading to higher load-independent power losses.

In addition to adequate oil delivery, it is imperative to remove and scavenge the oil as effectively and efficiently as possible after it has performed its primary function, i.e. lubricating or cooling. Failure to design an effective scavenge system can lead to a number of issues:

a) Hydraulic power losses may increase due to oil churning and excessive momentum exchange between the rotating parts and the oil. This will adversely affect gearbox efficiency.

b) Increased risk of gearbox flooding. Ineffective scavenging can cause the oil level in the sump region to rise sufficiently high to immerse the bottom of the annulus gear in oil (Figure 1.1, Figure 1.2). This, in turn, will result in the planet gears dipping into oil when orbiting around the sun gear, leading to a drastic increase in load-independent power losses and gearbox stresses.

c) Gearbox reliability may be adversely affected when failing to quickly remove the oil from the gearbox. This will inevitably result in longer residence times. Thus, the oil temperature may increase beyond acceptable levels, leading to premature oil degradation.

d) Recirculating oil and oil hiding present an issue with regard to both increased load-independent power losses and premature oil degradation.

e) Both oil atomisation and poor scavenge performance can lead to increased oil consumption. Although this is not significant in terms of operating costs, it can have a considerable impact on inspection intervals, gearbox reliability and emissions.

f) In an inadequately designed oil scavenge system, oil may be worked multiple times without intermediate cooling. This may be the case when oil exiting the bearings is subsequently ingested into the gear mesh. Very high local oil temperatures, as previously mentioned, may lead to premature degradation and gearbox reliability issues.

In order to design an effective oil scavenge system, the gearbox components must be designed in a way that rapid removal of oil is achieved. Controlling and guiding the oil flow from the region where it is injected towards the housing walls and into the sump becomes essential to mitigate the risks described above. In order to enable this, information about the air-oil flow field behaviour inside the gearbox is required. This knowledge can either be acquired by experimental flow visualisation, typically using a test rig, or numerical flow simulation. There are two areas in particular in which the air-oil flow field behaviour needs to be investigated and characterised: the regions where the lubricating and cooling oil jets impinge on the gears and gear meshes, respectively (Figure 1.5), and the regions where oil exits the journal bearings.

Whilst a number of authors, most notably Akin et al [15], Townsend [16], Arisawa et al [17, 18, 19], Fondelli et al [20, 21], Massini et al [22], Keller et al [23] and Ambrose et al [24], made considerable efforts to analyse and characterise oil jet impingement on single rotating gears or gear meshes, considerable knowledge gaps (section 1.2.4) persist for the external oil flow from journal bearings in epicyclic gearboxes.

1.2.5 Currently Existing Knowledge Gaps

The knowledge gaps associated with external journal bearing oil flow are consistent with the challenges related to fluid flow path management reported in section 1.2.4. In order to address these, research on external oil flow from a journal bearing in a high-power epicyclic gearbox is urgently required. Knowledge gaps exist in the following areas:

a) It is currently unknown what the preferred flow regime of the oil leaving the journal bearing should be, e.g. film flow, droplet flow, sheet formation, sheet separation and sheet disintegration into ligaments and droplets.
b) It is currently unknown how the oil flow path should be controlled or guided in order to remove the oil as quickly as possible from the vicinity of the bearing.
c) The oil flow path directions and velocities are currently unknown.
d) It is currently unknown how the oil merges into and mixes with the air surrounding the bearing.
e) The oil flow regimes, e.g. film flow, sheet formation and sheet disintegration mechanisms, are currently unknown.
f) It is currently unknown how the oil interacts with other gearbox components.
g) Parameters affecting the oil outflow behaviour of a journal bearing, specifically with respect to adherence and separation of film flow, are currently unknown.
h) Due to lack of knowledge described in a) to g), there are currently no guidelines, rules or criteria on how a journal bearing design should be assessed with respect to its external oil flow behaviour.

It should be noted that, where applicable, an understanding of the areas listed above is required throughout the whole operating envelope of the bearing. This is necessary in order to identify how different operating conditions, which are defined by the rotational speed, journal bearing eccentricity, i.e. lubricating gap height, temperature, i.e. oil viscosity, and oil mass flow rate, affect the oil outflow behaviour.

1.3 Objectives

The objectives of this research project are twofold. Firstly, CFD analysis capabilities for external oil flow from a journal bearing shall be developed, and, secondly, these capabilities shall be used to address the challenges and associated knowledge gaps described in sections 1.2.4 and 1.2.5. The following objectives apply to a journal bearing in an epicyclic gearbox in planetary configuration (Figure 1.1).

1) Develop validated CFD analysis capabilities to evaluate external oil flow from a journal bearing, i.e. provide best practices with regard to geometry simplification, meshing strategies, application of boundary conditions, use of numerical models and numerical solution strategies.

2) Gain insight into external oil flow from a journal bearing through CFD analysis and experimental flow field investigations, i.e. address knowledge gaps highlighted in section 1.2.5.
3) Develop capabilities to evaluate external oil flow from a journal bearing based on analytical and empirical knowledge, i.e. create flow maps derived from experimental investigations which allow the flow regime of the oil leaving the journal bearing to be identified.
4) Inform and influence the design of the domain under investigation with respect to risks and opportunities related to the external fluid flow behaviour.
5) Provide accurate boundary conditions for other CFD models used for modelling the air-oil flow field behaviour inside gearboxes and bearing chambers.

2 State-of-the-Art Knowledge and Literature Review

In the previous chapter, it was established that, due to the high loads transmitted by an epicyclic gearbox in a large turbofan aero-engine, and due to bearing life requirements, journal bearings are the preferred choice to locate the planet gears (section 1.2.1). Because of the power losses generated by the gearbox (section 1.2.2), considerations with respect to heat management (section 1.2.3) play an important role during the design process. Sufficient amounts of lubricant and coolant must be supplied to ensure efficient and reliable operation of the gearbox. The necessity of effectively managing the oil outflow from the journal bearings into the external environment was discussed and associated challenges were highlighted (section 1.2.4).

The focus of this chapter is on investigating the fundamentals of fluid flow in journal bearings (section 2.1) both internally (section 2.2) and externally (section 2.3). This will allow the principle underlying physical phenomena to be highlighted. Understanding the characteristics of internal journal bearing fluid flow is essential, as they are closely linked to the external fluid flow behaviour. Whilst internal journal bearing flow is well understood and documented in the literature, external journal bearing oil flow has not yet been comprehensively reviewed. Section 2.3 intends to close this current knowledge gap.

External oil flow from a journal bearing in an epicyclic gearbox, and, in fact, any other type of fluid flow, is governed by the conservation laws of physics. The mathematical representations of these laws are known as continuity, momentum and energy equations, all of which are discussed in detail in section 2.4.

The fluid flow equations can be solved using computational fluid dynamics (CFD) analysis. The fundamentals of CFD are described in section 2.5. A number of well-established CFD codes solve the fluid flow governing equations for discrete control volumes. This method is known as the finite volume method, which is described in section 2.6. Many flows in engineering applications are characterised by random and chaotic fluctuations of the flow velocity and other flow properties. The modelling of these fluctuations is covered in section 2.7. The last section of this chapter, section 2.8, reviews relevant techniques for the modelling of multiphase flows, as choosing an adequate approach is an essential part of the analysis process.

2.1 Fundamentals of Fluid Flow in Journal Bearings

The journal bearing under investigation is formed by a pin, which is fixed to the planet carrier, and the planet gear (Figure 2.1). The domain under investigation contains a region of internal (areas shaded in green) and external (areas shaded in light rose) journal bearing oil flow. The inlet to the external flow domain coincides with the outlet of the internal flow domain (Figure 2.2).

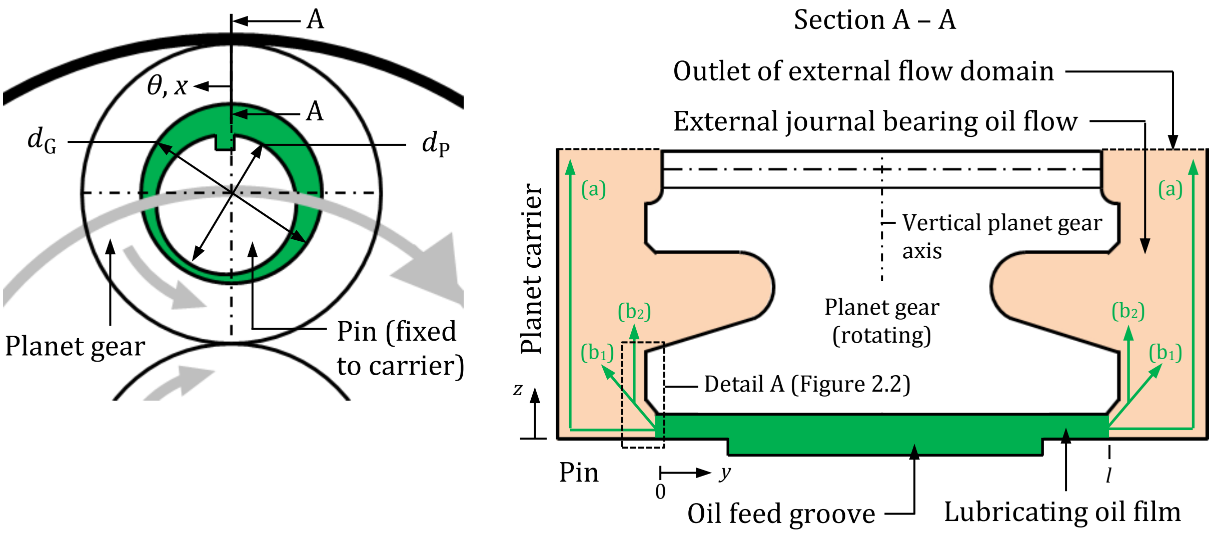

Figure 2.1: Domain under investigation with possible oil outflow directions (a) and (b)

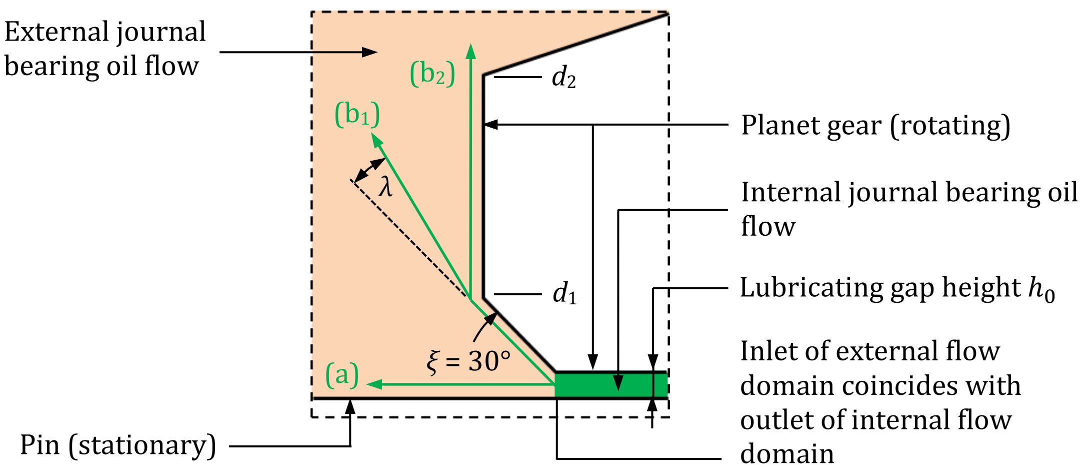

Figure 2.2: Detail A (Figure 2.1)

Figure 2.1 and Figure 2.2 contain a number of symbols which are introduced at this stage, as some of the following sections will refer to them. The inner gear diameter and the outer pin diameter, for instance, are denoted d_G and d_P, respectively. The polar and the Cartesian coordinate along the journal bearing's circumference are described by θ and x, and the y-coordinate and the z-coordinate are pointing in the bearing's axial and radial directions, respectively. The origin of the coordinate system is shown in Figure 2.1. The gear chamfer angle is denoted ξ. For the case under investigation, ξ is 30°. Flow paths (a), (b_1) and (b_2) show the possible outflow directions of the oil leaving the lubricating gap. Axial oil outflow follows flow path (a). Radial oil outflow follows either flow path (b_1) or (b_2). In order for the oil to follow flow path (b_1), its linear momentum must be sufficiently high to cause flow separation from the lower edge of the gear base (diameter d_2 in Figure 2.2). If that is the case, the various forces acting on the oil film at this location will cause a deflection of the film away from the extended gear chamfer surface towards the vertical planet gear axis, as shown in Figure 2.2. The associated deflection angle is denoted λ. If the oil flow does not separate from the lower edge of the gear base (diameter d_2 in Figure 2.2), it will remain attached to the planet gear and follow its contour until it separates from the upper edge of the gear base (diameter d_1 Figure 2.2). The flow path of the oil in the external journal bearing domain is examined in more detail in section 2.3.2.

At the outlet of the internal domain, flow properties like the velocity magnitudes, the velocity distributions and the directions, must be consistent with those at the inlet to the external domain. The flow properties at the outlet of the internal flow domain are governed by the flow behaviour inside the lubricating gap, which, in turn, is governed by the fluid pressure distribution inside the lubricating gap. It is therefore imperative to understand the internal journal bearing oil flow behaviour in more detail (section 2.2).

The flow behaviour of the air-oil mixture in the external flow domain will depend on the air flow structure and the oil's momentum and inertia. How much one phase is affected by the other will depend on the state of the oil phase. It can be continuous, e.g. in the form of a film or a sheet, discontinuous, e.g. in the form of ligaments or droplets, or dispersed, e.g. in the form of particles. In areas where the oil exists as a continuous phase, its flow behaviour will be determined by its current momentum. This is due to the fact that the oil's density, ρ, is in the order of 1,000 times higher than that of the air. In this case, the air flow field will have little effect on the oil flow behaviour. In contrast, in areas where the oil is discontinuous or dispersed, its flow behaviour will be more strongly affected by the air flow field.

When oil emerges from the lubricating gap (internal flow domain) into the external flow domain, it will initially be in a continuous state. Thus, the oil flow behaviour will be driven by its momentum, i.e. its flow velocity components in the axial, radial and circumferential directions, and its mass. As the oil flow passes through the domain (Figure 2.1), it will interact with the air flow and the components bounding the external domain, namely the planet carrier, the pin and the rotating planet gear. These interactions may cause the initially continuous oil phase to disintegrate and break up into ligaments and droplets of different sizes. Section 2.3 discusses the fundamentals of external journal bearing oil flow in more detail.

2.2 Internal Journal Bearing Flow Characteristics

As highlighted in the previous section, it is imperative to understand the internal journal bearing oil flow behaviour in detail. Through analytical considerations, the aim of this section is to provide a mathematical description of the flow velocity profiles in the circumferential, axial and radial directions at an arbitrary point inside the lubricating gap. This will allow the flow velocity components at the outlet of the internal flow domain (Figure 2.2) to be assessed. They must be consistent with those at the inlet to the external domain. In Figure 2.1, the region characterised by internal journal bearing oil flow is shaded in green, whilst the region characterised by external journal bearing outflow is shaded in light rose.

Internal journal bearing oil flow, as any other type of fluid flow, is governed by the laws of physics for the conservation of mass, momentum and energy. Due to the geometrical properties of journal bearings, according to Khonsari and Booser [25], these sets of governing equations (section 2.4) can be simplified significantly based on the following assumptions.

1) The fluid is assumed to be Newtonian, i.e. there is a direct proportionality between shear stress and shearing velocity.
2) Inertia and body force terms are assumed to be negligible compared to viscous terms, i.e. $\rho\, \mathrm{D}u/\mathrm{D}t = 0$ and $F_\mathrm{B} = 0$.
3) Variation of pressure across the film is assumed to be negligibly small, i.e. $\partial p/\partial z = 0$, so that the pressure field is two-dimensional only.
4) The flow is laminar.
5) Curvature effects are negligible. This implies that the lubricating film thickness is much smaller than the length or width of the bearing. This allows the physical domain to be unwrapped and considered in the Cartesian coordinate system, which is defined in Figure 2.1.

The above assumptions can be justified by an order-of-magnitude analysis [25]. When applying these assumptions to the equations for the conservation of mass and momentum in the circumferential direction, x, and the axial direction, y, the following relationships, given in Cartesian coordinates, are obtained.

The continuity equation for a compressible fluid in steady-state conditions is:

$$\frac{\partial(\rho u)}{\partial x}+\frac{\partial(\rho v)}{\partial y}+\frac{\partial(\rho w)}{\partial z}=0 \tag{2.1}$$

The x-momentum equation is:

$$\frac{\partial p}{\partial x}=\frac{\partial}{\partial z}\left(\mu\frac{\partial u}{\partial z}\right) \tag{2.2}$$

The y-momentum equation is:

$$\frac{\partial p}{\partial y}=\frac{\partial}{\partial z}\left(\mu\frac{\partial v}{\partial z}\right) \tag{2.3}$$

Based on assumption 3 above, there is no momentum in the z-direction. Through integration of equations (2.2) and (2.3), the flow velocity components in the x and y-directions can be obtained. Using appropriate boundary conditions for a stationary pin and a rotating planet gear, the flow velocity components in the circumferential and the axial directions, u and v, respectively, are given by

$$u=\underbrace{\frac{1}{2\mu}\frac{\partial p}{\partial x}\left(z^2-zh\right)}_{\text{Poiseuille flow term}}+\underbrace{\frac{z}{h}\frac{\omega_{\mathrm{G}}\,d_{\mathrm{G}}}{2}}_{\text{Couette flow term}} \tag{2.4}$$

$$v=\frac{1}{2\mu}\frac{\partial p}{\partial y}\left(z^2-zh\right) \tag{2.5}$$

In the equations above, μ is the dynamic viscosity of the fluid, and $\partial p/\partial x$ and $\partial p/\partial y$ are the pressure gradients in the circumferential and the axial directions, x and y, respectively. The radial coordinate across the lubricating gap height, h, is denoted z (Figure 2.1). It has a value of zero at the cylindrical surface of the pin (diameter d_{P} in Figure 2.1) and the value of h at the corresponding cylindrical surface of the planet gear bore (diameter d_{G} in Figure 2.1). The angular velocity of the rotating planet gear is given by ω_{G}. The lubricating gap height, h, can be calculated with the following equation [27].

$$h=C+e\cos\theta \tag{2.6}$$

In the equation above, C is the radial clearance between the inner gear diameter, d_{G}, and the outer pin diameter, d_{P} (Figure 2.1), e is the eccentricity and θ is the circumferential location.

Equation (2.4) shows that the flow velocity in the circumferential direction, u, is composed of a Poiseuille flow term and a Couette flow term. In contrast, the axial flow velocity, v, consists only of a Poiseuille flow term (equation (2.5)).

Couette flow is a shear-induced phenomenon with a constant change of velocity between two surfaces, whilst Poiseuille flow is a pressure-induced phenomenon. Due to no-slip conditions on the surfaces of the pin and the planet gear, the flow velocity components, u and v, take the respective values of these features. The Couette flow profile between the two surfaces is linear, whilst the Poiseuille flow profile is parabolic.

In order to determine the flow velocity distributions across the lubricating gap height, h, at an arbitrary point inside the lubricating gap, the pressure gradients in both the x and the y-directions, and thus the pressure distribution inside the lubricating oil film, must be known (equation (2.4) and equation (2.5)). Integrating the continuity equation (equation (2.1)) across the lubricating gap height, h, and assuming that

a) the density, ρ, is constant across h, and
b) there is no relative axial movement between the pin and the gear surfaces,

yields:

$$\underbrace{\frac{\partial}{\partial x}\left(\frac{\rho h^3}{12\mu}\frac{\partial p}{\partial x}\right)+\frac{\partial}{\partial y}\left(\frac{\rho h^3}{12\mu}\frac{\partial p}{\partial y}\right)}_{\text{Poiseuille terms}}=\frac{1}{2}\rho h\underbrace{\frac{\partial}{\partial x}(U_{\mathrm{P}}+U_{\mathrm{G}})}_{\text{Physical stretch}}\dots$$

$$\dots+\frac{1}{2}\rho(U_{\mathrm{P}}+U_{\mathrm{G}})\underbrace{\frac{\partial h}{\partial x}}_{\text{Physical wedge}}+\frac{1}{2}(U_{\mathrm{P}}+U_{\mathrm{G}})h\underbrace{\frac{\partial \rho}{\partial x}}_{\text{Density wedge}}\dots \tag{2.7}$$

$$\dots-\underbrace{\rho U_{\mathrm{G}}\frac{\partial h}{\partial x}}_{\text{Geometric squeeze}}+\underbrace{\rho(W_{\mathrm{G}}-W_{\mathrm{P}})}_{\text{Normal squeeze}}+\underbrace{h\frac{\partial \rho}{\partial t}}_{\text{Local expansion}}$$

In the equation above, ρ is the density of the fluid, h is the lubricating gap height, μ is the dynamic viscosity of the fluid, and $\partial p/\partial x$ and $\partial p/\partial y$ are the pressure gradients in the circumferential and the axial directions, x and y, respectively. The term $\partial/\partial t$ denotes the time derivative. The velocities of the surfaces of the gear and the pin are expressed by U_{G} and U_{P}, respectively. The normal gear and pin velocities, W_{G} and W_{P}, are generated by the relative motion of the surfaces normal to the direction of motion. Equation (2.7) is known as the general Reynolds equation. A full derivation from the Navier-Stokes equations has been carried out by numerous authors, for example Hamrock [26], who also provides a detailed description of the different terms in equation (2.7). Analysis carried out by Hamrock [26] concluded that the terms of physical stretch action, density wedge action and local expansion do not significantly contribute to the generation of pressure within the liquid film. Neglecting these terms yields the simplified Reynolds equation

$$\frac{\partial}{\partial x}\left(\frac{\rho h^3}{12\mu}\frac{\partial p}{\partial x}\right)+\frac{\partial}{\partial y}\left(\frac{\rho h^3}{12\mu}\frac{\partial p}{\partial y}\right)=\frac{1}{2}\rho(U_{\mathrm{P}}-U_{\mathrm{G}})\frac{\partial h}{\partial x}+\rho(W_{\mathrm{G}}-W_{\mathrm{P}}). \tag{2.8}$$

For steady-state operation of the journal bearing under investigation (Figure 2.1), U_{P} and W_{P} are zero, as the component is stationary with respect to the planet carrier. As W_{G} is equal to $U_{\mathrm{G}}\,\partial h/\partial x$, equation (2.8) can be rewritten as follows.

$$\frac{\partial}{\partial x}\left(\frac{\rho h^3}{12\mu}\frac{\partial p}{\partial x}\right)+\frac{\partial}{\partial y}\left(\frac{\rho h^3}{12\mu}\frac{\partial p}{\partial y}\right)=\frac{1}{2}U_{\mathrm{G}}\frac{\partial(\rho h)}{\partial x}. \tag{2.9}$$

Equation (2.9) not only allows the fluid properties to vary in the x and the y-directions, but also permits the bearing surfaces to be of finite length in the y-direction. Side leakage, i.e. flow in the y-direction, is associated with the second term on the left hand side of equation (2.9) and of high importance when analysing the oil outflow behaviour from a journal bearing. If the change of pressure in the y-direction, $\partial p/\partial y$, cannot be neglected, as is the case for journal bearings of finite length, an analytical solution to equation (2.9) does not exist. Instead, an iterative numerical approach must be used to obtain a solution. The internal journal bearing domain is therefore divided into calculational cells and a finite difference scheme is typically applied in order to approximate the partial differential equation (PDE) (equation (2.9)) by a series of algebraic equations that can be solved using a matrix solver. This method is described in detail by Khonsari and Booser [25].

There are a number of commercial software tools available to solve the Reynolds equation numerically, and thus obtain the fluid pressure distribution within the lubricating film of a journal bearing. The Gas Turbines and Transmissions Research Centre (G2TRC) at the University of Nottingham, for example, uses the multiphysics software package COMSOL [28]. For the journal bearing under investigation, the internal fluid film pressure distribution was determined using COMBROS [29]. The necessary work associated with setting up and running the COMBROS model, and post-processing its results was performed by Rolls-Royce Deutschland (RRD), as this work was not in scope for the research work presented in this thesis.

Figure 2.3 schematically shows the fluid pressure distribution within the lubricating film of the journal bearing under investigation at maximum load conditions.

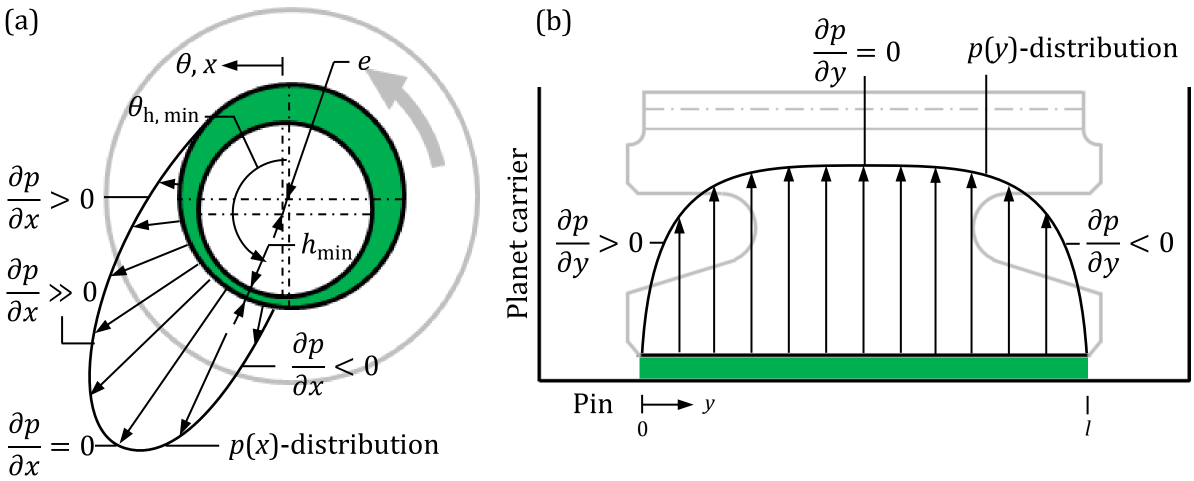

Figure 2.3: Fluid pressure distribution within the lubricating film of the journal bearing under investigation at maximum load conditions in the circumferential (a) and the axial (b) directions

Figure 2.4 shows a 2D contour plot of the fluid film pressure distribution in the journal bearing under investigation at maximum load conditions. Areas shaded in blue indicate areas of low pressure, whereas areas shaded in red indicate regions of high pressure.

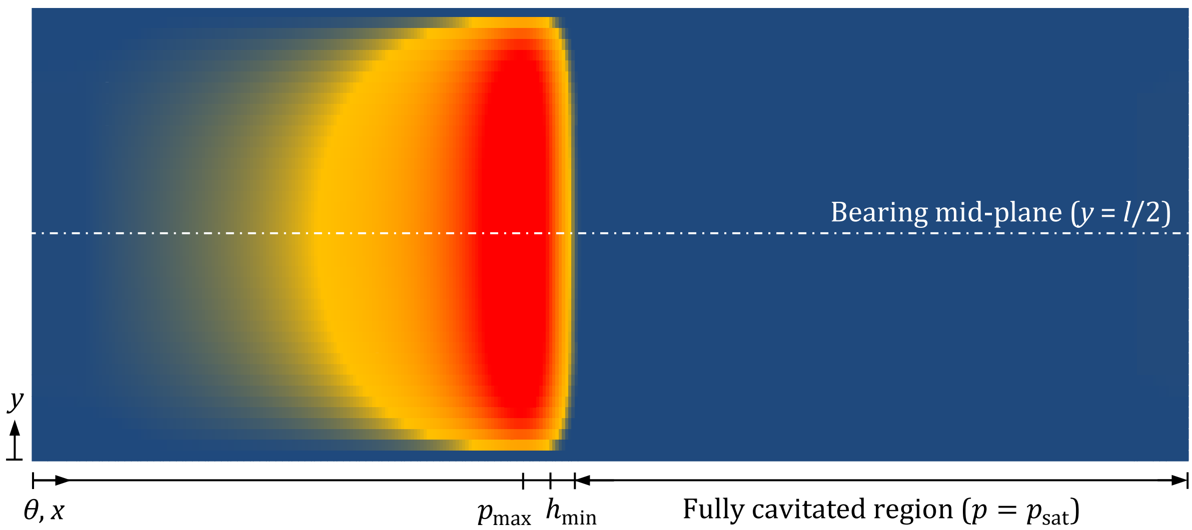

Figure 2.4: 2D contour plot of fluid film pressure distribution in journal bearing under investigation at maximum load conditions

In order for COMBROS [29] to solve the Reynolds equation (equation (2.9)), an ambient pressure boundary condition, $p = p_{\mathrm{amb}}$ was applied to the bearing end-faces ($y = 0$ and $y = l$). The conditional formatting capability of Microsoft Excel was used to visualise the fluid film pressure field, as COMBROS [29] does not include a graphical user interface (GUI). Close to the bearing end-faces ($y = 0$ and $y = l$), the grid spacing was chosen to be denser compared to other areas to better resolve the high axial pressure gradients, $\partial p/\partial y$. Since the fluid film pressure values, however, were visualised on an equidistant grid, their graphical representation shown in Figure 2.4 appears slightly distorted in the y-direction. Figure 2.5 shows the normalised circumferential pressure distribution at bearing mid-plane ($y = l/2$) at maximum load conditions.

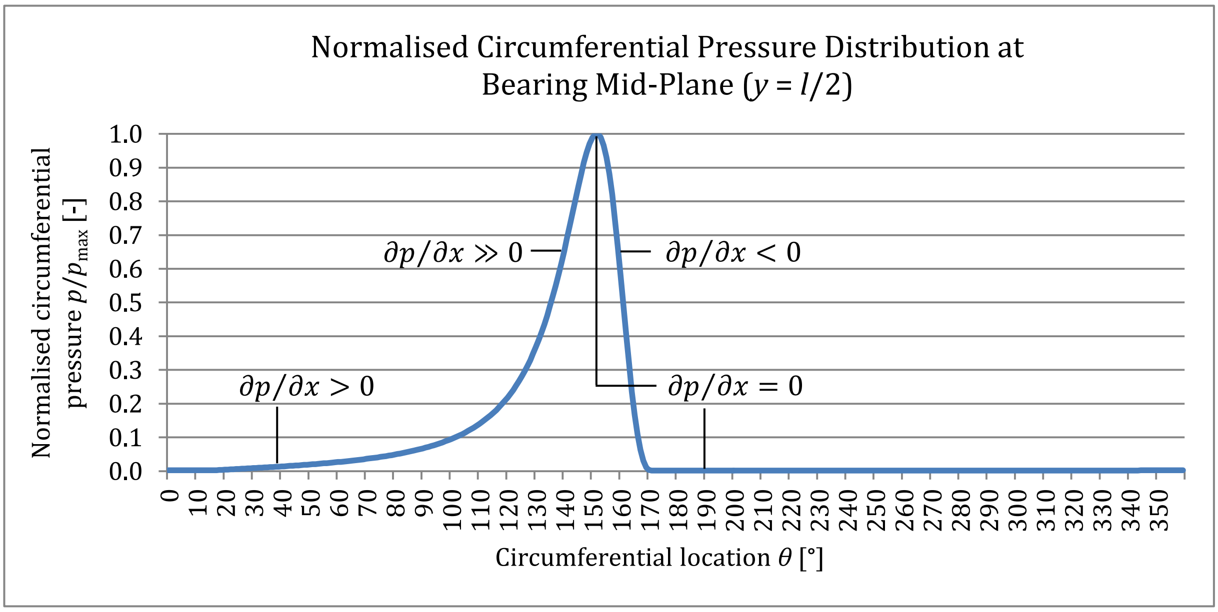

Figure 2.5: Normalised fluid film pressure distribution at bearing mid-plane ($y = l/2$) in journal bearing under investigation at maximum load conditions

Having determined the pressure values inside the lubricating fluid film, the pressure gradients, $\partial p/\partial y$ and $\partial p/\partial x$, respectively, can be derived, and thus the velocity profiles in the axial and the circumferential directions can be reconstructed. Figure 2.6 qualitatively shows the parabolic velocity profile in the axial direction for a positive and a negative axial pressure gradient, respectively. The velocity profile is described by equation (2.5).

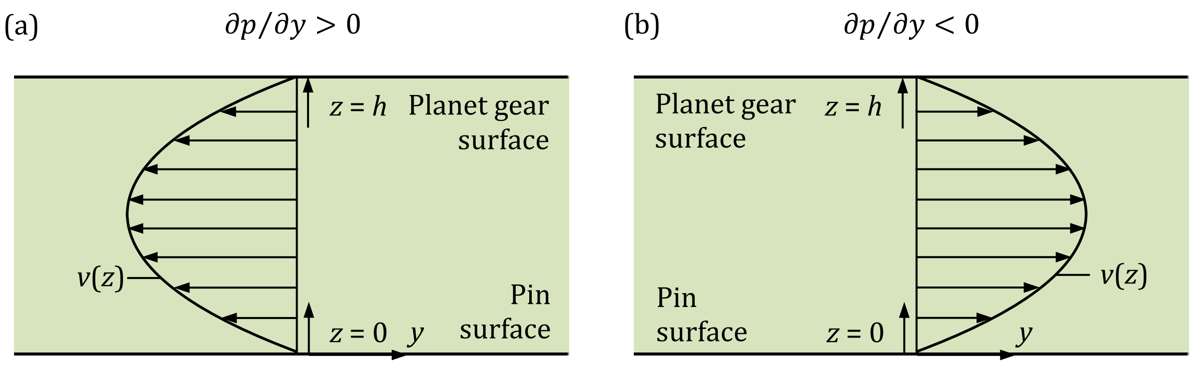

Figure 2.6: Velocity profile in the axial direction, y, for $\partial p/\partial y > 0$ (a) and $\partial p/\partial y < 0$ (b)

Figure 2.7 qualitatively shows the velocity profile in the circumferential direction for different circumferential pressure gradients. The velocity profile is described by equation (2.4).

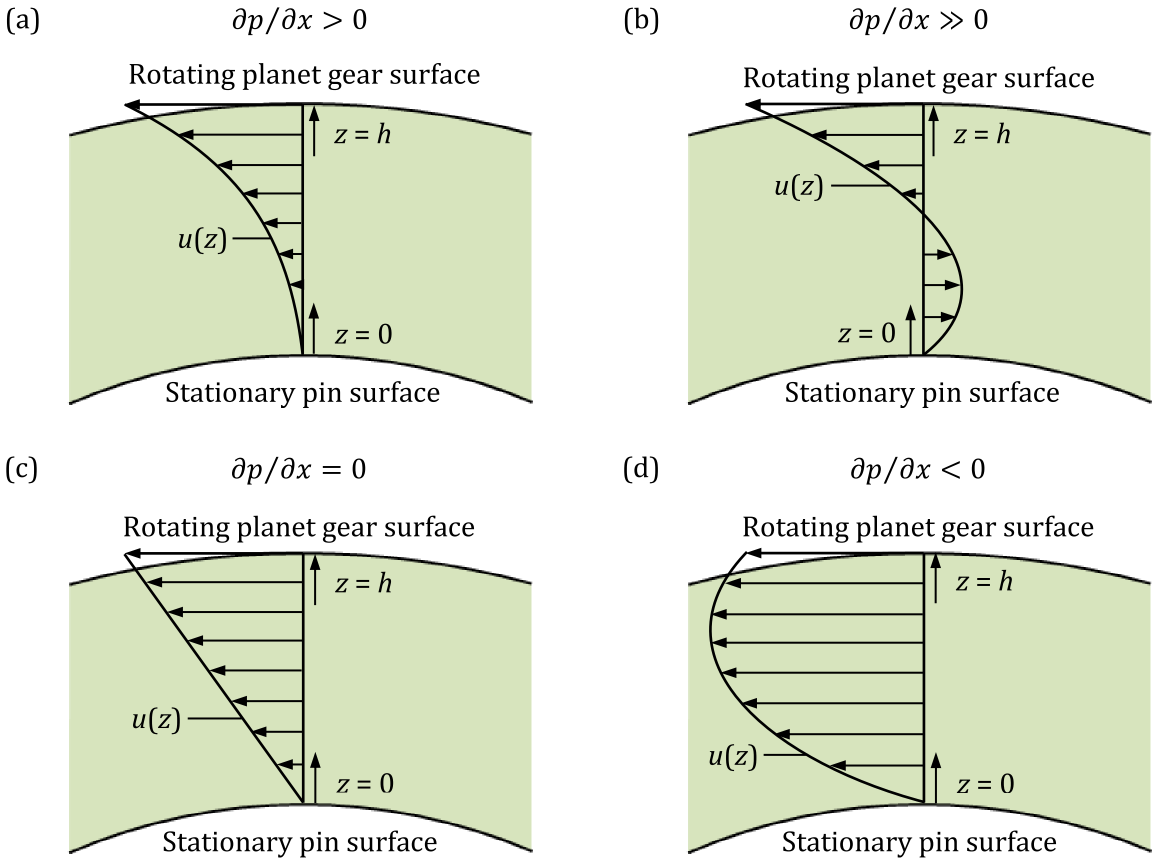

Figure 2.7: Velocity profiles in the circumferential direction, *x*, for different pressure gradients, $\partial p/\partial x$

Figure 2.7 (a) shows a typical velocity profile in the circumferential direction, x, for a modest positive pressure gradient, $\partial p/\partial x > 0$ (Figure 2.5), as it occurs in the convergent part of the lubricating gap at locations where h is still relatively large, i.e. far away from the maximum pressure location, $x_{p,\,\max}$. The velocity profile follows the function described by equation (2.4) and consists of a Couette flow and a Poiseuille flow component. As the pressure gradient, $\partial p/\partial x$, is positive, the Poiseuille flow component is directed against the Couette flow component.

For high positive pressure gradients, $\partial p/\partial x \gg 0$ (Figure 2.5), as they occur in the convergent part of the gap at locations where h is smaller, i.e. closer to $x_{p,\,\max}$, this can lead to localised backflow, as shown in Figure 2.7 (b).

At location $x_{p,\,\max}$, where the maximum film pressure is reached, $\partial p/\partial x$ equals zero (Figure 2.5). Hence, the Poiseuille flow term in equation (2.4) disappears and the flow velocity profile is linear (Couette flow), as shown in Figure 2.7 (c).

For negative pressure gradients, $\partial p/\partial x < 0$ (Figure 2.5), the Poiseuille flow component acts in the same direction as the Couette flow component (Figure 2.7 (d)). It should be noted that the maximum film pressure, $p_{\max}$, occurs before the minimum gap height, $h_{\min}$, is reached (Figure 2.3 (a)). Hence, at the location of the minimum gap height, $x_{h,\,\min}$, the pressure gradient in the circumferential direction is negative and the velocity profile qualitatively resembles that shown in Figure 2.7 (d).

In the divergent part of the gap, the film pressure reduces rapidly to the point at which cavitation occurs. Assuming that the lubricant is incompressible, cavitation is a requirement in order for the bearing to generate load carrying capability.

Two types of cavitation are encountered in liquid-film bearings [25]. Gaseous cavitation, for example, occurs when air, which is dissolved in the lubricant, comes out of solution, expands and forms bubbles as the film pressure drops below the saturation value, p_{sat}. This type of cavitation is typically encountered by statically loaded journal bearings, like the one under investigation. According to Szeri [27], p_{sat} is equal or just below the ambient atmospheric pressure, p_{amb}, and constant within the cavitation region. Vapour cavitation occurs when vapour is being formed due to the film pressure dropping below the lubricant's vapour pressure, p_{vap}. This type of cavitation is typically encountered in dynamically loaded journal bearings. As the pressure in the cavitation region, p_{cav}, is assumed to be constant, the pressure gradients in the x and the y-directions, $\partial p/\partial x$ and $\partial p/\partial y$, respectively, are zero. Hence, a Couette flow profile, as shown in Figure 2.7 (c), forms in the x-direction and no axial flow component is present.

As demonstrated above, analysing the general Reynolds equation (equation (2.7)) and the terms for the flow velocity components in the circumferential and the axial directions (equations (2.4) and (2.5)) in detail, allows tremendous insights into the internal journal bearing fluid flow behaviour to be gained.

Solving the Reynolds equation is sufficiently accurate for most engineering problems and CFD analysis are usually not performed in the preliminary design stage of journal bearings. If, however, three-dimensional and complex bearing geometries are involved, or when more detailed solutions are required, CFD analyses need to be carried out in order to solve the Navier-Stokes equations. Guo et al [30], for example, computed the fluid film pressure distribution in a journal bearing with the CFD solver CFX-TASCflow and compared the results to those obtained with tools that solve the Reynolds equation, namely VT-FAST and VT-EXPRESS, which were both developed by the Virginia Tech University, and DyRoBeS-BePerf, developed by Chen [31]. Good agreement of the results was found.

Moreover, Uhkötter [32] used a CFD approach in order to investigate mixing processes in the oil feed grooves of journal bearings; an effect that cannot be captured by the Reynolds equation.

In order to confirm the validity of one key assumption of the Reynolds equation, namely laminar flow, for the journal bearing under investigation, the Reynolds numbers, Re_u and Re_v, were calculated for the flow velocity components in the circumferential and the axial directions, u and v, respectively. Re relates inertial to viscous forces and can be calculated by

$$\mathrm{Re}_u = \frac{\omega_\mathrm{G}\, d_\mathrm{G}\, h_0 \rho}{2\,\mu}. \tag{2.10}$$

$$\mathrm{Re}_v = \frac{v_0\, h_0 \rho}{\mu}. \tag{2.11}$$

In the equations above, ω_G is the angular gear velocity, d_G is the diameter of the planet gear bore (Figure 2.1), h_0 is the lubricating gap height at zero-eccentricity, which is given by half the difference between the gear bore diameter, d_G, and the pin diameter, d_P (Figure 2.1).

$$h_0 = \frac{d_\mathrm{G} - d_\mathrm{P}}{2} \tag{2.12}$$

The liquid's density is denoted ρ, μ is the liquid's dynamic viscosity and v_0 is the mean flow velocity component in the axial direction. It can be calculated based on the known oil volume flow rate, $\dot{V}_\mathrm{in}$, supplied to the bearing and the outflow area, A_out.

$$v_0 = \frac{\dot{V}_\mathrm{in}}{A_\mathrm{out}} = \frac{4\dot{V}_\mathrm{in}}{\pi(d_\mathrm{G}^2 - d_\mathrm{P}^2)} \tag{2.13}$$

When reaching a critical Reynolds number of $\mathrm{Re}_\mathrm{crit} = 2{,}000$ [27], the flow becomes turbulent. The transition between the laminar and the turbulent regime is preceded by flow instabilities. In general, a journal bearing can experience parallel and centrifugal flow instabilities [27]. Parallel flow instabilities are characterised by the Reynolds number, Re, whilst centrifugal instabilities, which can occur in flows with curved streamlines, are characterised by the Taylor number, Ta. It relates centrifugal forces to viscous forces and can be calculated by

$$\mathrm{Ta} = \frac{2\,h_0}{d_\mathrm{G}}\,\mathrm{Re}^2. \tag{2.14}$$

The critical Taylor number, $\mathrm{Ta}_\mathrm{crit}$, for the transition from laminar to turbulent flow, which is characterised by the formation of Taylor vortices, is 1,708 [33]. Centrifugal instability can only occur in systems with a rotating inner surface [33]. Thus, for the specific case under investigation only parallel flow instabilities can occur, providing Re is sufficiently large.

In order to confirm the validity of the use of the Reynolds equation (equation (2.7)) for the case under investigation, the Reynolds numbers, Re_u and Re_v, were calculated at maximum load conditions. With $\mathrm{Re}_u = 1{,}440$ and $\mathrm{Re}_v = 100$, the flow is fully laminar.

2.3 External Journal Bearing Flow Characteristics

External journal bearing flow characteristics can be considered for the single-phase flow field and the two-phase air-oil flow field, both of which will be investigated in the following sections. The aim of this section is to provide an appreciation of the flow behaviour and the flow structures within the external domain of a journal bearing. Considering the single-phase air flow field (section 2.3.1) and the two-phase air-oil flow field (section 2.3.2 and section 2.3.3) for the domain under investigation, allows key flow behaviours to be anticipated and similarities to existing experimental and analytical data to be identified. This provides valuable information, which will be referred to in the appropriate sections for the validation of the CFD analysis of simplified models.

2.3.1 Single-Phase Flow Field Considerations

When considering an epicyclic gearbox in star configuration (Figure 1.2), the domain under investigation consists of a stationary pin and planet carrier, and a rotating planet gear. In the literature, this configuration is generally described as a rotor-stator system. The domain, which is bounded by the stationary and the rotating components, is referred to as the rotor-stator cavity. Due to the importance of rotor-stator cavities in the secondary air system of aero-engine compressors and turbines, extensive analytical, experimental and numerical investigations have been carried out with single-phase air flow on free and enclosed discs.

Most notably, according to Schlichting and Gersten [34], research with single-phase air flow over a free rotating disc was carried out by von Kármán [35], who was the first to solve the fluid flow governing equations (section 2.4) for this application. In order to do so, von Kármán [35] introduced a non-dimensional wall distance,

$$\zeta = y\sqrt{\frac{\omega_{\mathrm{D}}}{\nu}}. \tag{2.15}$$

In the equation above, y is the axial coordinate, i.e. the coordinate normal to the disc surface, ω_{D} is the angular velocity of the disc and ν is the kinematic viscosity of the surrounding fluid. By using the following definitions for the circumferential, the axial and the radial velocity components, u, v and w, respectively,

$$u = r\,\omega_{\mathrm{D}}\,G(\zeta), \quad v = \sqrt{\omega_{\mathrm{D}}\,\nu}\,H(\zeta), \quad w = r\,\omega_{\mathrm{D}}\,F(\zeta), \tag{2.16}$$

von Kármán [35] was able to determine the velocity field generated by a rotating disc (Figure 2.8).

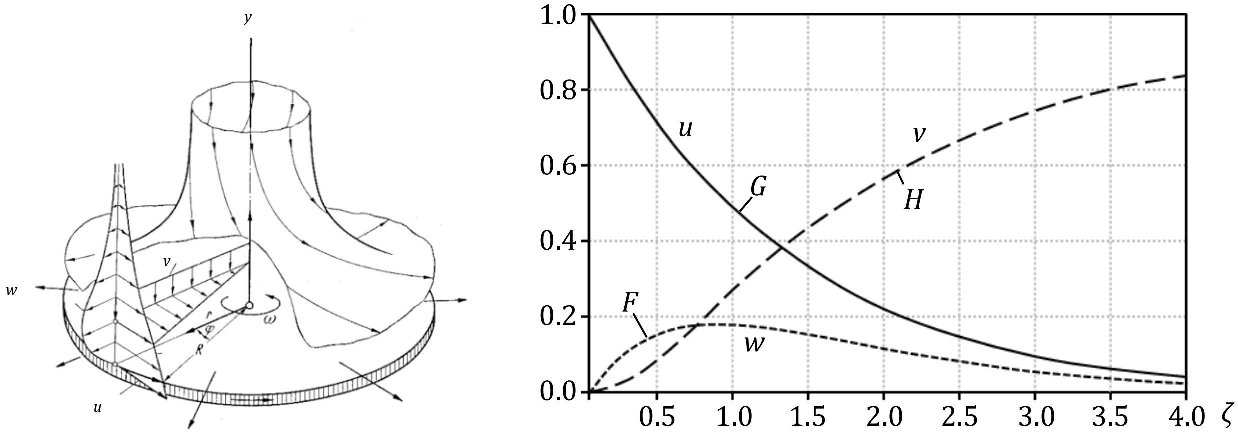

Figure 2.8: Fluid flow velocity distribution on a rotating disc in a fluid at rest according to von Kármán [35]

Within the relatively small boundary layer, there occurs a pumping effect forcing the fluid particles to move radially outwards. In order to satisfy continuity, additional fluid is entrained axially. Consequently, a three-dimensional flow field develops. Depending on the Reynolds number,

$$\mathrm{Re} = \frac{u\,r\,\rho}{\mu} = \frac{\omega_{\mathrm{D}}\,r^2\,\rho}{\mu}, \tag{2.17}$$

the flow over a rotating disc can be laminar, transitional or turbulent. Re depends on the angular disc velocity, ω_{D}, the local radius, r, and the dynamic viscosity, μ. Measurements carried out by Theodorsen and Regier [36] showed that laminar flow prevails for Reynolds numbers which are lower than the critical Reynolds number, $\mathrm{Re}_{\mathrm{crit}} = 0.5 \times 10^5$. This value marks the beginning of the transition phase, which typically takes place between $0.5 \times 10^5 \leq \mathrm{Re}_{\mathrm{crit}} \leq 3.1 \times 10^5$. For even higher Reynolds numbers, the flow is fully turbulent. The values for $\mathrm{Re}_{\mathrm{crit}}$ may vary depending on properties like the disc roughness.

In order to determine the prevailing flow regime on the rotating planet gear, the Reynolds numbers were calculated for both air and oil at the upper domain boundary, i.e. the planet gear tip diameter (Figure 2.1). It is required to determine Re for both fluid phases, as the oil flow path is not known a priori. Surfaces exhibiting oil build-up can only be identified by appropriate experimental or numerical analysis of the domain under investigation. Knowing the Reynolds numbers is important, as the flow regime governs whether turbulence modelling is needed for CFD analysis of external oil flow from the journal bearing under investigation or not.

The following table summarises the values for Re for a non-orbiting planet gear configuration at different operating conditions.

Table 2.1: Summary of Reynolds numbers, Re, in domain under investigation

Operating condition	Re for air	Re for oil
Minimum operational load conditions	0.59×10^5	1.69×10^5
Typical operational load conditions	0.66×10^5	19.79×10^5
Maximum operational load conditions	3.42×10^5	24.84×10^5

Table 2.1 shows that, depending on the operating condition, the prevailing flow regimes for both air and oil, are either transitional or turbulent. Thus, turbulence modelling will be required when investigating the flow behaviour in the domain under investigation numerically.

As the domain under investigation is bounded by the stationary pin and planet carrier (Figure 2.1), it is necessary to review the influence of these components on the expected flow field behaviour. Fundamental investigations of enclosed disc systems have been carried out by Daily and Nece [37], Dorfman [38] and Owen and Rogers [39]. Due to the finite chamber dimensions, the flow field can expected to be very different compared to that generated by a free rotating disc. Figure 2.9 qualitatively shows the expected circumferential and radial velocity distributions, $u(y)$ and $w(y)$, respectively, for laminar flow according to Daily and Nece [37].

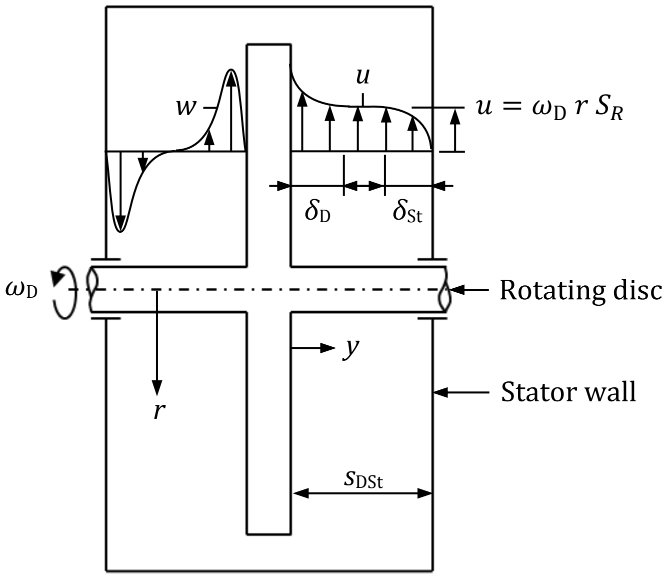

Figure 2.9: Enclosed disc with circumferential and radial velocity distributions, *u* and *w*, respectively, according to Daily and Nece [37]

In Figure 2.9, u and w are the circumferential and the radial velocities, respectively, r is the radial coordinate, y is the axial coordinate, ω_{D} is the disc's angular velocity, and S_R is the swirl ratio, which can take values between zero and one. The boundary layers forming on the disc (rotor) and the stator walls have the thickness δ_{D} and δ_{St}, respectively. There is a core of fluid rotating between the disc and the stator wall (Batchelor-type flow) with a circumferential velocity component of

$$u = \omega_{\mathrm{D}}\, r\, S_R. \tag{2.18}$$

The flow field can be categorised into four regimes, namely:

a) Regime I: Laminar flow, close clearance. The boundary layers of the disc and the stator wall are merged. As a result, there is a continuously varying velocity distribution across the axial gap, s_{DSt}, between the disc and the stator wall.
b) Regime II: Laminar flow, large clearance. The boundary layers of the disc and the stator wall are separated, i.e. the combined thickness of δ_{D} and δ_{St} is less than the axial gap s_{DSt}. As a result, there is a region with no change in velocity (Figure 2.9).
c) Regime III: Turbulent flow, close clearance. The boundary layers are merged as per regime I.
d) Regime IV: Turbulent flow, large clearance. The boundary layers are separated as per regime II.

In contrast to the rotor-stator system shown in Figure 2.9, however, the domain under investigation (Figure 2.1) is not fully enclosed, as there is no shroud or housing wall covering the top. Instead, the domain is open to the gearbox chamber. Open rotor-stator systems exhibit the same flow regimes as those observed in fully enclosed systems. They can be classified into systems with and without superposed radial flows (Figure 2.10).

A phenomenon that can occur in open systems is that of ingress. Owen and Rogers [39] stated that, when a superposed radial flow is present, the net flow will be radially outwards. However, this does not necessarily mean that all the flow is directed outwards. If the amount of fluid pumped out of the system by the rotor is larger than the amount of fluid supplied by the superposed flow, then ingress occurs (Figure 2.10b). This means that external fluid from the surroundings is entrained into the system. When the surrounding fluid is at rest, the flow structure will be altered such that the core rotation is reduced. For large clearance open rotor-stator systems with radially superposed mass flow, the core rotation can be reduced to zero, i.e. $S_R = 0$. As a consequence, flow structures with a superposed radial component are more complex compared to those observed in fully enclosed systems.

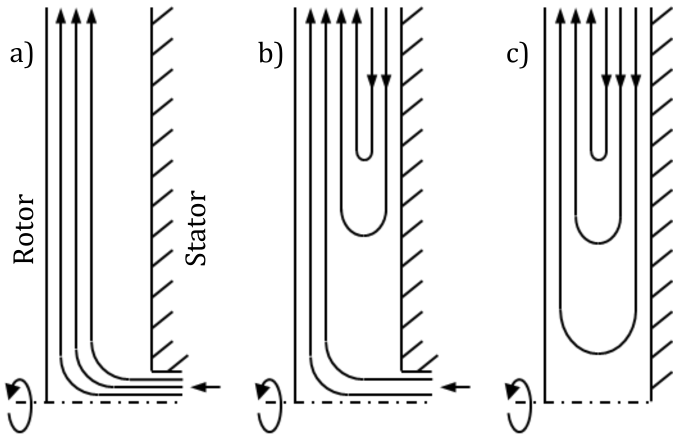

Figure 2.10: Schematic diagram of flow structures for large clearance rotor-stator systems according to Owen and Rogers [39] with large superposed outflow (a), small superposed outflow (b) and no superposed outflow (c)

Due to the fundamental research described above, the single-phase flow patterns generated by free rotating discs, and enclosed and open rotor-stator systems, are well understood.

2.3.2 Two-Phase Flow Field Considerations – Oil Flow Path

Considering the case of oil outflow from a journal bearing in an epicyclic gearbox in star configuration (Figure 1.2), the domain under investigation (Figure 2.1) can, in fact, be regarded as a rotor-stator system with superposed mass flow. The flow field developing in the domain under investigation, however, will be very much dependent on the oil flow regime, e.g. droplets, ligaments, sheets or films, and their characteristics. The flow behaviour will be driven by the displacement of the lighter flow component, i.e. air, by the denser one, i.e. oil. Depending on the oil properties, such as the density, ρ, the dynamic viscosity, μ, and the surface tension, σ, and the operating conditions, like the angular velocity of the gear, ω_{G}, the height of the lubricating gap, h, and the oil mass flow rate, $\dot{m}$, the following two principle flow paths can occur. Oil entering into the external flow domain:

a) travels axially along the pin surface towards the planet carrier, following flow path (a) in Figure 2.1 or
b) attaches to the rotating gear, from where it is driven radially outwards along the gear contour due to the centrifugal force, following flow path (b) in Figure 2.1.

Naturally, depending on the specific oil properties and operating conditions, the oil emerging from the lubricating gap can exhibit any combination of the two limiting cases described above.

If the oil outflow is characterised by high axial momentum and low internal fluid friction, i.e. low viscosity, it is anticipated that the fluid's axial velocity will only marginally reduce when emerging from the lubricating gap. Consequently, for this case, the oil film will travel in the axial direction across the pin surface towards the planet carrier, following flow path (a) in Figure 2.1.

In contrast, if the oil outflow is characterised by low axial momentum and high internal fluid friction, i.e. high viscosity, it is anticipated that the fluid's axial velocity will rapidly reduce when emerging from the lubricating gap. The film thickness will consequently increase. If it increases to an extent that the effects of body forces can no longer be neglected, the centrifugal force caused by the swirling motion of the fluid will drive it radially outwards. Thus, it will attach to the planet gear chamfer and it will follow the gear contour, i.e. flow path (b) in Figure 2.1. In this case, the flow will behave like the flow over a rotating cup or disc, which has been subject to analyses on numerous occasions (section 2.3.3).

If the oil emerging from the lubricating gap attaches to the rotating gear, it will either follow flow path (b_1) or (b_2) (Figure 2.2). Whether one or the other flow path is followed mainly depends on the magnitude of the forces acting on the liquid film at the location at which flow path (b) splits into either path (b_1) or (b_2) (diameter d_1 in Figure 2.2).

If the inertial force dominates over the centrifugal force generated by the rotating motion of the planet gear and the surface tension force, the flow path can be expected to follow path (b_1) (Figure 2.2). Both the centrifugal force and the surface tension force will lead to a deflection of the film away from the extended gear chamfer surface towards the vertical planet gear axis, as shown in Figure 2.2. The associated deflection angle in the y-z-plane is denoted λ.

If the centrifugal force and the surface tension force dominate over the inertial force, the flow path can be expected to follow path (b_2) (Figure 2.2). In order for the flow to follow path (b_2) (Figure 2.2), the liquid film must negotiate the step formed by the gear chamfer and the vertical face of the planet gear base (diameter d_1 in Figure 2.2). More specifically, the gear geometry in this area forms a backwards-facing inclined step.

Liquid flow over this type of feature has been investigated by Friedrich et al [45], who established a separation criterion for shear-driven films in separated flows based on a force balance model. In analogy to Friedrich's et al [45] definition shown in Figure 2.11, film separation indicates that the flow follows path (b_1), whereas bulk flow attachment to the wall indicates that the flow follows path (b_2).

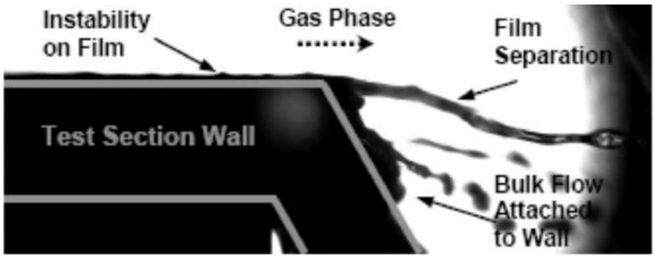

Figure 2.11: Film interaction with a separated gas flow at the corner of a backwards-facing inclined step according the Friedrich et al [45]

Friedrich et al [45] developed a force balance model based on the conservation of linear momentum. It accounts for inertial forces, surface tension forces and body forces, i.e. the gravitational force. The model was developed for a two-dimensional channel flow and allows the onset of film separation, as shown in Figure 2.11, to be predicted.

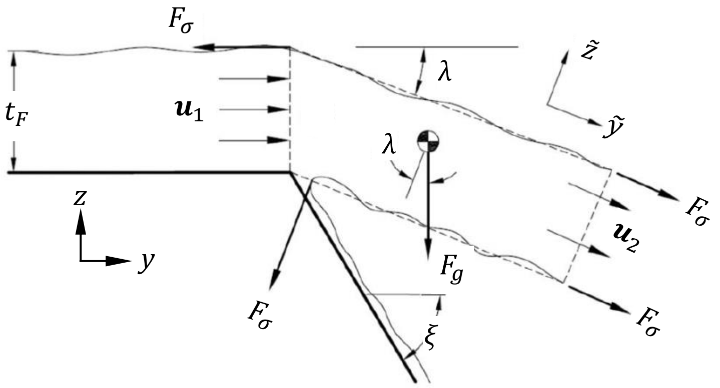

Figure 2.12: Momentum analysis for a control volume on a liquid film interacting with a separated gas flow at the corner of a backwards-facing inclined step according the Friedrich et al [45]

Balancing the forces in the local $\tilde{z}$-direction, which is perpendicular to the flow vector of the liquid film after separation, $\boldsymbol{u}_2$, yields

$$\rho|\boldsymbol{u}_1|^2 t_F \sin\lambda = \sigma \sin\lambda + \sigma + \rho\, g\, t_F\, l_\mathrm{b} \cos\lambda. \tag{2.19}$$

In the equation above, ρ is the liquid density, $\boldsymbol{u}_1$ is the liquid film velocity vector, t_F is the film thickness, λ is the deflection angle, σ is the surface tension, g is the gravitational acceleration and l_b is the film break-up length, which Friedrich et al [45] determined by using existing correlations established by Arai and Hashimoto [46]. With the equation above, the deflection angle, λ, can be calculated. If $\lambda > \xi$, the bulk flow will attach to the backwards-facing inclined step and no separation occurs. In contrast, if $\lambda < \xi$, bulk flow separation will occur. In order to make Friedrich's et al [45] force balance model applicable to rotating flows over backwards-facing inclined steps, it needs to be modified to account for the additional effects caused by the fluid's swirling motion (section 3.6).

2.3.3 Two-Phase Flow Field Considerations – Oil Flow Regime

If the oil emerging from the lubricating gap of the journal bearing attaches to the rotating planet gear, it will follow flow path (b), as shown in Figure 2.1. In this case, the flow will behave like the flow over a rotating cup or disc, which has been subject to analyses on numerous occasions.

The following sections introduce the different flow regimes and liquid disintegration mechanisms that have been observed during experimental tests in the past. The results of the historical investigations provide the tools to characterise the oil outflow behaviour of a journal bearing. Applied to the specific case under investigation, this provides additional data for the validation of the CFD analysis presented in chapter 4.

Fundamental studies of liquid disintegration by spinning cups were performed by Fraser et al [40] and, more recently, by Liu et al [41]. The cup geometries used by both Fraser et al [40] and Liu et al [41] are shown in Figure 2.13.

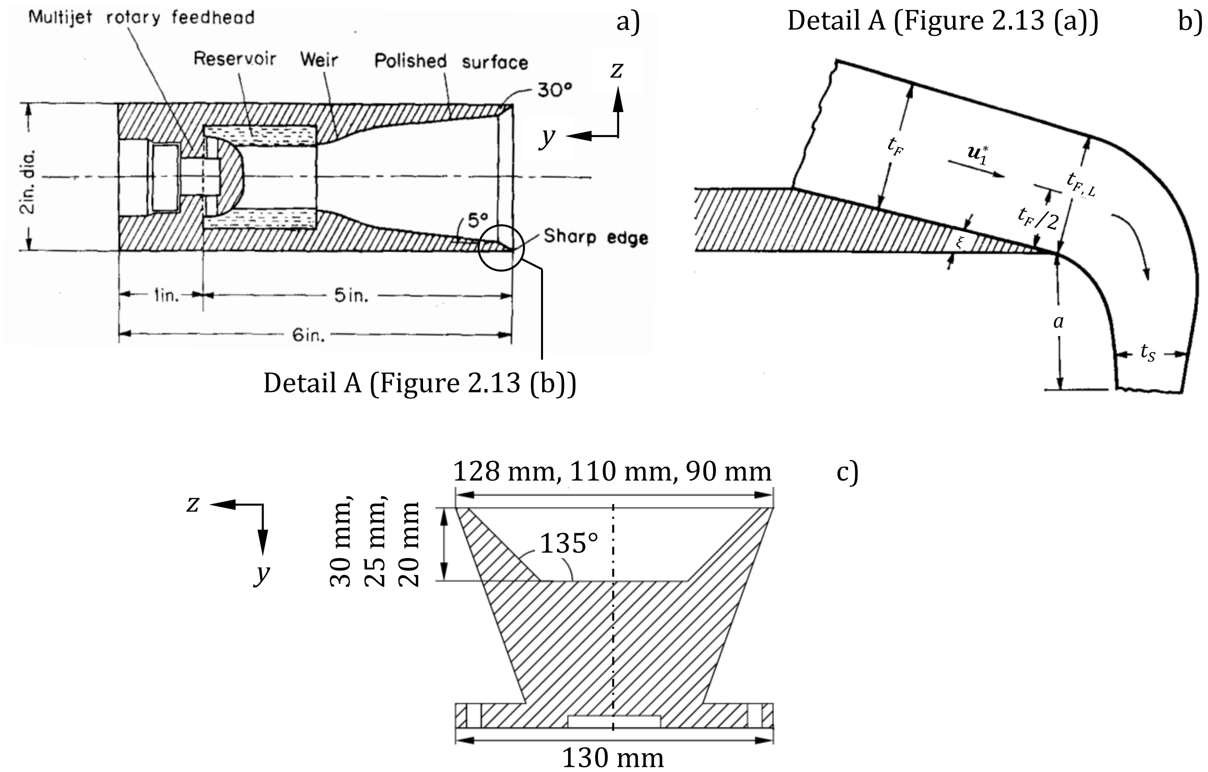

Figure 2.13: Details of cups used by Fraser et al [40] (a) and (b), and Liu et al [41] (c)

Whilst Fraser et al [40] used a cup with a small opening angle of $\xi = 5°$, Liu et al [41] used a cup with an opening angle of $\xi = 45°$, which is more similar to the chamfer angle applied to the gear base, which is $\xi = 30°$ (Figure 2.2).

The investigations of both groups of researchers concluded that, with increasing flow rate and/or rotational speed of the cup, the following disintegration regimes can be observed: direct droplet formation (Figure 2.14 (a), Figure 2.15 (a)), ligament formation (Figure 2.14 (b), Figure 2.15 (b)) and sheet formation (Figure 2.14 (c), (d) and (e), Figure 2.15 (c)).

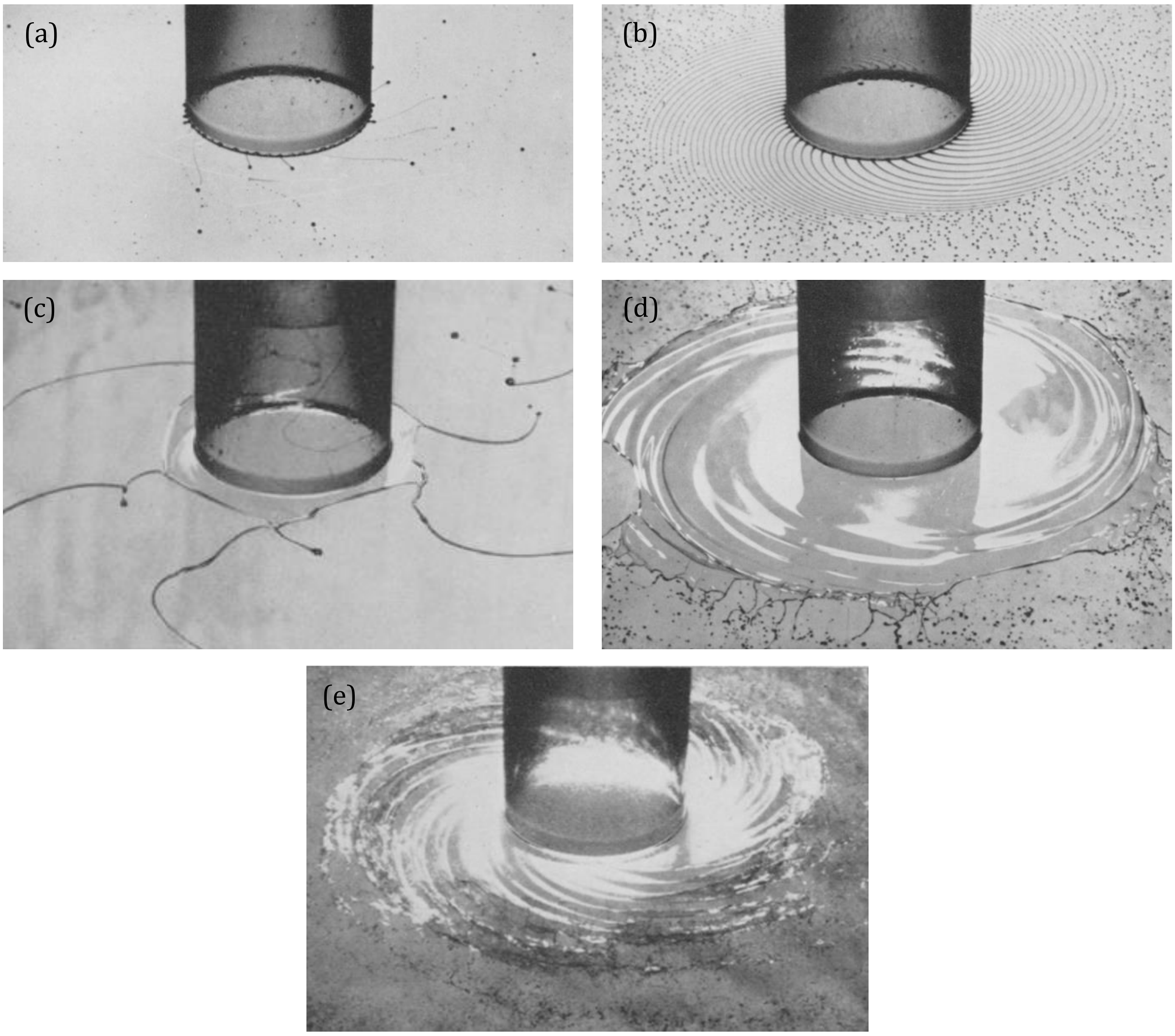

Figure 2.14: Fluid disintegration by a rotating cup with increasing speed and flow rate according to Fraser et al [40]. Direct droplet formation (a), ligament formation (b), sheet formation with rim disintegration (c), sheet formation with combined rim and wave disintegration (d), sheet formation with wave disintegration (e).

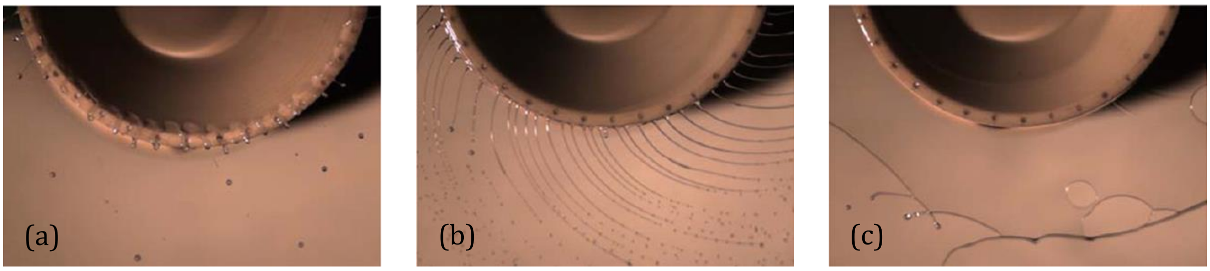

Figure 2.15: Fluid disintegration by a rotating cup with increasing speed and flow rate according to Liu et al [41]. Direct droplet formation (a), ligament formation (b), sheet formation (c).

When liquid is supplied to a diverging rotating cup, the frictional force will rapidly accelerate the fluid to the speed of the rotating cup. The resulting centrifugal force, opposed by viscous drag, causes the liquid layer to flow towards the rim of the cup. Disintegration occurs when surface tension and viscous forces are overcome by the centrifugal force. At high circumferential velocities, this process is aided by the aerodynamic action of the atmosphere.

In Figure 2.14 (a), which is characterised by a low liquid flow rate and a low rotational speed, the liquid spreads out towards the cup lip, where it forms a ring. As liquid continues to flow into the ring, its inertia increases and overcomes the restraining surface tension force. Figure 2.14 (a) shows the disturbances which appear on the outer edge and grow in size until liquid is centrifuged off as discrete droplets of uniform size. In the beginning, the droplet remains attached to the rim of the cup by a fine thread. When the droplet is finally detached, the retaining thread breaks down into a chain of small satellite droplets. Figure 2.15 (a) shows a similar disintegration mechanism. However, the oil flow rate is insufficient to form a ring at the cup lip and the oil film on the cup surface disintegrates into finger-like structures before the lip of the cup is reached.

When the liquid flow rate is increased, as shown in Figure 2.14 (b) and Figure 2.15 (b), the retaining threads grow in thickness and form long ligaments. As they extend into the atmosphere, these ligaments are stretched and finally broken down into strings of droplets.

When further increasing the flow rate, the ligaments are unable to remove all the liquid and the liquid ring at the rim of the cup is forced outwards. A thin sheet of liquid extends around the lip, as shown in Figure 2.14 (c) and Figure 2.15 (c). This type of sheet disintegration is called sheet rim disintegration.

Increasing the flow rate even further causes the liquid sheet to interact with the surrounding air. Exponentially growing waves, which extend from the cup lip and which are normal to the liquid flowlines, are formed. The generated fragments subsequently contract into unstable threads which, in turn, break down into droplets. This type of sheet disintegration is called combined sheet rim and wave disintegration and is illustrated in Figure 2.14 (d).

A further increase of flow rate and rotational speed causes the disintegration type to transition to sheet wave disintegration (Figure 2.14 (e)). Fraser et al [40] established that sheet wave disintegration occurs for circumferential cup velocities of more than 8 m/s. For circumferential cup velocities less than that combined sheet rim and wave disintegration or sheet rim disintegration prevail.

Fraser et al [40] carried out fundamental research on characterising the flow over the surface of a rotating cup with subsequent liquid disintegration. In their work, the authors stated relationships for the mean liquid velocity, $|\boldsymbol{u}_1^*|$, and the liquid film thickness, t_F, along the surface of the rotating cup. These relationships had previously been derived by Hinze and Milborn [44]. Subscript "1" denotes the conditions before liquid separation from the rim of the rotating component and superscript "*" indicates that the flow velocity vector, $\boldsymbol{u}_1$, is projected into the y-z-plane (Figure 2.13 (b)). Due to the opening angle of the cup, ξ, $\boldsymbol{u}_1^*$ has the axial and the radial flow velocity component, v_1 and w_1, respectively.

$$|\boldsymbol{u}_1^*| = \left(\frac{2\,\dot{V}^2\,n^2\,\sin\xi}{3\,d\,\nu}\right)^{\frac{1}{3}} \tag{2.20}$$

$$t_F = \left(\frac{3\,\dot{V}\,\nu}{2\,\pi^3\,d^2\,n^2\sin\xi}\right)^{\frac{1}{3}} \tag{2.21}$$

In the equation above, $\dot{V}$ is the volumetric flow rate, n is the rotational speed, ξ is the opening angle of the cup (Figure 2.13), d is the cup diameter and ν is the kinematic viscosity. Moreover, a criterion for sheet formation was established, which is given by the following relationship.

$$\frac{\rho\,n^{0.67}\,\dot{V}^{1.14}\,\nu^{0.19}}{\sigma\,d^{0.81}} > 0.363 \tag{2.22}$$

The transition volume flow rate, $\dot{V}_2$, from ligament to sheet formation is hence defined by

$$\dot{V}_2 = 0.411\,\frac{\sigma^{0.877}\,d^{0.710}}{\rho^{0.877}\,n^{0.588}\,\nu^{0.167}}. \tag{2.23}$$

In the equations above, ρ is the liquid's density, n is the rotational speed of the cup, $\dot{V}$ is the volumetric flow rate, ν is the liquid's kinematic viscosity, σ is the surface tension and d is the cup diameter at the lip.

Fraser et al [40] did not establish a criterion for ligament formation, as their research was focused on characterising liquid sheets and their properties. Two of the liquid sheet characteristics investigated were the break-up length, l_{b}, and the radial extent of the sheet, a, i.e. the radial distance between the lip of the cup and the point of sheet disintegration (Figure 2.16).

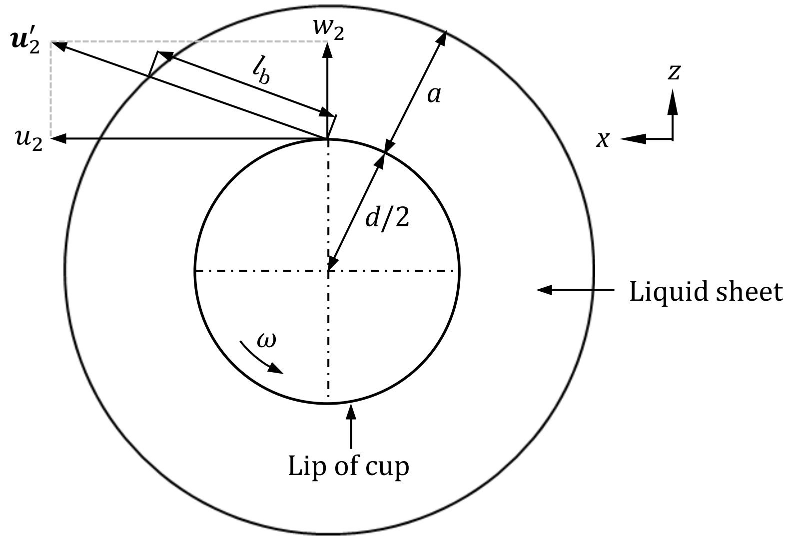

Figure 2.16: Geometry of liquid sheet according to Fraser et al [40]

Figure 2.16 schematically shows the difference between the radial extent of the sheet, a, and the liquid break-up length l_{b}. The circumferential and the radial velocity components are denoted u_2 and w_2, respectively. Subscript "2" denotes the conditions after liquid separation from the rim of the rotating component. Both velocity components, u_2 and w_2, combined give the vector $\boldsymbol{u}_2'$. The superscript indicates that the velocity vector, $\boldsymbol{u}_2$, is projected into the x-z-plane.

Fraser et al [40] recognised that under normal operating conditions, combined rim and wave disintegration (Figure 2.14 (d)) and wave disintegration (Figure 2.14 (e)) predominate. Depending on the sheet disintegration regime, i.e. combined rim and wave disintegration (subscript "rw") or wave disintegration (subscript "w"), the break-up length, l_{b}, and the radial extent of the sheet, a, can be calculated according to Fraser et al [40] as follows.

$$l_{\mathrm{b,\,rw}} = \left(15.6 \times 10^4\, \nu_R^{0.185}\, \frac{(\sigma\, \dot{m})^{\frac{2}{3}}}{(n\, d)^2}\right)^{\frac{1}{2}} \tag{2.24}$$

$$l_{\mathrm{b,\,w}} = \left(31.5 \times 10^4\, \nu_R^{0.25}\, \frac{(\sigma\, \dot{m})^{\frac{2}{3}}}{(n\, d)^2} + 0.6\right)^{\frac{1}{2}} \tag{2.25}$$

$$a_{\mathrm{rw}} = \left(15.6 \times 10^4\, \nu_R^{0.185}\, \frac{(\sigma\, \dot{m})^{\frac{2}{3}}}{(n\, d)^2} + \frac{d^2}{4}\right)^{\frac{1}{2}} - \frac{d}{2} \tag{2.26}$$

$$a_{\mathrm{w}} = \left(31.5 \times 10^4\, \nu_R^{0.25}\, \frac{(\sigma\, \dot{m})^{\frac{2}{3}}}{(n\, d)^2} + \frac{d^2}{4} + 0.6\right)^{\frac{1}{2}} - \frac{d}{2} \tag{2.27}$$

In the equations above, ν_R is the ratio of the kinematic viscosities of oil and water, σ is the surface tension, $\dot{m}$ is the oil mass flow rate, n is the rotational speed of the cup and d is the cup diameter. For equations (2.24) to (2.27), $l_{\mathrm{b,\,rw}}$, $l_{\mathrm{b,\,w}}$, a_{w}, a_{rw} and d are in inches, σ is in dyn per centimetre, $\dot{m}$ is in pounds per hour and n is in revolutions per minute.

Whilst the research carried out by Fraser et al [40] was focused on characterising the properties of oil sheets formed by liquid flow over rotating cups, Liu et al [41] concentrated their investigations on all three liquid disintegration types, i.e. droplet formation, ligament formation and sheet formation, and the transition conditions from one regime to another. In order to allow different operating conditions to be compared, Liu at al [41] defined the following non-dimensional quantities:

$$\dot{V}^+ = \frac{\dot{V}}{r^3\, \omega} \tag{2.28}$$

$$\mathrm{St} = \frac{\mu^2}{\rho\, r\, \sigma} \tag{2.29}$$

$$\mathrm{We} = \frac{\rho\, \omega^2\, r^3}{\sigma} \tag{2.30}$$

The non-dimensional volumetric flow rate, $\dot{V}^+$, relates the actual volumetric flow rate, $\dot{V}$, to the radius, r, and the angular velocity, ω, of the rotating cup. The stability number, St, relates viscous forces to inertial and surface tension forces, and the Weber number, We, is a measure of the relative importance of the fluid's inertia compared to its surface tension.

Based on their experiments, Liu et al [41] proposed the following correlations for the transition volume flow rate from direct droplet to ligament formation, $\dot{V}_1^+$, and from ligament to sheet formation, $\dot{V}_2^+$.

$$\dot{V}_1^+ = 6.5\ \mathrm{We}^{-1.161}\ \mathrm{St}^{-0.0705} \tag{2.31}$$

$$\dot{V}_2^+ = 5.13\ \mathrm{We}^{-0.789}\ \mathrm{St}^{0.036} \tag{2.32}$$

However, although geometrically similar to the dimensions of a planet gear with a journal bearing in an epicyclic gearbox, the experiments were conducted at significantly lower angular velocities and flow rates than those prevailing on a planet gear in an epicyclic gearbox in planetary configuration. Extrapolated results may be invalid, as they are no longer supported by experimental test data.

Experiments on liquid disintegration with operational parameters much more similar to those of a planet gear with a journal bearing in an epicyclic gearbox were conducted by Glahn et al [42]. The experimental configuration was an abstraction of a droplet generating source in an aero-engine bearing chamber. Instead of using a rotating cup, Glahn et al [42] utilised a rotating disc. The liquid disintegration modes observed on rotating discs are similar to those observed on rotating cups. However, the flow conditions at which the disintegration modes change from droplet to ligament formation and from ligament to sheet formation are different. In contrast to a rotating cup, a rotating disc exhibits significant slip between the bulk flow of the liquid and the rotating surface. Thus, the angular bulk velocity of the liquid is lower than that of the rotating disc. Hence, the transition from one disintegration mode to another occurs at higher Weber numbers.

Glahn et al [42] defined non-dimensional characteristic numbers which were later also used by Liu et al, albeit in a slightly different notation (equations (2.28) to (2.30)).

$$\dot{V}^{+} = \frac{\rho\, \dot{V}^{2}}{\sigma\, d^{3}} \tag{2.33}$$

$$\mathrm{Oh} = \frac{\mu}{\sqrt{\rho\, d\, \sigma}} \tag{2.34}$$

$$\mathrm{We}^{*} = \frac{1}{8}\frac{\rho\, \omega^{2}\, d^{3}}{\sigma} \tag{2.35}$$

The non-dimensional volumetric flow rate, $\dot{V}^{+}$, relates the liquid's density, ρ, and the actual volumetric flow rate, $\dot{V}$, to the liquid's surface tension, σ, and the disc diameter, d. The meaning of the Ohnesorge number, Oh, is equivalent to that of the stability number, St (equation (2.29)). The modified Weber number, We*, was defined with the disc diameter, d, rather than the disc radius, r (equation (2.30)). Based on their experimental results, Glahn et al [42] established correlations for the transition volume flow rate from direct droplet to ligament formation, $\dot{V}_1^{+}$, and from ligament to sheet formation, $\dot{V}_2^{+}$.

$$\dot{V}_1^{+} = 0.0854\, \mathrm{Oh}^{-0.9}\, \mathrm{We}^{*\,-0.85} \tag{2.36}$$

$$\dot{V}_2^{+} = 0.1378\, \mathrm{Oh}^{-0.33}\, \mathrm{We}^{*\,-0.435} \tag{2.37}$$

In order to compare their correlations for the transition volume flow rates, $\dot{V}_1^+$ and $\dot{V}_2^+$, respectively, Glahn et al [42] referred to historical data from Matsumoto et al [43], who had established a proposal for the transition from droplet to ligament formation,

$$\dot{V}_1^+ = 0.0333\ \mathrm{Oh}^{-0.9}\ \mathrm{We}^{*^{-0.85}}, \tag{2.38}$$

and Hinze and Milborn [44], who had established a correlation for the transition from ligament to sheet formation,

$$\dot{V}_2^+ = 0.5083\ \mathrm{Oh}^{-0.333}\ \mathrm{We}^{*^{-0.60}}. \tag{2.39}$$

The following table summarises the relevant correlations available for the transition volume flow rates from direct droplet formation to ligament formation, $\dot{V}_1^+$, and from ligament to sheet formation, $\dot{V}_2^+$, that are considered for the investigations presented in this thesis.

Table 2.2: Summary of relevant correlations available for $\dot{V}_1^+$ and $\dot{V}_2^+$ for liquid flow over rotating cups

	$\dot{V}_1^+$	$\dot{V}_2^+$
Fraser et al [40]	N/A	equation (2.23)
Liu et al [41]	equation (2.31)	equation (2.32)
Hinze and Milborn [44]	N/A	equation (2.39)

Table 2.3: Summary of relevant correlations available for $\dot{V}_1^+$ and $\dot{V}_2^+$ for liquid flow over rotating discs

	$\dot{V}_1^+$	$\dot{V}_2^+$
Glahn et al [42]	equation (2.36)	equation (2.37)
Matsumoto et al [43]	equation (2.38)	N/A

If the liquid attaches to the chamfer of the rotating gear and separates from the lower edge of the gear base (flow path (b_1) in Figure 2.2), it is expected to disintegrate in accordance with the observations made on spinning cups. However, if the liquid attaches to the chamfer of the rotating gear and separates from the upper edge of the gear base (flow path (b_2) in Figure 2.2), it is expected to disintegrate in accordance with the observations made on spinning discs.

The expected flow regime can be determined by comparing the actual non-dimensional flow rate, $\dot{V}^+$, with the transition flow rates, $\dot{V}_1^+$ and $\dot{V}_2^+$, respectively. For $\dot{V}^+ < \dot{V}_1^+$, direct droplet formation prevails, for $\dot{V}_1^+ < \dot{V}^+ < \dot{V}_2^+$, ligament formation prevails, and for $\dot{V}_2^+ < \dot{V}^+$, sheet formation prevails.

2.4 Fluid Flow Governing Equations

Any type of fluid flow, including external oil flow from a journal bearing in an epicyclic gearbox, can be described by the conservation laws of physics, namely conservation of mass, momentum and energy. The mathematical representations of these physical laws are known as continuity, momentum and energy equations, formal derivations of which have been carried out by multiple authors, for example, Schlichting and Gersten [34].

2.4.1 Continuity Equation

Conservation of mass (continuity) means that the net rate of a mass flow into and out of a differential control volume must be zero. The continuity equation for a compressible fluid in Cartesian coordinates takes the following form.

$$\frac{\partial \rho}{\partial t} + \frac{\partial(\rho u)}{\partial x} + \frac{\partial(\rho v)}{\partial y} + \frac{\partial(\rho w)}{\partial z} = 0 \tag{2.40}$$

In the equation above, ρ is the fluid density, t is the time, and u, v and w are the velocity components in the x, y and z-directions, respectively.

2.4.2 Momentum Equations

Conservation of momentum follows Newton's second law of motion, $F = ma$. Inertial forces are balanced with viscous forces, pressure forces and body forces. The momentum equations in Cartesian coordinates take the following form.

x-momentum equation:

$$\rho\left(\frac{\partial u}{\partial t}+u\frac{\partial u}{\partial x}+v\frac{\partial u}{\partial y}+w\frac{\partial u}{\partial z}\right)=\left(\frac{\partial}{\partial x}\tau_{xx}+\frac{\partial}{\partial y}\tau_{yx}+\frac{\partial}{\partial z}\tau_{zx}\right)-\frac{\partial p}{\partial x}+F_{\mathrm{B}x} \tag{2.41}$$

y-momentum equation:

$$\rho\left(\frac{\partial v}{\partial t}+u\frac{\partial v}{\partial x}+v\frac{\partial v}{\partial y}+w\frac{\partial v}{\partial z}\right)=\left(\frac{\partial}{\partial x}\tau_{xy}+\frac{\partial}{\partial y}\tau_{yy}+\frac{\partial}{\partial z}\tau_{zy}\right)-\frac{\partial p}{\partial y}+F_{\mathrm{B}y} \tag{2.42}$$

z-momentum equation:

$$\rho\left(\frac{\partial w}{\partial t}+u\frac{\partial w}{\partial x}+v\frac{\partial w}{\partial y}+w\frac{\partial w}{\partial z}\right)=\left(\frac{\partial}{\partial x}\tau_{xz}+\frac{\partial}{\partial y}\tau_{yz}+\frac{\partial}{\partial z}\tau_{zz}\right)-\frac{\partial p}{\partial z}+F_{\mathrm{B}z} \tag{2.43}$$

In the equations above, ρ is the fluid density, t is the time, and u, v and w are the velocity components in the x, y and z-directions, respectively. Viscous stresses are denoted τ. They can act as shear stresses, τ_{ij}, or normal stresses, τ_{ii}. The pressure is denoted p and F_{B} is the body force.

In engineering applications involving air and oil, the fluids are Newtonian, i.e. there is a linear relationship between the shear stress and the strain rate. For incompressible Newtonian fluids, the normal stress components are expressed by

$$\tau_{xx}=2\mu\,\frac{\partial u}{\partial x},\qquad \tau_{yy}=2\mu\,\frac{\partial v}{\partial y},\qquad \tau_{zz}=2\mu\,\frac{\partial w}{\partial z}, \tag{2.44}$$

and the shear stress components are expressed by

$$\tau_{xy}=\tau_{yx}=\mu\left(\frac{\partial u}{\partial y}+\frac{\partial v}{\partial x}\right),\ \ \tau_{xz}=\tau_{zx}=\mu\left(\frac{\partial u}{\partial z}+\frac{\partial w}{\partial x}\right),\ \ \tau_{yz}=\tau_{zy}=\mu\left(\frac{\partial w}{\partial y}+\frac{\partial v}{\partial z}\right). \tag{2.45}$$

In the equations above, μ is the dynamic viscosity of the fluid. Using the relationships above, the momentum equations for an incompressible Newtonian fluid can be simplified to give the following.

x-momentum equation:

$$\rho\left(\frac{\partial u}{\partial t}+u\frac{\partial u}{\partial x}+v\frac{\partial u}{\partial y}+w\frac{\partial u}{\partial z}\right)=\mu\left(\frac{\partial^2 u}{\partial x^2}+\frac{\partial^2 u}{\partial y^2}+\frac{\partial^2 u}{\partial z^2}\right)-\frac{\partial p}{\partial x}+F_{\mathrm{B}x} \tag{2.46}$$

y-momentum equation:

$$\rho\left(\frac{\partial v}{\partial t}+u\frac{\partial v}{\partial x}+v\frac{\partial v}{\partial y}+w\frac{\partial v}{\partial z}\right)=\mu\left(\frac{\partial^2 v}{\partial x^2}+\frac{\partial^2 v}{\partial y^2}+\frac{\partial^2 v}{\partial z^2}\right)-\frac{\partial p}{\partial y}+F_{\mathrm{B}y} \tag{2.47}$$

z-momentum equation:

$$\rho\left(\frac{\partial w}{\partial t}+u\frac{\partial w}{\partial x}+v\frac{\partial w}{\partial y}+w\frac{\partial w}{\partial z}\right)=\mu\left(\frac{\partial^2 w}{\partial x^2}+\frac{\partial^2 w}{\partial y^2}+\frac{\partial^2 w}{\partial z^2}\right)-\frac{\partial p}{\partial z}+F_{\mathrm{B}z} \tag{2.48}$$

Equations (2.46) to (2.48) are known as the Navier-Stokes equations for incompressible Newtonian fluids. They need to be solved in order to determine the fluid flow velocity components.

2.4.3 Energy Equation

Conservation of energy follows the first law of thermodynamics for a differential element of fluid. The total energy of a system is equal to the energy added to, and the work done by the system. The energy equation for incompressible Newtonian fluids in Cartesian coordinates is given by

$$\rho\, c_{\mathrm{p}}\left(\frac{\partial T}{\partial t}+u\frac{\partial T}{\partial x}+v\frac{\partial T}{\partial y}+w\frac{\partial T}{\partial z}\right)=\frac{\partial}{\partial x}\left(k\frac{\partial T}{\partial x}\right)+\frac{\partial}{\partial y}\left(k\frac{\partial T}{\partial y}\right)+\frac{\partial}{\partial z}\left(k\frac{\partial T}{\partial z}\right)+\Phi, \tag{2.49}$$

where

$$\begin{aligned}\Phi=\tau_{\mathrm{ij}}\frac{\partial u_{\mathrm{i}}}{\partial x_{\mathrm{j}}}=2\mu\left(\frac{\partial u}{\partial x}\right)^2+2\mu\left(\frac{\partial v}{\partial y}\right)^2+2\mu\left(\frac{\partial w}{\partial z}\right)^2+\mu\left(\frac{\partial u}{\partial y}+\frac{\partial v}{\partial x}\right)^2\\ +\mu\left(\frac{\partial v}{\partial z}+\frac{\partial w}{\partial y}\right)^2+\mu\left(\frac{\partial w}{\partial x}+\frac{\partial u}{\partial z}\right)^2\end{aligned} \tag{2.50}$$

In the equations above, ρ is the fluid density, c_{p} is the specific heat capacity at constant pressure, T is the temperature, u, v and w are the velocity components in the x, y and z-directions, respectively, k is the thermal conductivity, τ_{ij} are the normal $(\mathrm{i}=\mathrm{j})$ and the shear $(\mathrm{i}\neq\mathrm{j})$ stresses, and μ is the dynamic viscosity of the fluid.

Depending on the case under investigation, the energy equation (equation (2.49)) may or may not be necessary to solve. If the case under investigation is characterised by large temperature variations within the domain, and thus large fluid property variations, the energy equation (equation (2.49)) must be solved in order to obtain meaningful predictions for the temperature distribution and the flow velocity components. When considering internal journal bearing fluid flow (section 2.2), for instance, the variation of the dynamic viscosity, μ, with temperature is significant. This implies that the momentum equations are coupled with the energy equation. They must therefore be solved simultaneously by an appropriate numerical scheme [47]. In contrast, when considering external journal bearing fluid flow (section 2.3), the temperature variations in the domain under investigation are negligible. Thus the energy equation (equation (2.49)) does not need to be solved. A detailed justification for treating the external journal bearing domain isothermally is provided in section 3.1.7.

2.5 Fundamentals of Computational Fluid Dynamics (CFD) Analysis

Computational Fluid Dynamics (CFD) is the analysis of systems involving fluid flow. All commercial CFD codes, including ANSYS Fluent [48], which is used for the investigations presented in this thesis, consist of three main elements, namely a pre-processor, a solver and a post-processor.

Pre-processing consists of the input of a flow problem to a CFD software tool and the subsequent transformation of this input into a form suitable for the solver. Over the past six decades, different streams of numerical solution techniques were developed, one of which is the finite volume method (section 2.6). ANSYS Fluent [48], as well as other well-established CFD codes, uses this solution procedure, which contains the following steps:

a) Division of the domain into finite volumes, also called control volumes or calculational cells,
b) Integration of the governing equations of fluid flow (section 2.4) over all finite control volumes of the domain,
c) Conversion of the resulting integral equations into a system of algebraic equations (discretisation), which are subsequently linearised, and
d) Solution of the algebraic equations by an iterative method.

The conservation of a general flow variable, ϕ, e.g. a velocity component within a finite control volume, can be expressed as a balance between the various processes tending to increase or decrease it. In its most general form, which includes the consideration of compressible effects, this balance can be expressed by

$$\frac{\partial(\rho\phi)}{\partial t} + \nabla\cdot(\rho\phi\boldsymbol{u}) = \nabla\cdot(\Gamma\nabla\phi) + S_\phi, \tag{2.51}$$

where ρ is the fluid density, t is the time, $\boldsymbol{u}$ is the fluid velocity vector, Γ is the coefficient of diffusion and S_ϕ is a source term. Equation (2.51) is the transport equation for property ϕ. In words, it describes the following.

$$\begin{bmatrix}\text{Rate of change}\\ \text{of } \phi \text{ in the}\\ \text{control volume}\\ \text{with respect}\\ \text{to time}\end{bmatrix} + \begin{bmatrix}\text{Net rate of}\\ \text{increase of } \phi\\ \text{due to con-}\\ \text{vection into the}\\ \text{control volume}\end{bmatrix} = \begin{bmatrix}\text{Net rate of}\\ \text{increase of } \phi\\ \text{due to diffusion}\\ \text{into the}\\ \text{control volume}\end{bmatrix} + \begin{bmatrix}\text{Net rate of}\\ \text{creation of } \phi\\ \text{inside the}\\ \text{control}\\ \text{volume}\end{bmatrix} \tag{2.52}$$

CFD codes contain discretisation techniques suitable for the treatment of the key transport phenomena, such as convection (transport due to fluid flow) and diffusion (transport due to variations of the flow variable from point to point) as well as for the source terms, which are associated with the creation and the destruction of the flow variable, and the rate of change with respect to time. An iterative solution approach is required to solve the resultant system of equations. Once the simulation is converged, the computed flow variables of interest can be post-processed. This step consists of analysing and evaluating the computed flow variables in the domain under investigation.

2.6 The Finite Volume Method

A number of well-established CFD codes, including ANSYS Fluent [48], which is used for all investigations presented in this thesis, use the finite volume method. The conservation equation of a general flow variable, generically expressed through equation (2.51), is a non-linear, second-order PDE. Its formulation is defined for an Eulerian control volume (CV), also known as calculational cell. In order to compute the transport of a flow variable through the domain, the domain is discretised into multiple control volumes, for which the conservation equations are solved. Equation (2.51) is the starting point for the computational procedures in the finite volume method. In order to solve it for a flow variable, ϕ, it is integrated over the three-dimensional control volume.

$$\int_{CV} \frac{\partial(\rho\phi)}{\partial t}\mathrm{d}V + \int_{CV} \nabla\cdot(\rho\phi\boldsymbol{u})\mathrm{d}V = \int_{CV} \nabla\cdot(\Gamma\nabla\phi)\mathrm{d}V + \int_{CV} S_\phi \mathrm{d}V \tag{2.53}$$

Using Gauss's divergence theorem, equation (2.53) can be re-written as

$$\int_{CV} \frac{\partial(\rho\phi)}{\partial t}\mathrm{d}V + \int_{A} \boldsymbol{n}\cdot(\rho\phi\boldsymbol{u})\mathrm{d}A = \int_{A} \boldsymbol{n}\cdot(\Gamma\nabla\phi)\mathrm{d}A + \int_{CV} S_\phi \mathrm{d}V. \tag{2.54}$$

In the equation above, the first term on the left hand side expresses the rate of change of the total amount of fluid property ϕ in the control volume. The product $\boldsymbol{n}\cdot(\rho\phi\boldsymbol{u})$ expresses the flux component of fluid property ϕ due to the fluid flow along the vector $\boldsymbol{n}$, which is oriented normal to surface element dA. Hence, the second term on the left hand side of equation (2.54) is the net rate of decrease of fluid property ϕ of the fluid element due to convection. The product $\boldsymbol{n}\cdot(\Gamma\nabla\phi)$ can be interpreted as a diffusion flux in the direction of $\boldsymbol{n}$. The first term on the right hand side of equation (2.54) is therefore associated with a flux into the fluid element and represents the net rate of increase of fluid property ϕ of the fluid element due to diffusion. The second term on the right side of equation (2.54) gives the rate of increase of fluid property ϕ as a result of sources inside the fluid element. In time-dependent problems, equation (2.53) needs to be additionally integrated with respect to time, t, over a time-step, Δt.

Equation (2.54) is applied to each control volume, or calculational cell, in the domain. In order to solve it numerically, it needs to be discretised with respect to space (spatial discretisation) and time (temporal discretisation). The general discretised formulation of equation (2.54) is as follows.

$$\frac{\partial(\rho\phi)}{\partial t}V + \sum_{\mathrm{f}=1}^{\mathrm{m}} \boldsymbol{n}\cdot(\rho_\mathrm{f}\phi_\mathrm{f}\boldsymbol{u}_\mathrm{f})\cdot A_\mathrm{f} = \sum_{\mathrm{f}=1}^{\mathrm{m}} \boldsymbol{n}\cdot(\Gamma\nabla\phi_\mathrm{f})\cdot A_\mathrm{f} + S_\phi V \tag{2.55}$$

In the equation above, which in general is non-linear, subscript "f" refers to the face value.

2.6.1 Spatial Discretisation

In ANSYS Fluent [48], the values of fluid property ϕ are stored in the cell centres. As equation (2.55), however, is formulated for the cell faces, the values ϕ_f are interpolated from the cell centre values. For the convective term, i.e. the second term on the left hand side of equation (2.55), this is accomplished by using an upwind scheme. Upwinding means that the face values are derived from the quantities in the cells upstream and downstream relative to the direction of flow, but with a bias towards the upstream side. In ANSYS Fluent [48], several upwind schemes are available, namely first-order upwind, second-order upwind, power law and QUICK.

The diffusion term, i.e. the first term on the right hand side of equation (2.55), is discretised using a central-differencing scheme, which is always second-order accurate. In contrast to the upwind scheme, the central-differencing scheme uses both quantities in the cells upstream and downstream relative to the direction of flow, but without any bias to calculate the face values of fluid property ϕ.

2.6.2 Temporal Discretisation

Multiphase flow applications are inherently time-dependent. For this reason, in addition to the integration over the control volume, equation (2.54) has to be integrated with respect to time, t, over a time-step, Δt. A generic expression for the time evolution of property ϕ is given by

$$\frac{\partial \phi}{\partial t} = F(\phi), \tag{2.56}$$

where the function F incorporates any spatial discretisation. In ANSYS Fluent [49], the time derivative is discretised using a backward difference scheme, which can either be of first or second-order accuracy. First-order accurate temporal discretisation is given by

$$\frac{\phi^{\mathrm{n}+1} - \phi^{\mathrm{n}}}{\Delta t} = F(\phi), \tag{2.57}$$

whilst second-order accurate temporal discretisation is given by

$$\frac{3\phi^{\mathrm{n}+1} - 4\phi^{\mathrm{n}} + \phi^{\mathrm{n}-1}}{2\Delta t} = F(\phi), \tag{2.58}$$

where $\mathrm{n}+1$ denotes values at the next time-step, $t+\Delta t$, n denotes values at the current time-step, t, and $\mathrm{n}-1$ denotes values at the previous time-step, $t-\Delta t$.

A choice remains to be made with respect to the time-step for which $F(\phi)$ is evaluated. This can either be done for the current time-step, t, or for the next time-step, $t+\Delta t$. If $F(\phi)$ is evaluated at the current time-step, t, time integration is performed explicitly. If $F(\phi)$ is evaluated at the next time-step, $t+\Delta t$, time integration is performed implicitly.

The advantage of a fully implicit scheme is its superior stability [50] and lower sensitivity to the size of the time-step, Δt. In contrast, when using an explicit scheme, constraints are imposed on the size of the time-step, Δt, in order to ensure a stable and accurate solution of the discretised transport equation for fluid property ϕ.

2.6.3 Solution Algorithms

In order to solve equation (2.55) for fluid property ϕ, it is linearised. A linearised form of equation (2.55) can be written as

$$a_{\mathrm{P}}\phi = \sum_{\mathrm{nb}} a_{\mathrm{nb}}\phi_{\mathrm{nb}} + b, \tag{2.59}$$

where a_{P} and a_{nb} are the linearised coefficients for ϕ and ϕ_{nb}. Subscript "nb" refers to the neighbouring cells.

ANSYS Fluent [49] provides two different types of solvers, namely the pressure-based and the density-based solver. The pressure-based solver has traditionally been used for incompressible or mildly compressible flows. In contrast, the density-based approach was originally designed for high-speed compressible flows. Two solution algorithms exist under the pressure-based solver in ANSYS Fluent [48], namely a segregated and a coupled one (Figure 2.17).

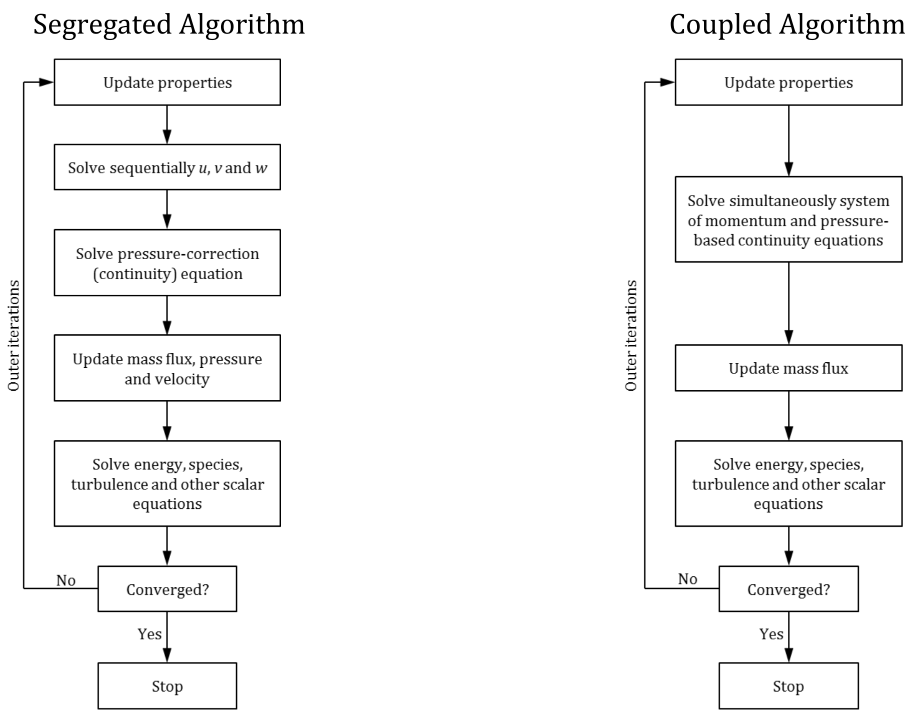

Figure 2.17: Overview of pressure-based solution methods in ANSYS Fluent [49]

The segregated algorithm solves the fluid flow governing equations sequentially. The SIMPLE (semi-implicit method for pressure-linked equations), SIMPLEC (SIMPLE-consistent) and PISO (pressure-implicit with splitting of operators) schemes are available. The coupled algorithm, in contrast, solves the momentum and the pressure-based continuity equations in a coupled manner (Figure 2.17). For time-dependent simulations, the loop shown in Figure 2.17 is repeated for every time-step Δt.

2.7 Turbulence Modelling

Laminar flow is completely described by the flow equations presented in section 2.4. The flow properties can be computed without making any additional assumptions or approximations. It is characterised by smooth and adjacent layers of fluid that slide past each other in an orderly fashion. There is no momentum exchange (mixing) taking place between the layers. Laminar flow is characterised by a Reynolds number, Re, which is smaller than the critical Reynolds number, Re_{crit}. As Re is a measure of the relative importance of inertial and viscous forces, laminar flow is dominated by the latter. If the Reynolds number of the flow exceeds its critical value, Re_{crit}, the flow becomes turbulent. Turbulent flow is characterised by random and chaotic variations of the flow velocity and all other flow properties. Due to the presence of vertical eddy motions, there is a high amount of momentum exchange (mixing) taking place.

There are three different categories of turbulent flow models, namely turbulence models for Reynolds-averaged Navier-Stokes (RANS) equations, large eddy simulations (LES) and direct numerical simulations (DNS), all of which will be described in more detail in the following sections. Turbulence models for RANS equations are by far the most relevant ones for engineering applications, especially in industry, which is due to the modest requirements for computing resources to achieve reasonably accurate flow computations.

2.7.1 Turbulence Models for Reynolds-Averaged Navier-Stokes Equations

The random nature of turbulent flow makes it practically unviable to fully describe the motion of all fluid particles. One approach to describe turbulent flow is to decompose the random and chaotic flow velocity, $u(t)$, into a steady mean value, $\bar{u}$, and a time-dependent fluctuating component, $\hat{u}(t)$.

$$u(t) = \bar{u} + \hat{u}(t) \tag{2.60}$$

This approach is called Reynolds decomposition and can be applied to all fluid properties. Applying the Reynolds decomposition to the fluid flow governing equations (section 2.4), leads to their turbulent form. Due to the large range of eddy length scales and the small time-scales required to fully resolve all turbulent flow structures, it is not practicable to solve the turbulent flow governing equations. Instead, time-averaging is used to derive mean flow equations, which account for the effects turbulence without explicitly modelling all fluctuations. The time-averaged mean flow equations are called Reynolds-Averaged Navier-Stokes (RANS) equations. A detailed derivation is given by Versteeg and Malalasekera [50]. The RANS equations, due to time-averaging, contain six additional stresses, namely three normal stresses and three shear stresses. These are also known as Reynolds stresses and can be expressed as follows.

$$\tau_{\mathrm{ij}} = -\rho\, \overline{\hat{u}_{\mathrm{i}}\hat{u}_{\mathrm{j}}} \tag{2.61}$$

When simulating turbulent flow with CFD, turbulence models have to be used in order to predict the Reynolds stresses and close the system of mean flow equations. Boussinesq [51] proposed that the Reynolds stresses are proportional to the mean rates of deformation, i.e.

$$\tau_{\mathrm{ij}} = -\rho\, \overline{\hat{u}_{\mathrm{i}}\hat{u}_{\mathrm{j}}} = \mu_t \left(\frac{\partial \bar{u}_{\mathrm{i}}}{\partial x_{\mathrm{j}}} + \frac{\partial \bar{u}_{\mathrm{j}}}{\partial x_{\mathrm{i}}} \right) - \frac{2}{3}\rho k \delta_{\mathrm{ij}}, \tag{2.62}$$

where μ_t is the turbulent or eddy viscosity, ρ is the fluid density, δ_{ij} is the Kronecker delta ($\delta_{\mathrm{ij}} = 1$ for i = j and $\delta_{\mathrm{ij}} = 0$ for i $\neq$ j) and k is the turbulent kinetic energy, which is defined as

$$k = \frac{1}{2}\left(\overline{\hat{u}^2} + \overline{\hat{v}^2} + \overline{\hat{w}^2} \right). \tag{2.63}$$

The Kronecker delta, δ_{ij}, is required to ensure that equation (2.62) is also valid for calculating the normal Reynolds stresses, τ_{xx}, τ_{yy}, and τ_{zz}. Turbulent transport of heat, mass and other scalar properties can be modelled similarly.

The development of turbulence models, which predict the Reynolds stresses, τ_{ij}, has been the focus of extensive research for many years. Historically, turbulence models have been developed for certain classes of flows. Further improvements made them more accurate and applicable to a wider range of flows. Based on the underlying assumptions made when developing these models, they vary greatly in terms of complexity. However, due to the complex nature of turbulence, a general turbulence model applicable to all types of flows is currently not available. The most commonly used turbulence models in modern engineering applications include mixing models, the Spalart-Allmaras model, the k–ε model, the Wilcox k–ω model, the Menter SST k–ω model and the Reynolds stress model (RSM) [50].

2.7.1.1 The Mixing Length Model

Mixing length models are simple models which describe the turbulent viscosity, μ_t, by means of an algebraic function that links μ_t to the mean velocity gradient.

$$\mu_t = \rho \ell_m^2 \left| \frac{\partial \bar{u}}{\partial y} \right| \tag{2.64}$$

The mixing length, ℓ_m, can be described by simple algebraic formulae, which depend on the type of flow [48]. No additional transport equation needs to be solved. Mixing length models are therefore classed as zero-equation models. They are easy to implement into a CFD code and computationally very efficient. They are well established and deliver good predictions for simple two-dimensional flows with thin shear layers, such as jets, mixing layers, wakes, boundary layers, and pipe and channel flows [48]. The downside is that they are incapable of describing separated or recirculating flows. However, in most flows experienced in engineering, separation and recirculation are phenomena that need to be accounted for. This led to the development of more sophisticated turbulence models, which perform better and are applicable to a wider range of flow classes. However, they are also computationally more expensive, as they rely on solving additional transport equations.

2.7.1.2 The Spalart-Allmaras Model

The Spalart-Allmaras turbulence model [52] is a one-equation model, i.e. one additional transport equation for the kinetic eddy viscosity, $\tilde{\nu}$, is solved. The following equation is used to compute the turbulent viscosity, μ_t.

$$\mu_t = \rho \nu_t f_{\nu 1} \tag{2.65}$$

The wall damping function, $f_{\nu 1}$, tends to one for high Reynolds numbers. At the wall, $f_{\nu 1}$ tends to zero. The transport equation for the kinetic eddy viscosity, ν_t, contains a length scale, ℓ, which is calculated by multiplying the von Kármán constant, κ, with the wall distance, y. In a one-equation model, the length scale, ℓ, needs to be specified. The Spalart-Allmaras turbulence model performs well for external aerodynamic flows, such as flows over aerofoils, where it can accurately predict flow separation. However, for more complex flows, the length scale parameter, ℓ, is difficult to define [50]. This makes the model unsuitable for more general internal flows. Additionally, the model is unable to account for transport processes in rapidly changing flows. The draw-backs of the Spalart-Allmaras turbulence model are partly addressed by turbulence models that solve more than one transport equation (sections 2.7.1.3 to 2.7.1.6).

2.7.1.3 The k–ε Model

The standard k–ε model was developed by Launder and Spalding [53] in order to address the shortcomings of the mixing length models (section 2.7.1.1). It was the first model that focused on the mechanisms that affect the turbulent kinetic energy. The advantage of this model is that it is not required to specify a length scale, ℓ. Instead, ℓ is calculated. This makes the k–ε model more general and applicable to a wider range of flows. Two additional transport equations are solved; one for the turbulent kinetic energy, k, and one for the rate of dissipation of turbulent kinetic energy, ε. Both parameters are used to compute a velocity scale, $\mathcal{v}$, and a length scale, ℓ.

$$\mathcal{v} = k^{1/2} \qquad\qquad \ell = \frac{k^{3/2}}{\varepsilon} \tag{2.66}$$

Whilst k can be calculated with equation (2.63), ε is given by

$$\varepsilon = 2\nu\,\overline{\hat{s}_{\mathrm{ij}} \cdot \hat{s}_{\mathrm{ij}}}. \tag{2.67}$$

The term $\hat{s}_{\mathrm{ij}}$ describes the fluctuating deformation rate of a fluid element in a turbulent flow. The turbulent viscosity, μ_t, is given by

$$\mu_t = C\rho\mathcal{v}\ell = \rho C_\mu \frac{k^2}{\varepsilon}. \tag{2.68}$$

In the equation above, ρ is the fluid density and C_μ is a dimensionless constant. The Reynolds stresses are calculated with equation (2.62). It assumes that the normal Reynolds stresses are isotropic.

The k–ε model is widely used and has been extensively validated on a number of different types of flows. Due to the fact that it focusses on modelling the mechanisms of turbulence, it is able to predict recirculating flows without the need for adjusting the model constants contained in the transport equations for k and ε on a case-by-case basis. The model performs particularly well in confined flows, where Reynolds shear stresses are most important [50]. However, the model's performance in some unconfined flows is poor. Moreover, it fails to accurately predict turbulence in flows with curved boundary layers and swirling flows, where Boussinesq's hypothesis of an isotropic turbulent viscosity, μ_t, is no longer valid.

There are a number of different variations of the k–ε model, e.g. the two-layer k–ε model and the renormalisation group (RNG) model, which significantly improved its performance, especially for low Reynolds number flows, where viscous stresses dominate over turbulent Reynolds stresses. This has been mainly achieved by implementing wall damping functions.

2.7.1.4 The Wilcox k–ω Model

In the standard k–ε model (section 2.7.1.3), the turbulent kinetic energy, k, and the rate of dissipation of the turbulent kinetic energy, ε, are used to define a velocity scale, ϑ, and a length scale, ℓ (equation (2.66)). Wilcox [54] proposed to express the length scale, which is required to calculate the turbulent viscosity, μ_t, with the turbulence frequency, ω, instead of ε.

$$\omega = \frac{\varepsilon}{k} \tag{2.69}$$

Dimensional analysis shows that the length scale, consequently, is given by

$$\ell = \frac{\sqrt{k}}{\omega}. \tag{2.70}$$

The turbulent viscosity, μ_t, is hence described by

$$\mu_t = \frac{\rho k}{\omega}. \tag{2.71}$$

The Reynolds stresses are computed in the same way as in the k–ε model (equation (2.62)). One of the advantages of the k–ω model compared to the k–ε model is that it does not require wall damping functions in low Reynolds number flows. Instead, the model equations can be integrated from the turbulent core flow down to the wall (section 2.7.1.7), which makes it less sensitive to the resolution of the calculational grid in the near-wall region. One disadvantage of the model, however, arises when modelling turbulence in free streams, where k and ω tend to zero. The turbulent viscosity, μ_t, for these conditions is undefined. For these cases, a small value of ω needs to be specified. According to Menter [55], the performance of the k–ω model in free stream flow conditions strongly depends on the chosen value for ω, which makes it unsuitable for external aerodynamics and aerospace applications.

2.7.1.5 The Menter SST k–ω Model

Menter [55] recognised that the results of the k–ε model were less sensitive to the assumed values in free stream flow conditions. He therefore suggested to modify the original k–ω model in order to combine the advantages of the k–ε model in regions far from the wall (free stream flow conditions) with the advantages of the k–ω model in the near-wall region. The result was a new two-equation turbulence model called the baseline model [56]. The shear stress transport (SST) k–ω model includes a modification to the definition of the eddy viscosity in the baseline model. It accounts for the effect of the transport of the principal turbulent shear stress and significantly improves the prediction of adverse pressure gradient flows, i.e. low Reynolds number flows.

The computation of the Reynolds stresses is similar to that of Wilcox's k–ω model, but the ε-equation is transformed by substituting $\varepsilon = k\omega$. Further key improvements of the SST k–ω model include revised model constants and the use of blending functions to ensure a smooth transition between the computed values for μ_t with the k–ε formulation in the far-field region and the k–ω formulation in the near-wall region.

2.7.1.6 The Reynolds Stress Model (RSM) and the Algebraic Stress Model (ASM)

One major draw-back of all two-equation models, such as the k–ε and the k–ω models, is that they rely on the Boussinesq approximation to calculate the Reynolds stresses (equation (2.62)). It assumes that the normal Reynolds stresses are isotropic, i.e. of equal magnitude in the x, y and z-directions. Experimental measurements of velocity fluctuations, however, showed that this assumption is inaccurate for many types of flows, including boundary layer flows and flows with complex strain fields or significant body forces [48].

The RSM approach is to compute each of the six Reynolds stresses separately in conjunction with a transport equation for the rate of dissipation of turbulent kinetic energy, ε. Hence, the RSM requires seven additional PDEs to be solved. Although this requirement makes it computationally much more expensive compared to zero, one or two-equation models, this allows directional effects of the Reynolds stresses to be accounted for. This makes the RSM the most complex turbulence model available. However, it is generally accepted that this model is the simplest with the potential to describe all mean flow properties without case-by-case adjustment [48]. The high demand of computational resources required for the RSM has two key implications: the model is less widely validated compared to zero, one, or two-equation models and often too computationally expensive for industrial applications. The extension and improvements of the RSM sub-models is an area of on-going research.

In order to overcome the disadvantage associated with the high complexity of the RSM, the algebraic stress model (ASM) was developed. The idea of the ASM approach is to replace the computation of the differential terms in the calculation of the Reynolds stresses with simpler, algebraic expressions. Instead of solving seven (six Reynolds stress equations and one transport equation for ε) PDEs for the RSM, the ASM requires solving six algebraic equations for six Reynolds stresses and two PDEs for the transport of k and ε. This makes the ASM computationally more economical. The disadvantages of the ASM, however, are that, similar to the RSM, validation is limited and the model is severely restricted in flows where its assumptions are not applicable.

2.7.1.7 Near-Wall Modelling

Solid surfaces, like walls, affect fluid flow characteristics significantly. Due to the no-slip condition, the fluid velocity at the wall is zero relative to the surface. In a region known as the boundary layer, the fluid velocity transitions from zero to the free stream velocity. The boundary layer thickness, δ, is typically defined as the distance from the solid surface to the point where the local flow velocity, u, reaches 99% of the free stream velocity [34]. The boundary layer can be divided into an inner and an outer region (Figure 2.18).

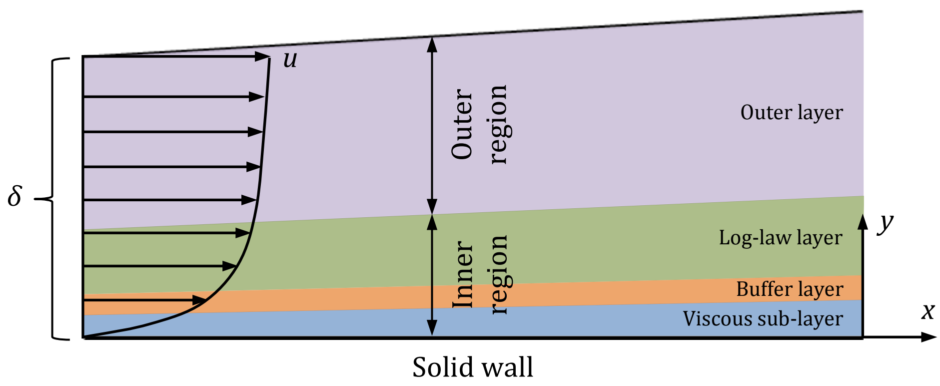

Figure 2.18: Schematic of boundary layer structure

The inner region can be divided into three sub-layers, namely the laminar or viscous sub-layer closest to the wall, the buffer layer and the log-law layer. The viscous sub-layer is dominated by viscous stresses. It is also called the linear sub-layer because of the linear relationship between the flow velocity, u, and the wall distance, y. The flow in this layer is laminar. The buffer layer is a transition region, where both viscous and turbulent stresses are of equal importance. The log-law layer is dominated by turbulent stresses and viscous stresses are negligible. The outer region, or outer layer, is dominated by inertial effects from the free stream and is not directly affected by viscous effects.

When characterising boundary layers, it is useful to express the flow velocity, u, and the wall distance, y, as non-dimensional quantities, u^+ and y^+, respectively.

$$u^+ = \frac{\overline{u}}{u_\tau} = \frac{\overline{u}}{\sqrt{\frac{\tau_w}{\rho}}} \tag{2.72}$$

In the equation above, $\overline{u}$ is the mean flow velocity and u_τ is the shear velocity. The wall shear stress, τ_w, in turn, can be calculated with equation (2.45) by using the velocity gradient at the wall, $\partial u/\partial y|_w$. The non-dimensional wall distance, y^+, is defined as

$$y^+ = \frac{\rho u_\tau y}{\mu}. \tag{2.73}$$

When plotting the relationship between u^+ and y^+ (Figure 2.19), the structure of the boundary layer is revealed.

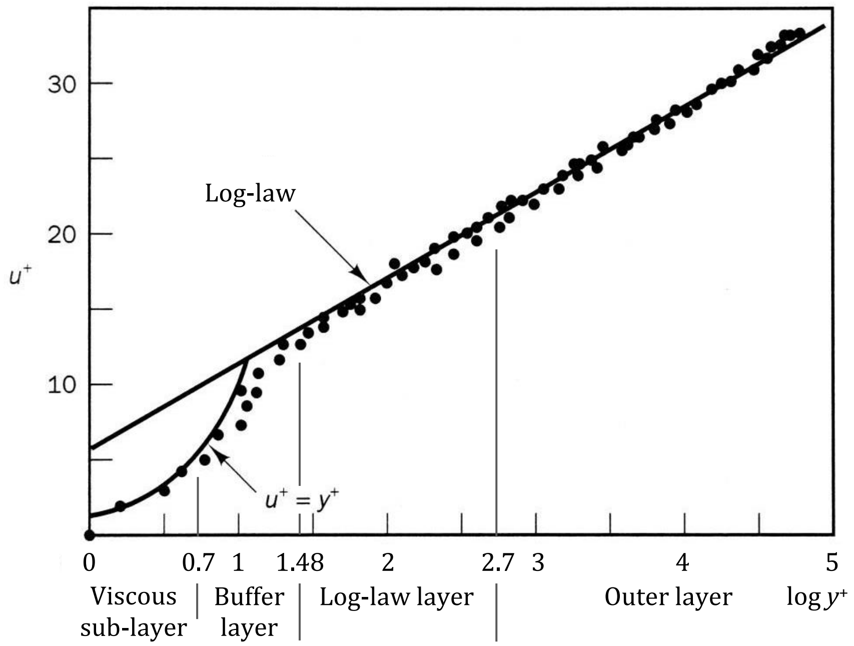

Figure 2.19: Velocity distribution in the boundary layer on a solid surface. Figure reproduced from Versteeg and Malalasekera [50].

In CFD, there are generally two different approaches available to model boundary layers. The first one is to explicitly resolve the velocity profile of the boundary layer by placing an appropriate number of calculational cells within the boundary layer region. The second one utilises the identified relationships between u^+ and y^+ to reconstruct the boundary layer velocity profile. The viscous sub-layer and the buffer layer extend to a y^+ value of approximately 30 ($\log y^+ \approx 1.48$, Figure 2.19). In order to fully resolve the velocity profile of the boundary layer, at least 10 calculational cells should be placed within this region [48]. If there is a demand for high accuracy results, it is recommended to place the first cell centroid at $y^+ \approx 1$ ($\log y^+ \approx 0$). This is especially the case when modelling heat transfer, as this requires accurate predictions of the wall shear stresses, τ_w. Depending on the geometry of the domain under investigation and the flow boundary conditions, explicitly resolving the boundary layer can result in very large overall cell counts. Especially for high Reynolds number flows, the viscous sub-layer can be very thin. Consequently, the size of the cells adjacent to the wall must be accordingly small. For this reason, it is not always possible or economical to use this approach.

An alternative method is to utilise the known relationships between u^+ and y^+ in the different layers of the inner and outer regions of the boundary layer (Figure 2.19). In CFD codes, these relationships are contained within wall functions. When using this approach, it is sufficient for the first cell centroid to be placed in the log-law region between $30 < y^+ < 500$ ($1.48 < \log y^+ < 2.7$, Figure 2.19). It must be avoided to place cells in regions with $y^+ < 30$, as this will lead to inaccurate predictions of the wall shear stresses. Based on the domain under investigation and the flow conditions, it can be very difficult to meet this requirement. In order to address this issue, the k–ε turbulence model, for example, is equipped with the option to use enhanced wall treatment with scalable wall functions. This makes the model relatively insensitive to the y^+ value of the cell centroid closest to the wall.

The requirement for resolving the velocity profile of the boundary layer may not be the only criterion to be considered when specifying the number of cells in the near-wall region. Oil flows in confined spaces, such as bearing or gearbox chambers, tend to generate films on the chamber walls. Depending on the bearing or gearbox chamber dimensions and operating conditions, the oil film thickness on the chamber wall will vary. Bristot [57] investigated the oil flow behaviour in a bearing chamber of a two-shaft aero-engine for small and medium-sized aircraft. It was concluded that the oil film thickness on the chamber wall at maximum load conditions was approximately one millimetre. Depending on the numerical method used to capture or track the phase interphase, an appropriate number of calculational cells across the oil film is required to ensure an accurate and sharp interphase reconstruction (section 3.1.5). As a guideline, Tkaczyk and Morvan [58] stated that, when using the VOF method, at least 10 calculational cells are required to accurately model the liquid film. In a typical bearing chamber application, this requirement leads to y^+ values lower than 10. In this case, the boundary layer should be explicitly resolved.

2.7.2 Large Eddy Simulation (LES)

Turbulent flows exhibit rotational flow structures, called turbulent eddies, with a wide range of length scales. The characteristics of large and small eddies are different. Whilst small eddies are nearly isotropic, large eddies are more anisotropic as they interact with the mean (free stream) flow by extracting energy from it. The RANS-approach attempts to model the behaviour of all eddies. However, the behaviour of large eddies is problem-dependent, meaning their behaviour changes with the geometry of the domain under investigation. This is the reason why a universal RANS turbulence model has not yet been developed.

The large eddy simulation (LES) approach resolves the large eddies by a time-dependent computation of their behaviour. The behaviour of small eddies, which are generally more universal in their behaviour, on the other hand, is modelled. As a result, sub-grid stresses (SGS) are introduced which account for the interaction between the unresolved small eddies and the resolved large eddies. Sub-grid stresses are modelled and computed in conjunction with the flow equations (section 2.4) for each control volume.

Using LES is computationally very expensive due to the time-dependent nature of the approach and the requirement to have a computational grid that is sufficiently fine to resolve large eddies. However, advances in high performance computing (HPC) made LES viable for applications where large eddies have a significant effect on the mean flow development and behaviour. This, for instance, includes vortex shedding behind bodies, flows in diffusing passages, pipe bends and combustion chambers. The presence of large eddies, moreover, results in pressure fluctuations. Their characteristics can be used in aero-acoustic applications to predict noise from high speed flows.

2.7.3 Direct Numerical Simulation (DNS)

Direct numerical simulations (DNS) take LES (section 2.7.2) one step further and resolve all eddies, which includes the smallest ones. The governing flow equations for continuity (equation (2.40)) and momentum (equations (2.46), (2.47) and (2.48)) are computed directly. This includes the computation of the fastest fluctuations. Due to the large range of eddy length scales, the computational grid needs to be sufficiently fine to capture even the smallest eddies. Moreover, the chosen time-step must be sufficiently small to resolve even the fastest fluctuations of the flow velocity components. This combination makes DNS the most computationally expensive approach available. It is currently only used in an academic context. Using DNS, however, can have significant benefits and can provide very detailed insights into turbulent flow behaviours and characteristics. Due to the direct computation of the flow governing equations, DNS results can be used to improve existing or develop new turbulence models. Additionally, it can also be used to validate turbulence models. Post-processing of DNS results allow turbulent quantities to be visualised which cannot be experimentally measured. The approach allows fundamental research on turbulent flows to be carried out. By including or excluding individual aspects of the flow physics, their effects and sensitivities on the flow development and flow behaviours can be studied.

2.8 Review of Relevant Numerical Modelling Techniques for Multiphase Flows

This section aims to provide an overview of the techniques relevant for modelling external oil flow from a journal bearing. As the oil emerges from the lubricating gap and mixes with the air surrounding the bearing, the fluid inside the domain under investigation (Figure 2.1) consists of two phases, namely air and oil. In this context, the term "phase" refers to the flow component, i.e. air or oil, and not to the state of the flow component, i.e. gaseous, liquid or solid.

A fundamental issue when computing multiphase flows is to accurately model the interface between the phases, as the physical properties of the fluids change. Its resolution will therefore affect the modelling of the interaction between the phases, and thus also the accuracy of the flow behaviour prediction.

The modelling approaches can be categorised according to their kinematic description. There are two different mathematical representations of fluid flow, namely the Eulerian and the Lagrangian approach. The Eulerian approach describes the flow field through its properties as a function of space and time. The velocity is mathematically described by the following function.

$$\boldsymbol{u} = f(\boldsymbol{x}, t) \tag{2.74}$$

In the equation above, $\boldsymbol{u}$ is the fluid particle's velocity vector, $\boldsymbol{x}$ is its position vector and t is the time. The Eulerian frame of reference is typically used in laboratory conditions, where flow properties, such as pressure or temperature, are recorded by fixed probes as they are passed by a number of fluid particles.

With the Lagrangian approach, the location of individual fluid particles is tracked. A fluid particle's path is followed and identified by its position at any given time. The fluid particle's velocity is mathematically described by the following function.

$$\boldsymbol{x} = f(\boldsymbol{x}_0, t) \tag{2.75}$$

In the equation above, $\boldsymbol{x}$ is the fluid particle's position, $\boldsymbol{x}_0$ is its initial position and t is the time. In oceanography, for example, buoys are deposited on the surface of the sea and their positions are recorded as they vary over time.

Depending on the type of multiphase flow to be modelled, either description is used in CFD analysis. Techniques using the Eulerian formulation include the Volume of Fluid (VOF) method, the Eulerian Thin Film Model (ETFM) and the Lattice Boltzmann Method (LBM). Techniques using the Lagrangian formulation include the Discrete Phase Model (DPM) and the Smoothed Particle Hydrodynamics (SPH) approach. All of the methods mentioned above will be explained in more detail in the following sections.

2.8.1 The Volume of Fluid (VOF) Method

The VOF method is an Eulerian approach for modelling multiphase flows. It was developed in the late 1970s by Hirt and Nichols [59]. The fluid is treated as a mixture of the phases involved, for which a single set of momentum equations is solved (equations (2.41) to (2.43)). The fluid's physical properties are averaged between those of the composing fluids and weighted by the volume of each phase present inside the calculational cell. For this purpose, the phase volume fraction, α, is defined as a scalar function. It can take values between zero and one. When considering a two-phase fluid mixture consisting of a gas and a liquid, for example, and α is used to track the volume fraction of the liquid phase, a value of $\alpha = 0$ implies that the cell is fully filled with gas. Consequently, $\alpha = 1$ implies that the cell is fully filled with liquid. Cells with phase volume fractions between zero and one contain the phase interface.

The density, ρ, and the dynamic viscosity, μ, required for solving the momentum equations, are averaged using the following relationships.

$$\rho = \alpha_{\mathrm{g}}\rho_{\mathrm{g}} + \alpha_{\mathrm{lq}}\rho_{\mathrm{lq}} \tag{2.76}$$

$$\mu = \alpha_{\mathrm{g}}\mu_{\mathrm{g}} + \alpha_{\mathrm{lq}}\mu_{\mathrm{lq}} \tag{2.77}$$

In the equations above, subscript "g" indicates the gas phase and subscript "lq" indicates the liquid phase. Due to its formulation in the Eulerian frame of reference, the volume fraction equation is space and time-dependent. Hence, analyses using the VOF method require a transient treatment. In order to track the location of the phase interface through the domain, the VOF model solves the continuity equation for the phase volume fraction, which, in its compressible form, is given by:

$$\frac{1}{\rho}\left[\frac{\partial}{\partial t}(\alpha\rho) + \nabla \cdot (\alpha\rho\boldsymbol{u})\right] = \frac{1}{\rho}(S_\alpha + \dot{m}_{\mathrm{net}}) \tag{2.78}$$

In the equation above, ρ and α are the density and the volume fraction value of the phase, respectively, t is the time, $\boldsymbol{u}$ is the flow velocity vector, S_α is the phase mass flow source term and $\dot{m}_{\mathrm{net}}$ is the net mass transfer per unit volume between the phases. Mass transfer from one phase to the other will occur in case of evaporation, condensation, or cavitation, as observed, for example, with internal journal bearing fluid flow (section 2.2).

Equation (2.78) has to be solved for all $\mathrm{n} - 1$ phases involved. The volume fraction of phase n is computed based on the sum of all phase volume fractions being equal to one. For the external oil flow from a journal bearing, no mass flow source terms are present and no mass transfer between the phases takes place. Thus, the right hand side of equation (2.78) becomes zero.

$$\frac{1}{\rho}\left[\frac{\partial(\alpha\rho)}{\partial t} + \nabla \cdot (\alpha\rho\boldsymbol{u})\right] = 0 \tag{2.79}$$

The VOF method uses a donor-acceptor scheme to determine the amount of fluid advected through the faces of the calculational cell. The direction of the flow velocity vector, $\boldsymbol{u}$, determines the donor and acceptor cells, i.e. cells losing and gaining fluid volume, respectively. The VOF method uses information about the fluid volume fractions and their derivatives to determine the location and the orientation of the phase interface, and improve the computation of the fluxes through the cell faces. Several different methods were developed to reconstruct the phase interface. In ANSYS Fluent [48], the following relevant phase interface reconstruction schemes are available.

a) Geometric reconstruction scheme,
b) Compressive interface construction scheme for arbitrary meshes (CICSAM),
c) Compressive scheme,
d) High resolution interface capturing (HRIC) scheme

For the specific case under investigation, based on their high accuracy, the geometric reconstruction scheme and the compressive scheme were considered. Both are described in detail in section 3.1.5.

2.8.2 Eulerian Thin Film Model (ETFM)

One of the issues with the VOF method is that flow features need to be resolved by an appropriate number of calculational cells. When capturing wall films in aero-engine bearing chambers, for instance, this can result in cell heights with a y^+ value in the region of 10. For the type of chamber required to house an epicyclic gearbox for a large turbofan aero-engine, oil film thicknesses are expected to be three orders of magnitude smaller than the gearbox chamber diameter. This makes the use of the VOF method computationally very expensive, as a large number of cells is required to discretise the entire domain. The ETFM offers an efficient alternative by avoiding the explicit resolution of the liquid film. Instead, the flow governing equations are depth-averaged, assuming that the flow is two-dimensional without a radial flow velocity component. Velocity and temperature profiles, for instance, are implemented through algebraic functions, similar to the approach used when modelling turbulence with wall functions (section 2.7.1.7). The ETFM contains a number of sub-models to account for different physical mechanisms, such as droplet impingement, splashing, film separation from edges and film stripping, which occurs at high shear rates between the gas and the liquid phase. The University of Nottingham conducted extensive research to extend and improve the ETFM. Notable contributions were made by Williams [61], who improved the droplet impact model, analysed instability effects and accounted for recirculating regions, and by Kay et al [62], who extended the thermal formulation of the ETFM for oil pooling conditions. Kakimpa et al [63] addressed various shortcomings of the ETFM by developing a robust approach to switch between thin and thick film solutions.

Using the ETFM for modelling multiphase flow in unconfined domains is problematic. The prevailing flow regime of the oil as it emerges from the lubricating gap of the bearing and mixes with the air surrounding the bearing is unknown. Thus, surfaces that potentially exhibit a build-up of an oil film are not known a priori.

2.8.3 Lattice Boltzmann Method (LBM)

LBM is a relatively recent method used to model multiphase flows. In contrast to conventional CFD methods, which typically solve the (macroscopic) flow governing equations (section 2.4) by using the finite volume method, LBM is a particle-based method. It uses microscopic models and mesoscopic kinetic equations [64]. The fundamental idea of LBM is to construct simplified kinetic models that incorporate the essential physics of the microscopic and mesoscopic processes so that the macroscopic fluid flow properties obey the (macroscopic) flow governing equations (section 2.4). For this purpose, a simplified form of the Boltzmann equation, which describes the kinetics of a fluid or particles statistically on a molecular level, is solved on a lattice along with collision models. The lattice Boltzmann equation contains probabilistic distribution functions for the position and the momentum of a typical fluid particle and a collision term. The Navier-Stokes equations (section 2.4) can be derived from the lattice Boltzmann equation.

The modelling of two-phase flow can be achieved by using a particle tracking method [24]. With this method, massless marker particles are spread over the volume occupied by a fluid with a free surface. The discrete markers are advected with the fluid flow. The phase interface is located where particles of different types are adjacent to each other. Compared to the phase interface reconstruction schemes available for the VOF method (section 3.1.5), the phase interface computation with the LBM method is less accurate and more research is likely to be carried out in this area.

As with more conventional CFD methods, turbulence models are required to account for the random and chaotic variations of the flow properties. LBM can be extended to include the turbulence models used for the closure of the RANS equations (section 2.7.1). However, LBM can also be used for LES (section 2.7.2) and DNS (section 2.7.3).

In the simplified lattice Boltzmann equation, convection is modelled linearly. Combined with particle collision processes, this allows the non-linear macroscopic advection through multi-scale expansion to be recovered. Using this approach is computationally much more efficient than solving the macroscopic flow equations (section 2.4). Hence, a turbulence modelling approach as adopted in LES can be used without the penalty of unfeasibly long computational times. This has been recognised by commercial LBM solvers such as XFlow [65], which incorporate an LES-like approach to turbulence modelling.

The features described above make LES an attractive alternative to conventional CFD methods that are based on the finite volume formulation. As LBM is a fairly recent development, the availability of validation cases is still limited. Ambrose et al [24] used this method to simulate oil jet impingement on a meshing gear pair. Comparisons with the results of CFD simulations using the VOF method (section 2.8.1) and simulations using smoothed particle hydrodynamics (SPH, section 2.8.5) showed very good agreement, demonstrating the feasibility of the method in a gearbox chamber environment.

2.8.4 Discrete Phase Model (DPM)

The Discrete Phase Model (DPM) is a method to track the trajectories of particles, e.g. droplets, bubbles etc., in the Lagrangian frame of reference. Typically, the particles are immersed in a continuous phase, such as air or water, which is described in the Eulerian frame of reference. Particles are considered as point masses with a spherical shape and with representative terms for inertia, drag and the force of gravity. DPM is capable of accounting for heat and mass transfer to and from the particles. The particles themselves, however, do not interact with each other. Commercial CFD solvers, such as ANSYS Fluent [48], provide the option to include one-way or two-way coupling between the phases. With a one-way coupling, the continuous phase influences the discrete phase via drag and turbulence. The discrete phase, however, has no effect on the continuous phase. With a two-way coupling, the discrete phase additionally influences the continuous phase via source terms of mass, momentum and energy. Dispersion of particles due to turbulent fluctuations in the flow can be modelled using either stochastic tracking or a particle cloud model [49].

DPM is typically used to model very fine droplets or combusting particles with a discrete phase volume fraction of less than 10% [49]. For the specific case under investigation, DPM can become a viable option when used in conjunction with other multiphase models (section 2.8.6), for example when a high level of liquid atomisation into very small droplets is observed.

2.8.5 Smoothed Particle Hydrodynamics (SPH)

The smoothed particle hydrodynamics (SPH) method is a Lagrangian approach developed in the 1970s to investigate astrophysics problems [66]. The method uses statistical techniques to recover the analytical expressions for the fluid’s physical variables. Similar to DPM, the fluid is modelled as a set of discrete particles, which are characterised by inter-particle forces to simulate pressure, viscosity, surface tension and other relevant forces.

One of the advantages of this method is that, unlike the Eulerian methods, mass conservation is always satisfied. Additionally, due to its formulation, SPH is a meshless method. Hence, the definition of an appropriate numerical grid prior to the simulation is not required. When using SPH to simulate multiphase problems, the interface between the phases is automatically defined by the position of the particles. Therefore, associated methods for interface tracking are not required.

The main challenges in the application of the SPH method to multiphase flows are related to modelling liquids, modelling the interactions between different fluid phases and modelling boundary conditions, such as walls, inlets, outlets and pressure boundaries. The SPH approach was originally developed for simulating single-phase fluid flow. However, in many engineering applications, and specifically in gearbox and bearing chambers, the interactions between the fluid phases are fundamental to the flow field behaviour. At the University of Nottingham, this problem was addressed by Kruisbrink et al [67, 68] through the development of concepts for continuous wall and pressure boundaries. Initial limitations of two-phase flow modelling with SPH were associated with the density ratio between the two phases. In order to obtain realistic solutions for air-oil mixture flows, density ratios between 800 and 1,000 are required. Subsequent work by Korzilius et al [69] led to successful testing of density ratios in this order of magnitude, making SPH a viable alternative to conventional multiphase CFD methods.

Further challenges arise when applying SPH to model thin films and droplet break-up. Modelling these regimes with satisfactory resolution requires a large number of particles. This, in turn, increases the computational cost of the simulation even though the code is highly parallelisable. Turbulence modelling is still a very active field of SPH research. Violeau and Issa [70] implemented a number of different turbulence models, including the mixing length model, the k–ε model, the Reynolds stress model and an LES turbulence model, into an SPH code and compared their performances. Although the quality of benchmark results, which were obtained with the original SPH method [66], could be improved, the performance compared to grid-based methods was still poor.

Based on the advantages of the SPH method and the recent progress made in enhancing the method's capabilities, SPH is a promising approach for future simulations of air-oil-mixture flows, having its strength in being a meshless method.

2.8.6 Hybrid Models

In order to combine the advantages of the VOF method (section 2.8.1), the ETFM (section 2.8.2) and the DPM (section 2.8.4), hybrid models have been developed and applied to industrial cases.

A DPM-ETFM model, for instance, was used by Jacobs [71] to model the two-phase flow behaviour within an aero-engine's rear bearing chamber. Although the application of this hybrid model was shown to be feasible, uncertainties with respect to the droplet generation mechanisms were still present. The thin film model proved to be unsuitable for the regions of the bearing chamber where deep pools were formed.

The lack of applicability of the thin film model, particularly in the sump region, led to combining the DPM (section 2.8.4) and the VOF method (section 2.8.1). A hybrid DPM-VOF (and vice versa) model was introduced by Tkaczyk and Morvan [72], where DPM was used to model droplet flow and the VOF method was used to model the film that was eventually formed on the chamber walls due to droplet impact. This model was also shown to be working in a VOF-DPM configuration, for example when secondary droplets are generated from a film after primary droplet impact. The main advantage of this technique lies in the reduction of the calculational cell count inside the chamber. Thus, a reduction of the computational requirements can be achieved. Due to using a Lagrangian frame of reference for tracking the oil droplets, a fine mesh is only required in the near-wall regions, where an oil film is formed. The hybrid DPM-VOF model was further developed by Adeniyi et al [73, 74, 75], who verified and enhanced the DPM-VOF code to include drag acting on the droplets, the effect of droplet splashing, and convective heat transfer between the air and the droplets.

3 Methodology for Computational Flow Investigations

In the previous chapter, the fundamentals of fluid flow in journal bearings (section 2.1), both internally (section 2.2) and externally (section 2.3), were discussed and principle underlying physical phenomena were highlighted. Moreover, a framework for the mathematical description of fluid flow in general was provided (section 2.4) and the basics of computational fluid dynamics analysis (section 2.5) were discussed. This included an overview of the finite volume method (section 2.6) and turbulence modelling (section 2.7). Moreover, relevant numerical modelling techniques for multiphase flows (section 2.8) were reviewed and advantages and disadvantages of each method with respect to modelling external oil flow from a journal bearing were highlighted.

The focus of this chapter is to provide details about the methods used for the analysis of the cases under investigation. This includes the specifics of the VOF method (section 3.1), which was used to model the two-phase flow behaviour within the domain under investigation (Figure 2.1), the detailed analysis approach (section 3.2), the computational grid generation approach used to discretise the domain under investigation into finite volumes (section 3.3), and the development of the inlet boundary condition for external oil flow from a journal bearing with a constant lubricating gap height (section 3.4) and a convergent-divergent lubricating gap height (section 3.5). In order to extend the available options for validating the CFD model results presented in chapter 4, this chapter also contains the development of a force balance model (section 3.6), which helps to predict the oil flow path direction for the case of radial oil outflow (flow path (b) in Figure 2.1).

3.1 The Volume of Fluid (VOF) Method

Based on its capabilities, the VOF method (section 2.8.1) was used for all investigations presented in this thesis. The main advantage of this method lies in its ability to capture a wide range of flow regimes, providing the computational grid is sufficiently fine. Whilst section 2.8.1 addressed some generic aspects of this method, in this section, more information will be provided on detailed aspects for the specific application under investigation.

When solving the volume fraction equation (equation (2.79)) for the phase volume fraction value, α, it needs to be integrated and discretised in space (section 2.6.1) and time (section 2.6.2). The discretisation can be performed with an explicit or an implicit formulation.

3.1.1 Spatial Discretisation Scheme for a General Flow Variable

In order to solve the discretised transport equation for a general flow variable (equation (2.55)), the cell face values, ϕ_{f}, are required (section 2.6.1). For the investigations presented in this thesis, the cell face values of the convective term are interpolated from the cell centre values using a second order upwind scheme. With this scheme, the second-order accuracy is achieved at the cell faces through a Taylor series expansion of the cell-centred solution about the cell centroid. For the diffusion term, by default, a central-differencing scheme is used, which is always second-order accurate.

3.1.2 Temporal Discretisation Scheme for a General Flow Variable

In order to compute a time-dependent evolution of a flow field, the spatially discretised transport equation for a general flow variable (equation (2.55)) needs to be additionally discretised with respect to time (section 2.6.2). For the investigations presented in this thesis, time integration of all general flow variables, except the phase volume fraction value, α, is always performed implicitly. Whether first or second order accuracy can be achieved is dictated by the choice of the discretisation scheme for the phase volume fraction equation (equation (2.79)). If an explicit discretisation scheme is chosen (section 3.1.3), time integration will be performed with first order accuracy. If an implicit discretisation scheme is chosen (section 3.1.4), time integration can be performed with first or second order accuracy. When possible, second order accuracy was chosen.

3.1.3 Explicit Temporal Discretisation Scheme for the Volume Fraction Equation

When tracking the phase interface, the volume fraction equation (equation (2.79)) has to be solved. Using an explicit temporal discretisation scheme and applying a standard finite-difference interpolation to the volume fraction values computed at the previous step, n, equation (2.79) becomes

$$\frac{\alpha^{\mathrm{n}+1}\rho^{\mathrm{n}+1}-\alpha^{\mathrm{n}}\rho^{\mathrm{n}}}{\Delta t}V+\sum_{\mathrm{f}=1}^{\mathrm{m}}\left(\rho^{\mathrm{n}}\dot{V}_{\mathrm{f}}^{\mathrm{n}}\alpha_{\mathrm{f}}^{\mathrm{n}}\right)=0. \tag{3.1}$$

In the equation above, α is the phase volume fraction, ρ is the fluid density, $\mathrm{n}+1$ is the new (current) time-step, n is the previous time-step, Δt is the size of the time-step, V is the cell volume, $\dot{V}_{\mathrm{f}}$ is the volume flux through the face of the calculational cell and α_{f} is the face value of the volume fraction.

Equation (3.1) can be solved directly without an iterative process. Compared to an implicit formulation (section 3.1.4), it is relatively easy to implement in a CFD code and it can be solved quickly. In order to ensure numerical stability and accurate results for the computation of the phase volume fraction values, the time-step, Δt, for the transient phase interface advection through the domain is limited by the Courant number, C. It is defined as follows.

$$C=\frac{u\Delta t}{\Delta x} \tag{3.2}$$

In the equation above, u is the flow velocity component in the x-direction, Δt is the time-step and Δx is the grid spacing in the x-direction. C can be defined equivalently for the y and z-directions. When using an explicit discretisation scheme, C must be less than or equal to one. Hence, Δt must be chosen such that the fluid is never advected by more than one cell distance at each time-step.

3.1.4 Implicit Temporal Discretisation of the Volume Fraction Equation

Using an implicit temporal discretisation scheme and applying a standard finite-difference interpolation to solve the volume fraction equation (equation (2.79)) yields the following formulation.

$$\frac{\alpha^{\mathrm{n+1}}\rho^{\mathrm{n+1}} - \alpha^{\mathrm{n}}\rho^{\mathrm{n}}}{\Delta t} V + \sum_{\mathrm{f=1}}^{\mathrm{m}} \left(\rho^{\mathrm{n+1}} \dot{V}_{\mathrm{f}}^{\mathrm{n+1}} \alpha_{\mathrm{f}}^{\mathrm{n+1}}\right) = 0 \tag{3.3}$$

As the equation above requires the phase volume fraction values at the new (current) time-step, $\mathrm{n}+1$, equation (3.3) must be solved iteratively. Compared to an explicit formulation (section 3.1.3), it is more complex to implement into a CFD code. Due to the iterative solution process, it is computationally more demanding. The advantage of implicit schemes, however, is that their numerical stability is not limited by the Courant number, C. Hence, larger time-steps, Δt, can be applied, as the liquid can be advected by more than one cell distance at each time-step.

3.1.5 Phase Interface Computation

The geometric reconstruction scheme and the compressive scheme are the most widely used phase interface reconstruction schemes because they maintain an accurate interface shape and don't show excessive diffusion [60]. When using the geometric reconstruction scheme, the phase interface is approximated by line segments. This piecewise linear interface construction (PLIC) provides a nearly smooth surface. It is schematically shown in Figure 3.1.

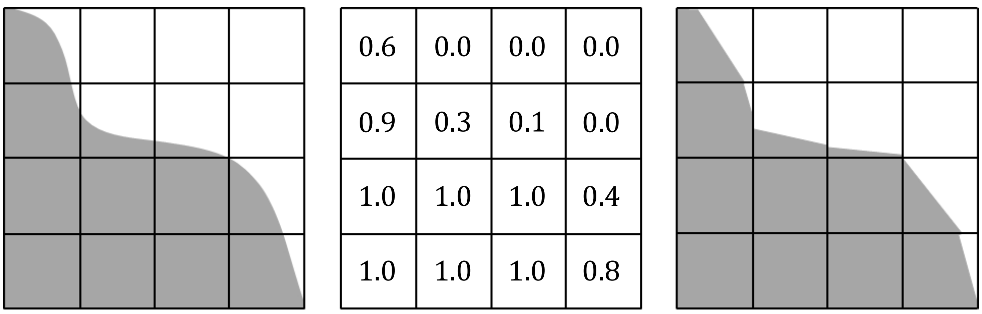

Figure 3.1: Schematic diagram of phase interface reconstruction with true interface (left), volume fractions (middle) and piecewise linear interface construction (PLIC) (right)

It is considered to be the most accurate of the options available and it produces the sharpest phase interface [60]. However, it requires an explicit temporal discretisation of the volume fraction equation (section 3.1.3). Thus, the time-step for the transient computation of the phase interface advection through the domain is limited by the Courant number, C.

The compressive scheme is a higher order differencing scheme, which captures the phase interface based on algebraic information. It performs a second order interpolation of the interface using a slope limiter. The following formulation is used.

$$\alpha_{\mathrm{f}} = \alpha_{\mathrm{d}} + \beta \nabla \alpha_{\mathrm{d}}. \tag{3.4}$$

In the equation above, α_{f} is the face value of the volume fraction, α_{d} is the volume fraction value of the donor cell and β is the slope limiter. For the compressive scheme, the slope limiter value is $\beta = 2$. The advantage of the compressive scheme is that it can be used with an implicit temporal discretisation of the volume fraction equation (section 3.1.4). Thus, the time-step for the transient computation of the phase interface advection through the domain is not limited by the Courant number, C. Seo [60] pointed out that a compressive phase interface reconstruction with implicit temporal discretisation of the volume fraction equation, along with an implicit, bounded second order time discretisation for all other flow variables, provides a sharp interface which is comparable to the most accurate geometric reconstruction scheme.

As shown in Figure 3.1, the phase volume fraction value, α, can take values between zero and one. Calculational cells with $0 < \alpha < 1$ contain the phase interphase. For a perfectly sharp interface, the transition from $\alpha = 0$ to $\alpha = 1$ (and vice versa) occurs as a step function. In CFD, however, due to the finite size of the calculational cells and numerical diffusion, which arises from truncation errors, the transition is gradual. It is important to highlight that this gradual transition is not physical, but a result of how the interface is modelled. It is accepted practice to define the phase interface location at a phase volume fraction value of $\alpha = 0.5$.

3.1.6 Phase Interaction Models

When using the VOF model, additional choices have to be made with regard to the modelling of phase interactions, such as mass transfer mechanisms, surface tension and wall adhesion effects. The following paragraphs will describe and justify the settings used for the domain under investigation.

Mass transfer mechanisms, in general, include phenomena such as cavitation, evaporation and condensation, or boiling. For the specific case under investigation, mass transfer is not expected to take place. In the external flow domain (Figure 2.1), cavitation will not occur, as the pressure variations caused by the oil flow through the domain and the rotating motion of the planet gear and planet carrier are too small.

In flows that contain droplets, surface tension effects become important if the Weber number is significantly larger than one.

$$\mathrm{We} = \frac{\rho u^2 d}{\sigma} \tag{3.5}$$

In the equation above, ρ is the liquid density, u is the liquid velocity, d is the droplet diameter and σ is the surface tension. As droplet sizes and velocities are not known a priory, surface tension effects may be important and have therefore been taken into account by enabling the default ANSYS Fluent [49] continuous surface force model, which was used for all investigations presented in this thesis.

In ANSYS Fluent [49], the level of wall adhesion can be adjusted by defining the contact angle, o, between the liquid phase and the gas phase. The contact angle, o, is typically measured inside the denser of the two fluid phases involved (Figure 3.2).

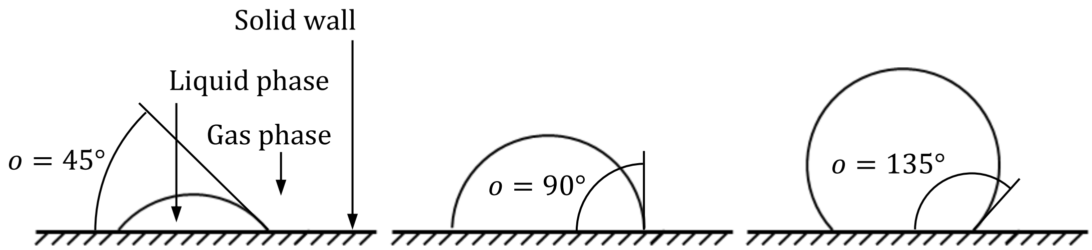

Figure 3.2: Definition of different contact angles, *o*

Contact angles are very sensitive to surface properties and surface contamination. They are difficult to measure due to the dynamic behaviour of fluids. The repeatability of contact angle measurements is therefore generally poor. As there was no opportunity to measure the contact angle as part of the presented work, a sensitivity study was carried out to cover a range of possible contact angles from 10° to 135° (section 4.1.6). The study showed that the predicted flow path is insensitive to the specified contact angle. For this reason, wall adhesion effects have not been accounted for.

3.1.7 Energy Model

In general, the energy model available in ANSYS Fluent [48] allows heat transfer mechanisms to be accounted for. Heat transfer from or into the liquid must be evaluated, as the associated temperature change may affect the liquid's viscosity sufficiently to alter the flow field behaviour. In the external flow domain (Figure 2.1), heat transfer from or into the liquid phase can occur through direct interaction with the gas phase, the components bounding the domain under investigation or through radiation. However, the temperature differences between the fluids and the solids are assumed to be small. Hence, the effect on the liquid temperature caused by these mechanisms is negligible.

An effect that needs to be considered in systems with fast moving components and liquids with a strong dependency between temperature and viscosity is that of viscous heating. The liquid's temperature rise due to this mechanism can be estimated by analysing the work done by the rotating component on the liquid. The following considerations with respect to viscous heating aim to provide an order-of-magnitude analysis for the total temperature rise that can be expected.

A measure for the work done by the rotating planet gear is the required power to spin it at a certain rotational speed.

$$P_{\mathrm{G}} = M_{\mathrm{G}}\omega_{\mathrm{G}} \tag{3.6}$$

In the equation above, M_{G} is the torque of planet gear and ω_{G} is its angular velocity. In ANSYS Fluent [48], torque values are accessible through the dimensionless moment coefficient,

$$c_m = \frac{M_{\mathrm{G}}}{\frac{1}{2}\rho_{\mathrm{ref}}\, v_{\mathrm{ref}}^2\, A_{\mathrm{ref}}\, l_{\mathrm{ref}}}. \tag{3.7}$$

In the equation above, ρ_{ref}, v_{ref}, A_{ref} and l_{ref} are the reference values for the density, the velocity, the area and the length, respectively, used by ANSYS Fluent [48]. Assuming that all of the power required to spin the planet gear is converted into heat, the following relationship can be used to estimate the upper limit of the liquid temperature rise, ΔT.

$$\Delta T = \frac{M_{\mathrm{G}}\omega_{\mathrm{G}}}{c_{\mathrm{p}} \cdot \dot{m}} \tag{3.8}$$

In the equation above, M_G is the torque of the planet gear, ω_G is the angular gear velocity, c_p is the specific heat capacity of the liquid at constant pressure, and $\dot{m}$ is the liquid mass flow rate.

CFD analyses of maximum load conditions, which are presented in section 4.1.4, were used to estimate the c_m value of the planet gear surfaces bounding the external flow domain. Post-processing of the analysis results concluded that $c_m \sim 0.42$. Hence, at maximum load conditions, the estimated temperature rise of the oil due to viscous heating is less than 0.5°C. This translates into a viscosity change of less than 1% at this particular operating point. For this reason, the external flow domain (Figure 2.1) is modelled isothermally, i.e. at constant temperature.

3.1.8 Turbulence Model

Based on the review of relevant turbulence models (section 2.7), the SST k–ω model was chosen to model the effects of turbulence on the mean flow behaviour for all investigations presented in this thesis. It was selected for the following reasons.

- Compared to other turbulence models, the SST k–ω model has advantages with respect to modelling turbulence in the near-wall region.
- As demonstrated by Bristot [57], the SST k–ω model is suitable for simulating multiphase bearing chamber flows.
- The vast experience of the University of Nottingham's G2TRC showed that the SST k–ω model is the preferred choice for a wide range of multiphase flow applications.

3.1.9 Turbulence Damping

The VOF method averages the fluid properties in each calculational cell based on the value of the fluid volume fraction. Thus, averaged flow quantities will be assigned to both fluid phases in cells that contain the phase interface, as a single set of momentum equations is solved. In flows with a high velocity gradient at the interface between the fluids, this will generate high turbulence quantities and non-physical momentum transfer between the phases. Turbulence damping is therefore an available option in ANSYS Fluent [48] to accurately model these types of flows. When simulating the oil flow behaviour in a bearing chamber of a two-shaft aero-engine for small and medium-sized aircraft, Bristot [57] showed the profound effect that the turbulence damping value can have on the predicted flow behaviour. In an aero-engine bearing chamber, the oil flow along the chamber wall is primarily driven by windage effects of the air phase. In contrast, the oil flow emerging from the lubricating gap of a journal bearing in an epicyclic gearbox is primarily driven by the rotating motion of the planet gear (section 2.1). As the physical mechanism that drives the oil flow is not the shear of the gas phase, but a rotating wall, turbulence damping is not considered to be required [57].

3.1.10 Solution Method

In epicyclic gearboxes, based on the orbital and rotational velocities of the gears, in general, flow velocities are expected to be in a range consistent with incompressible or mildly compressible flow. Therefore, for all investigations presented in this thesis, the pressure-based solver is used. As previously discussed in section 2.6.3, ANSYS Fluent [48] offers two different solution algorithms to solve the discretised transport equation (2.55) for fluid property ϕ, namely segregated ones and a coupled one. The coupled solver's rate of solution convergence is usually superior compared to that of the segregated solver. This is due to solving the momentum and continuity equations in a closely coupled manner. For this reason, the coupled solver is chosen for the investigations presented in this thesis even though it is computationally more expensive.

The geometry of the domain under investigation presents unique challenges for choosing appropriate solution parameters. The large range of domain length scales from 6 μm (minimum lubricating gap height) to more than 40 mm (radial distance between pin surface and gear tip radius, Figure 2.1), imposes a number of constraints on the calculational mesh topology (section 3.3). As a result, some high aspect ratio cells in the main circumferential flow direction cannot be avoided. Since the fluid flow property gradients in this direction tend to be smaller compared to those perpendicular to the main direction of flow, this is not expected to affect the quality of the simulations. It does, however, adversely affect the convergence behaviour of the case under investigation.

In order to achieve convergence, depending on the specific case under investigation, the flow Courant number had to be reduced significantly from its default value to a minimum of 0.1. In this context, adjusting the flow Courant number is a means to under-relax the fluid flow equations (section 2.4). This is known as implicit under-relaxation and used to stabilise the convergence behaviour of the outer iterations during each time-step (Figure 2.17 (b)) [49]. It is equivalent to a location-specific time-step. The under-relaxation of equations should not be confused with the explicit under-relaxation of flow variables, which can be adjusted in addition to the flow Courant number. The global Courant number is controlled through the choice of the size of the time-step, Δt.

In order to further enhance the convergence behaviour, every case was initially run with single-phase air only. Once the air field was converged, the oil flow was enabled.

3.2 Analysis Approach

In epicyclic gearboxes, the kinematics of the gears is complex, especially when considering a planetary configuration (Figure 1.1). The sun gear drives a number of planet gears, which, in turn, rotate about their own axis and orbit around the sun gear. Therefore, it is practicable to decompose the epicyclic gearbox system into simpler sub-models. Starting from a simple model, this approach allows key underlying physical phenomena to be identified and their effects on the outflow behaviour to be assessed. It is proposed to progressively extend the initial simple model in a step-wise manner to include the radial journal bearing eccentricity, e, and the orbiting motion of the planet gear. Thus, the kinematic conditions in an epicyclic gearbox in planetary configuration (Figure 3.3) are fully represented.

In its most basic form, a journal bearing can be approximated by two concentric cylinders, which form an axially and circumferentially constant lubricating gap height, h_0 (Figure 3.3 (a)). At this first stage, the cylinder representing the gear rotates about a stationary, i.e. non-orbiting, cylinder representing the pin.

At the second stage, an orbit radius is applied to the model. This allows the effect of the centrifugal force, generated by the orbiting motion of the planet gear, on the external journal bearing oil flow behaviour to be assessed (Figure 3.3 (b)). It should be noted that also for orbiting cases, the Reynolds equation governing the internal fluid flow behaviour of a general journal bearing (section 2.2) is valid, as the lubricating film thickness is sufficiently small to neglect body forces, such as the centrifugal force.

At the third stage, radial gear eccentricity is applied to a journal bearing model with a stationary, i.e. non-orbiting cylinder representing the pin. Radial gear eccentricity will result in a convergent-divergent lubricating gap height as it occurs in an actual journal bearing. At this stage, the model fully resembles a journal bearing in an epicyclic gearbox in star configuration (Figure 3.3 (c)).

At the final stage, an orbit radius is applied to the model used in the previous step. The kinematic conditions of an epicyclic gearbox in planetary configuration are now fully resembled (Figure 3.3 (d)). Assessing the effects of radial gear eccentricity and orbiting motion on the external journal bearing oil flow behaviour separately from each other allows key physical mechanisms and their sensitivities to be identified.

(a) Non-orbiting model with constant lubricating gap height ($e = 0$)

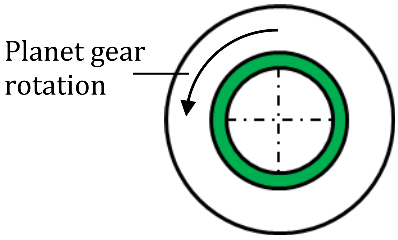

(b) Orbiting model with constant lubricating gap height ($e = 0$)

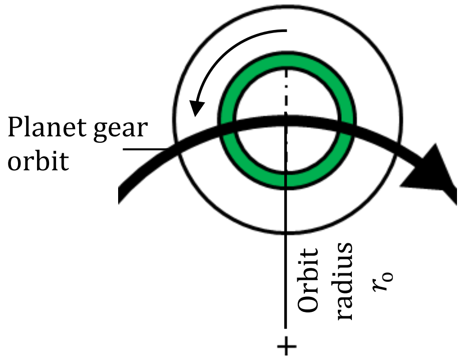

(c) Non-orbiting model with convergent-divergent lubricating gap height ($e > 0$)

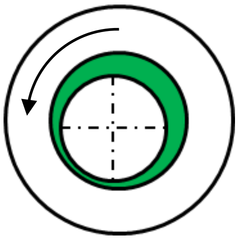

(d) Orbiting model with convergent-divergent lubricating gap height ($e > 0$)

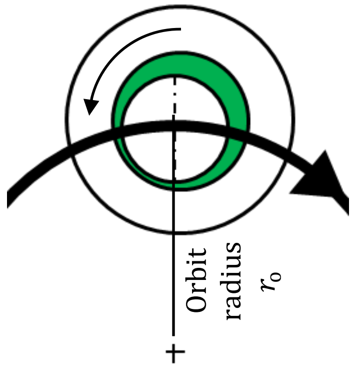

Figure 3.3: Progressive extension of journal bearing model in a step-wise manner

3.3 Computational Grid Generation Approach

In order to solve the fluid flow governing equations (section 2.4), the domain under investigation needs to be divided into finite volumes (section 2.5), which form a computational grid. Two different types of computational grids are generally available, namely structured and unstructured.

Structured grids use quadrilateral (2D) or hexahedral cells (3D), whilst unstructured grids typically use triangular (2D) or tetrahedral cells (3D). In contrast to unstructured grids, structured grids are characterised by a unique relationship between every calculational cell and its neighbours. For this reason, a structured mesh, in general, is computationally more effective.

It relies on blocks to describe the geometry of a domain. For relatively simple domain geometries, a blocking structure can easily be generated. For complex domain geometries, however, this will be more difficult or sometimes even nearly impossible. For these cases, unstructured meshes are to be used, as they do not rely on a blocking structure. Hence, they are more flexible. Flexibility with regard to representing complex geometries and cell clustering in areas where a high resolution is required, i.e. where a fluid flow property is subject to large gradients, is a key advantage of unstructured meshes over structured meshes.

For simple domain geometries, such as channels or ducts, a structured mesh can not only be computationally more effective, but it can also be better aligned with the flow direction than an unstructured mesh. This helps to minimise numerical diffusion, which arises from truncation errors that are a consequence of representing the fluid flow equations in a linearised discrete form. This advantage, however, is no longer applicable to more complex flows, for example with recirculations, where the flow is no longer aligned to the mesh.

One key advantage of structured meshes over unstructured meshes is that the quadrilateral or hexahedral cells allow much larger aspect ratios than triangular or tetrahedral cells. This can help to reduce the overall cell count in the domain.

For multiphase flow analysis, additional requirements with respect to the mesh topology are imposed by the numerical modelling technique (section 2.8) that is used. For three-dimensional multiphase flow analysis with the VOF method (section 2.8.1), cube-shaped cells, i.e. cells with an aspect ratio close to one, are preferred in order to allow accurate phase interface reconstruction.

Based on the above-mentioned advantages of a structured mesh topology over an unstructured one, and the fact that a blocking structure can easily be established for the domain under investigation, a structured mesh is used for all investigations presented in this thesis.

As described in section 2.7.1.7, a sufficient number of cells across oil films, which are expected to form on the surfaces bounding the domain under investigation (Figure 2.1), is required to accurately resolve the phase interface. As this typically results in y^+ values in the order of 10, it was decided to explicitly resolve the boundary layer. For this reason, the height of the first cell adjacent to the wall was chosen such that a y^+ value of less than one was achieved. In order to avoid an unnecessary high cell count in regions where this is not required, i.e. in regions where the fluid flow properties are subject to small gradients, the cell height was expanded away from the wall with a growth factor of typically 1.2. The mesh parameters were chosen such that regular hexahedral cells, i.e. cells with an aspect ratio close to one, were created. However, due to the large range of domain length scales from 6 µm (minimum lubricating gap height) to more than 40 mm (radial distance between pin surface and gear tip radius, Figure 2.1), and the constraints imposed by the blocking structure, the growth factor of

1.2 had to be exceeded occasionally and some high aspect ratio cells could not be avoided. As high aspect ratio cells are only present in the main flow direction, where fluid property gradients tend to be smaller compared to those perpendicular to the main flow direction, the quality of the simulations is not adversely affect. For a non-orbiting journal bearing model with a constant lubricating gap height, h_0, this statement will be verified by the analysis presented in section 4.1.5.2.

The mesh was created in a two-dimensional space and subsequently rotated about the journal bearing's axis to form a three-dimensional geometry. This approach generally results in a high mesh quality. For cases considering journal bearing eccentricity, the pin surface was moved off-centre with respect to the inner planet gear diameter. In order to achieve the correct eccentricity angle, $\theta_{\mathrm{h,\,min}}$ (Figure 2.3), the whole model was subsequently rotated by the appropriate angle about the planet gear's axis.

3.4 Inlet Boundary Condition for External Oil Flow from a Journal Bearing with a Constant Lubricating Gap Height

When investigating external oil outflow from a simplified journal bearing with a constant lubricating gap height, h_0, with CFD, an appropriate inlet boundary condition into the external domain (Figure 2.1) has to be defined. As previously discussed in section 2.2, the inlet boundary condition into the external domain is defined by the flow and liquid properties at the outlet of the internal flow domain (Figure 2.2).

Typically, journal bearings are supplied with oil through an axial feed groove on the pin, as shown in Figure 2.1. For the specific case under investigation, the length of the groove extends over 80% of the bearing length. As the design is symmetric with respect to the vertical planet gear axis (Figure 2.1), there is a distance of 10% of the bearing length on each side that is undisturbed by any design features. This distance can be interpreted as the available entrance length, l_{ent}. Due to the continuous supply of oil into the lubricating gap and the rotating motion of the planet gear, the flow develops velocity components in the axial and the circumferential directions, u and v, respectively.

3.4.1 Axial Velocity Distribution

In the axial direction, the flow is driven by the oil feed pressure. As the pressure gradient in the axial direction, $\partial p/\partial y$, is different from zero, and assuming fully developed laminar flow conditions when entering into the external domain, a Poiseuille flow profile develops. The velocity profile between the pin and the planet gear surface is parabolic, as described by equation (2.5). A graphical representation of the velocity profile is shown in Figure 2.6.

The assumption of fully developed flow in the axial direction, y, is justified, as the lubricating gap height, h_0, is very small compared to the available entrance length, l_{ent}. Thus, the ratio l_{ent}/h_0 is very high. For the specific case under investigation, l_{ent}/h_0 equals 150. According to Incropera and DeWitt [76], the required entrance length, $l_{\mathrm{ent,\,rq}}$, for laminar flow to fully develop is given by

$$\frac{l_{\mathrm{ent,\,rq}}}{h_0} \approx 0.05\ \mathrm{Re}_v. \tag{3.9}$$

The Reynolds number for the flow velocity component in the axial direction, Re_v, was previously calculated in section 2.2. For the specific case under investigation, the ratio $l_{\mathrm{ent}}/l_{\mathrm{ent,\,rq}}$ equals 30. Hence, l_{ent} is sufficiently long for the laminar flow to fully develop.

The oil volume flow rate, $\dot{V}_{\mathrm{sup}}$, and thus the mass flow rate, $\dot{m}_{\mathrm{sup}}$, supplied to the journal bearing are known based on its geometric dimensions and operating conditions. Due to the conservation of mass, the same amount of oil that is supplied into the lubricating gap through the feed groove will have to leave the lubricating gap and pass through the external flow domain. Considering a simplified journal bearing with a constant lubricating gap height, h_0, and neglecting any pressure losses inside the lubricating gap, the oil inlet mass flow rate into the external domain, $\dot{m}_{\mathrm{in}}$, is evenly distributed around the bearing's circumference. Hence, every bearing sector will experience the same amount of oil entering into the external domain. For this reason, a mass flow inlet was chosen as inlet boundary condition type for the simplified model under investigation. When using this inlet boundary condition type, the flow is released perpendicular to the surface it is applied to. Hence, at the inlet boundary, the circumferential velocity component, u, equals zero. At this location, the axial inlet flow velocity component, v, is determined as a bulk property based on the prescribed inlet mass flow rate, the oil density and the annular area of the space between the planet gear and the pin. Thus, v is constant across the lubricating gap height and, consequently, the velocity gradient between the pin and the planet gear, $\partial v/\partial z$, equals zero.

In order to obtain the desired velocity profiles across the lubricating gap, namely a Couette flow profile in the circumferential direction and a Poiseuille flow profile in the axial direction, at the point of entering into the external flow domain, the flow must have travelled over the required entrance length, $l_{\mathrm{ent,\,rq}}$ to fully develop. Therefore, the mass flow inlet boundary must be offset by the distance $l_{\mathrm{ent,\,rq}}$ from the entrance to the external flow domain (Figure 3.4).

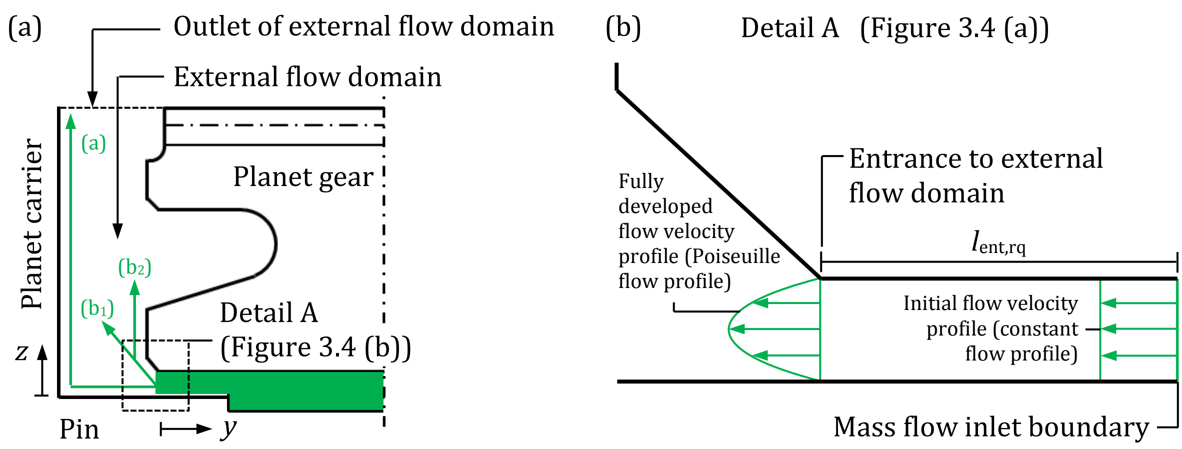

Figure 3.4: Inlet boundary condition in the axial direction for external oil flow from a journal bearing with a constant lubricating gap height

Alternatively, the inlet boundary can be modelled by imposing a fully developed axial flow velocity profile (Poiseuille flow profile) over the lubricating gap height, h_0, at the bearing end-face ($y = 0$), i.e. directly at the entrance to the external flow domain. The flow velocity profile is described by equation (2.5). For a constant lubricating gap height, this profile is constant around the bearing's circumference. In ANSYS Fluent [48], velocity profiles can be modelled by means of user defined functions (UDFs). UDFs provide the user with a high degree of flexibility when standard inlet boundary condition types are insufficient to describe the conditions of the actual domain under investigation. The UDF source code is included in Appendix 3. Using this approach is particularly attractive when modelling full 360° cases, as it removes the need to discretise the internal flow domain with the length $l_{\mathrm{ent,\,rq}}$. Thus, the overall count of calculational cells can be reduced. Utilising this approach becomes essential when investigating journal bearings with a convergent-divergent gap (section 3.5.1), as the flow velocity profile changes around the bearing's circumference.

3.4.2 Circumferential Velocity Distribution

Considering a journal bearing with a constant lubricating gap height, h_0, and neglecting any pressure losses inside the lubricating gap in the circumferential direction, x, the fluid pressure $p(x)$ is constant. Thus, the pressure gradient in this direction, $\partial p/\partial x$, is zero. The flow in the x-direction is only driven by the rotating motion of the planet gear. As the flow is laminar (section 2.2), this shearing action will cause a Couette flow profile to develop. The velocity profile between the pin and the planet gear surface is linear, as described by equation (2.4). Figure 3.5 shows a graphical representation of the velocity profile at the bearing end-faces ($y = 0$ and $y = l$, respectively (Figure 2.1)), where $\partial p/\partial x = 0$.

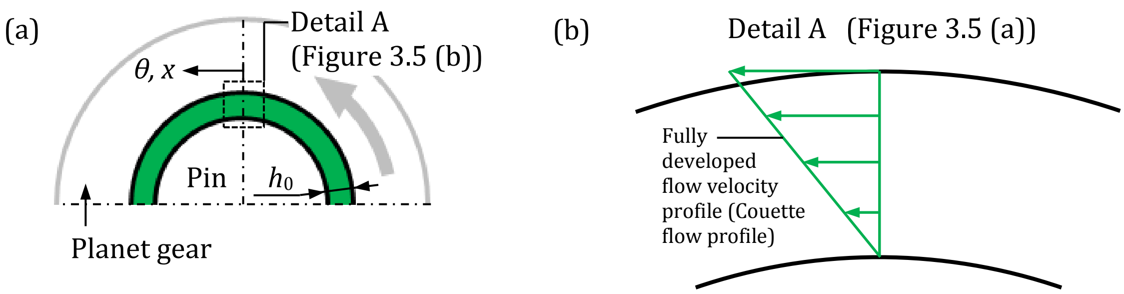

Figure 3.5: Inlet boundary condition in the circumferential direction for external oil flow from a journal bearing with a constant lubricating gap height

When using a mass flow inlet boundary at the distance $l_{\text{ent, rq}}$ from the entrance to the external flow domain (Figure 3.4), the Couette flow profile develops naturally as the oil travels through the lubricating gap. Alternatively, similar to what has been described in section 3.4.1, the inlet boundary can be modelled by imposing a fully developed circumferential flow velocity profile (Couette flow profile) over the lubricating gap height, h_0, at the bearing end-face ($y = 0$), i.e. directly at the entrance to the external flow domain. The flow velocity profile is described by equation (2.4). For a constant lubricating gap height, it is constant around the bearing's circumference. The UDF source code is included in Appendix 3.

3.5 Inlet Boundary Condition for External Oil Flow from a Journal Bearing with a Convergent-Divergent Lubricating Gap Height

When considering a journal bearing with a convergent-divergent lubricating gap height, h, the inlet boundary conditions into the external flow domain (Figure 2.1) are more complex compared to those of a simplified journal bearing with a constant lubricating gap height, h_0. As previously discussed in section 2.2, a convergent-divergent lubricating gap height, h, results in a variable fluid pressure inside the lubricating gap. Figure 2.4 and Figure 2.5 qualitatively showed the fluid pressure distribution, $p(x, y)$, in the journal bearing under investigation at maximum load conditions.

The fluid pressure distribution and, more specifically, the fluid pressure gradients in the circumferential and the axial directions, $\partial p/\partial x$ and $\partial p/\partial y$, respectively, affect the inlet velocity profiles into the external flow domain profoundly. In the following sections 3.5.1 and 3.5.2, the velocity profiles, velocity distributions and pressure gradient distributions are evaluated at the bearing end-faces, $y = 0$ and $y = l$, respectively (Figure 2.1). These planes mark the entrance to the external flow domain. Due to bearing symmetry, the fluid flow properties and conditions at $y = 0$ and $y = l$ must be consistent.

3.5.1 Axial Velocity Distribution

As previously described in section 2.2, in a journal bearing, an axial flow velocity component, v, is generated due to the varying fluid pressure inside the lubricating gap. The magnitude of v can be determined by solving equation (2.5). The equation shows that the physical mechanism for the generation of v is the pressure gradient in the axial direction, $\partial p/\partial y$. In order to determine v at the bearing end-face, $\partial p/\partial y$ needs to be evaluated at this specific axial location.

The pressure distribution, and thus the fluid pressure gradients inside the lubricating gap for the journal bearing under investigation at maximum load conditions, were determined with COMBROS [29]. As previously highlighted in section 2.2, the necessary work associated with setting up and running the COMBROS model, and post-processing its results was performed by Rolls-Royce Deutschland (RRD). For given operating conditions, COMBROS [29] computes the fluid pressure values on specific user-defined grid points by solving the Reynolds equation (equation (2.9)). The pressure gradient in the axial direction, $\partial p/\partial y$, can be approximated by the pressure difference, Δp, between the first two grip points, which, for the specific case under investigation, are separated by the distance $\Delta y = 0.0125\, l$. The distribution of $\Delta p/\Delta y$ at the bearing end-face around the bearing's circumference at maximum load conditions is shown in Figure 3.6.

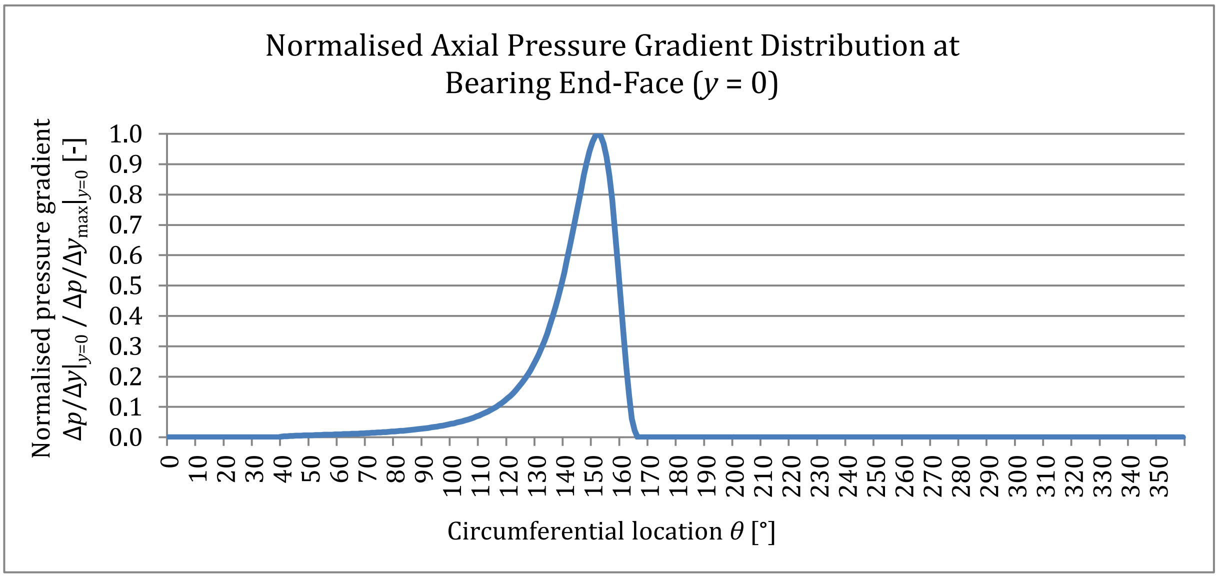

Figure 3.6: Normalised axial pressure gradient distribution at bearing end-face (y = 0) at maximum load conditions

As shown in Figure 3.6, $\partial p/\partial y$ is equal to zero in the regions between $0° \leq \theta \leq 38°$ and $166° \leq \theta < 360°$. In the convergent part of the lubricating gap, this is due to the fact that the amount of oil supplied to the bearing is insufficient to completely fill the gap in this region. Instead, the gap is partly filled with air and partly filled with oil. With increasing values of θ, the gap height reduces and the effective flow area becomes smaller. The oil is forced to flow sideways in the axial direction. The air is displaced by the oil until, at $\theta = 38°$, the lubricating gap is small enough for the oil to fill it completely. At this point, $\partial p/\partial y$ takes a non-zero value and oil starts to emerge from the lubricating gap into the external flow domain.

As previously discussed in section 2.2, in the divergent part of the gap, the film pressure reduces rapidly to the saturation pressure, p_{sat}, at which gaseous cavitation occurs. According to Szeri [27], p_{sat} is equal or just below the ambient atmospheric pressure, p_{amb}, and constant within the cavitation region. For this reason, $\partial p/\partial y$, is zero in the region between $166° \leq \theta < 360°$ and no outflow will occur.

Between $38° < \theta < 166°$, $\partial p/\partial y$ steadily increases. It peaks at $\theta = 152°$ and subsequently drops sharply to p_{sat}. It should be noted that $\partial p/\partial y$ peaks at the same circumferential location ($\theta = 152°$) as the fluid film pressure, p.

As $\partial p/\partial y$ is known at every location, θ, around the bearing's circumference, the axial outflow velocity profiles at the bearing end-face can be calculated using equation (2.5). For visualisation purposes, it is practical to plot the mean axial outflow velocity, v_{mean}, which can be determined by integrating equation (2.5) across the radial coordinate, z, within the limits of zero and h.

$$v_{\text{mean}} = \frac{1}{h}\int_{0}^{h} \frac{1}{2\mu}\frac{\partial p}{\partial y}(z^2 - zh)dz = \frac{1}{12\mu}\frac{\partial p}{\partial y}h^2 \tag{3.10}$$

Figure 3.7 shows the normalised mean axial velocity distribution around the bearing's circumference at maximum load conditions. The circumferential gear velocity, $\omega_{\text{G}} r_{\text{G}}$, was chosen as normalisation parameter, where ω_{G} is the gear's angular velocity and r_{G} is the radius of the cylindrical surface of the planet gear bore (diameter d_{G}, Figure 2.1). Consistent with the axial pressure gradient distribution, $\partial p/\partial y\,(\theta)$, around the bearing's circumference (Figure 3.6), outflow only occurs in the region between $38° < \theta < 166°$. The maximum mean axial outflow velocity occurs at $\theta = 101°$, where it reaches 44% of the gear's circumferential velocity.

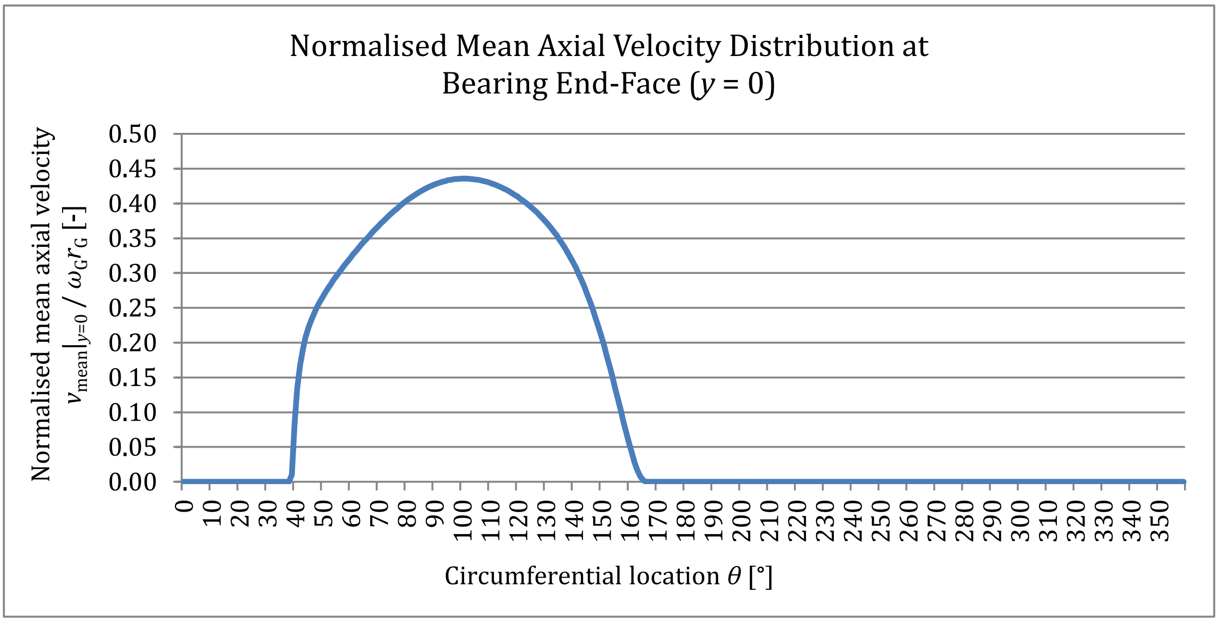

Figure 3.7: Normalised mean axial velocity distribution at bearing end-face (y = 0) at maximum load conditions

When modelling the external oil flow from an orbiting journal bearing, an accurate representation of the velocity profiles into the external domain must be used. The UDF for the axial inlet velocity into the external domain must be able to reproduce a Poiseuille flow profile across the lubricating gap height, h, that varies in magnitude around the bearing's circumference in accordance with the axial velocity distribution shown in Figure 3.7.

The Poiseuille flow profile for the axial outflow velocity, v, is given by equation (2.5), which is repeated here for completeness.

$$v = \underbrace{\frac{1}{2\mu}\frac{\partial p}{\partial y}}_{v_{\text{flux}}} \underbrace{(z^2 - zh)}_{A} \tag{3.11}$$

Dimensionally, the equation above comprises a velocity flux term, v_{flux}, i.e. a velocity per area, and an area term, A. Whilst v_{flux} is primarily a function of the bearing's operating condition and lubricant properties, A is a function of the bearing's geometry. In ANSYS Fluent [48], geometrical data is easily accessible through the node locations of the calculational mesh. For this reason, it is practical to evaluate the v_{flux}–term separately. The distribution of the normalised axial velocity flux around the bearing's circumference at maximum load conditions is shown in Figure 3.8.

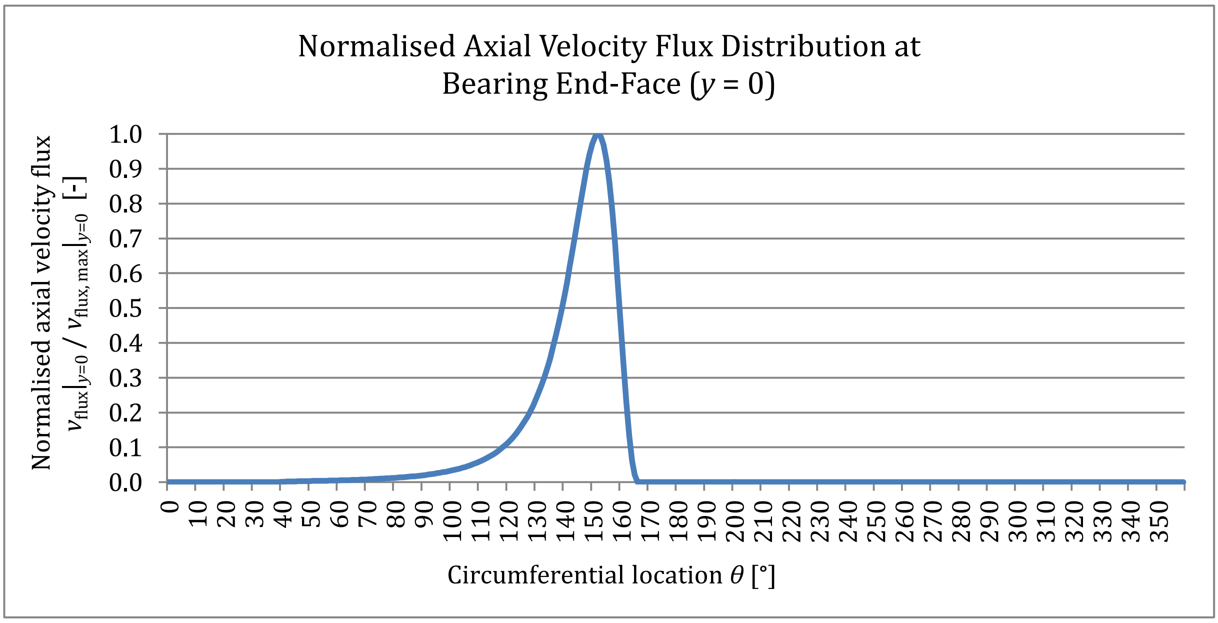

Figure 3.8: Normalised axial velocity flux distribution at bearing end-face (y = 0) at maximum load conditions

Qualitatively, the v_{flux}-distribution, $v_{\text{flux}}(\theta)$, is similar to that of the $\partial p/\partial y$-distribution, $\partial p/\partial y\,(\theta)$, shown in Figure 3.6. It should be noted that the additional term $1/(2\mu)$ in the v_{flux}-distribution (equation (3.11)) is not constant around the bearing's circumference. As the fluid pressure increases in the convergent part of the gap, the fluid temperature increases accordingly. This results in a reduction of the dynamic viscosity, μ, for increasing fluid pressure values.

In order to implement a representative axial velocity distribution as an inlet boundary condition into the external domain, the UDF needs to replicate the curve shown in Figure 3.8. There are numerous ways to approximate, interpolate and fit data. For the data set given in Figure 3.8, three options have been considered, namely cubic spline fitting, conventional polynomial fitting and Chebyshev polynomial fitting.

Cubic spline fitting is an attractive option, as the approximate function, $\tilde{v}_{\mathrm{flux}}\,(\theta)$, is smooth in the first derivative and continuous in the second derivative, both within a specified interval and at its boundaries [77]. For the given data set shown in Figure 3.8, n number of intervals have to be defined, as a single cubic spline is unable to produce approximate values, $\tilde{v}_{\mathrm{flux}}$, with a sufficiently small error. Cubic spline definition for n number of intervals with first derivative smoothness and second derivative continuity at the interval boundaries requires significant efforts in pre-processing. For this reason, cubic spline fitting has not been pursued further.

A much simpler and probably more intuitive approach is to approximate $v_{\mathrm{flux}}\,(\theta)$ by fitting conventional polynomials of the following form.

$$\tilde{v}_{\mathrm{flux}}(\theta) = \sum_{\mathrm{i}=0}^{\mathrm{m}} C_{\mathrm{i}}\theta^{\mathrm{i}} \tag{3.12}$$

In Microsoft Excel, this can be achieved by using the line estimation function “LINEST”. This function can be used to fit data with polynomials of the order $\mathrm{m} \leq 6$ based on minimising the sum of the squares of the errors, $v_{\mathrm{flux,\,i}} - \tilde{v}_{\mathrm{flux,\,i}}$. In order to accurately approximate the data shown in Figure 3.8, a piecewise polynomial approach is required. Thus, 10 intervals were defined, for each of which a sixth order polynomial was computed. The polynomial intervals and coefficients are summarised in Appendix 1.

Choosing a piecewise polynomial approach, naturally, leads to discontinuities at the interval boundaries. If these are small, however, this may be acceptable. Using the proposed polynomials in Appendix 1 in the region between $38° < \theta < 166°$, results in an average approximation error,

$$\bar{\epsilon} = \frac{1}{\mathrm{n}} \sum_{\mathrm{i}=1}^{\mathrm{n}} \left|\left(v_{\mathrm{flux,\,i}} - \tilde{v}_{\mathrm{flux,\,i}}\right)\right|, \tag{3.13}$$

of $\bar{\epsilon} = 0.0094\%$. The largest approximation error,

$$\epsilon_{\mathrm{max}} = |(v_{\mathrm{flux}} - \tilde{v}_{\mathrm{flux}})|_{\mathrm{max}}, \tag{3.14}$$

is $\epsilon_{\mathrm{max}} = 0.17\%$. Considering the very small errors made in the approximation of v_{flux}, the discontinuities at the interval boundaries become practically irrelevant.

Whilst this approach works, it is not very robust as the error in the approximation of v_{flux} strongly depends on the number of intervals and the interval length. Moreover, depending on the given data set, high-order polynomials can show oscillating behaviour.

A mathematically much more elegant approach is to use a Chebyshev approximation. Unlike conventional polynomials, which use the base function θ^{i} (equation (3.12)), the Chebyshev approximation uses the base function $T_{\text{i}}(\hat{\theta})$. The polynomial is constructed as follows.

$$\tilde{v}_{\text{flux}}(\theta) = \sum_{\text{i}=0}^{\text{m}} C_{\text{i}} T_{\text{i}}(\hat{\theta}) \tag{3.15}$$

The base functions, $T_{\text{i}}(\hat{\theta})$, as well as the normalised circumferential location, $\hat{\theta}$, are defined within the interval from -1 to $+1$. Thus, for the specific case under investigation, θ must be transformed such that $\theta_{\text{min}} = 38°$ corresponds to $\hat{\theta}_{\text{min}} = -1$ and $\theta_{\text{max}} = 166°$ corresponds to $\hat{\theta}_{\text{max}} = +1$. This can be achieved through the following general relationship.

$$\hat{\theta} = \frac{2(\theta - \theta_{\text{min}})}{\theta_{\text{max}} - \theta_{\text{min}}} - 1 \tag{3.16}$$

The base functions, $T_{\text{i}}(\hat{\theta})$, are defined as follows. The recurrence relation for $T_{\text{m}}(\hat{\theta})$ is referred to as the Clenshaw recurrence [77].

$$\begin{aligned} T_0 &= 1 \\ T_1 &= \hat{\theta} \\ T_2 &= 2\hat{\theta}^2 - 1 \\ T_{\text{n}} &= 2\hat{\theta}\, T_{\text{n}-1} - T_{\text{n}-2} \end{aligned} \tag{3.17}$$

Consistent with conventional polynomial fitting, the coefficients, C_{i}, for the Chebyshev approximation were determined such that the sum of the squares of the errors, $v_{\text{flux, i}} - \tilde{v}_{\text{flux, i}}$, is minimised. For the specific case under investigation, C_{i}, were determined using an existing FORTRAN code [78], which is largely based on the numerical recipes provided by Press et al [77]. As the matrix to be solved is positive definite, the Cholesky decomposition [77] was used to compute C_{i}. The Chebyshev polynomial was truncated after $\text{m} = 44$, as the errors, ϵ, between the actual values, v_{flux}, and the approximate values, $\tilde{v}_{\text{flux}}$,were acceptably small. The coefficients are summarised in Appendix 2. Using the Chebyshev polynomial proposed in Appendix 2 in the region between $38° < \theta < 166°$, results in an average approximation error of $\bar{\epsilon} = 0.0063\%$ (equation (3.13)). The largest approximation error is $\epsilon_{\text{max}} = 0.076\%$.

The advantages of using a Chebyshev polynomial as opposed to conventional piecewise polynomials are evident. The Chebyshev polynomial is:

a) Continuous and smooth over the whole interval, $38° < \theta < 166°$.
b) More robust to create and reproduce due to a).
c) For the specific case under investigation it is more accurate with less coefficients (45 Chebyshev polynomial coefficients compared to 53 non-zero conventional polynomial coefficients).

With known coefficients, C_{i}, the Chebyshev polynomial can be reconstructed in ANSYS Fluent [48]. The UDF source code is included in Appendix 3. This source code is applied to an inlet velocity boundary condition, as shown in Figure 3.9. An entrance length for the flow to fully develop is no longer required as the axial velocity profile across the lubricating gap height and the axial velocity distribution around the bearing's circumference are imposed by the UDF.

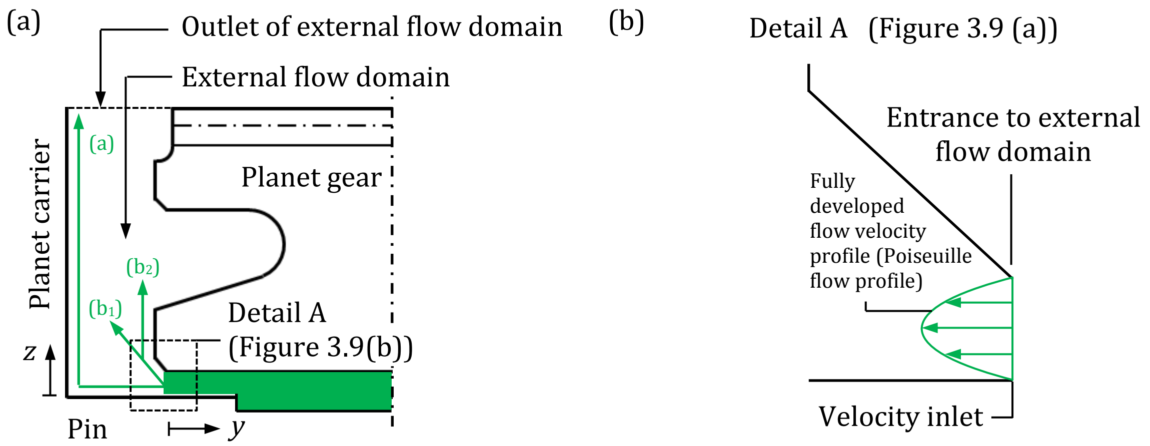

Figure 3.9: Inlet boundary condition in the axial direction for external oil flow from a journal bearing with a convergent-divergent lubricating gap height

In order to verify the correctness of the developed axial inlet velocity profile, $v(z)$, and velocity distribution, $v(\theta)$, the resultant total mass flow rate entering into the external journal bearing domain, $\dot{m}_{\text{in}}$, which can be calculated from the velocity inlet boundary condition (Figure 3.9), is compared to the mass flow rate supplied to the bearing, $\dot{m}_{\text{sup}}$. In steady state journal bearing operating conditions, due to continuity, the oil mass flow rate supplied to the bearing, which is a known design parameter, and the oil mass flow rate entering into the external flow domain, must be consistent.

The mean outflow velocity across the gap height, v_{mean}, can be determined with equation (3.10). It varies depending on the circumferential location, θ, i.e. $v_{\text{mean}} = f(\theta)$. As the temperature distribution around the bearing's circumference of the oil entering into the external flow domain is known from internal journal bearing flow analysis (section 2.2), the oil's density can be calculated and a mass flow rate distribution, $\dot{m}_{\mathrm{in}}(\theta)$, can be derived. Integrating $\dot{m}_{\mathrm{in}}(\theta)$ over the bearing's circumference yields the total oil mass flow rate entering into the external flow domain, $\dot{m}_{\mathrm{in}}$. For the specific case under investigation, the difference between $\dot{m}_{\mathrm{in}}$ and the mass flow rate supplied to the bearing, $\dot{m}_{\mathrm{sup}}$, is –1.7 % relative to $\dot{m}_{\mathrm{sup}}$. Thus, it can be concluded that the developed inlet velocity profile and velocity distribution provide consistent bulk flow quantities.

3.5.2 Circumferential Velocity Distribution

The journal bearing under investigation is exposed to ambient pressure, p_{amb}, which acts on the bearing end-faces ($y = 0$ and $y = l$, respectively (Figure 2.1)). As p_{amb} is constant, the pressure gradient in the circumferential direction, $\partial p/\partial x$, is zero. Thus, in the equation for the circumferential velocity component, u (equation (2.4)), only the Couette flow term remains. The development of a Couette flow profile due to the shearing action of the planet gear was previously discussed in section 3.4.2 for a journal bearing with a constant lubricating gap height, h_0. The mechanisms causing fluid to flow in the circumferential direction are, in fact, very similar for these two cases. The only difference is that, for a convergent-divergent gap, the gradient of the circumferential velocity component along the radial coordinate of the gap height, $\partial u/\partial z$, increases as h becomes smaller. The velocity profile between the pin and the planet gear surface is described by equation (2.4). Figure 3.10 shows a graphical representation of the velocity profile at the bearing end-faces ($y = 0$ and $y = l$, respectively (Figure 2.1)), where $\partial p/\partial x = 0$.

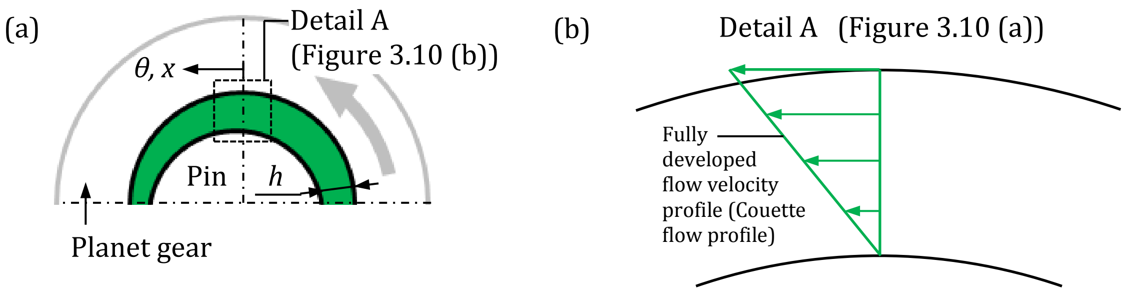

Figure 3.10: Inlet boundary condition in the circumferential direction for external oil flow from a journal bearing with a convergent-divergent lubricating gap height

When investigating a non-orbiting journal bearing, the circumferential velocity vector, $\boldsymbol{u}$, is described with respect to the pin axis. It only comprises a tangential contribution, $\boldsymbol{u}_{\mathrm{tan}}$. However, when investigating an orbiting journal bearing computationally, the circumferential velocity vector, $\boldsymbol{u}$, is described with respect to the orbit centre. It comprises a tangential and a radial contribution, $\boldsymbol{u}_{\mathrm{tan}}$ and $\boldsymbol{u}_{\mathrm{rad}}$, respectively, as shown in Figure 3.11.

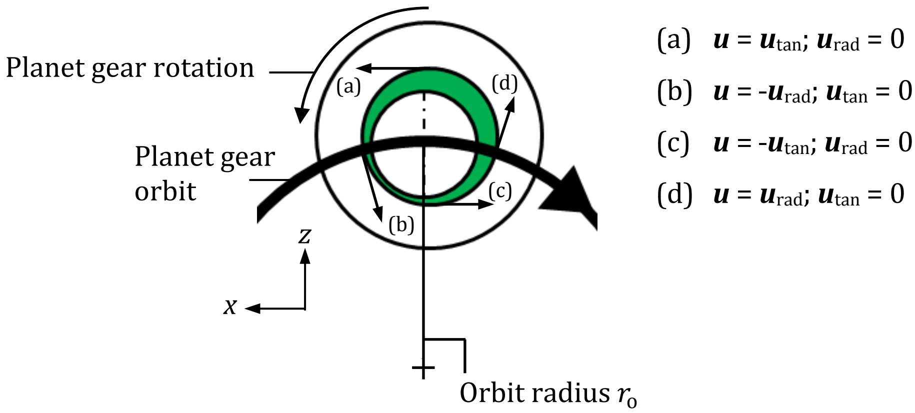

Figure 3.11: Tangential and radial contributions, $\boldsymbol{u}_{\mathrm{tan}}$ and $\boldsymbol{u}_{\mathrm{rad}}$, respectively, of the circumferential velocity vector, $\boldsymbol{u}$, for an orbiting journal bearing

When defining the UDF for u, the above conditions need to be considered. The source code for the circumferential velocity distribution of an orbiting journal bearing is included in Appendix 3.

3.6 Extension of Friedrich's et al [45] Force Balance Model

As previously highlighted in section 2.3.2, a force balance model can be used to predict the oil flow path along the gear contour. Whether the flow path follows direction (b_1) or (b_2) in Figure 2.2 mainly depends on the magnitude of the centrifugal force, the surface tension force and the inertial force acting on the liquid film.

The need for modifications to Friedrich's et al [45] force balance equation (equation (2.19)) arises from the differences between two-dimensional channel flows and three-dimensional flows over rotating components. The key differences are as follows.

- The occurrence of an additional flow velocity component, u, in the circumferential direction. The resultant flow velocity vector, $\boldsymbol{u}$, will therefore be subjected to flow angles that are different compared to the geometrical angles of the domain under investigation (Figure 3.12).
- Different liquid break-up characteristics due to more complex interactions between the gear, the liquid and the surrounding air. The correlations used by Friedrich et al [45] to determine the liquid break-up length are invalid for the case under investigation.

- At high rotational speeds, the gravitational force, F_g, is negligible compared to the centrifugal force, F_c, generated by the rotating motion of the component under investigation.

Figure 3.12 schematically shows the circumferential, the axial and the radial flow velocity components, u, v and w, respectively, of a three-dimensional flow over a backwards-facing inclined step, as it is formed by the geometry of the planet gear base, before (blue vectors, index 1) and after (green vectors, index 2) deflection. As previously highlighted in section 2.3.2, a deflection of the liquid flow path away from extended gear chamfer surface will occur due to the forces acting on the liquid. Although fluid flow along a rotating gear is not shear-driven by the gas phase surrounding the component, it is affected by the same forces as identified by Friedrich et al [45], namely inertial forces, surface tension forces and body forces.

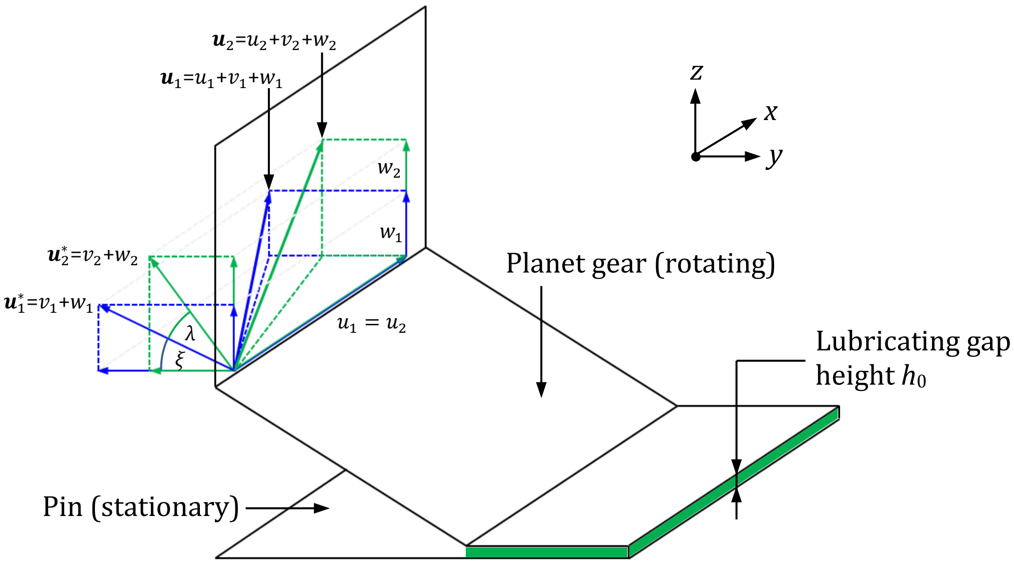

Figure 3.12: Velocity components of a three-dimensional flow over a backwards-facing inclined step before (blue) and after (green) deflection

A graphical representation of the forces acting on the oil flow as it separates from the lower edge of the gear base (diameter d_1 in Figure 2.1) is shown in Figure 3.13. The force balance is applied in the z-y-plane (Figure 3.12).

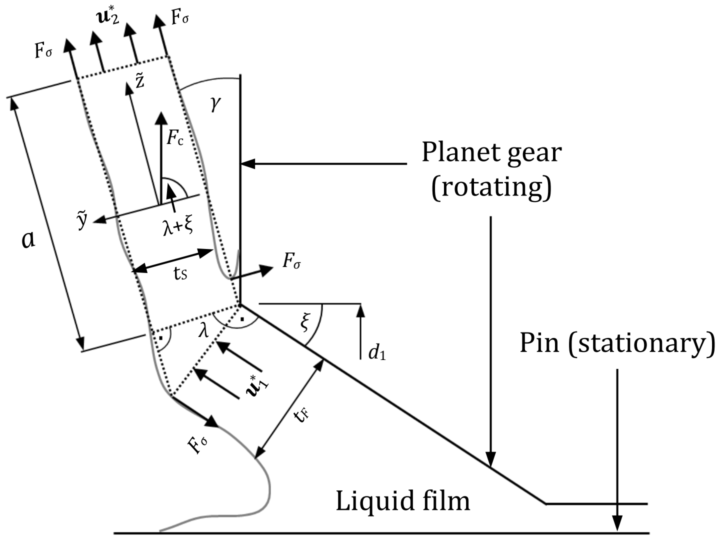

Figure 3.13: Modified force balance model of liquid flow over a backwards inclined step based on Friedrich et al [45]

Balancing the forces in the $\tilde{y}$-direction yields

$$\rho|\boldsymbol{u}_1^*|^2 t_F \sin\lambda = \sigma\sin\lambda + \sigma + \rho\, t_S\, a\left(1 - F_{slip}\right)^2 \omega_{\mathrm{G}}{}^2 \frac{d_1}{2}\cos(\lambda+\xi). \tag{3.18}$$

In the equation above, ρ is the liquid density, $\boldsymbol{u}_1^*$ is the resultant velocity vector of the liquid's axial and radial velocity component, v and w, respectively, t_F is the film thickness, λ is the flow deflection angle, σ is the surface tension, t_S is the sheet thickness, a is the radial extent of the sheet, and F_{slip} is the slip factor between the circumferential bulk flow velocity of the liquid, u, and the circumferential velocity of the gear, u_{G}.

$$F_{slip} = \frac{u_{\mathrm{G}} - u}{u_{\mathrm{G}}} \tag{3.19}$$

The angular velocity of the planet gear is denoted ω_{G}, d_1 is the lower diameter of the gear base, at which oil separation occurs and ξ is the gear chamfer angle.

Solving equation (3.18) for the deflection angle, λ, allows γ, the angle between the liquid sheet and the vertical surface of the planet gear base (Figure 3.13), to be determined.

$$\gamma = 90° - \lambda - \xi \tag{3.20}$$

If γ equals zero, the liquid sheet is deflected fully vertical, i.e. it attaches to the vertical planet gear surface. Based on its definition, the maximum value of γ is $90° - \xi$. Note that theoretically, especially for high rotational speeds and low flow rates, γ can become negative. In these cases, the axial velocity component of the liquid sheet, v_2, would become negative. Although this is possible in theory, these cases have no practical relevance as the flow attaches to the vertical planet gear surface.

Equation (3.18) contains a number of unknown variables, namely $|\boldsymbol{u}_1^*|$, t_F, t_S, a and F_{slip}, all of which will be further discussed in the following paragraphs.

The magnitude of the resultant film velocity in the y-z-plane, $|\boldsymbol{u}_1^*|$, can be calculated with equation (2.20) and the film thickness, t_F, can be calculated with equation (2.21). According to Fraser et al [40], the sheet thickness, t_S, is given by

$$t_S = \frac{\dot{V}}{2\pi|\boldsymbol{u}_1|\sqrt{\frac{d^2|\boldsymbol{u}_1^*|^2}{4|\boldsymbol{u}_1|^2} + ad + a^2}}. \tag{3.21}$$

In the equation above, $\dot{V}$ is the liquid volume flow rate, $|\boldsymbol{u}_1|$ is the magnitude of the liquid flow velocity vector (Figure 3.12, equation (3.22)), d is the cup diameter, $|\boldsymbol{u}_1^*|$ is the magnitude of the resultant film velocity in the y-z-plane, which can be calculated with equation (2.20), and a is the radial extent of the liquid sheet (Figure 2.16), which can be calculated with equation (2.26) or (2.27), depending on whether combined sheet rim and wave disintegration ($u_1 < 8$ m/s) or sheet wave disintegration ($u_1 > 8$ m/s) prevails. The magnitude of resultant flow velocity, $|\boldsymbol{u}_1|$, which is required for the calculation of the sheet thickness, t_S, is determined by the rotational speed of the cup. Both Fraser et al [40] and Liu et al [41] highlighted that, due to friction between the liquid and the cup wall, the liquid rapidly attains the same peripheral speed as the cup itself, i.e. $F_{slip} = 0$. For liquid flow over rotating discs, however, F_{slip} is larger than zero as the Coriolis force, which acts normal to the radial velocity component, w, generates slip between the bulk flow and the disc surface. Hence, $|\boldsymbol{u}_1|$ can be expressed by

$$\begin{aligned} |\boldsymbol{u}_1| &= \sqrt{|\boldsymbol{u}_1^*|^2 + \left(\left(1 - F_{slip}\right)|u_1|\right)^2} \\ &= \sqrt{|\boldsymbol{u}_1^*|^2 + \left(\left(1 - F_{slip}\right)\omega_\mathrm{G}\frac{d_1}{2}\right)^2}. \end{aligned} \tag{3.22}$$

In most applications, $|\boldsymbol{u}_1^*|$ will be negligibly small compared to the term $\omega_\mathrm{G}\, d_1/2$. However, in high-power gearbox systems, flow rates are generally high. Thus, $|\boldsymbol{u}_1^*|$ can be in the order of $0.2 \dots 0.3\ \omega_\mathrm{G}\, d_1/2$. Hence, it can no longer be neglected.

Glahn et al [42] investigated the droplet trajectories at the point of separation from the rim of a rotating disc. One of the authors' key conclusions was that the impact of the liquid flow rate on the spray characteristics, i.e. the droplet sizes, is negligible. Moreover, it was shown that the ratio of the total droplet velocity, $|\boldsymbol{u}_1|$, and the disc rim velocity, $\omega_{\mathrm{G}}\, d_1/2$, is independent of the droplet size. At the rim, $|\boldsymbol{u}_1|$ was measured to be 80% of the disc's circumferential velocity. Droplets separated from the rim at an angle of 15°. Thus, u_1 was approximately 77% of the circumferential disc velocity. Accordingly, F_{slip} was 0.23. It is assumed that at the point of flow separation from the rim of the disc, the droplet velocities and the bulk flow velocity are identical. The slip factor derived from the research work carried out by Glahn et al [42] will later be used in chapter 6 to validate the oil flow path direction predicted by the CFD models (section 6.1.1).

4 Computational Flow Investigations

In the previous chapter, details about the methods used to investigate oil outflow from a journal bearing were presented. This included, for instance, the specifics of the adopted VOF method (section 3.1). Due to the complex kinematics of an epicyclic gearbox in planetary configuration, it is practicable to decompose the gearbox system into simpler sub-models. The approach for a progressive extension of an initially simple model in a step-wise manner was described in section 3.2. In order to solve the flow governing equations numerically, a calculational grid is required. Section 3.3 discussed the approach for its generation. A valid simulation of the oil outflow from a journal bearing can only be achieved if representative inlet boundary conditions for the external domain are used. In section 3.4, the inlet boundary conditions in the axial and the circumferential directions were presented for a simplified journal bearing with a constant lubricating gap height. In section 3.5, the considerations were extended to include the axial and the circumferential inlet boundary conditions for a journal bearing with a convergent-divergent lubricating gap height. In order to validate the numerical flow path prediction analytically, a force balance model was proposed in section 3.6, which is based on the work carried out by Friedrich et al [45].

The focus of this chapter is to provide the results of the computational flow investigations. Consistent with the analysis approach presented in section 3.2, initial investigations will be performed on a simplified, non-orbiting journal bearing model with a constant lubricating gap height (section 4.1). For this particular case, the domain is symmetric about the planet gear's rotational axis. Thus, a sector model is used. The general set-up, including the model boundary condition types, will be discussed in section 4.1.1. For initial investigations, sector model analyses are particularly attractive as flow behaviour sensitivities in the external journal bearing domain can be explored at relatively low computational cost. Theoretical considerations previously presented in section 2.3.2 concluded that the oil flow in the external domain of a journal bearing can, in principle, follow two different flow path directions, i.e. axial (flow path (a) in Figure 2.1) or radial (flow path (b) in Figure 2.1). The results presented in section 4.1.2 will demonstrate that both flow paths can occur depending on the specific oil properties and the operating conditions of the bearing. Sector analyses can be very efficient to assess the oil outflow behaviour of a journal bearing with a constant lubricating gap height. However, the time required for simulations to reach steady-state flow field conditions indicated that a significant speed-up would be required for cases that cannot be addressed with this approach. When assessing the effect of the orbiting motion of the planet bearing, for instance, or when assessing the oil outflow behaviour of a journal bearing with a convergent-divergent lubricating gap height, a full 360° model is needed as the domain is no longer symmetric about the gear's axis. For this reason, section 4.1.3 explores different options to reduce the computational time of the initial baseline model, with the aim to make full 360° journal bearing model analyses viable in an industrial context. With a robust and quick to run model in place, full steady-state flow field conditions (section 4.1.4) can be performed. Moreover, this allows additional sensitivities (sections 4.1.5 to 4.1.7) to be assessed, which could not previously be explored due to simulation time limitations.

The findings and conclusions from the investigations presented in section 4.1 create the basis for further, more complex analyses, including the external oil flow from an orbiting journal bearing with a constant lubricating gap height (section 4.2), and from a non-orbiting and orbiting journal bearing with a convergent-divergent gap height (sections 4.3 and 4.4).

4.1 Non-Orbiting Journal Bearing with Constant Lubricating Gap Height

In this section, oil outflow from a non-orbiting journal bearing with a constant lubricating gap height is investigated with a sector model. The use of a sector model is valid as the domain under investigation is symmetric about the planet gear's rotational axis. Section 4.1.1 explains in detail how the model has been set up. The simulation results and conclusions are presented in sections 4.1.2 and 4.3.3, respectively.

4.1.1 CFD Model Set-Up

In this section, the CFD model set-up for the initial investigations will be discussed. The model set-up consists of generating the computational mesh, applying appropriate boundary conditions and choosing appropriate numerical settings for the simulation. The general approach of generating the computational mesh for the domain under investigation has previously been described in section 3.3. Figure 4.1 shows a 2D plane of the baseline mesh used for the initial CFD investigations presented in this section.

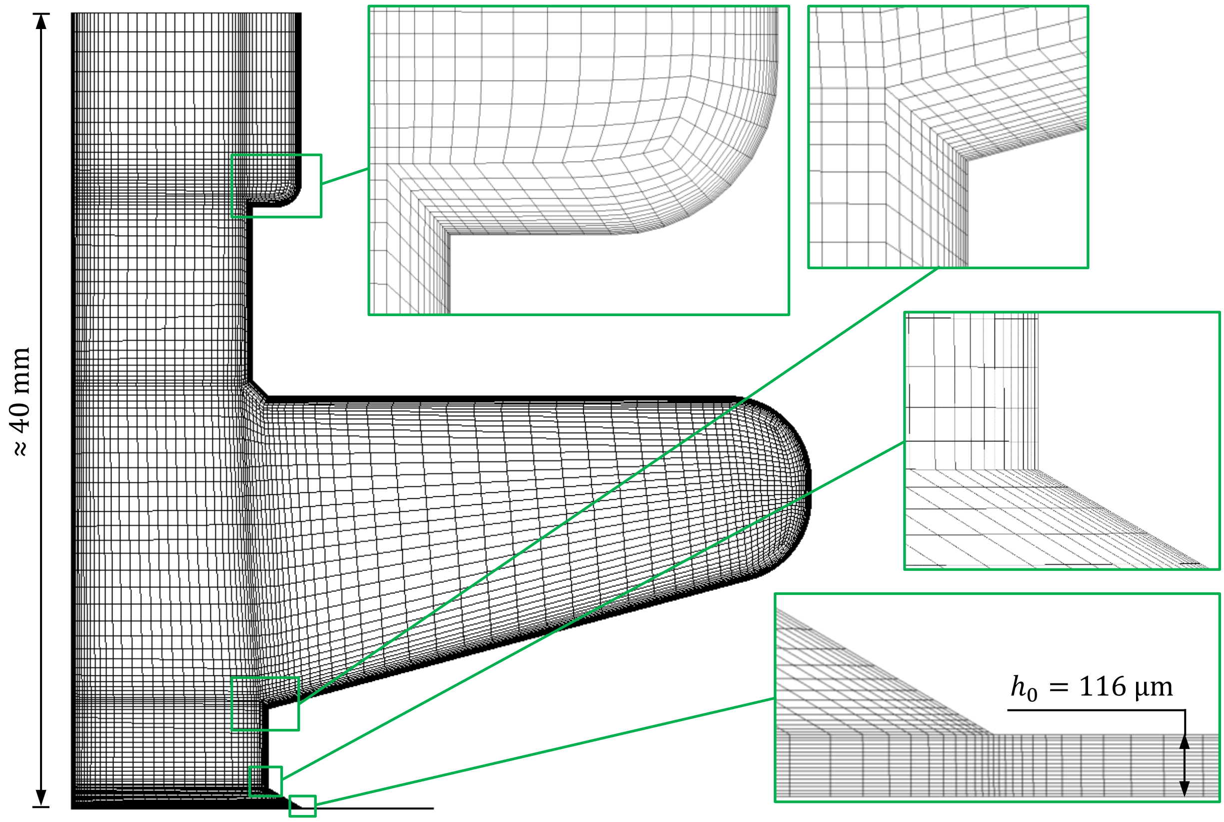

Figure 4.1: 2D computational baseline grid for initial CFD investigations

The 2D mesh was subsequently rotated about gear's axis to create a 20° sector model, as shown in Figure 4.2. Key mesh parameters are summarised in Table 4.1.

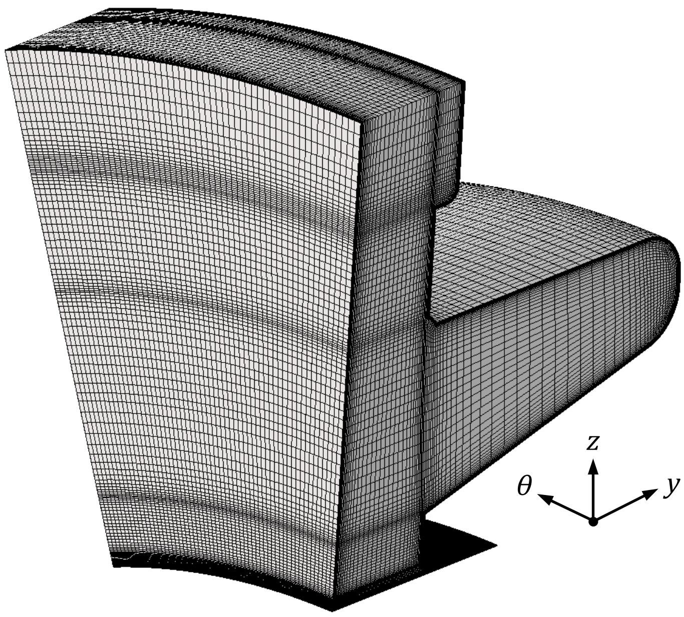

Figure 4.2: 3D computational baseline grid for initial CFD investigations

Table 4.1: Baseline mesh properties for initial CFD investigations

Mesh parameter	Value
Cell count in each 2D plane	11,192
Cell count in circumferential direction	59 (60 node points)
Total cell count in 20° sector	660,328
Lubricating gap height, h_0	116 μm
Number of cells across h_0	17 (18 node points)
Height of first cell perpendicular to wall	0.01 mm
Cell growth factor	1.1…1.4

In order to better highlight the boundary condition types that have been applied to the domain under investigation, Figure 4.3 shows the domain boundaries schematically. For illustration purposes, dimensions are not to scale.

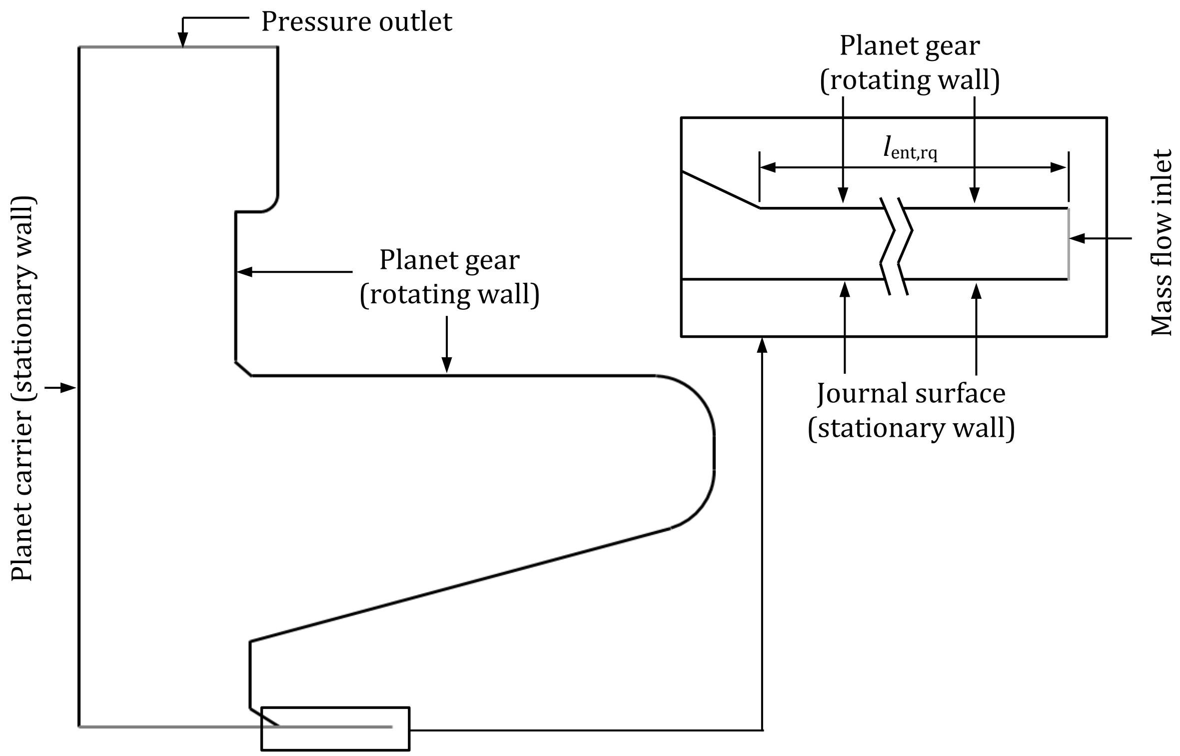

Figure 4.3: Boundary condition types applied to domain under investigation

Case specific boundary conditions, such as the angular velocity, ω_G, of the rotating gear wall, the oil inlet mass flow rate, $\dot{m}_{in}$, and the time-step, Δt, will be detailed in the appropriate sections. A complete list of all numerical settings is included in Appendix 5.

4.1.2 CFD Analysis Results – Quasi-Steady-State

In this section, the results of the initial CFD investigations are presented. Theoretical considerations previously discussed in section 2.3.2 concluded that the oil flow path direction depends on the following four key parameters:

a) Angular velocity of the gear, ω_G,
b) Dynamic viscosity of the oil, μ,
c) Oil inlet mass flow rate, $\dot{m}_\mathrm{in}$,
d) Lubricating gap height, $h_0 = (d_\mathrm{G} - d_\mathrm{P})/2$

As the gear diameter, d_G, is fixed, the dependency of the oil flow path direction on $\dot{m}_\mathrm{in}$ and h_0 can be combined to a dependency on the outflow velocity, v_0.

$$v_0 = \frac{\dot{m}_\mathrm{in}}{\rho\, A_0} = \frac{4\dot{m}_\mathrm{in}}{\rho\,\pi(d_\mathrm{G}^2 - d_\mathrm{P}^2)} = \frac{\dot{m}_\mathrm{in}}{\rho\,\pi(d_\mathrm{G} h_0 - h_0^2)} \tag{4.1}$$

Thus, three independent parameters need to be assessed, namely the angular gear velocity, ω_G, the dynamic oil viscosity, μ, and the outflow velocity, v_0. A change in μ represents a change of the oil temperature, T. For the initial CFD investigations, the following parameter combinations for ω_G, T and v_0 were chosen.

Case 1: $\omega_\mathrm{G} = \omega_\mathrm{G,\,max\,load}$, $v_0 = 0.14\omega_\mathrm{G} r_\mathrm{G}$, $T = 20°\mathrm{C}$
Case 2: $\omega_\mathrm{G} = \omega_\mathrm{G,\,max\,load}$, $v_0 = 0.14\omega_\mathrm{G} r_\mathrm{G}$, $T = 31°\mathrm{C}$
Case 3: $\omega_\mathrm{G} = \omega_\mathrm{G,\,max\,load}$, $v_0 = 0.14\omega_\mathrm{G} r_\mathrm{G}$, $T = T_\mathrm{max\,load}$
Case 4: $\omega_\mathrm{G} = \omega_\mathrm{G,\,max\,load}$, $v_0 = 0.32\omega_\mathrm{G} r_\mathrm{G}$, $T = 20°\mathrm{C}$
Case 5: $\omega_\mathrm{G} = \omega_\mathrm{G,\,min\,load}$, $v_0 = 0.14\omega_\mathrm{G} r_\mathrm{G}$, $T = 31°\mathrm{C}$
Case 6: $\omega_\mathrm{G} = \omega_\mathrm{G,\,min\,load}$, $v_0 = 0.14\omega_\mathrm{G} r_\mathrm{G}$, $T = 20°\mathrm{C}$

The reasons for choosing the specific parameter values above are to demonstrate the different oil flow paths that can occur in principle, and to show the separate effects of each parameter variation on the oil outflow behaviour. The following paragraphs provide a justification as to why the specific parameter values were selected.

The angular gear velocities for minimum load conditions, $\omega_\mathrm{G,\,min\,load}$, and maximum load conditions, $\omega_\mathrm{G,\,max\,load}$, were chosen to assess the effect of a variation of ω_G on the oil outflow behaviour. For the journal bearing under investigation, $\omega_\mathrm{G,\,max\,load} \approx 7.5\,\omega_\mathrm{G,\,min\,load}$.

The outflow velocity, $v_0 = 0.14\omega_G r_G$, was chosen based on analytical considerations. As an actual journal bearing has a convergent-divergent lubricating gap height, h, instead of a constant one, h_0, oil outflow can only occur in the convergent part of the gap, which extends over 50% of the bearing's circumference. Hence, to achieve consistent values for v_0 in a journal bearing with a constant lubricating gap height, h_0, where outflow occurs over 100% of the bearing's circumference, the oil inlet volume flow rate, $\dot{V}_{in}$, must be twice that of a journal bearing with a convergent-divergent gap height, h. The outflow velocity, $v_0 = 0.14\omega_G r_G$, is therefore based on $\dot{V}_{in} = 2\dot{V}_{in,\,max\,load}$. The outflow velocity, $v_0 = 0.32\omega_G r_G$, was chosen based on the analytical considerations presented in section 3.5.1. The distribution of v around the bearing's circumference is known (Figure 3.7). Thus, the average outflow velocity at maximum load conditions, $v_0 = 0.32\omega_G r_G$, can easily be determined.

The temperature $T = 20°C$ was chosen as most experimental investigations documented in the literature were carried out at room temperature. The temperature $T = 31°C$ was chosen as for this value the kinematic oil viscosity, ν, is consistent with that of the liquid used by Fraser et al [40]. Later, this will enable a better qualitative comparison to the flow regimes observed on rotating cups. The temperature $T = T_{max\,load}$ was chosen to assess the effect of a significantly lower dynamic oil viscosity, μ, on the outflow behaviour. Within the considered temperature range, $20°C \leq T \leq 31°C$, μ changes by a factor of approximately two. This factor increases to approximately 30 when considering the temperature range $20°C \leq T \leq T_{max\,load}$.

Figure 4.4 shows the predicted oil flow path direction for Case 1 in quasi-steady-state conditions. In Figure 4.4, the phase interface is visualised by an iso-surface (green) that indicates 50% oil volume fraction. Areas shaded in blue indicate that the oil is in full contact with the appropriate surface of the planet gear, the pin or the planet carrier.

In order to achieve the most accurate phase interface computation possible, for the initial CFD investigations presented in this section, the geometric reconstruction scheme (section 3.1.5) was chosen. This requires the time-step, Δt, for the simulation to be set such that the Courant number, C, is always smaller than or equal to one. The term quasi-steady-state, in this context, is used to describe a time-independent flow field in the vicinity of the gear base. This does not imply that the flow field reached full steady-state conditions in all parts of the domain.

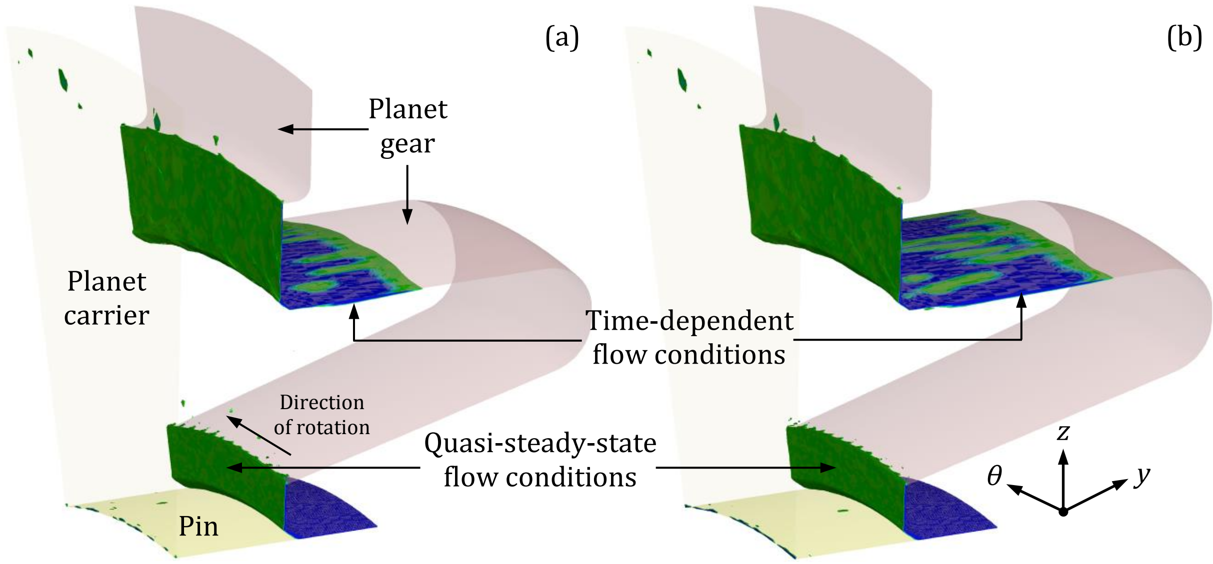

Figure 4.4: Oil flow path prediction with geometric phase interface reconstruction for Case 1 with ω_G=$\omega_{G,\ max\ load}$, v_0=0.14$\omega_G r_G$ and T=20°C at t=0.03 s (a) and t=0.045 s (b)

After emerging from the lubricating gap, the oil attaches to the chamfer of the rotating planet gear. The centrifugal force drives the oil radially outwards along the gear contour. The oil separates as a sheet from the upper edge of the gear base (diameter d_2 in Figure 2.2). The sheet subsequently disintegrates into very small droplets, which eventually impact on the upper part of the planet gear. Over time, an oil film is formed in this area which, due to the centrifugal force, spreads out axially. Whilst some of the oil flows in the negative y-direction, i.e. around the upper gear chamfer and along the gear contour in a radial direction, some of the oil flows in the positive y-direction into the undercut of the gear. Although the flow field in the vicinity of the gear base has reached steady-state conditions, the oil film in the gear undercut still migrates axially as more and more droplets impact on the film. In order to assess the predicted oil flow path direction, it is sufficient for the flow field to reach steady-state conditions in the vicinity of the gear base, i.e. quasi-steady-state conditions.

Figure 4.5 shows the flow path predictions for Cases 1 to 6 mentioned above for quasi-steady-state flow field conditions. As can be seen in Figure 4.5, a variation of the angular gear velocity, ω_G, the oil outflow velocity, v_0, and the oil temperature, T, can affect the oil flow path behaviour profoundly.

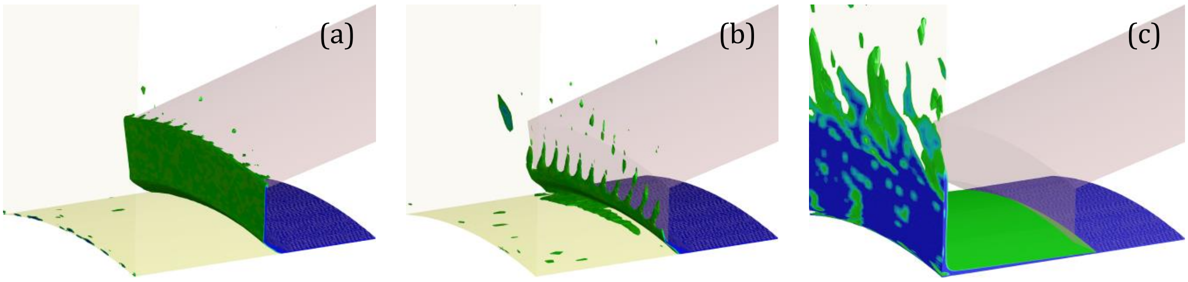

Case 1: ω=$\omega_{G,\ max\ load}$, v_0=0.14$\omega_G r_G$, T=20°C at t=0.03 s

Case 2: ω=$\omega_{G,\ max\ load}$, v_0=0.14$\omega_G r_G$, T=31°C at t=0.02 s

Case 3: ω=$\omega_{G,\ max\ load}$, v_0=0.14$\omega_G r_G$, T=$T_{max\ load}$ at t=0.015 s

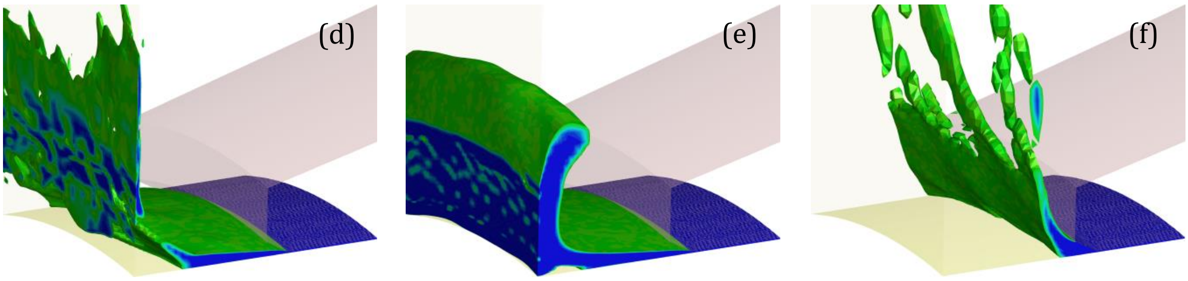

Case 4: ω=$\omega_{G,\ max\ load}$, v_0=0.32$\omega_G r_G$, T=20°C at t=0.013 s

Case 5: ω=$\omega_{G,\ min\ load}$, v_0=0.14$\omega_G r_G$, T=31°C at t=0.07 s

Case 6: ω=$\omega_{G,\ min\ load}$, v_0=0.14$\omega_G r_G$, T=20°C at t=0.05 s

Figure 4.5: Prediction of the oil outflow direction with geometric phase interface reconstruction. Case 1 (a), Case 2 (b), Case 3 (c), Case 4 (d), Case 5 (e), Case 6 (f).

Cases 1 to 3 show the effect of T on the oil flow path prediction. With otherwise identical boundary conditions for ω_G and v_0, the oil flow path direction changes from radial outflow (Cases 1 and 2) to axial outflow (Case 3). A comparison of Cases 5 and 6 reveals a similar behaviour, but for lower values of ω_G. In general, higher values of T promote axial oil outflow. This type of dependency is to be expected, as T significantly affects the oil's dynamic viscosity, μ, and thus the fluid's internal friction. A comparison between Cases 1 and 4 demonstrates a change of the oil flow path prediction due to a change of the outflow velocity, v_0. Higher values of v_0 promote axial oil outflow. Cases 2 and 5 show how the oil flow path is affected by a change of ω_G. Higher values of ω_G promote radial oil outflow.

From the initial quasi-steady-state CFD investigations, the following conclusions can be drawn:

a) Analytical considerations with respect to possible oil outflow directions (section 2.3.2) could be confirmed.
b) A higher angular gear velocity, ω_G, promotes radial oil outflow.
c) A higher oil temperature, T, i.e. a lower dynamic oil viscosity, μ, promotes axial oil outflow.
d) A higher oil outflow velocity, v_0, promotes axial oil outflow.

An additional aspect that was revealed by the initial CFD investigations was that the computational times required to reach quasi-steady-state flow field conditions were very long. For example, Case 1 (Figure 4.5) had to be run for more than five days on an high performance computing (HPC) facility with 96 computing cores.

Table 4.2 summarises the computational times required to simulate 0.001 s of elapsed flow time on an HPC facility with 96 computing cores for the six cases presented in Figure 4.5.

Table 4.2: Overview of computational times required to simulate 0.001 s of elapsed flow time on 96 computing cores – Case 1 to 6

Case No.	ω [1/s]	v_0 [-]	T [°C]	Phase interface computation	Time-step Δt [s]	C [-]	Comp. time t [min]
1	$\omega_{\text{max load}}$	$0.14\omega_G r_G$	20	Geo reconstruct	4×10^{-7}	0.5	263
2	$\omega_{\text{max load}}$	$0.14\omega_G r_G$	31	Geo reconstruct	4×10^{-7}	0.5	234
3	$\omega_{\text{max load}}$	$0.14\omega_G r_G$	$T_{\text{max load}}$	Geo reconstruct	4×10^{-7}	0.4	230
4	$\omega_{\text{max load}}$	$0.32\omega_G r_G$	20	Geo reconstruct	2×10^{-7}	0.5	568
5	$\omega_{\text{min load}}$	$0.14\omega_G r_G$	31	Geo reconstruct	5×10^{-7}	0.5	166
6	$\omega_{\text{min load}}$	$0.14\omega_G r_G$	20	Geo reconstruct	5×10^{-7}	0.5	187

The time-step, Δt, was chosen such that the Courant number, C, was well below one. This was required to ensure that C was equal to or smaller than one during the entire course of the transient flow evolution.

For analyses that include a convergent-divergent lubricating gap or an orbit radius, a full 360° model is required. Using the same mesh density, the calculational cell count would increase 18-fold. The computational time for a given elapsed flow time increases in a non-linear fashion with the number of calculational cells used to discretise the domain under investigation. Thus, CFD analyses of a full 360° model would be unviable as the time required to reach quasi-steady-state flow field conditions would increase far beyond acceptable limits. For this reason, an alternative approach is needed to simulate the oil path (section 4.1.3).

4.1.3 CFD Model Run-Time Reduction

In order to reduce the computational time needed for the initial CFD model to reach quasi-steady-state flow conditions, the following options are available.

a) Reduction of calculational cell count
b) Increase of number of computational cores
c) Reduction of iterations per time-step through use of non-iterative time advancement
d) Increase of time-step, Δt, for the transient computation of the flow behaviour

The option to reduce the calculational cell count in the domain under investigation must be considered carefully. As previously described in section 2.7.1.7, the required mesh resolution near the wall is determined by the chosen approach to model the boundary layer and its properties. Additionally, oil films on the wall need to be appropriately resolved for accurate modelling. In order to maintain a high quality mesh, the cell growth factor, if possible, should be limited to 1.2. Moreover, a coarser mesh will lead to a less accurate phase interface computation. For these reasons, a reduction of the calculational cell count to discretise the domain is heavily constrained and must be thoroughly assessed. Using this approach adversely affects the resolution of computed flow field and a case-by-case judgement is required to determine whether this is acceptable or not.

The computational time required to simulate a given elapsed flow time, t, can also be reduced by using more computing power. In both academic and industrial environments HPC resources are not unlimited as the facilities are typically shared between multiple users and projects. For the case under investigation, a maximum number of 192 computing cores could be used routinely. However, the time advantage gained by using a larger number of computing cores yields diminishing returns due to inefficiencies in code parallelisation. Using this option for the specific case under investigation would decrease the computational time, but not the level necessary for simulating full 360° journal bearing models.

Non-iterative time advance (NITA) is an option which can significantly reduce the computational effort required to reach quasi-steady-state flow field conditions. With this approach, only one single outer iteration is performed per each time-step, Δt. The NITA scheme was tested for bearing chamber flows by Bristot [57]. Even though the author did not report his experience, personal conversations revealed that convergence issues occurred. For this reason, the NITA scheme was not explored further as part of the research work presented in this thesis.

The most powerful option for reducing the computational effort required to simulate a given elapsed flow time, t, is to increase the time-step, Δt, of the transient simulation of the flow field behaviour. In order to do so, the numerical scheme used for the temporal discretisation of the volume fraction equation (section 3.1) must allow for Courant numbers, C, larger than one. As the initially used geometric phase interface reconstruction scheme is only available with explicit temporal discretisation, the phase interface computation was changed to the compressive scheme (section 3.1.5), which is available with both explicit and implicit temporal discretisation. Using the latter allows the Courant number to be larger than one.

For quasi-steady-state conditions, i.e. an elapsed flow time of $t = 0.03$ s, Figure 4.6 shows in detail how a change of the phase interface reconstruction scheme, a change of the temporal discretisation scheme and a change of the time-step, Δt, affect the oil flow path prediction in general, and the resolution of the phase interface in particular. Key boundary conditions are consistent with those for Case 1 (Figure 4.5), i.e. $\omega_{\mathrm{G}} = \omega_{\mathrm{G,\,max\,load}}$, $v_0 = 0.14\omega_{\mathrm{G}} r_{\mathrm{G}}$, $T = 20$°C. In Figure 4.6, the phase interface is visualised by an iso-surface (green) that indicates 50% oil volume fraction. Areas shaded in blue indicate that the oil is in full contact with the appropriate surface of the planet gear, the pin or the planet carrier.

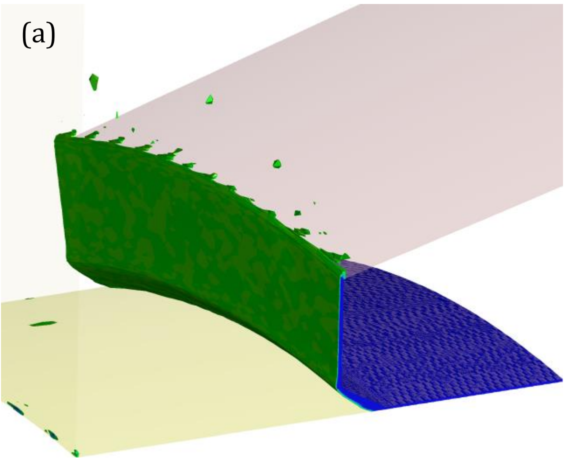

Case 1 with explicit geometric phase interface reconstruction, Δt=4×10^{-7} s, C=0.5

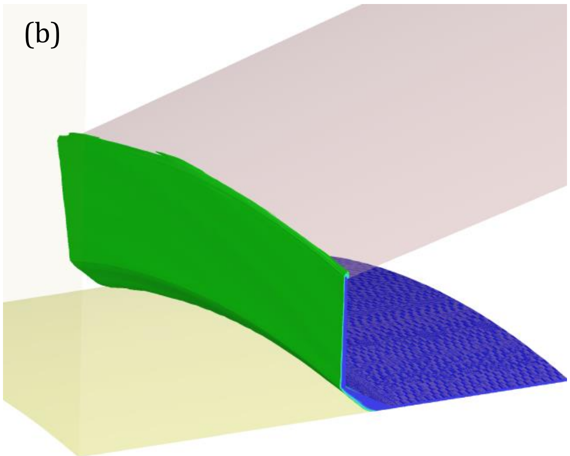

Case 1 with explicit compressive phase interface reconstruction, Δt=4×10^{-7} s, C=0.5

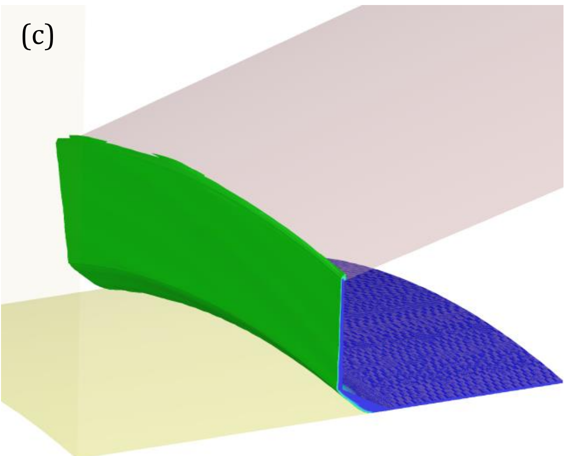

Case 1 with implicit compressive phase interface reconstruction, Δt=4×10^{-7} s, C=0.5

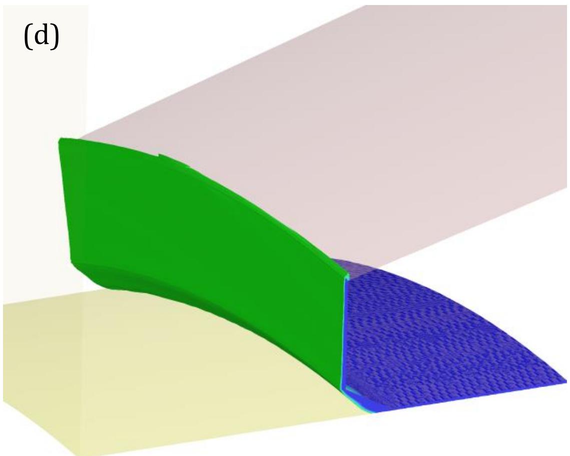

Case 1 with implicit compressive phase interface reconstruction, Δt=100×10^{-7} s, C=12.5

Figure 4.6: Effect of different numerical settings on the oil flow path prediction and the phase interface resolution for Case 1 (Figure 4.5) at *t*=0.03 s

The predicted oil flow path direction, i.e. radial outflow, is independent of the considered phase interface reconstruction schemes (geometric reconstruction and compressive scheme), the considered temporal discretisation schemes (explicit and implicit), and the considered time-steps ($4 \times 10^{-7}\text{s} \leq \Delta t \leq 100 \times 10^{-7}\text{s}$). The resolution of the phase interface, as shown in Figure 4.6 (a) and Figure 4.6 (b), however, is affected by the choice of the phase interface reconstruction scheme. For identical settings with respect to the temporal discretisation scheme (explicit) and the time-step, $\Delta t = 4 \times 10^{-7}\text{s}$, the compressive scheme is unable to capture detailed flow structures, such as ligaments and droplets. This is due to the fact that the compressive scheme is more diffusive and therefore less accurate than the geometric reconstruction scheme.

Moreover, a comparison between Figure 4.6 (b) and Figure 4.6 (c), and between Figure 4.6 (c) and Figure 4.6 (d), respectively, shows that, when using the compressive scheme, the phase interface resolution is independent of the considered temporal discretisation schemes (explicit and implicit) and the considered time-steps ($4 \times 10^{-7}\text{s} \leq \Delta t \leq 100 \times 10^{-7}\text{s}$).

Table 4.3 shows an overview of the computational times required to simulate a given elapsed flow time of $t = 0.001$ s on an HPC facility with 96 computing cores. Using the compressive phase interface reconstruction in conjunction with implicit temporal discretisation and a time-step of $\Delta t = 100 \times 10^{-7}$ s (Case 1 (d) in Table 4.3) reduces the computational time by 94.3% compared to the baseline case (Case 1 (a) in Table 4.3).

Table 4.3: Overview of computational times required to simulate 0.001 s of elapsed flow time on 96 computing cores – Case 1 (a) to 1 (d)

Case No.	Outflow direction	Phase interface computation	Temporal discretisation scheme	Time-step, Δt [s]	C	Computational time, t [min]
1 (a)	radial	Geo reconstruct	explicit	4×10^{-7}	0.5	263
1 (b)	radial	Compressive	explicit	4×10^{-7}	0.5	235
1 (c)	radial	Compressive	implicit	4×10^{-7}	0.5	275
1 (d)	radial	Compressive	implicit	100×10^{-7}	12.5	15

In order to demonstrate that the use of the compressive scheme with implicit temporal discretisation and a time-step of $\Delta t = 100 \times 10^{-7}$ s has no adverse effect on the flow path prediction when axial oil outflow prevails, a similar study was conducted for key boundary conditions consistent with those for Case 3 (Figure 4.5), i.e. $\omega_\text{G} = \omega_\text{G, max load}$, $v_0 = 0.14\omega_\text{G} r_\text{G}$, $T = T_\text{max load}$. Figure 4.7 shows how a change of the phase interface reconstruction scheme, a change of the temporal discretisation scheme and a change of the time-step, Δt, affect the oil flow path prediction in general, and the resolution of the phase interface in particular. In Figure 4.7, the phase interface is visualised by an iso-surface (green) that indicates 50% oil volume fraction. Areas shaded in blue indicate that the oil is in full contact with the appropriate surface of the planet gear, the pin or the planet carrier.

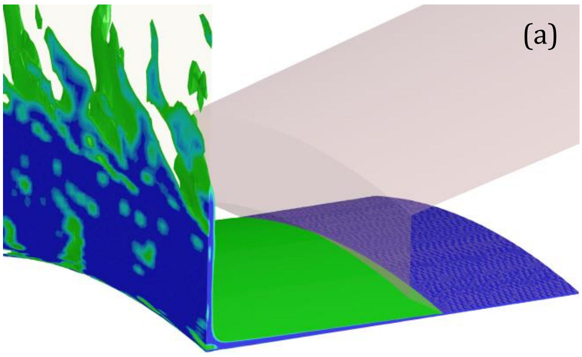

Case 3 with explicit geometric phase interface reconstruction, Δt=4×10^{-7} s, C=0.4

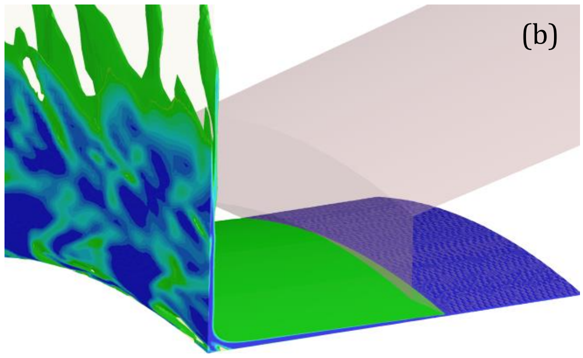

Case 3 with explicit compressive phase interface reconstruction, Δt=4×10^{-7} s, C=0.4

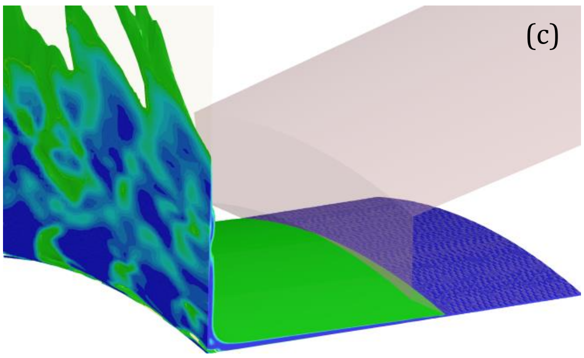

Case 3 with implicit compressive phase interface reconstruction, Δt=4×10^{-7} s, C=0.4

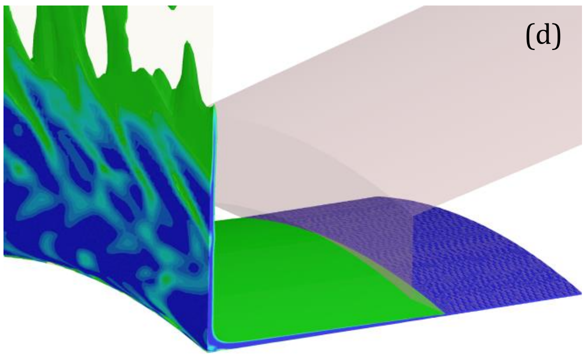

Case 3 with implicit compressive phase interface reconstruction, Δt=100×10^{-7} s, C=10

Figure 4.7: Effect of different numerical settings on the oil flow path prediction and the phase interface resolution for Case 3 (Figure 4.5) at *t*=0.015 s

The predicted oil flow path direction, i.e. axial outflow, is independent of the considered phase interface reconstruction schemes (geometric reconstruction and compressive scheme), the considered temporal discretisation schemes (explicit and implicit), and the considered time-steps ($4 \times 10^{-7}\text{s} \leq \Delta t \leq 100 \times 10^{-7}\text{s}$). In contrast to the observation made with radial oil outflow (Figure 4.6), a comparison between Figure 4.7 (a) and Figure 4.7 (b) shows that the resolution of the phase interface is not notably affected by a change from the geometric phase interface reconstruction scheme to the compressive scheme. The increased diffusivity of the compressive scheme, however, means that droplets generated by the oil film as it impacts on the planet carrier, cannot be resolved. For the investigations presented in this thesis, this fact is of secondary importance.

Moreover, consistent with previous observations made for radial oil outflow, the resolution of the phase interface is independent of the considered temporal discretisation schemes (explicit and implicit) and the considered time-steps ($4 \times 10^{-7}\,\mathrm{s} \leq \Delta t \leq 100 \times 10^{-7}\,\mathrm{s}$). This is demonstrated by a comparison of Figure 4.7 (b) and Figure 4.7 (c), and Figure 4.7 (c) and Figure 4.7 (d), respectively.

Table 4.4 shows an overview of the computational times required to simulate a given elapsed flow time of $t = 0.001$ s on an HPC facility with 96 computing cores. Using the compressive phase interface reconstruction in conjunction with implicit temporal discretisation and a time-step of $\Delta t = 100 \times 10^{-7}$ s (Case 3 (d) in Table 4.4) reduces the computational time by 92.6% compared to the baseline case (Case 3 (a) in Table 4.4).

Table 4.4: Overview of computational times required to simulate 0.001 s of elapsed flow time on 96 computing cores – Case 3 (a) to 3 (d)

Case No.	Outflow direction	Phase interface computation	Temporal discretisation scheme	Time-step, Δt [s]	C	Computational time, t [min]
3 (a)	axial	Geo reconstruct	explicit	4×10^{-7}	0.4	230
3 (b)	axial	Compressive	explicit	4×10^{-7}	0.4	188
3 (c)	axial	Compressive	implicit	4×10^{-7}	0.4	218
3 (d)	axial	Compressive	implicit	100×10^{-7}	10	17

From the CFD oil flow path predictions shown in Figure 4.6 and Figure 4.7, and the data provided in Table 4.3 and Table 4.4, the following conclusions can be drawn:

a) The oil flow path direction is independent of the chosen phase interface computation scheme.

b) The compressive scheme is unable to capture detailed flow structures, such as ligaments and droplets. This is due to the fact that the compressive scheme is more diffusive and therefore less accurate than the geometric reconstruction scheme.

c) For a given time-step, Δt, and a given number of iterations per time-step, the compressive scheme with explicit temporal discretisation is faster than the geometric reconstruction scheme. This is due to the fact that the compressive phase interface reconstruction is computationally less expensive. However, for a given time-step, Δt, and a given residual for a flow quantity as a convergence criterion, the compressive scheme may be slower. Experience showed that the convergence behaviour of the simulation degraded when switching to the compressive scheme, i.e. more iterations per time-step, Δt, were required to reach a given residual level.

d) For a given time-step, Δt, and a given number of iterations per time-step, the compressive scheme with implicit temporal discretisation is slower than the compressive scheme with explicit temporal discretisation. This is due to the implementation of the implicit numerical scheme into the CFD code. An iterative solution process is required (section 3.1.4). In contrast, an explicit formulation does not require an iterative solution process (section 3.1.3).

When using the compressive scheme with implicit temporal discretisation, an increase in the time-step, Δt, that results in a Courant number of $C = 10$ does not have any effect on the oil flow path prediction or phase interface resolution for the case under investigation. However, the levels of the residual values of the flow variables, ϕ, at the end of each time-step increase by approximately one order of magnitude from 1×10^{-4} to 1×10^{-3}.

For the case under investigation, an accurate prediction of the oil flow path direction is required. Choosing a compressive phase interface reconstruction scheme with implicit temporal discretisation and an increased time-step, Δt, allowed the overall computational time to be reduced by more than 92%. This level of reduction of computational effort is needed to make simulations of full 360° models viable. For the benefit of a much faster computation, the loss of resolution of detailed flow structures, such as ligaments and droplets, is acceptable for the case under investigation.

4.1.4 CFD Analysis Results – Full Steady-State

With a robust and fast CFD sector model in place, full steady-state conditions can now be assessed. Full steady-state conditions are characterised by a time-independent distribution of the oil inside the entire external journal bearing domain. In order to quantify full steady-state conditions, the dimensionless moment coefficient, c_m, and the normalised mass flow imbalance, $I_{\dot{m}}$, were monitored, recorded and assessed. Whilst c_m was previously defined by equation (3.7), $I_{\dot{m}}$ is given by the ratio between the difference of the mass flow rate entering the external flow domain through the mass flow inlet (Figure 4.3), $\dot{m}_{\text{in}}$, and the mass flow rate leaving the external domain through the pressure outlet (Figure 4.3), $\dot{m}_{\text{out}}$, and $\dot{m}_{\text{in}}$.

$$I_{\dot{m}} = \frac{\dot{m}_{\text{in}} - \dot{m}_{\text{out}}}{\dot{m}_{\text{in}}} \tag{4.2}$$

Figure 4.8 and Figure 4.9 show the full steady-state flow field conditions in the domain under investigation for radial (Case 1, Figure 4.5) and axial (Case 3, Figure 4.5) oil outflow, respectively. Oil film thicknesses, t_F, are provided at selected locations for comparison. The oil film thicknesses, t_F, were determined perpendicular to the wall up to an oil volume fraction value of 0.5. In Figure 4.8 (a) and Figure 4.9 (a), the phase interface is visualised by an iso-surface (green) that indicates 50% oil volume fraction. Areas shaded in blue indicate that the oil is in full contact with the appropriate surface of the planet gear, the pin or the planet carrier. Figure 4.8 (b) and Figure 4.9 (b) show the air volume fraction contours in the sector mid-plane.

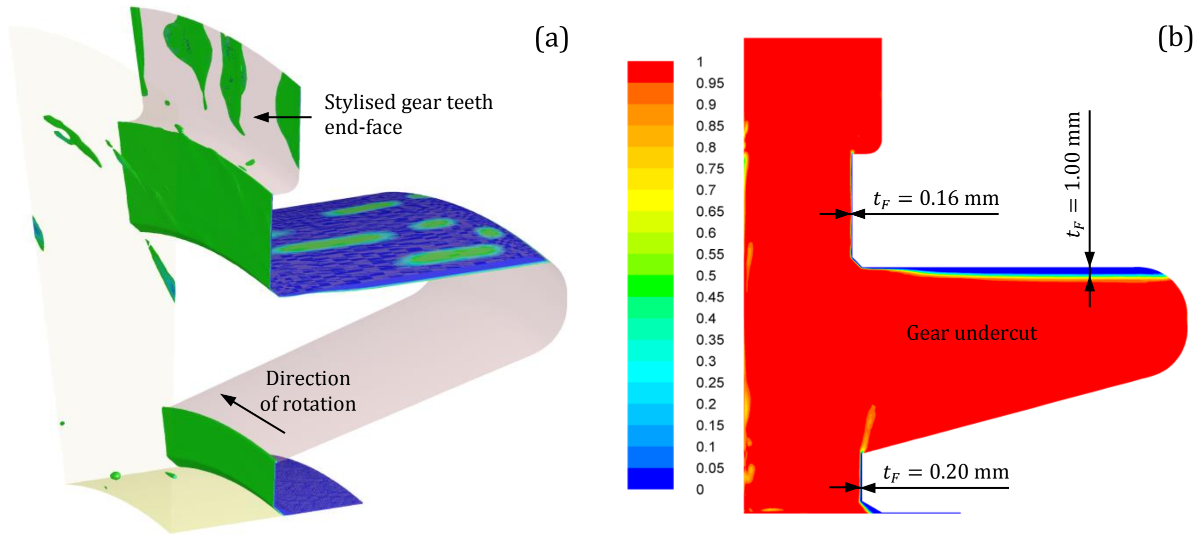

Figure 4.8: Oil flow path prediction with compressive phase interface reconstruction for Case 1 (d) with ω_G=$\omega_{G,\,\text{max load}}$, v_0=0.14$\omega_G r_G$ and T=20°C at t=0.30 s. Contours of 50% oil volume fraction iso-surface (a) and air volume fraction contours in sector mid-plane (b).

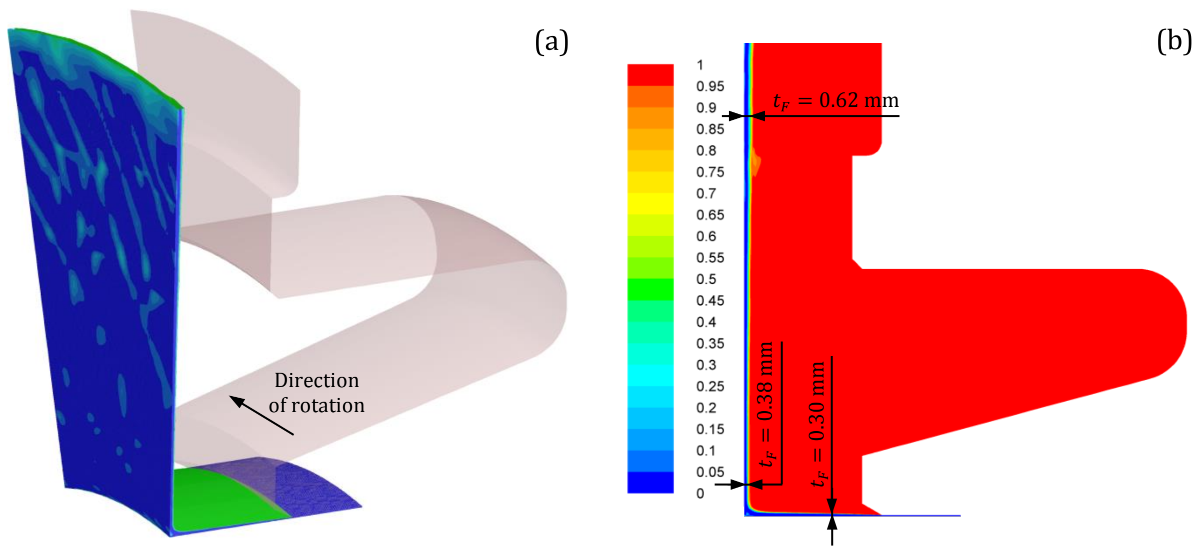

Figure 4.9: Oil flow path prediction with compressive phase interface reconstruction for Case 3 (d) with ω_G=$\omega_{G,\,\text{max load}}$, v_0=0.14$\omega_G r_G$ and T=$T_{\text{max load}}$ at t=0.11 s. Contours of 50% oil volume fraction iso-surface (a) and air volume fraction contours in sector mid-plane (b).

Figure 4.10 to Figure 4.13 show the values for c_m and $I_{\dot{m}}$ over time to confirm time-independent flow field conditions for both radial (Case 1 (d)) and axial oil outflow (Case 3 (d)).

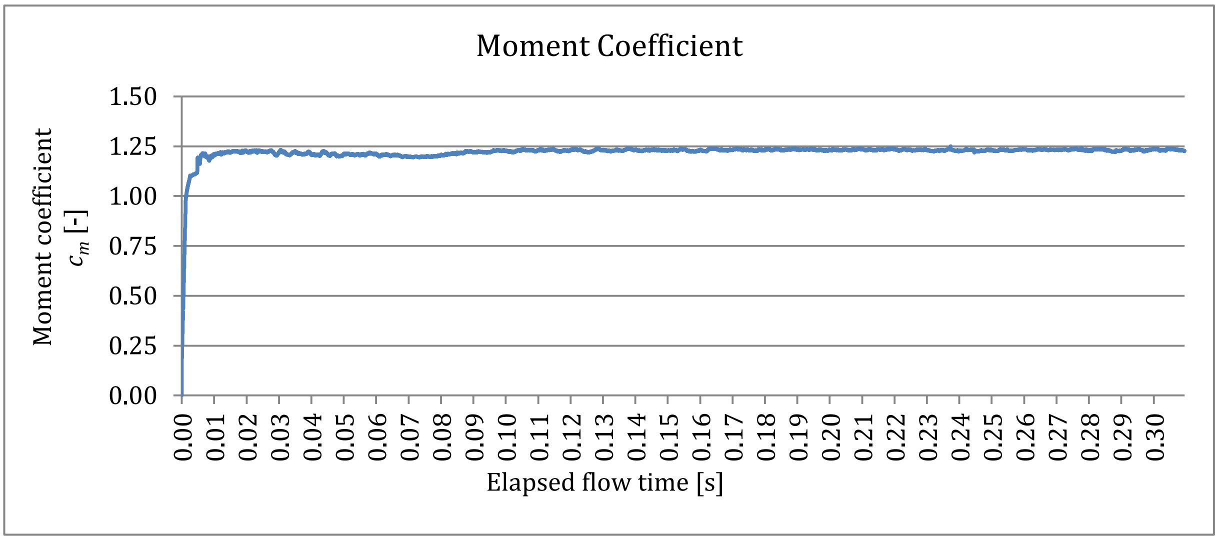

Figure 4.10: Moment coefficient over time for Case 1 (d) with ω_G=$\omega_{G,\text{ max load}}$, v_0=0.14$\omega_G r_G$ and T=20°C

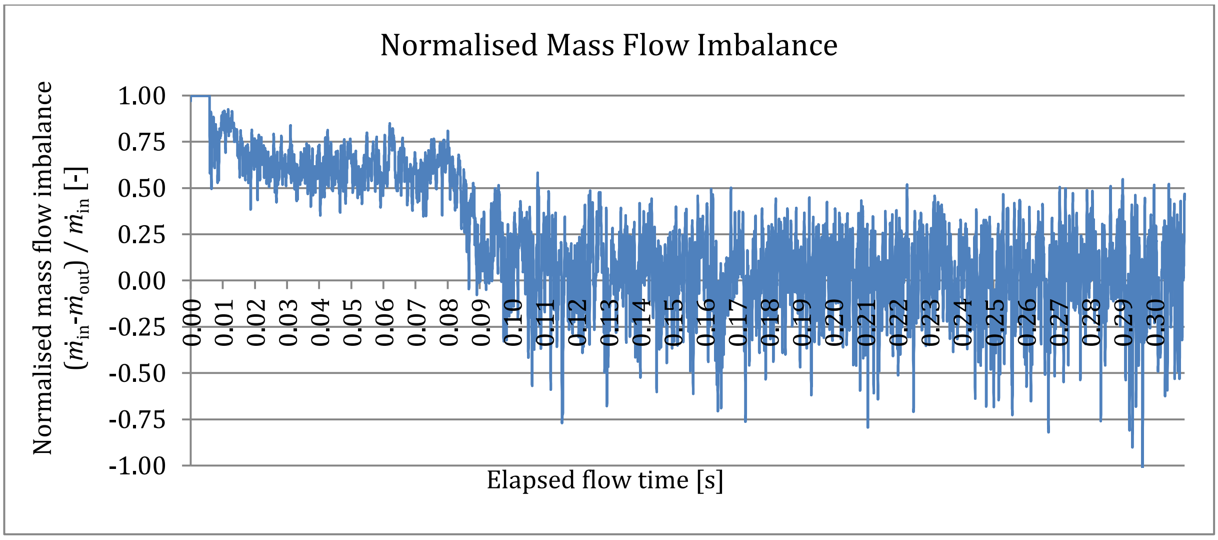

Figure 4.11: Normalised mass flow imbalance over time for Case 1 (d) with ω_G=$\omega_{G,\text{ max load}}$, v_0=0.14$\omega_G r_G$ and T=20°C

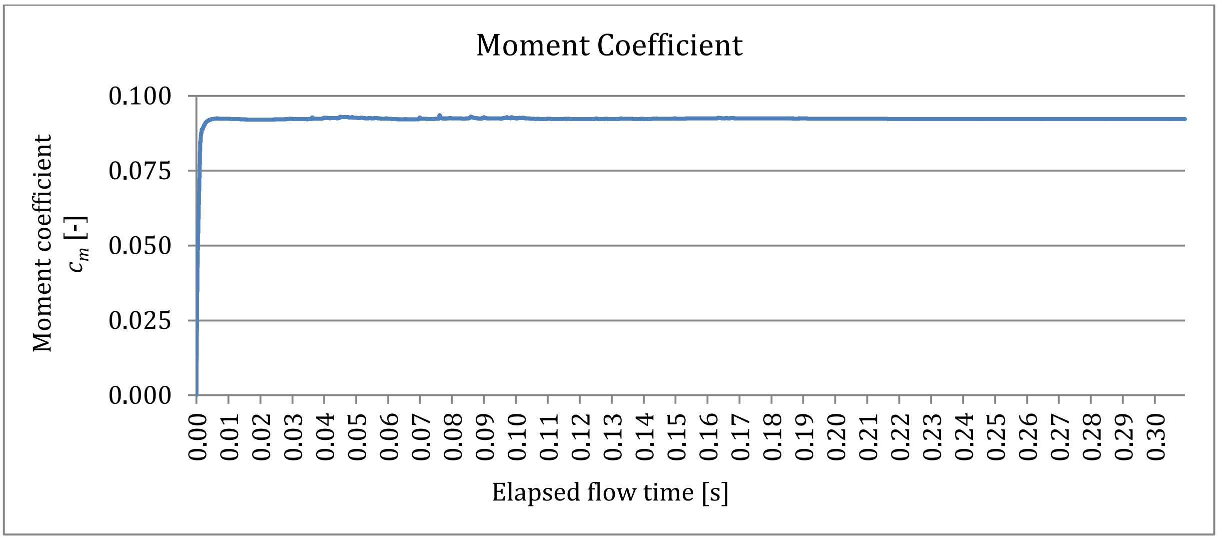

Figure 4.12: Moment coefficient over time for Case 3 (d) with ω_G=$\omega_{G,\text{ max load}}$, v_0=0.14$\omega_G r_G$ and T=$T_{\text{max load}}$

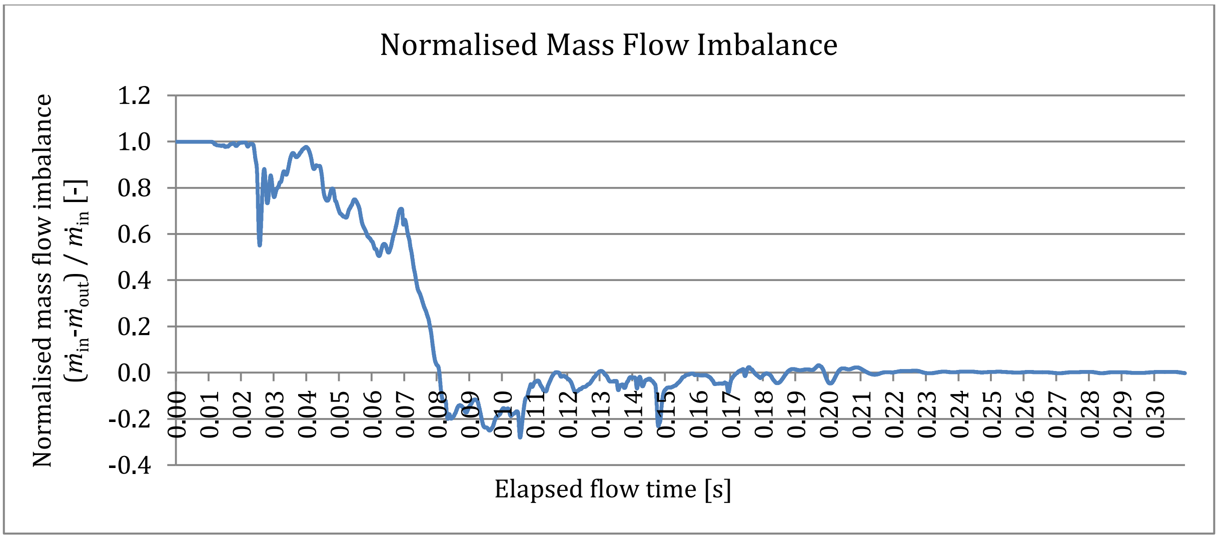

Figure 4.13: Normalised mass flow imbalance over time for Case 3 (d) with ω_G=$\omega_{G,\text{ max load}}$, v_0=0.14$\omega_G r_G$ and T=$T_{\text{max load}}$

Figure 4.10 to Figure 4.13 show that the moment coefficient, c_m, is insufficient to judge whether full steady-state flow field conditions have been reached or not.

When radial oil outflow prevails, Figure 4.10 suggests that c_m is converged after an elapsed flow time of 0.01 s (0.87 gear revolutions). Figure 4.11, however, shows that $I_{\dot{m}}$ at that point in time is still larger than 0.5. This indicates that the mass flow rate entering into the external flow domain, $\dot{m}_{\text{in}}$, is still twice as big as the mass flow rate leaving the external flow domain, $\dot{m}_{\text{out}}$. After an elapsed flow time of 0.12 s (10.4 gear revolutions), $I_{\dot{m}}$ stabilises at a value close to zero. The average value of $I_{\dot{m}}$ in the time period between t = 0.20 s and t = 0.30 s is 0.013. Hence, 1.3% of $\dot{m}_{\text{in}}$ continues to increase the mass of the oil in the domain under investigation. In order to verify that this is not due to numerical rounding errors, the ANSYS Fluent [48] reporting function for the sum of the residuals of the mass imbalance over all calculational cells was used. Its value of -2.1×10^{-7} kg/s is four orders of magnitude smaller than $I_{\dot{m}}$. The large, high-frequency fluctuations of $I_{\dot{m}}$ over time (Figure 4.11) are indicative of highly dispersed droplet flow.

When axial oil outflow prevails, Figure 4.12 suggests that c_m is converged after an elapsed flow time of approximately 0.005 s (0.44 gear revolutions). However, Figure 4.13 shows that 0.22 s (19.2 gear revolutions) of elapsed flow time are required in order for $I_{\dot{m}}$ to stabilise around a near-zero value. The average value of $I_{\dot{m}}$ in the period between $t = 0.22$ s and $t = 0.30$ s is 0.002, i.e. $\dot{m}_{\text{in}}$ exceeds $\dot{m}_{\text{out}}$ by only 0.2%.

When axial oil outflow occurs, the transient behaviour of $I_{\dot{m}}$ (Figure 4.13) shows significantly less fluctuations than previously observed with radial oil outflow (Figure 4.11). The main reason for that is that the oil is less dispersed. Instead of droplet flow, film flow prevails.

It should be noted that between the two assessed cases, i.e. Case 1 (d) and Case 3 (d), the difference of the converged c_m values is more than one order of magnitude. This is explained by the two different oil temperatures used to simulate the oil outflow behaviour, i.e. $T = 20°\text{C}$ and $T = T_{\text{max load}}$.

Radial oil outflow (Figure 4.8) at representative engine operating conditions may be problematic, particularly for an epicyclic gearbox operating in planetary configuration. The oil film thickness, t_F (Figure 4.8 (b)), in the undercut of the gear depends on the oil properties and the centrifugal force, F_{c}, acting on the film. F_{c}, in turn, is a combination of the centrifugal forces generated by the planet gear rotation about its own axis and the planet gear's orbiting motion around the sun gear. Depending on the angular location, θ, F_{c} will vary, and so will t_F. An uneven oil mass distribution in the undercut of the gear can lead to imbalance forces. These can be mitigated by applying a slope to the surface in question. This will generate a force component parallel to the surface, which helps to guide the oil towards the domain outlet. As a result, t_F, and hence imbalance forces, will be reduced. This recommended design change is further detailed in section 6.3.2, Figure 6.5.

Applying a sloped surface should be considered even if axial oil outflow is predicted for engine representative conditions. Due to oil splashing from the planet carrier, oil is still likely to accumulate in the undercut of the gear. This behaviour was suggested by the experimental flow path investigations presented in section 5.6. The numerical investigations for conditions consistent with Case 3 (d), as shown in Figure 4.9, could not confirm this behaviour due to the specific numerical models used to simulate this case. The compressive phase interface reconstruction scheme, which had to be used in order to simulate a reasonably long elapsed flow time with acceptable computational effort, is unable to resolve small droplets.

In addition to the insights already presented, the combined results for the c_m values recorded for radial oil outflow with an oil temperature of $T = 20°C$, i.e. Case 1 (d) (Figure 4.10) and axial oil outflow with an oil temperature of $T = T_{\text{max load}}$, i.e. Case 3 (d) (Figure 4.12), allow an estimation to be made for the c_m value of a hypothetical case with radial oil outflow and an oil temperature of $T = T_{\text{max load}}$. This estimation is required to fully justify the isothermal modelling of external journal bearing oil outflow in general, as previously discussed in section 3.1.7.

As described in section 4.1.1, the CFD sector models were set up with an entrance length, l_{ent} (Figure 4.3), to ensure fully developed velocity profiles in the circumferential and the axial directions at the point where the oil enters into the external flow domain. Detailed analysis of the transient evolution of c_m for Case 1 (d) revealed that, at the point in time when the oil begins to enter into the external flow domain, the recorded c_m value is $c_{m,\text{ int}} = 0.98$. The total c_m value at full steady-state flow field conditions, as shown in Figure 4.10, is $c_m = 1.23$. The difference, $c_m - c_{m,\text{ int}} = c_{m,\text{ ext}} = 0.25$, can be attributed to the interactions of the oil with the gear surfaces bounding the external flow domain. Thus, $c_{m,\text{ ext}}$ accounts for only 20.3% of c_m.

When assessing the transient evolution of c_m for Case 3 (d) in detail, it can be shown that the c_m value at the point in time when the oil begins to enter into the external flow domain is $c_{m,\text{ int}} = 0.092$. Assuming that for the hypothetical case of radial oil outflow with an oil temperature of $T = T_{\text{max load}}$ the same relative contribution of $c_{m,\text{ ext}}/c_m = 0.203$ persists, $c_{m,\text{ ext}}$ must be equal to 0.024. Using the approach previously presented in section 3.1.7, this translates into a temperature rise, ΔT, of less than 0.5°C for a full 360° model. The effect of such a small temperature rise on the oil properties, including its dynamic viscosity, is negligible. Thus, the isothermal treatment of the flow in the external domain is justified.

From the full steady-state CFD investigations, the following conclusions can be drawn:

a) The moment coefficient, c_m, is insufficient to judge whether full steady-state flow field conditions have been reached or not.

b) The normalised mass flow imbalance, $I_{\dot{m}}$, is a parameter which allows
   - full steady-state flow field conditions to be identified and
   - a prediction to be made about the prevailing flow regime.

c) For the cases under investigation, i.e. Case 1 (d) and Case 3 (d), 10.4 and 19.2 gear revolutions, respectively, are required to reach full steady-state flow field conditions.

d) It is recommended to apply a slope to the surface which exhibits oil build-up in the undercut of the gear (Figure 4.8 (b)) to mitigate potential imbalance forces that originate from an uneven distribution of the oil film thickness, t_F. Additional details are presented in section 6.3.

e) The magnitude of c_m for engine representative oil temperatures justifies isothermal modelling of external journal bearing oil outflow.

4.1.5 Model Sensitivity – Computational Grid Density

A sensitivity study has been conducted to assess the potential effect of the computational grid density on the oil flow path prediction. As shown in sections 4.1.2 and 4.1.4, journal bearing oil outflow is highly three-dimensional. Therefore, two separate grid density studies were conducted. The potential sensitivity of the oil flow path prediction was assessed with respect to the grid density in the axial and the radial directions (y-z-plane, Figure 4.2) and with respect to the grid density in the circumferential direction, θ (Figure 4.2). In section 4.1.5.1 and section 4.1.5.2, the phase interface is visualised by an iso-surface (green) that indicates 50% oil volume fraction. Areas shaded in blue indicate that the oil is in full contact with the appropriate surface of the planet gear, the pin or the planet carrier.

4.1.5.1 Grid Density Study – y-z-Plane

Compared to the baseline computational grid (section 4.1.1), one lower-density mesh and three higher-density meshes were created. Key mesh parameters are summarised in Table 4.5.

Table 4.5: Mesh properties for computational grid density study – y-z-plane

Mesh parameter	Mesh 1	Baseline mesh	Mesh 3	Mesh 4	Mesh 5
Cell count in each 2D plane	9 k	11 k	25 k	40 k	55 k
Cell count in circumferential direction	59 (60 nodes)	59 (60 nodes)	59 (60 nodes)	59 (60 nodes)	59 (60 nodes)
Total cell count in 20° sector	534 k	660 k	1,474 k	2,362 k	3,250 k
Lubricating gap height, h_0	116 µm	116 µm	116 µm	116 µm	116 µm
Number of cells across h_0	17 (18 nodes)	17 (18 nodes)	17 (18 nodes)	17 (18 nodes)	17 (18 nodes)
Height of first cell perpendicular to wall	0.05 mm	0.01 mm	0.01 mm	0.01 mm	0.005 mm
Cell growth factor	1.1…1.4	1.1…1.4	1.1…1.4	1.1…1.4	1.1…1.4

The effect of the grid density on the oil flow path prediction has been studied for both radial, i.e. Case 1 (d), and axial, i.e. Case 3 (d), oil outflow at quasi-steady-state flow field conditions. These were reached after an elapsed flow time of $t = 0.030$ s (Case 1 (d)) and $t = 0.015$ s (Case 3 (d)), respectively. The results are summarised in Table 4.6.

Table 4.6: Results of computational grid density study – *y*-*z*-plane

	Case 1 (d) – radial oil outflow	Case 3 (d) – axial oil outflow
Mesh 1	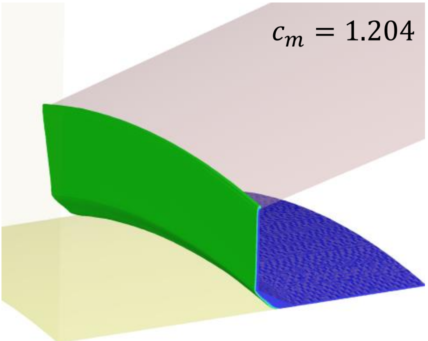	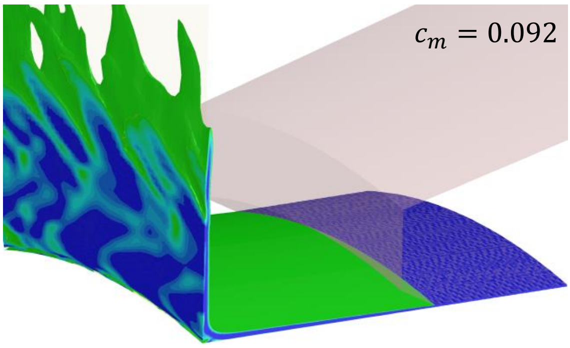
Baseline mesh	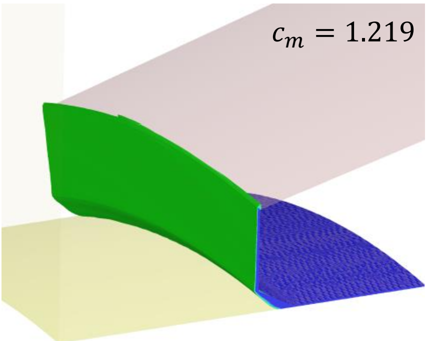	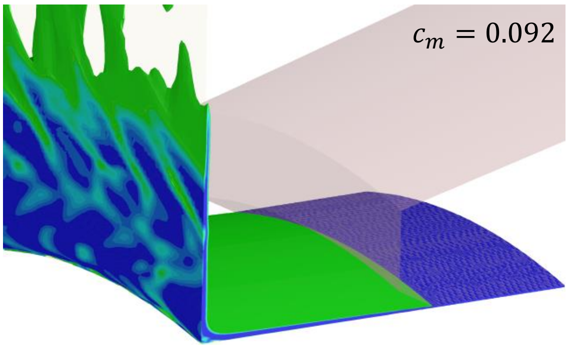
Mesh 3	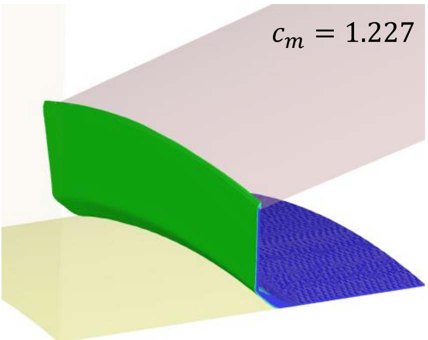	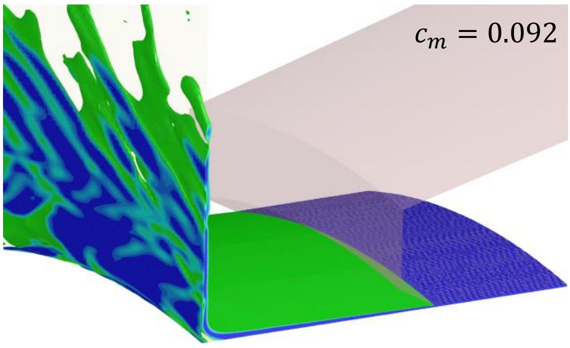

Mesh 4	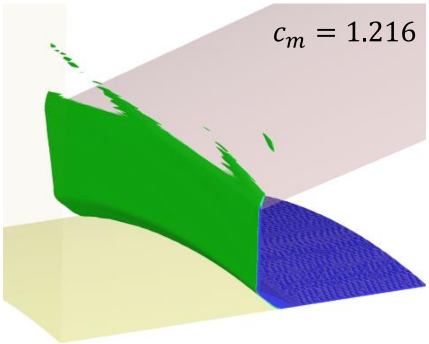	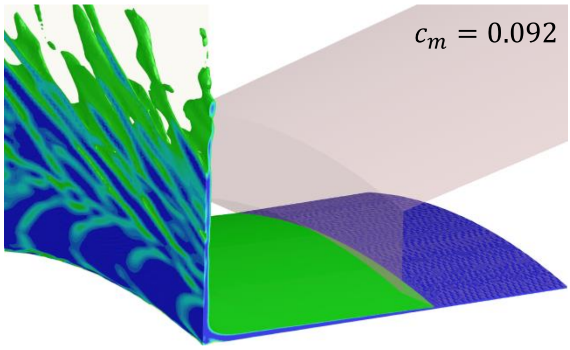
Mesh 5	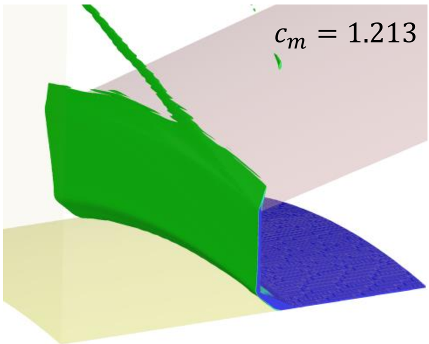	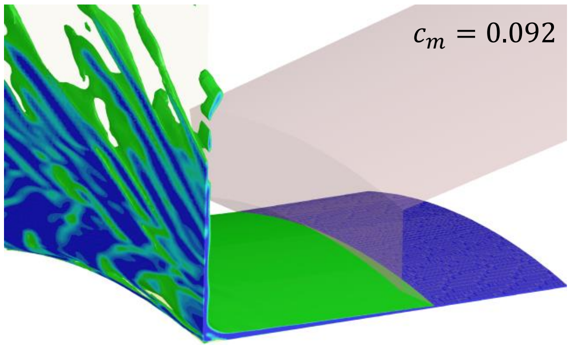

As shown by the simulation results presented in the table above, the oil flow path directions are independent of the chosen computational grid density in the y-z-plane within the investigated range. A comparison of the c_m values for the planet gear sector does not show a clear correlation with regard to mesh density.

For radial oil outflow (Case 1 (d)), denser meshes reveal ligament-type flow structures that separate from the edge of the generated oil sheet. As the mesh density increases, the phase interface becomes sharper, i.e. interface smearing is reduced. Reduced phase interface smearing, in turn, is characterised by a smaller distance between cells with an oil volume fraction value, α, of zero and one, respectively. The oil sheet itself extends further in the radial direction. The point of oil separation from the gear contour is unaffected by the density of the mesh.

For axial oil outflow (Case 3 (d)), denser meshes show finer flow structures on the planet carrier. Single droplets can be resolved close to the wall, where the mesh is particularly dense.

4.1.5.2 Grid Density Study – θ-Direction

The potential sensitivity of the oil flow path prediction was assessed with respect to the mesh density in the θ-direction. For this purpose, the baseline computational mesh (section 4.1.1) was utilised with different numbers of cells in the circumferential direction. Compared to the baseline mesh, one lower-density mesh and two higher-density meshes were created. Key mesh parameters are summarised in the table below.

Table 4.7: Mesh properties for computational grid density study – θ-direction

Mesh parameter	Mesh 1	Baseline mesh	Mesh 3	Mesh 4
Cell count in each 2D plane	11 k	11 k	11 k	11 k
Cell count in circumferential direction	29 (30 nodes)	59 (60 nodes)	89 (90 nodes)	119 (120 nodes)
Total cell count in 20° sector	325 k	660 k	996 k	1,332 k

Consistent with the approach followed for the grid density study in the y-z-plane, the grid density study in the θ-direction was carried out for both radial (Case 1 (d)) and axial (Case 3 (d)) oil outflow at quasi-steady-state flow field conditions. The results for an elapsed flow time of $t = 0.03$ s (Case 1 (d)) and $t = 0.015$ s (Case 3 (d)), respectively, are summarised in Table 4.8.

Table 4.8: Results of computational grid density study – θ-direction

	Case 1 (d) – radial oil outflow	Case 3 (d) – axial oil outflow
Mesh 1	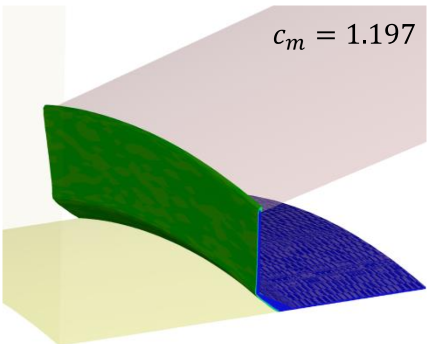 $c_m = 1.197$	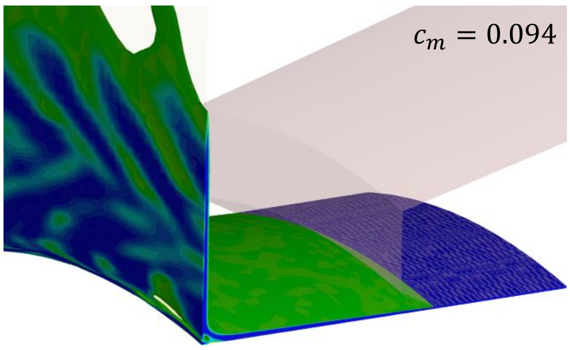 $c_m = 0.094$
Baseline mesh	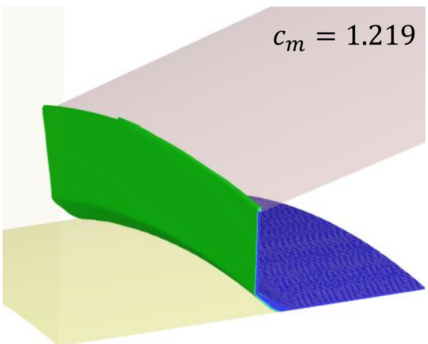 $c_m = 1.219$	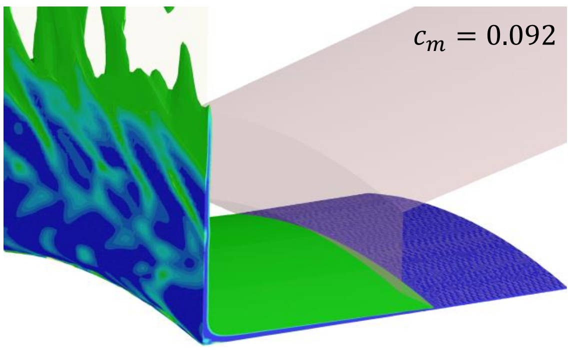 $c_m = 0.092$

Mesh 3	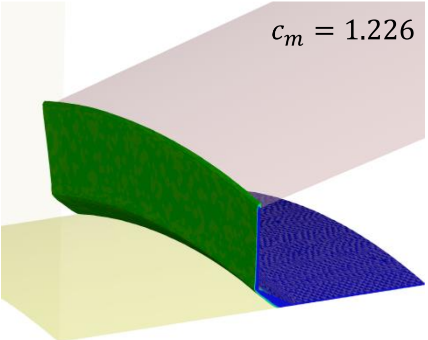	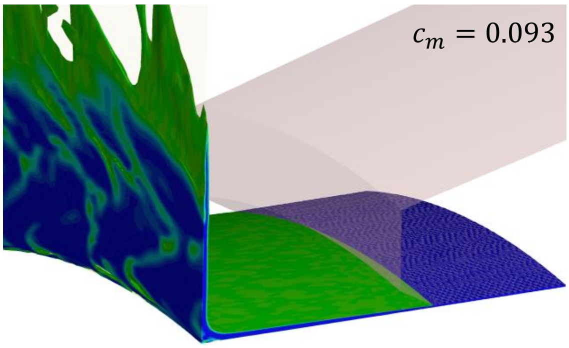
Mesh 4	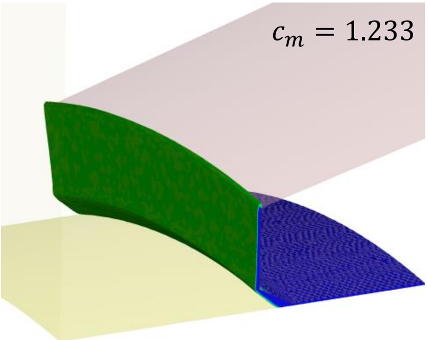	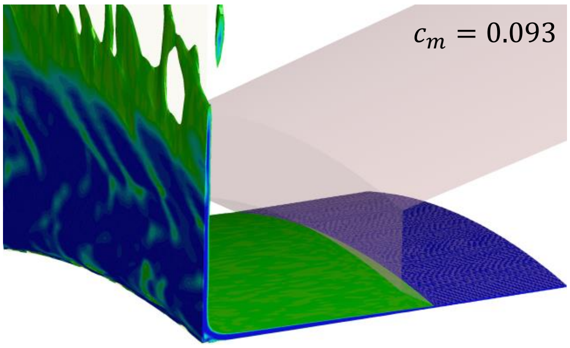

As shown by the simulation results presented in the table above, the oil flow path directions are independent of the chosen computational grid density in the θ-direction within the investigated range.

For radial oil outflow (Case 1 (d)), denser meshes reveal no difference in the oil flow path prediction and no notable differences in the resolution of the phase interface. The c_m value for the planet gear sector steadily increases with increasing mesh density. However, the difference between the c_m values for the densest and the baseline mesh is just over 1%, which is negligibly small.

For axial oil outflow (Case 3 (d)), denser meshes show finer flow structures on the planet carrier. Oil fingers along the planet carrier become more clearly visible. A comparison of the c_m values for the planet gear sector does not show a clear correlation with respect to mesh density.

4.1.5.3 Key Conclusions from Grid Density Study

The grid density studies presented in sections 4.1.5.1 and 4.1.5.2 allow the following conclusions to be drawn:

a) The predicted oil flow path directions are independent of the chosen computational grid density within the investigated ranges.

b) Denser meshes are capable of resolving ligament-type flow structures and fingers. In some instances, high-density meshes are able to capture single, primary droplets.

c) Within the investigated range of mesh densities, the choice of the computational grid only depends on the desired resolution of the phase interface and the time available to compute the fluid flow behaviour in the domain under investigation for a given elapsed flow time, t.

4.1.6 Model Sensitivity – Wall Adhesion Effects

As previously discussed in section 3.1.6, the research work presented in this thesis did not allow contact angle measurements to be made. For this reason, a sensitivity study was conducted to assess the potential effect of the contact angle, o, on the oil flow path prediction. For the investigations, the baseline computational grid was used (section 4.1.1). Consistent with the approach used for the computational grid density study (section 4.1.5) both radial (Case 1 (d)) and axial (Case 3 (d)) oil outflow, respectively, were assessed at quasi-steady-state conditions, i.e. $t = 0.03$ s and $t = 0.015$ s, respectively.

Kalin and Polajnar [79] investigated the static contact angles between different types of oil and steel. In any case, o never exceeded a value of 45°. As the authors' study did not include measurements of dynamic contact angles, and due to the uncertainties associated with contact angle measurements (section 3.1.6), the sensitivity study presented in this section was carried out for $10° \leq o \leq 135°$. The results are summarised in Table 4.9. In Table 4.9, the phase interface is visualised by an iso-surface (green) that indicates 50% oil volume fraction. Areas shaded in blue indicate that the oil is in full contact with the appropriate surface of the planet gear, the pin or the planet carrier.

Table 4.9: Results of contact angle study

	Case 1 (d) – radial oil outflow	Case 3 (d) – axial oil outflow
No wall adhesion	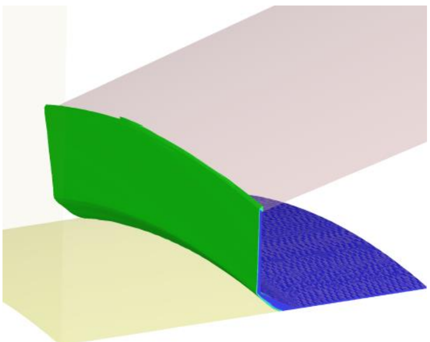	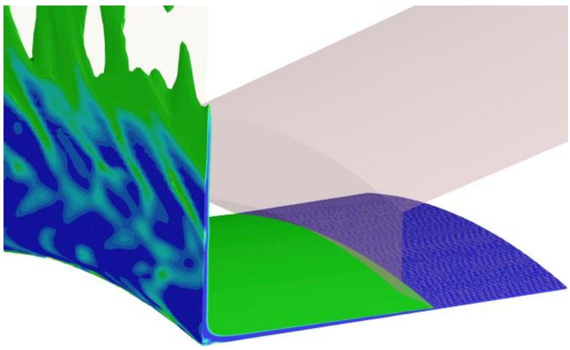

$o = 10°$	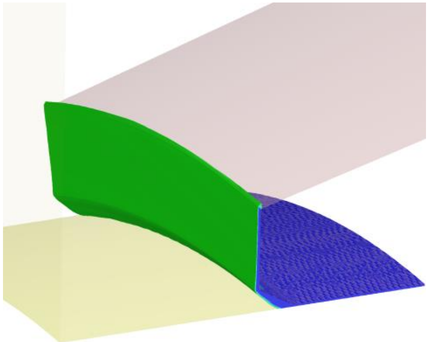	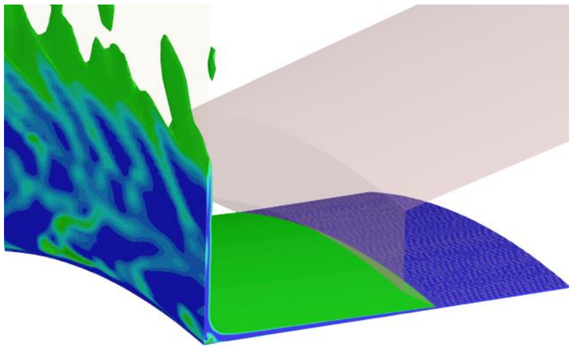
$o = 45°$	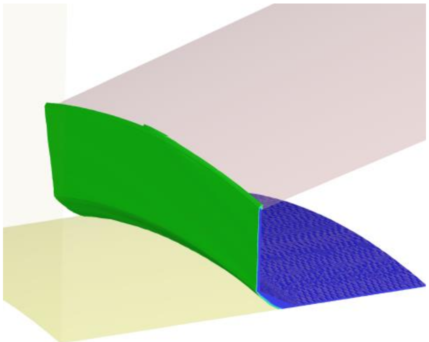	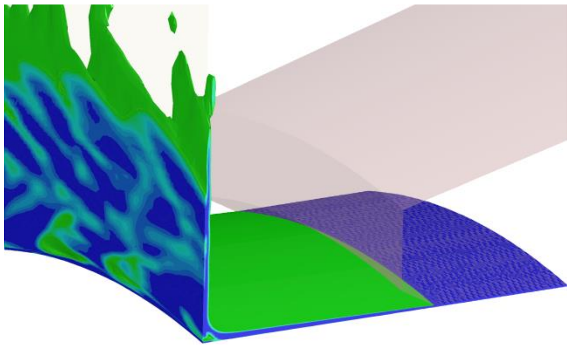
$o = 90°$	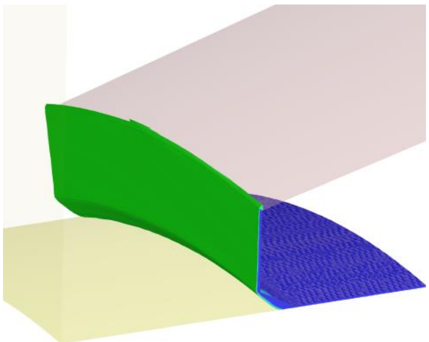	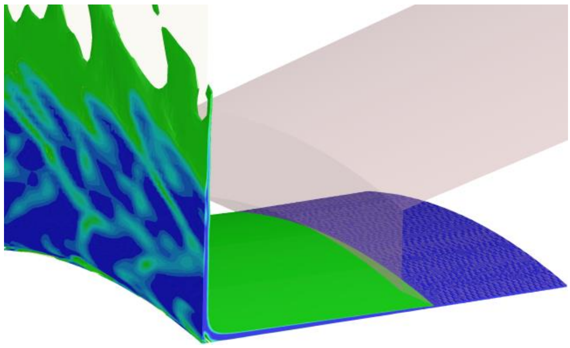
$o = 135°$	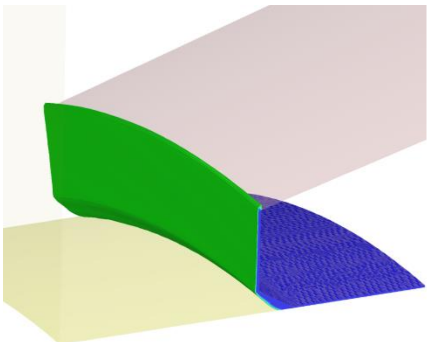	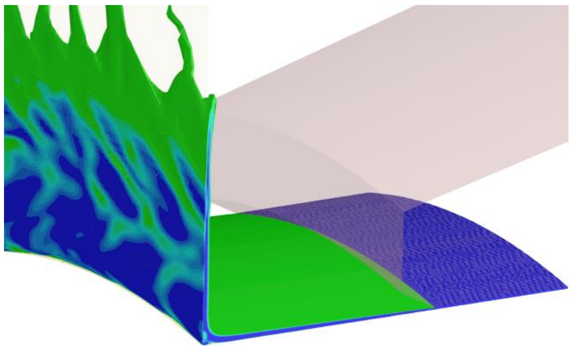

As shown by the simulation results presented in the table above, the predicted oil flow path directions are independent of the contact angle, o, within the investigated range.

For radial oil outflow (Case 1 (d)), no visible changes to flow structures can be observed. For axial outflow (Case 3 (d)), minor changes are noticeable with respect to the progression of the oil film along the planet carrier. Oil fingers, for instance, evolve slightly differently depending on the value of o. However, for the bulk flow analysis presented in this thesis, these differences are irrelevant. For this reason, wall adhesion effects will not be considered further.

4.1.7 Model Sensitivity – Wall Conditions

The full steady-state CFD analysis presented in section 4.1.4 showed that for radial oil outflow (Case 1 (d)) a small percentage of the inlet mass flow rate, $\dot{m}_{\mathrm{in}}$, continues to increase the mass of the oil inside the domain under investigation even after an elapsed flow time of $t = 0.300$ s (27 gear revolutions). It is anticipated that this oil mass will eventually be deposited on the walls bounding the domain. For instance, Figure 4.8 shows signs of oil build-up on the planet carrier wall. After a sufficiently long elapsed flow time, it is expected that, regardless of the oil flow path direction, i.e. radial or axial oil outflow, all walls will exhibit a thin coating of oil. This is mainly caused by secondary droplet generation due to liquid-solid interaction, e.g. oil interaction with the walls bounding the domain under investigation, liquid-gas interaction, e.g. oil interaction with the air, and liquid-liquid interaction, e.g. oil droplet impingement on films.

In absolute terms, the oil film thickness on the domain walls is expected to be very small. However, compared to the height of the lubricating gap, h_0, it is expected to be significant. Hence, the regions most prone to experiencing a potential change of the oil flow path behaviour due to oil-wetted domain walls, are those with geometric domain boundary length scales that are of the same order of magnitude as the expected oil film thickness on the walls. One of these regions is located at the point where the oil enters into the external domain (Figure 2.2). This region in particular may not only be wetted by oil droplet deposition, but also due to capillary effects. For contact angles, o, smaller than 90°, the surface tension force will cause the oil inside the lubricating gap to migrate towards the gap's exit, where it forms a meniscus (Figure 4.14).

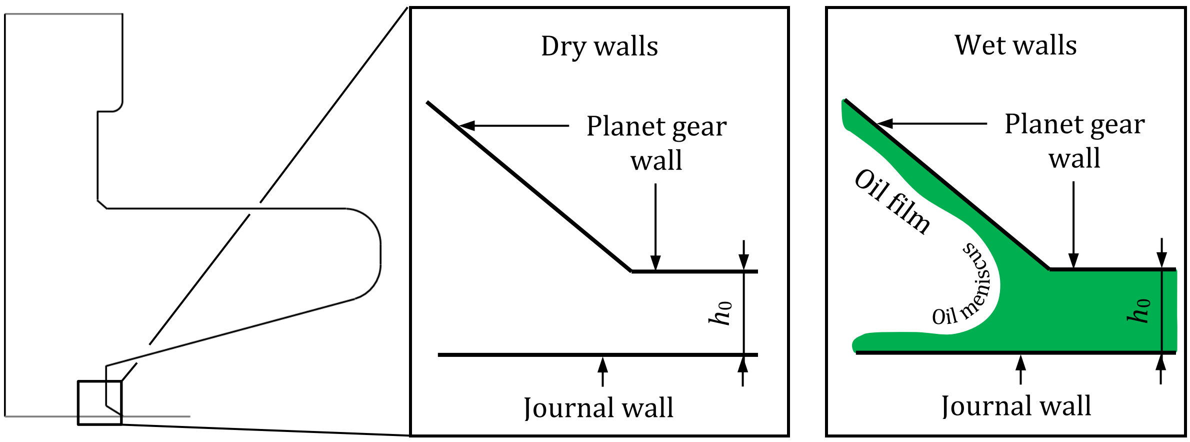

Figure 4.14: Schematic of wet and dry domain walls at lubricating gap exit

Based on the considerations above, oil-wetted domain walls are deemed a more realistic representation of the actual conditions in a gearbox. Therefore, a study was conducted to assess the potential effect of oil-wetted domain walls on the oil flow path prediction. The boundary conditions for Case 3 (d) were used for the assessment, which is presented in Table 4.10. In Table 4.10, the phase interface is visualised by an iso-surface (green) that indicates 50% oil volume fraction. Areas shaded in blue indicate that the oil is in full contact with the appropriate surface of the planet gear, the pin or the planet carrier.

Table 4.10: Effect of oil-wetted domain walls on oil flow path prediction for Case 3 (d) with ω_G=$\omega_{G,\,\text{max load}}$, v_0=0.14$\omega_G r_G$ and T=$T_{\text{max load}}$

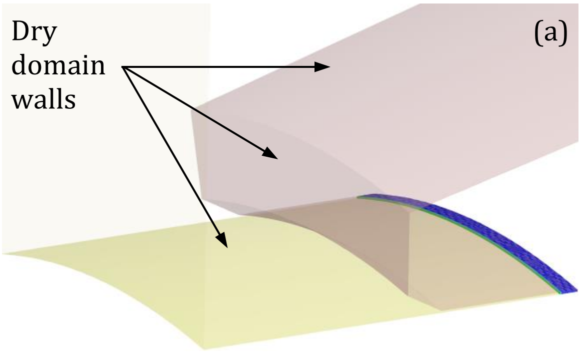

Initially dry domain walls at t = 0.000 s

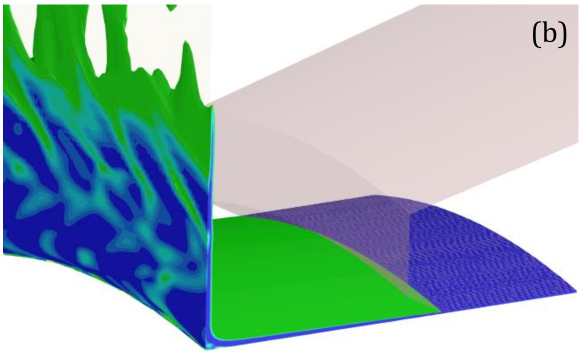

Initially dry domain walls at t = 0.015 s

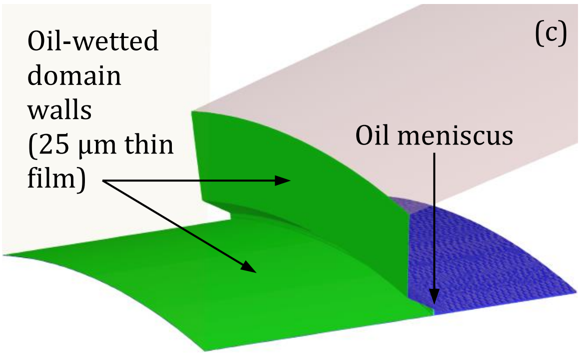

Initially wet domain walls at t = 0.000 s

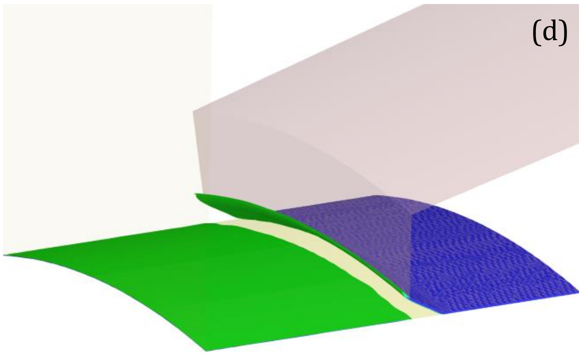

Initially wet domain walls at t = 0.030 s

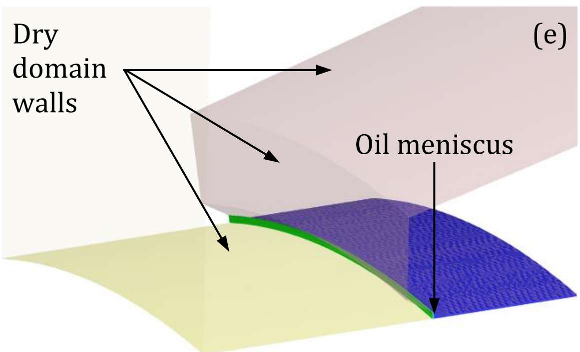

Initial oil meniscus at t = 0.000 s

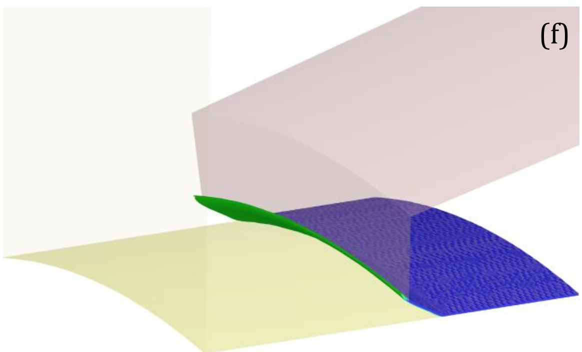

Initial oil meniscus at t = 0.030 s

For all cases with initially dry domain walls, the lubricating gap was patched with a small amount of oil adjacent to the inlet boundary (Table 4.10 (a)). This was primarily done for visualisation purposes to allow the 50% oil volume fraction iso-surface (green) to be set up.

For cases with initially wet domain walls (Table 4.10 (b)), a thin 25 μm oil film was patched on to the gear chamfer wall, the vertical wall of the gear base and the pin wall. The planet carrier wall and all other remaining gear walls have not been patched as no effect on the prediction of the oil flow path is expected. Moreover, based on the discussion above, an oil meniscus was patched into the transition region between the gear chamfer and the lubricating gap (Table 4.10 (b)). As previously shown in section 4.1.6, the oil flow path prediction is insensitive to the contact angle between the oil and the surfaces of the gear and the pin.

The results presented in Table 4.10 show that the initial conditions of the domain walls, i.e. dry or wet, do affect the flow path prediction of the oil as it exits the lubricating gap. Whilst with initially dry domain walls axial oil outflow prevails, initially wet domain walls cause the oil to attach the chamfer of the rotating gear. It subsequently separates from the lower edge of the gear base (diameter d_1 in Figure 2.2). As wall adhesion effects are not taken into account, the initially wet vertical wall of the gear base dries up (Table 4.10 (d)). This is caused by two mechanisms, namely oil entrainment into the oil sheet as it separates from the lower edge of the gear base (diameter d_1 in Figure 2.2) and oil removal due the centrifugal force acting on the oil film. Similarly, oil is also entrained from the pin wall, leading to a dry area in the vicinity of the lubricating gap exit.

Table 4.10 (e) and (f) show that the presence of an oil meniscus at the exit of the lubricating gap alone is sufficient to cause the oil flow path direction to change, i.e. the predicted oil flow path direction is consistent with that obtained when using oil-wetted domain walls as initial boundary condition (Table 4.10 (c) and (d)). Using only a patched oil meniscus instead of fully wetted walls as initial boundary condition provides the benefit of maintaining unobstructed visual access into the domain. During its transient evolution, this allows the oil flow path behaviour to be assessed more easily and more clearly.

It should be noted that the identified dependency of the oil flow path direction on the conditions of the domain walls does not change the conclusions previously drawn in section 4.1.2. The different outflow directions shown in Figure 4.5, i.e. axial outflow, radial outflow with oil separating from the lower edge of the planet gear base (diameter d_1 in Figure 2.2), and radial outflow with oil separating from the upper edge of the planet gear base (diameter d_2 in Figure 2.2), persist. However, the specific operating conditions and liquid properties, at which a change in the flow path direction occurs, will be different depending on the chosen initial wall condition, i.e. dry domain walls or an oil meniscus (Table 4.10 (c) and (e), respectively).

4.2 Orbiting Journal Bearing with Constant Lubricating Gap Height

In the previous section, a non-orbiting journal bearing sector model has been analysed. The predicted oil flow path direction was assessed depending on key boundary conditions, such as angular gear velocity, ω_G, the outflow velocity, v_0, and the oil temperature, T. Oil flow path sensitivities were explored with respect to the density of the computational grid, wall adhesion effects and initial wall conditions.

The findings and conclusions from the analysis presented in section 4.1 are now used to set up a full 360° journal bearing model with a constant lubricating gap height, h_0, that orbits around the sun gear. This allows the effect of the centrifugal force generated by the orbiting motion, $F_\mathrm{c,C}$, on the oil outflow behaviour to be assessed.

4.2.1 CFD Model Set-Up

The CFD model set-up for this case is based on the set-up used for the initial CFD investigations shown in section 4.1.1. The baseline mesh density was chosen as it provides an acceptable compromise between the phase interface resolution and the computational time required to simulate a given elapsed flow time, t. In order to reduce the computational effort required to solve the governing fluid flow equations (section 2.4), the mass flow inlet boundary condition (Figure 3.4 and Figure 3.5), as it was used for the sector analysis, was replaced with a velocity inlet boundary condition, which imposes the known axial (Poiseuille flow) and circumferential (Couette flow) flow velocity profiles directly at the inlet to the external flow domain ($y = 0$ mm, Figure 2.1). For completeness, Figure 3.4 and Figure 3.5 are repeated below to highlight the changes made to inlet region of the model.

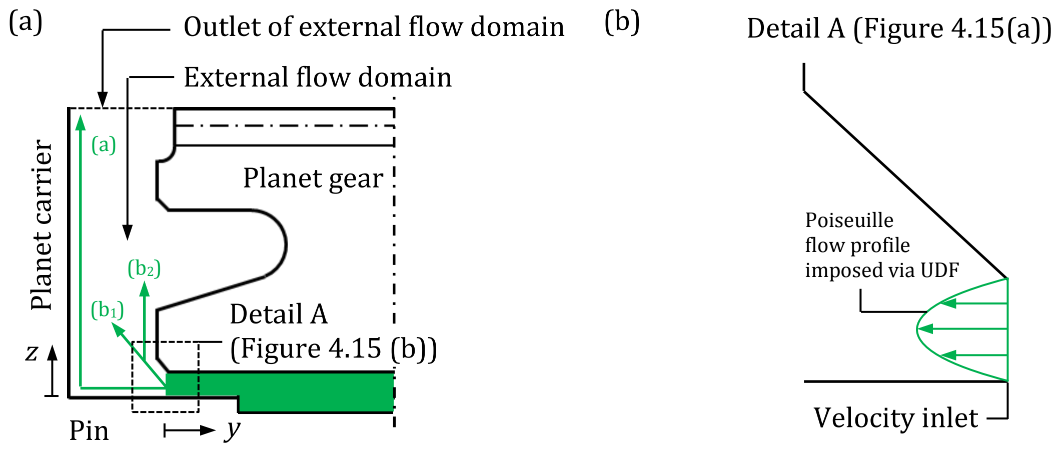

Figure 4.15: Inlet boundary condition in the axial direction for external oil flow from a journal bearing with a constant lubricating gap height

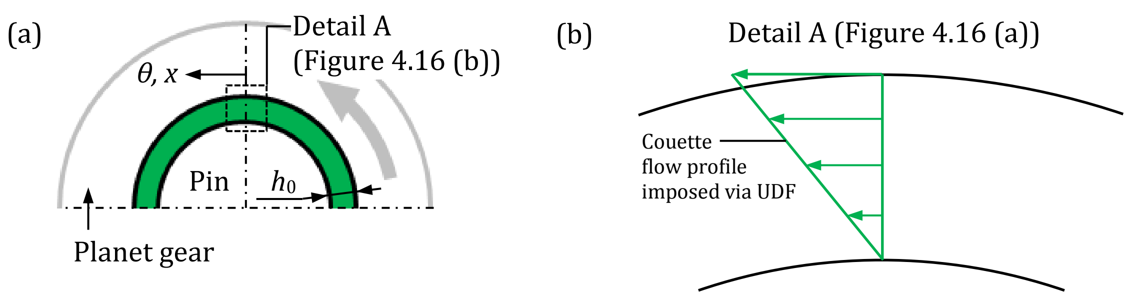

Figure 4.16: Inlet boundary condition in the circumferential direction for external oil flow from a journal bearing with a constant lubricating gap height

The UDFs used to describe the velocity profiles in both the axial and the circumferential directions are included in Appendix 3. Due to the lubricating gap height being constant around the bearing's circumference, both the axial and the circumferential velocity profiles across the gap height are independent of the circumferential position, θ.

Using a velocity inlet, as shown in Figure 4.15 and Figure 4.16, respectively, instead of a mass flow inlet allows the entrance length, $l_{\mathrm{ent,rq}}$, which was previously needed to achieve fully developed flow velocity profiles at the bearing end-face, to be omitted. Thus, the overall cell count could be reduced by 12% without compromising the phase interface resolution in the external flow domain. Key mesh parameters and properties are listed in Table 4.11.

Table 4.11: Key mesh parameters and properties for CFD investigations of an orbiting journal bearing with constant lubricating gap height

Mesh parameter	Value
Cell count in each 2D plane	9,849
Cell count in circumferential direction	1079 (1080 node points)
Total cell count in 360° mesh	10,627,071
Lubricating gap height, h_0	116 µm
Number of cells across h_0	17 (18 node points)
Height of first cell perpendicular to wall	0.01 mm
Cell growth factor	1.1…1.4

The considerations and investigations previously presented in section 4.1.7 concluded that patching an oil meniscus between the gear chamfer and the pin surface, as shown in Table 4.10 (e), provides the preferred initial wall condition. Thus, the model investigated in this section was set up to include a patched oil meniscus at the exit of the lubricating gap. The boundary condition types applied to all remaining domain surfaces are identical to those used for the initial CFD investigations (section 4.1.1). For the particular case investigated in this section, the oil outflow behaviour is assessed at maximum load conditions. Key operational parameters are summarised in Table 4.12. A complete list of all boundary conditions and numerical settings is included in Appendix 6.

Table 4.12: Key operational parameters at maximum load conditions for CFD investigations of an orbiting journal bearing with constant lubricating gap height

Operational parameter	Value
Angular gear velocity relative to angular carrier velocity, ω_{G}	$\omega_{\mathrm{G,\,max\,load}}$
Angular carrier velocity, ω_{C}	$\omega_{\mathrm{C,\,max\,load}}$
Oil inlet mass flow rate, $\dot{m}_{\mathrm{in}}$	$2\dot{m}_{\mathrm{in,\,max\,load}}$
Circumferetial inlet velocity, u_0	$u_0 = f(z)$
Axial inlet velocity, v_0	$v_0 = f(z)$
Temperature, T	$T_{\mathrm{max\,load}}$

In order to simulate the orbiting motion of the planet gear around the sun gear, the angular velocity, $\omega_{\mathrm{C}} = \omega_{\mathrm{C,\,max\,load}}$, is applied to the planet carrier. In ANSYS Fluent [48], an orbiting motion can be achieved by enabling frame motion. For non-orbiting cases, the frame axis is consistent with that of the planet bearing. For orbiting cases, the frame axis is shifted by the distance between the planet bearing axis and the sun gear axis. In an epicyclic gearbox in planetary configuration, with a fixed ring gear, the planet carrier and the planet gears rotate in opposite directions (Figure 1.1).

The oil inlet mass flow rate, $\dot{m}_{\mathrm{in}} = 2\dot{m}_{\mathrm{in,\,max\,load}}$, was chosen to be twice that of the actual journal bearing. The full rationale for choosing this value was previously discussed in section 4.1.2. This ensures that the outflow velocity, v_0, is more representative of that of a journal bearing with a convergent-divergent lubricating gap height, h, where outflow can only occur in the convergent part of the gap. A complete list of all boundary conditions and numerical settings is included in Appendix 6.

4.2.2 CFD Model Results

This section summarises the CFD model results for an orbiting journal bearing with a constant lubricating gap height, h_0, at maximum load conditions (Table 4.1) after 1/8 and 1.0 planet carrier rotations, which are completed after an elapsed flow time of $t = 0.0046$ s and $t = 0.0358$ s, respectively. In the same period of time, the planet gear has completed 0.4 and 3.1 revolutions, respectively.

The resultant centrifugal force, F_{c}, varies around the planet gear's circumference as the centrifugal force generated by the planet gear rotation about its own axis, $F_{\mathrm{c,G}}$, is superimposed with the centrifugal force generated by the planet carrier rotation, $F_{\mathrm{c,C}}$. As Couette flow prevails in the circumferential direction at the entrance into the external domain, i.e. $y = 0$ mm (Figure 2.1), the oil bulk flow velocity in this direction is half of that of the rotating gear surface at this radius, i.e. $u = \omega_{\mathrm{G}} r_{\mathrm{G}}/2$. For some selected angular locations, θ, the centrifugal forces acting on the oil at the point of entering into the external domain are schematically shown in Figure 4.17.

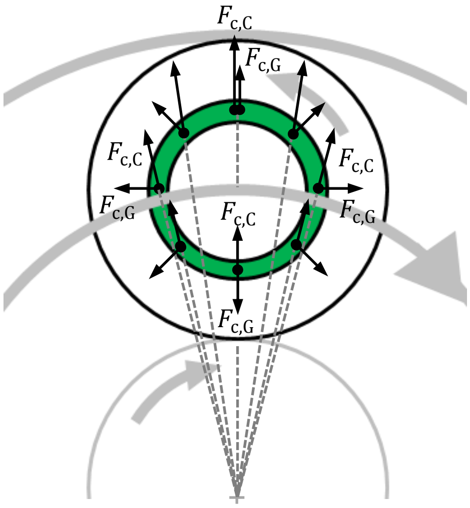

Figure 4.17: Schematic of the directions of the centrifugal forces, $F_{c,C}$ and $F_{c,G}$, acting on the oil film as it enters into the external flow domain of an orbiting journal bearing with a constant lubricating gap height

Because F_c varies in magnitude and direction around the journal bearing's circumference, it is practical to assess the flow field behaviour at key angular locations, θ. Figure 4.18 defines the planes in which the flow field behaviour will be assessed.

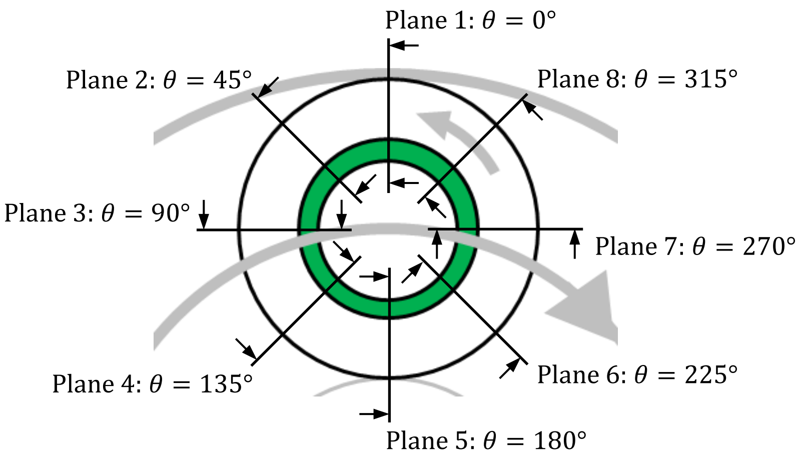

Figure 4.18: Definition of viewing planes for flow field assessment

Table 4.13 shows the air volume fraction contour plot for the planes defined in Figure 4.18 after 1/8 ($t = 0.0046$ s) and 1.0 ($t = 0.0358$ s) planet carrier rotations, respectively.

Table 4.13: CFD model results of an orbiting journal bearing with a constant lubricating gap height at maximum load conditions. Contours of air volume fractions.

	$t = 0.0046$ s	$t = 0.0358$ s
Plane 1 $\theta = 0°$ 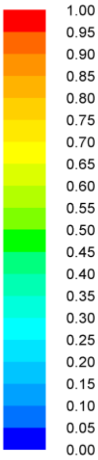	(a) 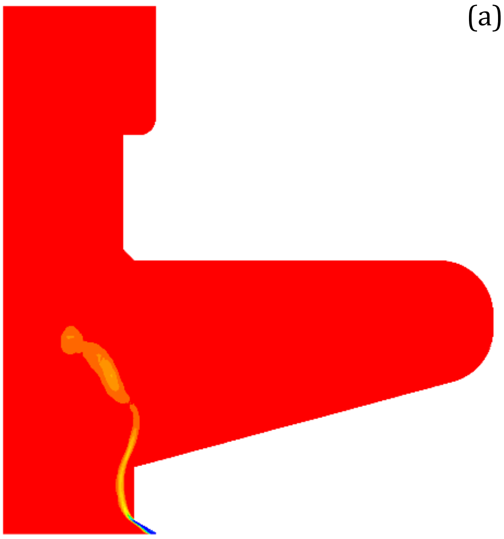	(b) 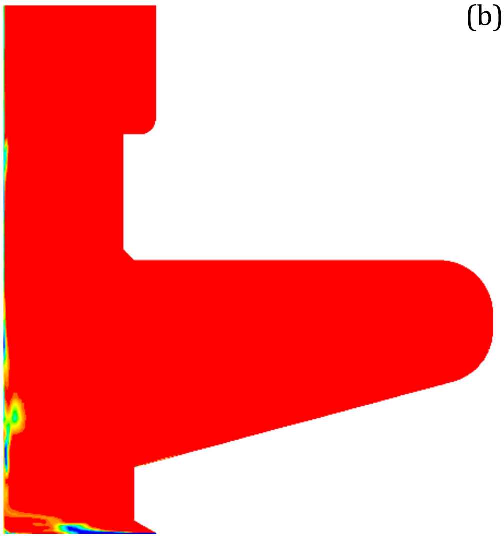
Plane 2 $\theta = 45°$ 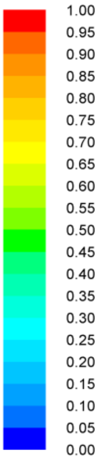	(c) 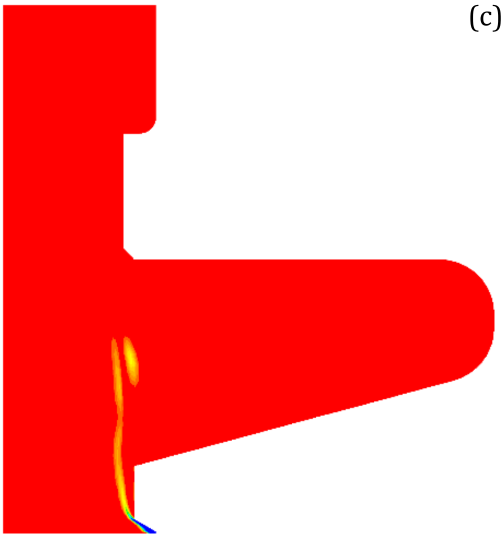	(d) 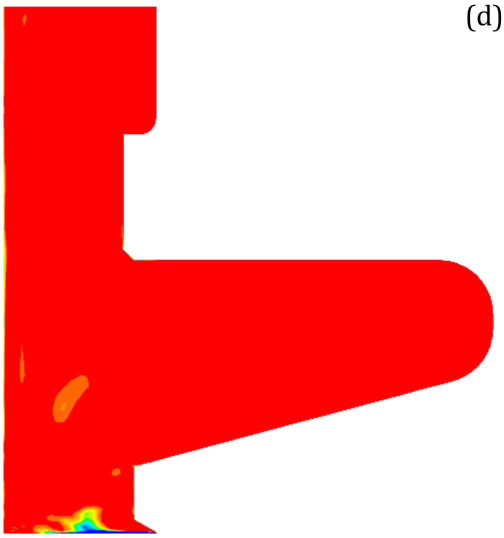

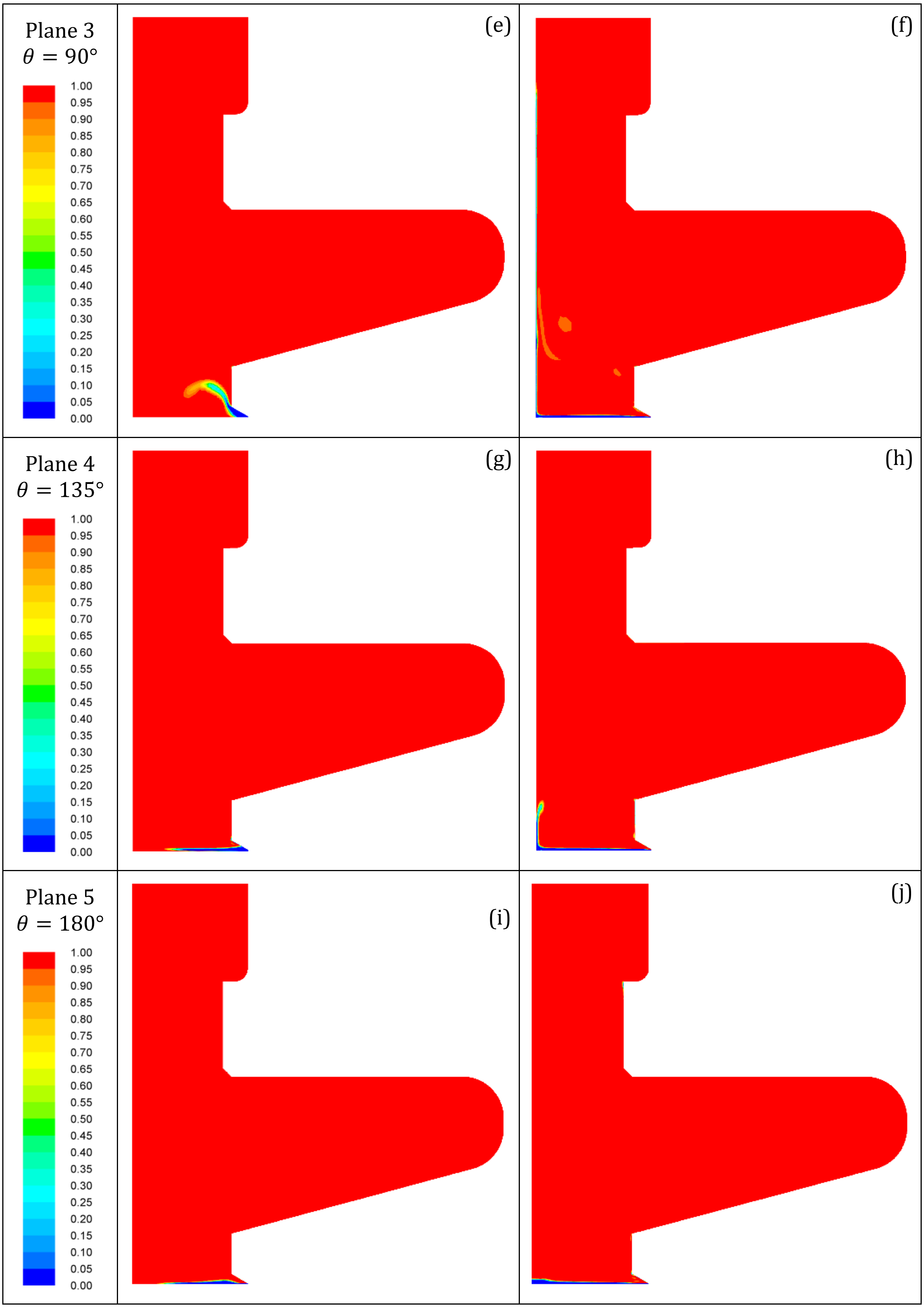
Plane 3
θ = 90°
1.00 0.95 0.90 0.85 0.80 0.75 0.70 0.65 0.60 0.55 0.50 0.45 0.40 0.35 0.30 0.25 0.20 0.15 0.10 0.05 0.00
(e)
(f)
Plane 4
θ = 135°
1.00 0.95 0.90 0.85 0.80 0.75 0.70 0.65 0.60 0.55 0.50 0.45 0.40 0.35 0.30 0.25 0.20 0.15 0.10 0.05 0.00
(g)
(h)
Plane 5
θ = 180°
1.00 0.95 0.90 0.85 0.80 0.75 0.70 0.65 0.60 0.55 0.50 0.45 0.40 0.35 0.30 0.25 0.20 0.15 0.10 0.05 0.00
(i)
(j)

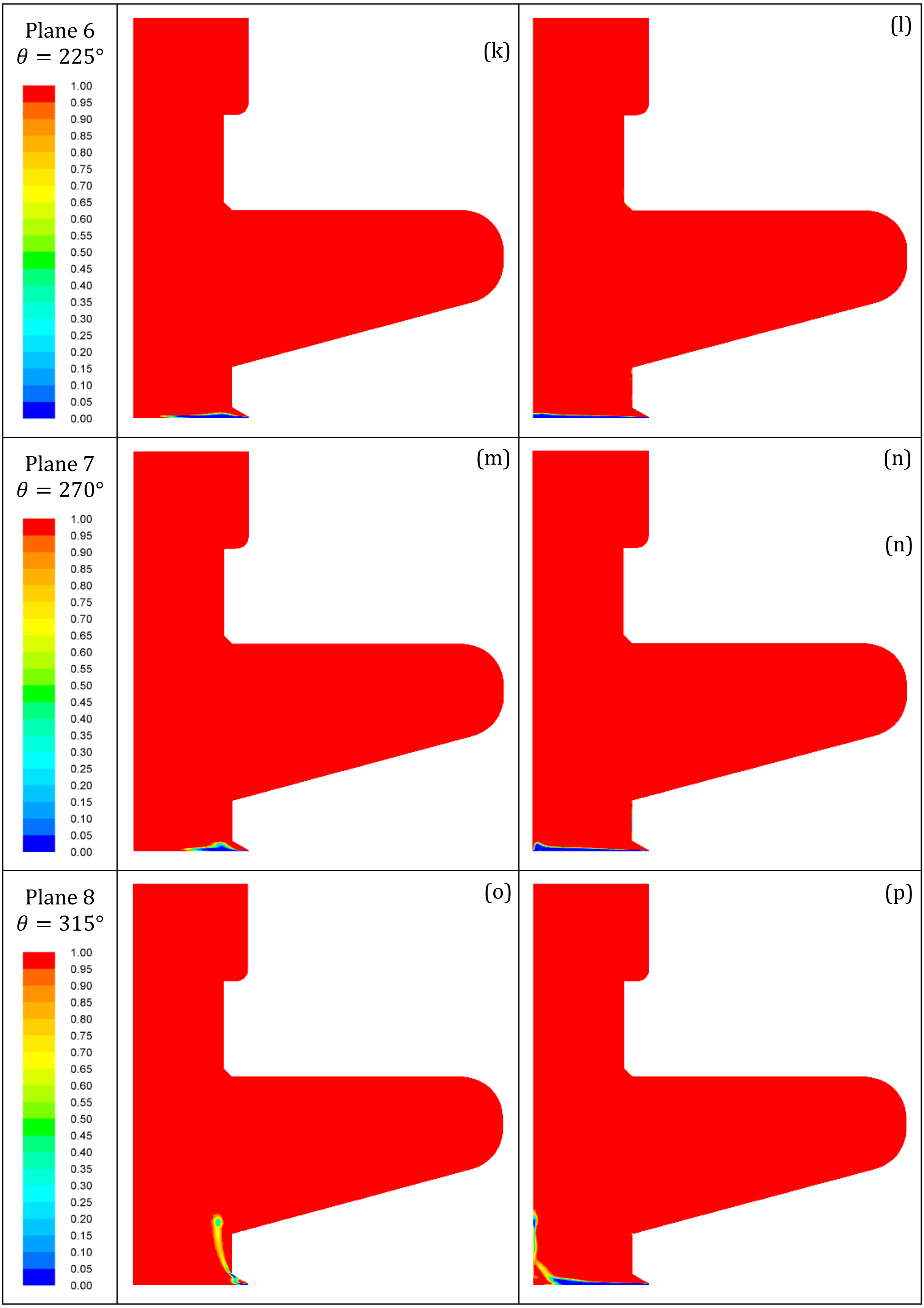
Plane 6
$\theta = 225°$
1.00 0.95 0.90 0.85 0.80 0.75 0.70 0.65 0.60 0.55 0.50 0.45 0.40 0.35 0.30 0.25 0.20 0.15 0.10 0.05 0.00
(k)
(l)
Plane 7
$\theta = 270°$
1.00 0.95 0.90 0.85 0.80 0.75 0.70 0.65 0.60 0.55 0.50 0.45 0.40 0.35 0.30 0.25 0.20 0.15 0.10 0.05 0.00
(m)
(n)
(n)
Plane 8
$\theta = 315°$
1.00 0.95 0.90 0.85 0.80 0.75 0.70 0.65 0.60 0.55 0.50 0.45 0.40 0.35 0.30 0.25 0.20 0.15 0.10 0.05 0.00
(o)
(p)

In plane 1, i.e. $\theta = 0°$, after 0.4 planet gear revolutions, the oil entering the external flow domain attaches to the planet gear chamfer and follows the gear's geometry before it separates from the lower edge of the gear base (diameter d_1 in Figure 2.2). This flow path behaviour is consistent with that observed when investigating Case 3 (d) with an oil meniscus patched into the transition region between the gear chamfer and the lubricating gap (section 4.1.7, Table 4.9 (e) and (f)). The only notable difference to Case 3 (d), which did not account for planet carrier rotation, is that now $F_{c,C}$ acts in addition to $F_{c,G}$. At the top dead centre position, i.e. $\theta = 0°$, both forces in question act in the same direction (Figure 4.17). Thus, no significant change in the flow path direction can be expected. After 3.1 planet gear revolutions, however, the flow path has changed from a radial (flow path (b_1) in Figure 2.1) to an axial direction (flow path (a) in Figure 2.1). This indicates that the flow path direction is strongly influenced by effects taking place in other regions of the domain under investigation. These will be discussed in the following paragraphs. Table 4.1 (b) shows that the oil film, which travels axially across the pin surface, lifts off and disintegrates before it reaches the planet carrier. This is due to the combined centrifugal forces, $F_{c,G}$ and $F_{c,C}$, acting on the film in this location, as shown in Figure 4.17.

Very similar flow path conditions can be observed in plane 2, i.e. $\theta = 45°$. At first, after 0.4 planet gear rotations, the oil separates from the lower edge of the gear base (diameter d_1 in Figure 2.2). Later, after 3.1 gear revolutions, this flow path follows an axial direction (Table 4.1 (d)). As previously observed at the top dead centre position, i.e. $\theta = 0°$ (Table 4.1 (b)), the film lifts off the pin surface before the planet carrier has been reached. In plane 2 ($\theta = 45°$), $F_{c,G}$ and $F_{c,C}$ act in different directions, as schematically shown in Figure 4.17. Thus, with respect to the planet gear axis, F_c has a radially outwards directed component and a circumferential component pointing against the direction of gear rotation.

In plane 3, i.e. $\theta = 90°$, similar to the conditions observed in plane 2, i.e. $\theta = 45°$, after 0.4 planet gear rotations, the oil separates from the lower edge of the gear base (diameter d_1 in Figure 2.2). However, the oil film along the gear chamfer is considerably thicker compared to that observed in plane 2 at the same point in time, i.e. after 0.4 planet gear rotations. Figure 4.17 illustrates that in plane 3, i.e. $\theta = 90°$, with respect to the planet gear axis, the radially outwards directed contribution of $F_{c,C}$ decreases compared to that in the previously considered view plane. Consequently, the circumferential contribution increases. This inhibits the oil flow in the circumferential direction, as the circumferential component of $F_{c,C}$ is directed against the direction of gear rotation. As the radially outwards directed component of F_c decreases with respect to the planet gear axis, after 3.1 planet gear rotations, the oil film no longer lifts off the pin surface. Instead, it travels across the pin until it reaches the planet carrier on which it forms a thin film.

In plane 4, i.e. $\theta = 135°$, axial oil outflow prevails at any point in time. As shown in Figure 4.17, the direction of F_c is such that its circumferential component, with respect to the planet gear axis, increases even further compared to that in plane 3, i.e. $\theta = 90°$, and the radial contribution decreases. As a result, after a sufficient elapsed flow time, t, the oil film reaches the planet carrier. There, it forms a thin film which is driven radially outwards with respect to the planet carrier axis. At this angular location, i.e. $\theta = 135°$, $F_{c,C}$, has a component which is directed radially inwards with respect to the planet gear axis.

In plane 5, i.e. $\theta = 180°$, similar to the oil outflow behaviour observed in plane 4, i.e. $\theta = 135°$, axial outflow prevails at any given point in time. In plane 5, $F_{c,G}$ and $F_{c,C}$ are opposing each other (Figure 4.17). F_c is insufficient to lift the oil film off the pin surface before it reaches the planet carrier. As indicated in Table 4.12 (j), the forces acting on the oil film are such that no oil film is formed on the planet carrier surface. Instead, driven by $F_{c,C}$, the oil is forced to follow the pin curvature towards higher radii with respect to the planet carrier axis. By doing so, the outflow behaviour in other regions of the domain is affected.

In plane 6, i.e. $\theta = 225°$, no significant changes of the oil outflow behaviour can be observed compared to that seen in plane 5, i.e. $\theta = 180°$. Axial oil outflow prevails at any point in time. The direction of $F_{c,C}$ is such that a significant circumferential contribution exists with respect to the planet gear axis. In contrast to the conditions discussed in plane 4, i.e. $\theta = 135°$, however, this circumferential contribution now acts in the same direction as the gear rotation. Overall, this leads to asymmetric outflow conditions with respect to the planet gear's vertical y-z-plane. The fact that the planet carrier surface is free of any oil indicates that the forces acting on the oil film are insufficient to drive it along the planet carrier wall. Instead, as previously observed in plane 5, i.e. $\theta = 180°$, the oil is forced to follow the pin curvature towards higher radii with respect to the planet carrier axis.

In plane 7, i.e. $\theta = 270°$, no significant changes of the oil outflow behaviour are observed compared to that seen in plane 5, i.e. $\theta = 180°$, and plane 6, i.e. $\theta = 225°$. A notable difference, however, is that the thickness of the oil film covering the pin surface is generally larger compared to that observed in the two previous view planes. This indicates an increased radially outwards directed component of F_c with respect to the planet gear axis. In fact, as schematically shown in Figure 4.17, at this angular location, i.e. $\theta = 270°$, $F_{c,C}$ consists of a component which is directed radially outwards with respect to the planet gear axis, whereas in the previous view planes 5 and 6, respectively, $F_{c,C}$ consisted of a component which was directed radially inwards.

In plane 8, i.e. $\theta = 315°$, after 0.4 planet gear rotations, the combined radial contributions of $F_{c,G}$ and $F_{c,C}$, with respect to the planet gear axis, are sufficiently large to cause radial oil outflow to occur. Oil entering the external domain attaches to the planet gear chamfer and follows the gear's geometry before it separates from the lower edge of the gear base (diameter d_1 in Figure 2.2). This flow path behaviour is very similar to that previously observed in plane 1, i.e. $\theta = 0°$, after the same elapsed flow time. After 3.1 planet gear revolutions, the flow path has changed from a radial (flow path (b_1) in Figure 2.1) to an axial direction (flow path (a) in Figure 2.1). As previously seen in plane 1, i.e. $\theta = 0°$, due to the combined centrifugal forces acting on the oil film, it lifts off from the pin surface before it reaches the planet carrier.

Table 4.14 shows 3D images of the oil outflow behaviour after an elapsed flow time of $t = 0.0046$ s and $t = 0.0358$ s, respectively. At these points in time, 1/8 and 1.0 planet carrier rotations were completed. This is equivalent to 0.4 and 3.1 planet gear revolutions, respectively. The chosen points in time are identical to those used for the 2D assessment of the oil outflow behaviour presented in Table 4.13. The combination of both 2D and 3D images of the oil outflow behaviour at two different points in time allows a better understanding of the actual flow conditions to be gained. Figure 4.19 illustrates the view points from which the 3D images shown in Table 4.14 were created.

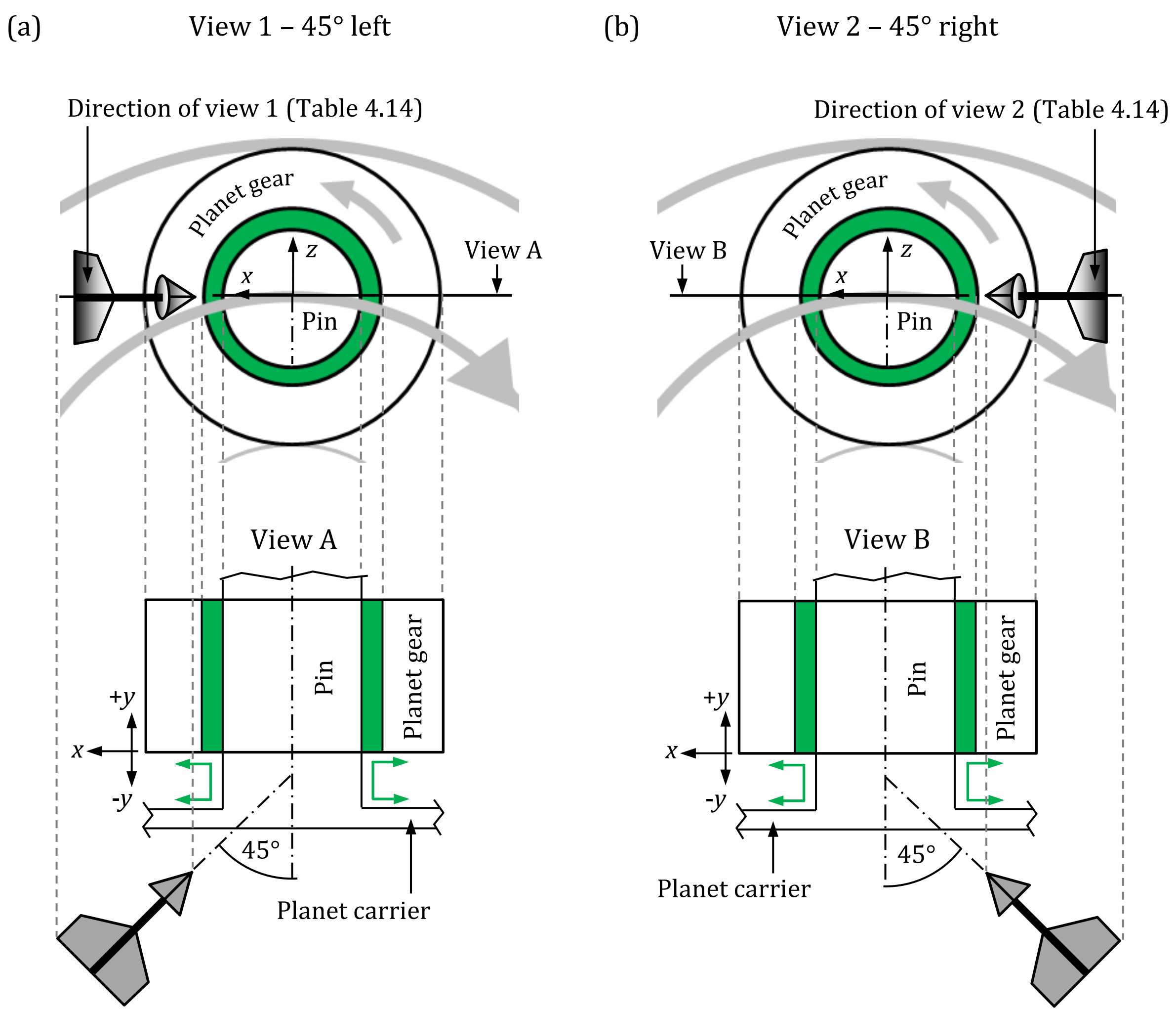

Figure 4.19: View point definition for 3D images shown in Table 4.14

The arrows shown in Figure 4.19 represent the direction of view chosen for the 3D images shown in Table 4.14. The observer's line of sight is in the planet gear's x-y-plane and at the same level as the pin axis. With respect to the y-z-plane, the line of sight is angled by 45°.

In Table 4.14, the phase interface is visualised by an iso-surface that indicates 50% oil volume fraction.

Table 4.14: CFD model results for an orbiting journal bearing with a constant lubricating gap height at maximum load conditions. Contours of 50% oil volume fraction coloured by axial distance, y.

<table>
<tr><th>View</th><th>t = 0.0046 s</th><th>t = 0.0358 s</th></tr>
<tr><td>View 1

45° left

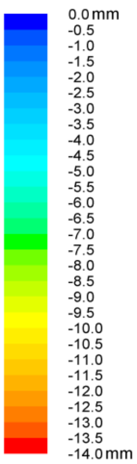
</td><td>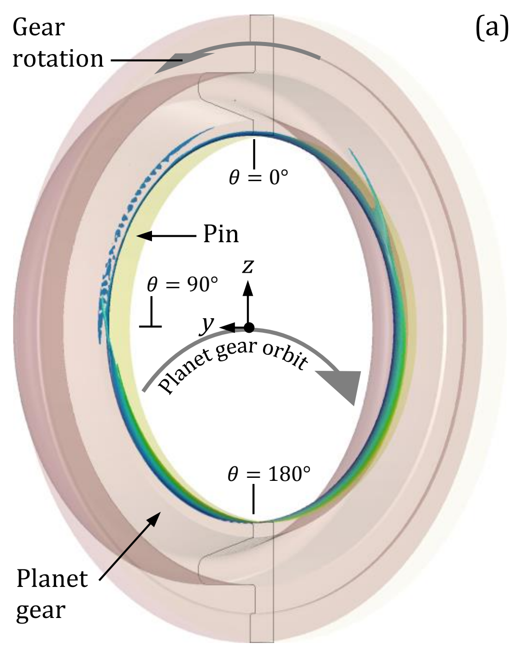
</td><td>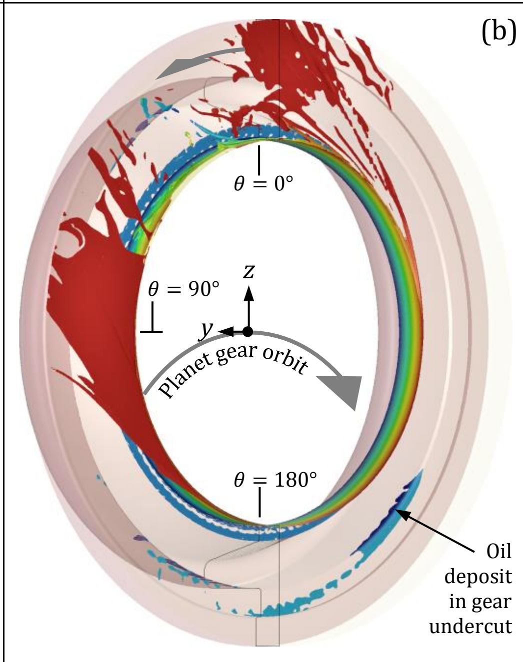
</td></tr>
<tr><td>View 2

45° right

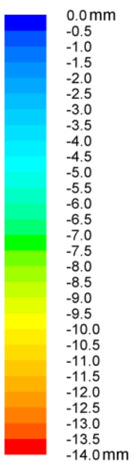
</td><td>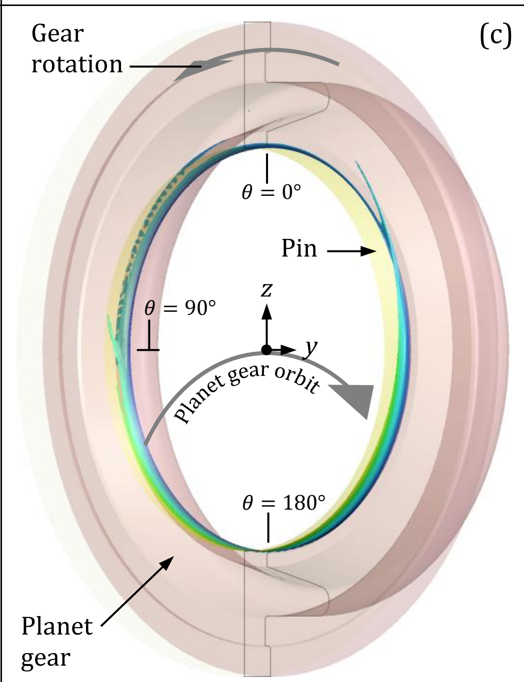
</td><td>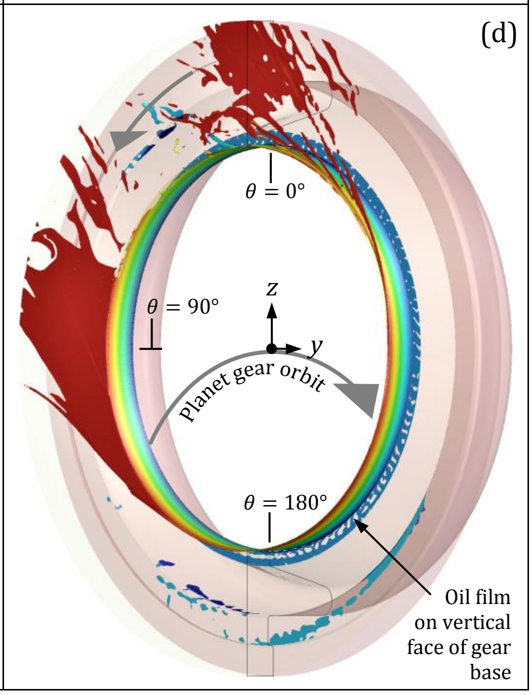
</td></tr>
</table>

In order to enhance clarity, the iso-surface is coloured by the axial distance from the gear base, y. Consistent with the convention introduced in Figure 2.1, the bearing end-face, i.e. the point where the oil enters into the external domain, is located at $y = 0$ mm. The planet carrier surface is located at $y = -14$ mm. Thus, oil that is attached to the gear or in close vicinity to it, is shaded in a blue colour and oil that is attached to the planet carrier or in close vicinity to it, is shaded in a red colour.

The 3D images provided in Table 4.14 show that outflow primarily occurs in the axial direction. Thus, an oil film is formed on the pin. Once the oil film has reached the planet carrier, oil is driven radially outwards with respect to the planet carrier axis. The flow pattern which develops on the planet carrier surface is asymmetric with respect to the y-z-plane for the following reasons.

a) In the region between $0° < \theta < 180°$, the circumferential velocity component of the oil entering into the external flow domain has a contribution which is directed radially inwards with respect to the planet carrier axis. In the region between $180° < \theta < 0°$, the circumferential velocity component of the oil entering into the external flow domain has a contribution which is directed radially outwards with respect to the planet carrier axis. Thus, there is a change of direction relative to the centrifugal force generated by the planet carrier rotation, $F_{c,C}$.

b) As the flow field behaviour is being assessed in the planet carrier fixed frame of reference, i.e. a rotating frame of reference, Coriolis effects occur.

Moreover, Table 4.14 shows that after an elapsed flow time of $t = 0.0358$ s, i.e. after one full carrier rotation and 3.1 planet gear rotations, respectively, an oil film has formed on the vertical face of the gear base (Table 4.14 (d)). This indicates that some radial oil outflow occurs even though the bulk of the flow enters the external domain in the axial direction. This is due to the fact that the rotating planet gear naturally entrains a small amount of oil. The 2D images provided in Table 4.13 show that the thickness of the oil film on the vertical face of the gear base is much smaller compared to that on the pin. Oil which attaches to the rotating planet gear eventually separates from the upper edge of the gear base (diameter d_2 in Figure 2.2) and impacts on the upper part of the gear undercut. Sector analyses presented in section 4.1.4 have shown that after a sufficiently long elapsed flow time, t, initially intermittent areas of deposited oil will merge to form a continuous oil film in the gear undercut. A similar behaviour is expected to prevail for the specific case under investigation.

4.2.3 Conclusions

From the analyses presented in section 4.2.2, the investigated case allows the following conclusions can be drawn.

a) Oil outflow occurs primarily in the axial direction. Some radial oil outflow can be observed due to natural liquid entrainment by the rotating planet gear.
b) Oil that is deposited in the gear undercut has the potential of creating imbalance forces acting on the planet gear (section 4.1.4).
c) The flow pattern is asymmetric with respect to the y-z-plane due to the planet gear rotation and Coriolis effects.

4.3 Non-Orbiting Journal Bearing with Convergent-Divergent Lubricating Gap Height

Oil outflow from a non-orbiting journal bearing with a convergent-divergent gap height was investigated at maximum load conditions to assess the effect of journal bearing eccentricity on the outflow behaviour. At this stage, the orbiting motion of the planet gear around the axis of the sun gear is not accounted for in order to separate the effects of the planet carrier rotation and the planet gear rotation on the flow field behaviour.

4.3.1 CFD Model Set-Up

The computational mesh used for the case under investigation was generated using the approach previously discussed in section 3.3. The existing model of a full 360° journal bearing with a constant lubricating gap height, h_0, was used as a basis (section 4.2.1). In order to achieve a convergent-divergent gap height, the pin surface was moved by the appropriate amount in the negative z-direction (Figure 4.20). Note that a convergent-divergent gap height can also be achieved by moving the planet gear geometry in the positive z-direction. However, this is not representative of actual engine conditions as the location of the planet gear is constrained by the sun gear and the ring gear. In order to achieve the correct bearing attitude, i.e. the correct angular position, θ, of the minimum gap height, h_{min}, the model was rotated by the appropriate angle about the planet gear axis (Figure 4.20).

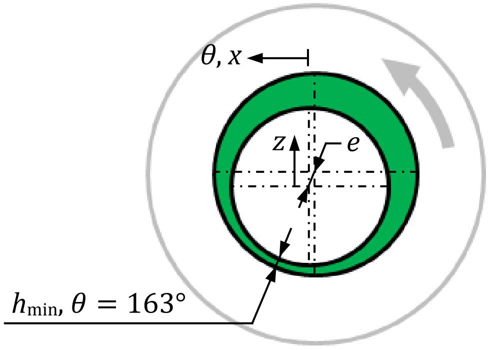

Figure 4.20: Bearing attitude at maximum load conditions

Key mesh parameters and properties are summarised in Table 4.15.

Table 4.15: Key mesh parameters and properties for CFD investigations of an orbiting journal bearing with convergent-divergent lubricating gap height

Mesh parameter	Value
Cell count in each 2D plane	9,849
Cell count in circumferential direction	1079 (1080 node points)
Total cell count in 360° mesh	10,627,071
Minimum gap height, h_{min}	6 μm
Maximum gap height, h_{max}	226 μm
Attitude angle, $\theta_{h,\,\mathrm{min}}$	163°
Number of cells across h	17 (18 node points)
Height of first cell perpendicular to wall	0.01 mm
Cell growth factor	1.1…1.4

The inlet boundary condition applied to the model is consistent with that described in section 3.5. A velocity inlet was used in order to prescribe the known axial (Poiseuille flow) and circumferential (Couette flow) flow velocity profiles and distributions directly at the inlet to the external flow domain ($y = 0$), as shown in sections 3.5.1 and 3.5.2, respectively. The UDFs used to describe the velocity profiles and velocity distributions are included in Appendix 4. Due to the convergent-divergent lubricating gap height, both the axial and the circumferential velocity profiles across the gap height are changing depending on circumferential position, θ, i.e. $u = f(z, \theta)$ and $v = f(z, \theta)$, respectively.

The considerations and investigations previously presented in section 4.1.6 concluded that patching an oil meniscus between the gear chamfer and the pin surface, as shown in Table 4.10 (e), provides the preferred initial wall condition. Thus, the model investigated in this section was set up to include a patched oil meniscus at the exit of the lubricating gap. The boundary condition types applied to all remaining domain surfaces are identical to those used for the initial CFD investigations (section 4.1.1). For the particular case investigated in this section, the oil outflow behaviour is assessed at maximum load conditions. Key operational parameters are summarised in Table 4.16. A complete list of all boundary conditions and numerical settings is included in Appendix 7.

Table 4.16: Key operational parameters at maximum load conditions for CFD investigations of a non-orbiting journal bearing with convergent-divergent lubricating gap height

Operational parameter	Value
Angular gear velocity relative to angular carrier velocity, ω_{G}	$\omega_{\mathrm{G,\,max\,load}}$
Angular carrier velocity, ω_{C}	0 rad/s
Oil inlet mass flow rate, $\dot{m}_{\mathrm{in}}$	$\dot{m}_{\mathrm{in,\,max\,load}}$
Circumferential inlet velocity, u	$u = f(z, \theta)$
Axial inlet velocity, v	$v = f(z, \theta)$
Temperature, T	$T_{\mathrm{max\,load}}$

4.3.2 CFD Model Results

This section summarises the CFD model results for a non-orbiting journal bearing with a convergent-divergent gap height, h, at maximum load conditions (Table 4.16) after 0.4 and 3.1 planet gear rotations, which are completed after an elapsed flow time of $t = 0.0046$ s and $t = 0.0358$ s, respectively. The points in time at which the flow fields are being assessed are identical to those chosen for the orbiting journal bearing case with a constant lubricating gap height, h_0, (section 4.2.2) in order to allow a like-for-like comparison between the two cases.

For a non-orbiting case, there is no planet carrier motion, and hence no centrifugal force is being generated by this component, i.e. $F_{c,C} = 0$. The resultant centrifugal force, F_c, is equal to the centrifugal force generated by the planet gear rotation, $F_{c,G}$, i.e. $F_c = F_{c,G}$. For the case under investigation, F_c is constant around the planet gear's circumference. For some selected angular locations, θ, the centrifugal force, $F_{c,G}$, acting on the oil at the point of entering into the external domain is schematically shown in Figure 4.21.

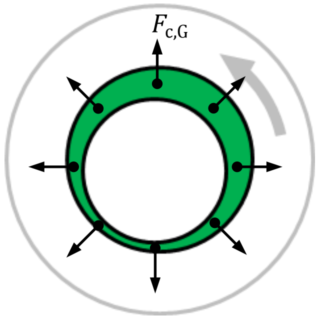

Figure 4.21: Schematic of the direction of the centrifugal force, $F_{c,G}$, acting on the oil film as it enters into the external flow domain of a non-orbiting journal bearing with a convergent-divergent lubricating gap height

For the case under investigation, the oil outflow velocity into the external domain varies depending on the radial coordinate across the gap height, z, and the circumferential location, θ. Due to the internal journal bearing film pressure distribution, at maximum load conditions, oil outflow only occurs in the region between $38° < \theta < 166°$ (section 3.5). It is therefore practical to assess the flow field behaviour at key angular locations, θ. Figure 4.22 defines the planes in which the flow field behaviour will be assessed.

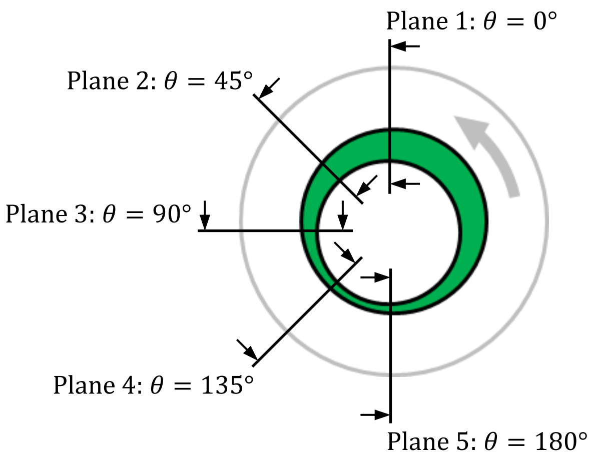

Figure 4.22: Definition of viewing planes for flow field assessment

Table 4.17 shows the air volume fraction contour plot for the planes defined in Figure 4.22 after 0.4 and 3.1 planet gear rotations, respectively.

Table 4.17: CFD model results of a non-orbiting journal bearing with a convergent-divergent lubricating gap height at maximum load conditions. Contours of air volume fractions.

	$t = 0.0046$ s	$t = 0.0358$ s
Plane 1 $\theta = 0°$ 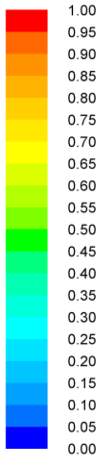 	(a) 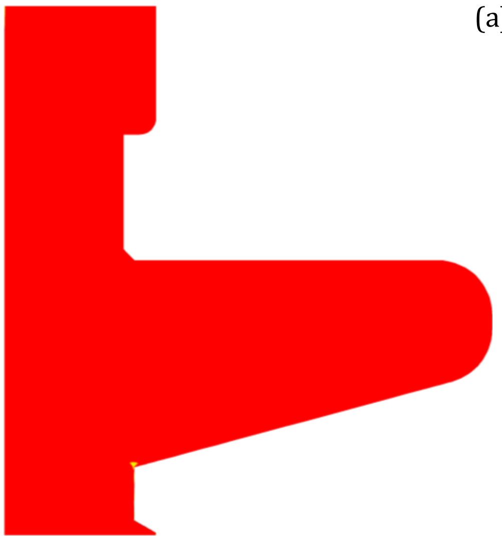	(b) 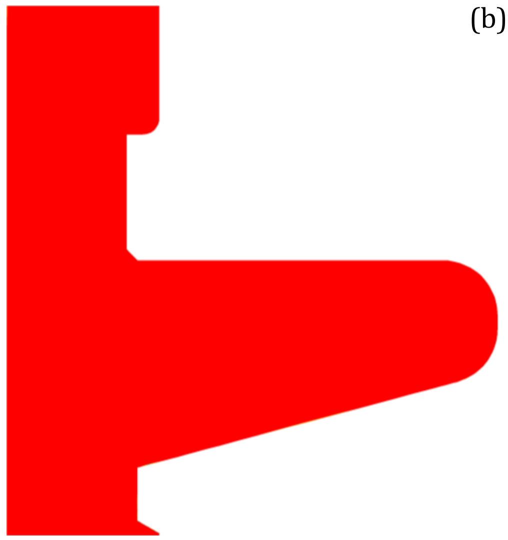
Plane 2 $\theta = 45°$ 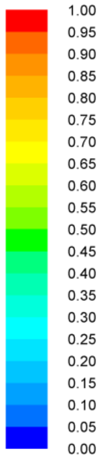 	(c) 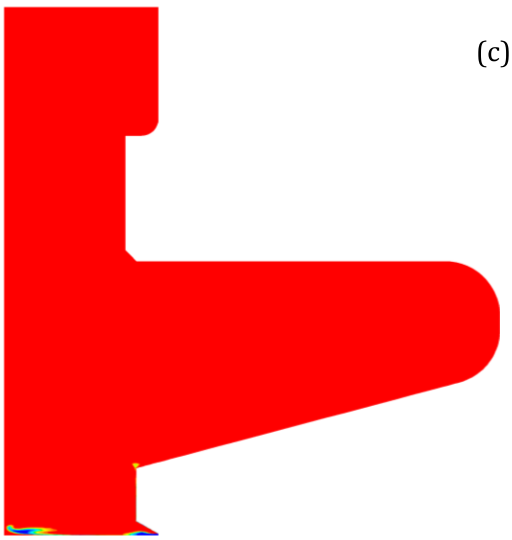	(d) 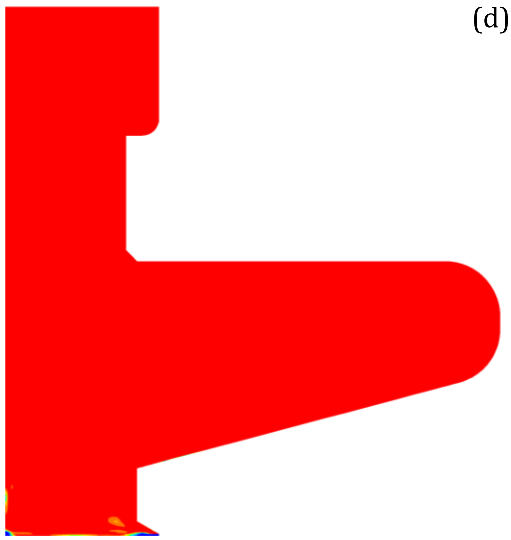

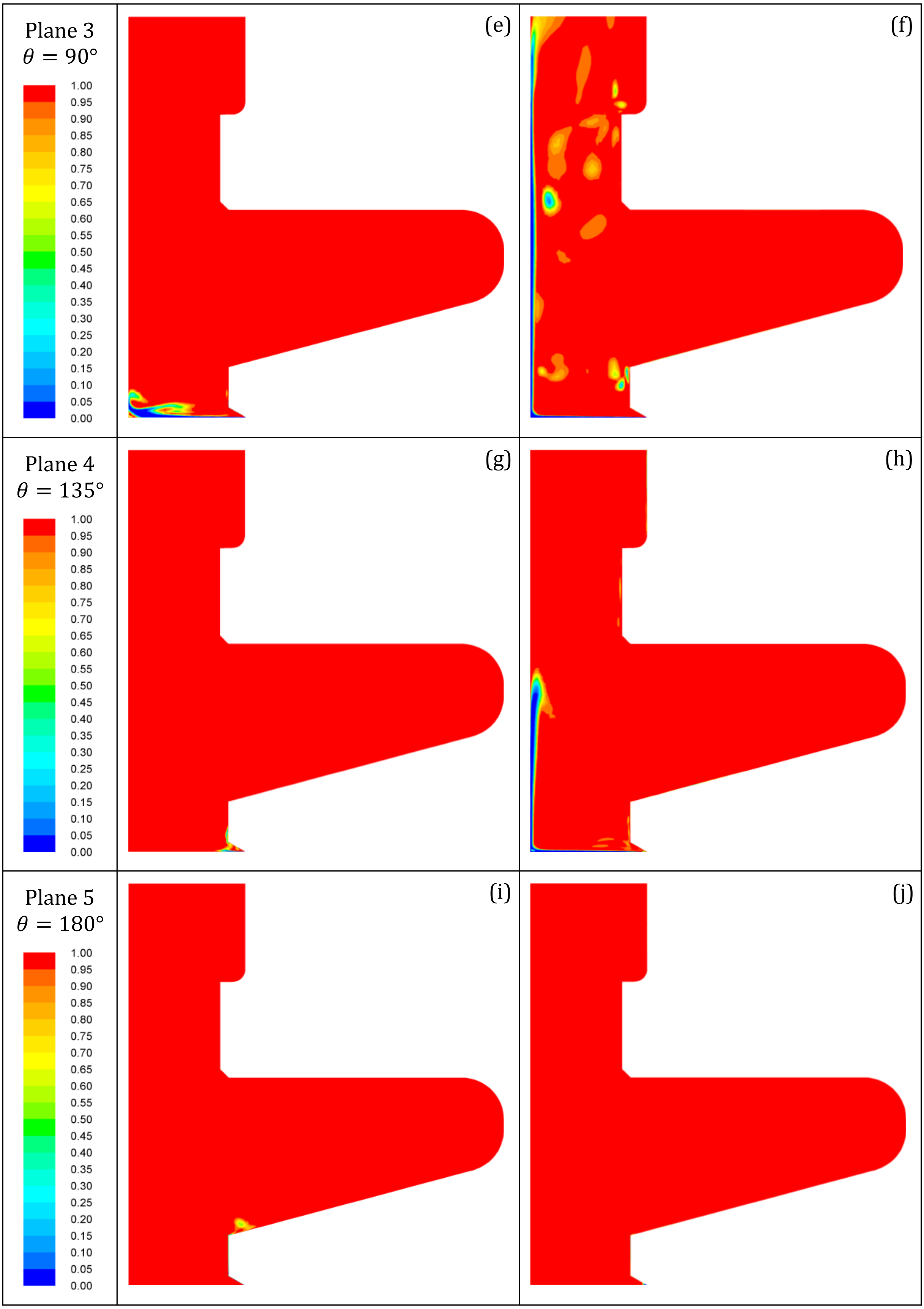

Plane 3
θ = 90°
1.00
0.95
0.90
0.85
0.80
0.75
0.70
0.65
0.60
0.55
0.50
0.45
0.40
0.35
0.30
0.25
0.20
0.15
0.10
0.05
0.00
(e)
(f)
Plane 4
θ = 135°
1.00
0.95
0.90
0.85
0.80
0.75
0.70
0.65
0.60
0.55
0.50
0.45
0.40
0.35
0.30
0.25
0.20
0.15
0.10
0.05
0.00
(g)
(h)
Plane 5
θ = 180°
1.00
0.95
0.90
0.85
0.80
0.75
0.70
0.65
0.60
0.55
0.50
0.45
0.40
0.35
0.30
0.25
0.20
0.15
0.10
0.05
0.00
(i)
(j)

In plane 1, i.e. $\theta = 0°$, at no point in time, oil will be entering into the external domain. However, as shown in Table 4.17 (a), a very thin film of oil has formed on the vertical face of the planet gear base after 0.4 planet gear rotations. This is due to the initially patched oil meniscus between the gear chamfer and the pin surface at the inlet into the external domain. The rotating motion of the gear causes the oil to rapidly attain a circumferential velocity component, u. The resultant centrifugal force drives the oil radially outwards along the gear contour where it causes wetting of the vertical face of the planet gear base. The 3D images provided in Table 4.18 demonstrate this more clearly.

In plane 2, i.e. $\theta = 45°$, oil outflow does occur with an axial velocity equal to 22% of the circumferential gear velocity at that radius, i.e. $v = 0.22\omega_G r_G$ (Figure 3.7). Compared to the maximum outflow velocity of $v = 0.44\omega_G r_G$, this is a moderate value. It is, however, sufficient to cause the oil to enter the external domain in the axial direction at any point in time. A comparison of the flow fields after 0.4 and 3.1 planet gear revolutions, respectively (Table 4.17 (c, d)), suggests that the oil film does not progress significantly in the axial direction over time. This is due to the highly three-dimensional nature of the oil outflow as the circumferential velocity component, u, carries the film out of plane 2 towards plane 3, i.e. $\theta = 90°$, in the direction of the planet gear rotation.

In plane 3, i.e. $\theta = 90°$, the magnitude of the axial oil outflow velocity into the external domain is close to its maximum value of $v = 0.44\omega_G r_G$. At any point in time, oil enters the external domain in the axial direction and forms a film on the pin, providing a sufficiently long period of time has elapsed. After 0.4 planet gear rotations, the oil film has reached the planet carrier and after 3.1 planet carrier rotations the film that is being formed on the planet carrier surface has almost progressed to the domain outlet. At this point in time, i.e. at $t = 0.0358$ s, the core of the domain contains noticeably more oil in the form of droplets. As the oil film at this angular position travels with a high axial velocity, v, secondary droplets are formed upon impact on the planet carrier.

In plane 4, i.e. $\theta = 135°$, compared to plane 3, the axial outflow velocity is reduced to 35% of the circumferential gear velocity, $\omega_G r_G$. The flow field behaviours after 0.4 and 3.1 planet gear revolutions, respectively, are similar compared to those observed in the previously assessed plane 3, i.e. $\theta = 90°$. Axial outflow prevails at any point in time. As v is lower, the oil film progresses over a shorter distance in the same elapsed flow time. Moreover, secondary droplet formation caused by the impact of the oil film on the planet carrier surface appears to be less compared the previous plane 3, i.e. $\theta = 90°$, where v was higher.

In plane 5, i.e. $\theta = 180°$, axial oil outflow no longer occurs as the view plane is well inside the cavitation region, which begins at $\theta = 166°$. After 0.4 planet gear revolutions, a thin intermittent oil film covers the vertical face of the planet gear base. This is due to oil being entrained from the initially patched oil meniscus between the planet gear chamfer and the pin surface. The oil film follows the gear contour and separates from the upper edge of the gear base (diameter d_2 in Figure 2.2, Table 4.17 (i)). As the oil film on the base of the planet gear is intermittent, it is not visible after 3.1 planet gear revolutions in this particular plane, i.e. $\theta = 180°$.

Due to cavitation, in the region between $166° \leq \theta \leq 38°$ no axial oil outflow occurs. The flow behaviour in this area of the domain is driven by the rotating motion of the planet gear. Oil which is picked up in the upstream region where outflow occurs, i.e. between $38° < \theta < 166°$, is carried along with the gear rotation in the circumferential direction. The assessment of the flow field behaviours in planes 1 to 5 showed that primarily axial outflow prevails for the conditions under investigation. For this reason, the amount of oil that is picked up by the rotating planet gear is small and only a thin intermittent oil film is formed on the vertical face of the planet gear base after 3.1 gear revolutions. Based on the investigations presented in section 4.1.4, it is anticipated that after a sufficiently long elapsed flow time, a thin but continuous oil film will cover the gear surfaces.

In order to show the three-dimensional nature of the oil outflow behaviour of a non-orbiting journal bearing with a convergent-divergent gap, this paragraph follows the same approach as previously chosen for the assessment of the oil outflow behaviour of an orbiting journal bearing with a constant lubricating gap height, h_0. Table 4.18 shows 3D images of the oil outflow behaviour after an elapsed flow time of $t = 0.0046$ s and $t = 0.0358$ s, respectively. At these points in time, 0.4 and 3.1 planet gear revolutions were completed. The chosen points in time are identical to those used for the 2D assessment of the oil outflow behaviour presented in Table 4.17. Figure 4.23 illustrates the view points from which the 3D images shown in Table 4.14 were created. The arrows shown in Figure 4.23 represent the direction of view chosen for the 3D images shown in Table 4.14. The observer's line of sight is in the x-y-plane and at the same level as the pin axis. With respect to the y-z-plane, the line of sight is angled by 45°.

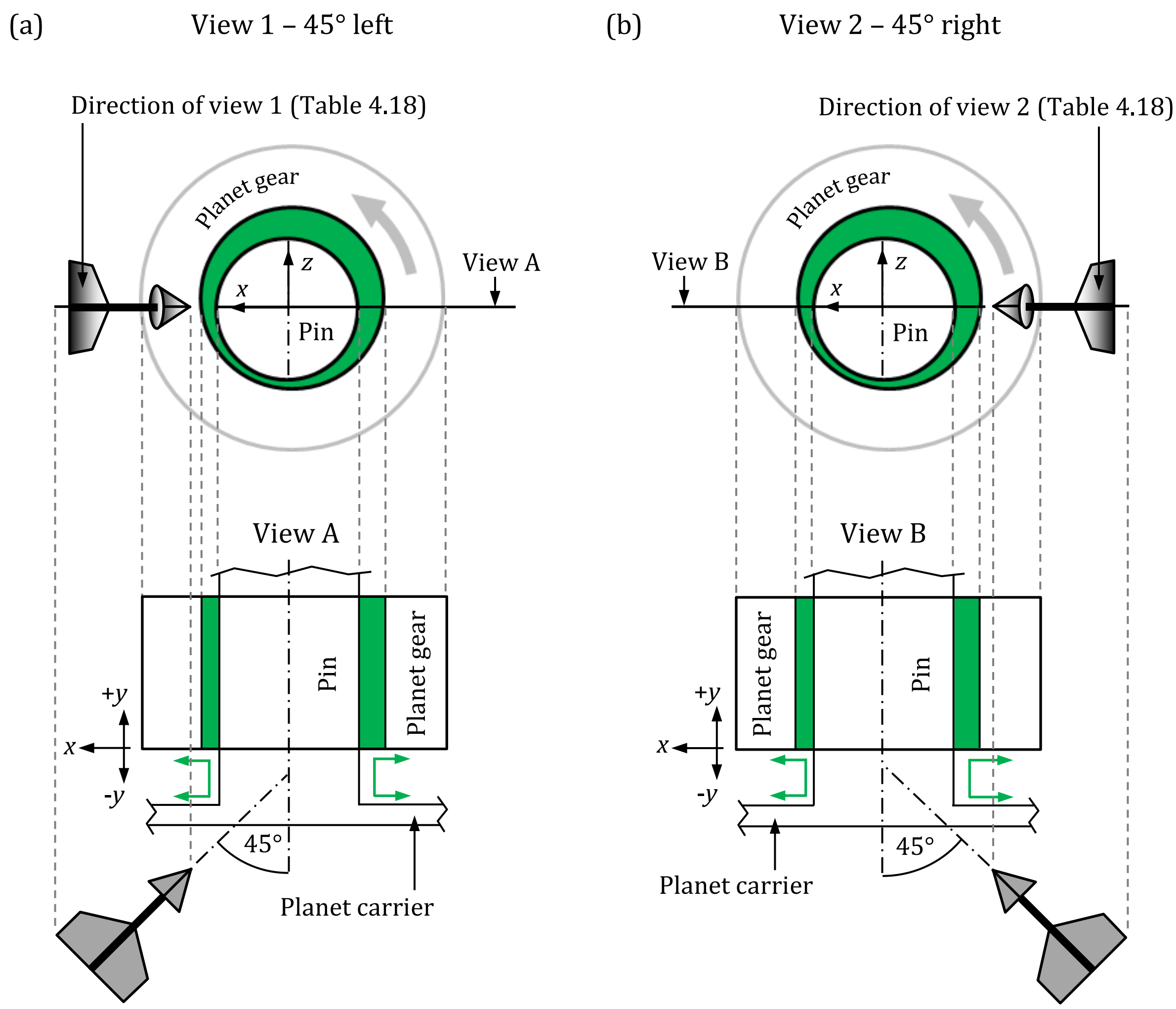

Figure 4.23: View point definition for 3D images shown in Table 4.18

In Table 4.18, the phase interface is visualised by an iso-surface that indicates 50% oil volume fraction. In order to enhance clarity, the iso-surface is coloured by the axial distance from the gear base, y. Consistent with the convention introduced in Figure 2.1, the bearing end-face, i.e. the point where the oil enters into the external domain, is located at $y = 0$ mm. The planet carrier surface is located at $y = -14$ mm. Thus, oil that is attached to the gear or in close vicinity to it, is shaded in a blue colour and oil that is attached to the planet carrier or in close vicinity to it, is shaded in a red colour.

Table 4.18: CFD model results for a non-orbiting journal bearing with a convergent-divergent gap height at maximum load conditions. Contours of 50% oil volume fraction coloured by axial distance, *y*.

View	$t = 0.0046$ s	$t = 0.0358$ s
View 1 45° left 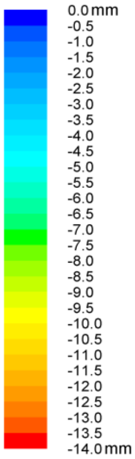	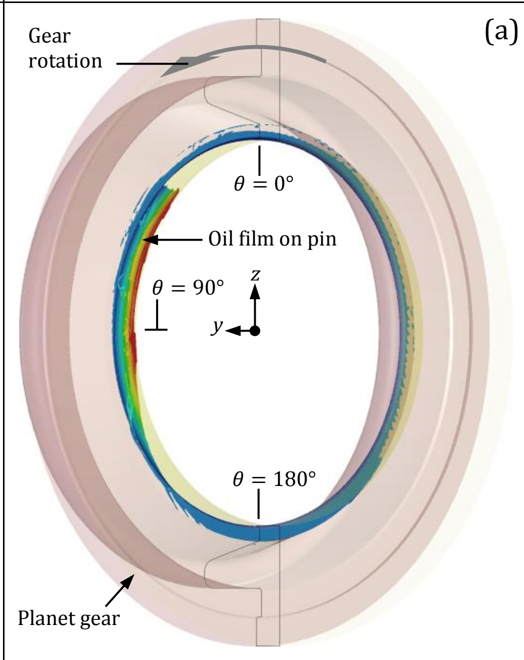	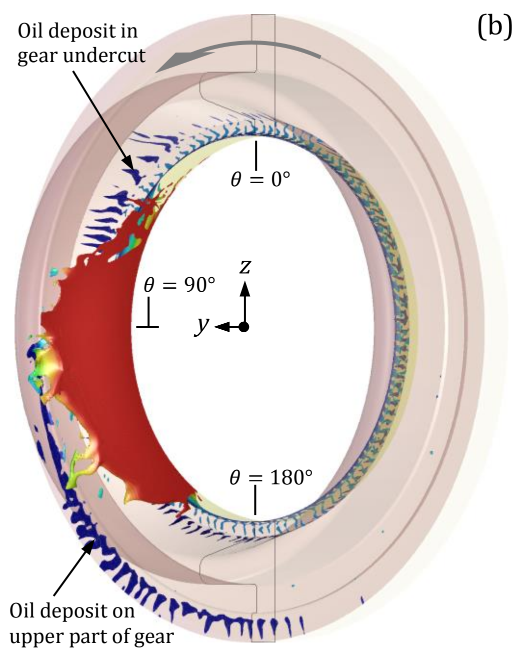
View 2 45° right 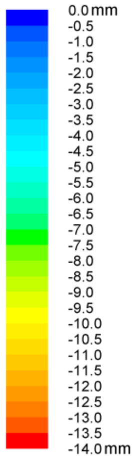	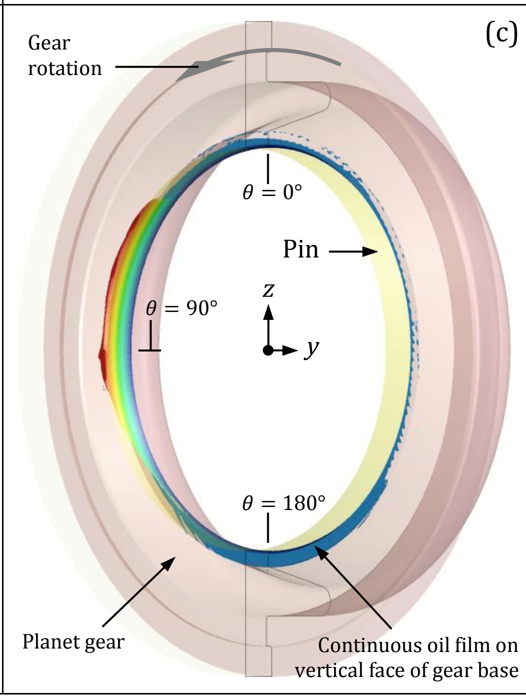	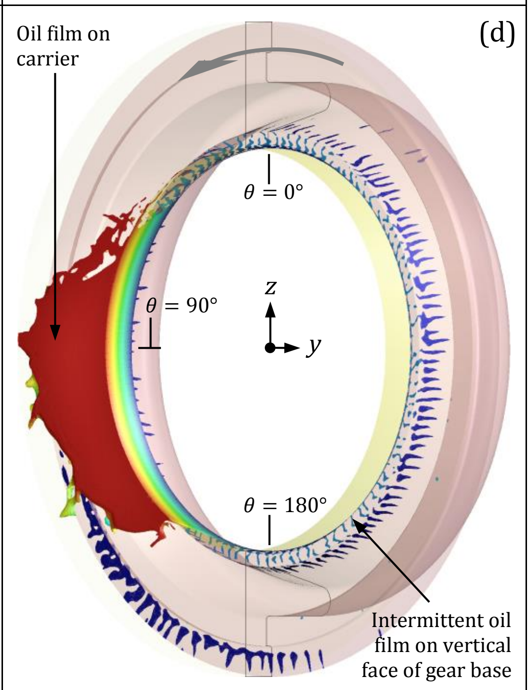

The 3D images provided in Table 4.18 show that outflow primarily occurs in the axial direction. In the region where outflow occurs, i.e. between $38° < \theta < 166°$, an oil film is formed on the pin. Once the oil film has reached the planet carrier, the oil is driven radially outwards with respect to the planet gear axis. This is caused by two different mechanisms. Firstly, when impinging on the planet carrier, some axial momentum is converted into a radial momentum component, and, secondly, the circumferential momentum component, which exists due to the swirling motion of the oil, creates a centrifugal force which forces the oil radially outwards. As the case under investigation does not account for the orbiting motion of the planet gear around the sun gear, no Coriolis effects occur.

After 0.4 planet gear rotations, i.e. an elapsed flow time of $t = 0.0046$ s, as shown in Table 4.18 (a, c), some radial oil outflow can be observed in the vicinity of the bottom dead centre location, i.e. $\theta \approx 180°$. As outflow does not occur in this region, any visible oil must originate from upstream locations where outflow does occur, i.e. $38° < \theta < 166°$. As previously discussed in section 3.5.1, the axial outflow velocity, v, varies continuously between $v = 0$ m/s and $v = 0.44\omega_G r_G$. Section 4.1.2 showed that the magnitude of v profoundly affects the outflow direction. Particularly for low values of v, which occur in the regions of $38° \lesssim \theta$ and $\theta \lesssim 166°$, respectively, radial oil outflow occurs. Moreover, it should be noted that initially, in transient conditions, radial oil outflow is likely to occur due to the radial acceleration of the patched oil meniscus between the gear chamfer and the pin surface (section 4.3.1).

After 3.1 gear rotations, i.e. an elapsed flow time of $t = 0.0358$ s, as shown in Table 4.18 (b, d), the continuous oil film on the vertical face of the gear base has been shed off. Only a thin intermittent oil film remains, which extends into the gear undercut. Oil that separates from the upper edge of the gear base (diameter d_2 in Figure 2.2) impacts on the upper part of the gear undercut, as shown in Table 4.18 (b). Sector analyses presented in section 4.1.4 have shown that after a sufficiently long elapsed flow time, t, initially intermittent areas of deposited oil will merge to form a continuous oil film. A similar behaviour is expected to prevail for the specific case under investigation.

4.3.3 Conclusions

From the analyses presented in section 4.3.2, the investigated case allows the following conclusions can be drawn.

a) Oil outflow occurs in a relatively small section of the journal bearing's circumference in the range $38° < \theta < 166°$.

b) Oil outflow occurs primarily in the axial direction. Some radial oil outflow can be observed due to natural liquid entrainment by the rotating planet gear.

c) The high outflow velocity of up to $v = 0.44\omega_G r_G$ causes significant secondary droplet formation when the oil film impacts on the planet carrier surface (Table 4.17 (e, f)).

d) Oil that is deposited in the gear undercut has the potential of creating imbalance forces acting on the planet gear (section 4.1.4).

4.4 Orbiting Journal Bearing with Convergent-Divergent Lubricating Gap Height

Oil outflow from an orbiting journal bearing with a convergent-divergent gap height was investigated at maximum load conditions to assess the additional effect of an orbiting motion on the outflow behaviour. At this last stage, the kinematic conditions of a journal bearing in an epicyclic gearbox in planetary configuration are fully resembled.

4.4.1 CFD Model Set-Up

The computational mesh used for the case under investigation was identical to that used for simulating the oil outflow behaviour of a non-orbiting journal bearing with a convergent-divergent gap height, h (section 4.3). This is permissible as in the planet carrier fixed frame of reference the bearing attitude, i.e. the location of the minimum gap height, h_{min}, relative to the bearing's circumference remains unchanged as the planet gear orbits around the sun gear (Figure 4.24).

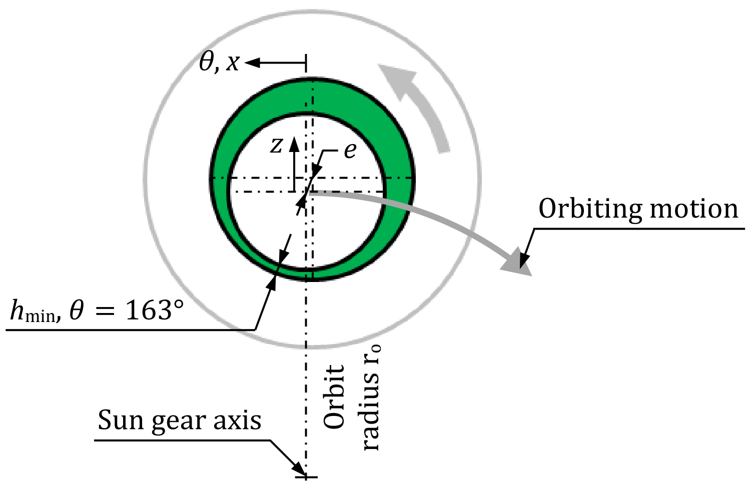

Figure 4.24: Bearing attitude at maximum load conditions

This is due to the fact that, in the planet carrier fixed frame of reference, the external forces, i.e. the gear teeth forces generated in the mesh between the planet gear and the ring gear, and between the planet gear and the sun gear, respectively, always act in the same location and the same direction relative to the planet gear. For completeness, key mesh parameters and properties are summarised in Table 4.19.

Table 4.19: Key mesh parameters and properties for CFD investigations of an orbiting journal bearing with convergent-divergent lubricating gap height

Mesh parameter	Value
Cell count in each 2D plane	9,849
Cell count in circumferential direction	1079 (1080 node points)
Total cell count in 360° mesh	10,627,071
Minimum gap height, $h_{\min}$	6 µm
Maximum gap height, $h_{\max}$	226 µm
Attitude angle, $\theta_{h,\,\min}$	163°
Number of cells across h	17 (18 node points)
Height of first cell perpendicular to wall	0.01 mm
Cell growth factor	1.1…1.4

The inlet boundary condition applied to the model is identical to the one used for simulating the oil outflow behaviour of a non-orbiting journal bearing with a convergent-divergent gap height (section 4.3). This is permissible as the inlet boundary condition was developed based on the assumption that, at the point where the oil emerges from the lubricating gap into the external domain, the flow can be described by the Reynolds equation. Thus, body forces, such as the centrifugal force generated by the planet carrier rotation, $F_{\mathrm{c,C}}$, can be neglected. The inlet boundary condition applied to the model is consistent with that described in section 3.5. A velocity inlet was used in order to prescribe the known axial (Poiseuille flow) and circumferential (Couette flow) flow velocity profiles and distributions directly at the inlet to the external flow domain ($y = 0$), as shown in sections 3.5.1 and 3.5.2, respectively. The UDFs used to describe the velocity profiles and velocity distributions are included in Appendix 4. Due to the convergent-divergent lubricating gap height, both the axial and the circumferential velocity profiles across the gap height are changing depending on circumferential position, θ, i.e. $u = f(z,\theta)$ and $v = f(z,\theta)$, respectively.

The considerations and investigations previously presented in section 4.1.6 concluded that patching an oil meniscus between the gear chamfer and the pin surface, as shown in Table 4.10 (e), provides the preferred initial wall condition. Thus, the model investigated in this section was set up to include a patched oil meniscus at the exit of the lubricating gap. The boundary condition types applied to all remaining domain surfaces are identical to those used for simulating the oil outflow behaviour of a non-orbiting journal bearing with a convergent-divergent gap height (section 4.3). For the particular case investigated in this section, the oil outflow behaviour is assessed at maximum load conditions. Key operational parameters are summarised in Table 4.20. A complete list of all boundary conditions and numerical settings is included in Appendix 7.

Table 4.20: Key operational parameters for maximum load conditions for CFD investigations of an orbiting journal bearing with convergent-divergent lubricating gap

Operational parameter	Value
Angular gear velocity relative to angular carrier velocity, ω_{G}	$\omega_{\mathrm{G,\,max\,load}}$
Angular carrier velocity, ω_{C}	$\omega_{\mathrm{C,\,max\,load}}$
Oil inlet mass flow rate, $\dot{m}_{\mathrm{in}}$	$\dot{m}_{\mathrm{in,\,max\,load}}$
Circumferential inlet velocity, u	$u = f(z, \theta)$
Axial inlet velocity, v	$v = f(z, \theta)$
Temperature, T	$T_{\mathrm{max\,load}}$

In order to simulate the orbiting motion of the planet gear around the sun gear, the angular velocity, $\omega_{\mathrm{C}} = \omega_{\mathrm{C,\,max\,load}}$, is applied to the planet carrier. In ANSYS Fluent [48], an orbiting motion can be achieved by enabling frame motion. For orbiting cases, the frame axis is shifted by the distance between the planet bearing axis and the sun gear axis. In an epicyclic gearbox in planetary configuration, with a fixed ring gear, the planet carrier and the planet gears rotate in opposite directions (Figure 4.24).

4.4.2 CFD Model Results

This section summarises the CFD model results for an orbiting journal bearing with a convergent-divergent lubricating gap height, h, at maximum load conditions (Table 4.20) after

1/8 and 1.0 planet carrier rotations, which are completed after an elapsed flow time of $t = 0.0046$ s and $t = 0.0358$ s, respectively. In the same period of time, the planet gear has completed 0.4 and 3.1 revolutions, respectively. The points in time at which the flow fields are being assessed are identical to those chosen for the orbiting journal bearing case with a constant lubricating gap height, h_0, (section 4.2.2) and the non-orbiting journal bearing case with a convergent-divergent gap height, h, (section 4.3.2) in order to allow a like-for-like comparison between the three cases.

Similar to an orbiting journal bearing with a constant lubricating gap height, h_0, (section 4.2.2), the resultant centrifugal force, F_{c}, varies around the planet gear's circumference as the centrifugal force generated by the planet gear rotation about its own axis, $F_{\mathrm{c,G}}$, is superimposed with the centrifugal force generated by the planet carrier rotation, $F_{\mathrm{c,C}}$. For completeness, for some selected angular locations, θ, the centrifugal forces acting on the oil at the point of entering into the external domain are schematically shown in Figure 4.25.

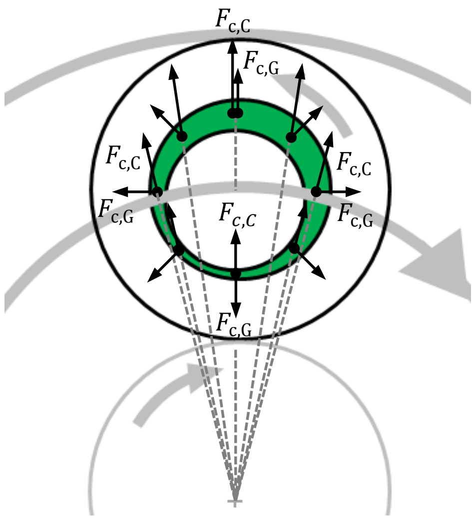

Figure 4.25: Schematic of the directions of the centrifugal forces, $F_{\mathrm{c,C}}$ and $F_{\mathrm{c,G}}$, acting on the oil film as it enters into the external flow domain of an orbiting journal bearing with a convergent-divergent lubricating gap height

As previously discussed in section 3.5 and section 4.3.2, for a journal bearing with a convergent-divergent lubricating gap height, the oil outflow velocity into the external domain varies depending on the radial coordinate across the gap height, z, and the circumferential location, θ. Due to the internal journal bearing film pressure distribution, at maximum load conditions, oil outflow only occurs in the region between $38° < \theta < 166°$ (section 3.5). It is therefore practical to assess the flow field behaviour at same key angular locations, θ, as previously used for the non-orbiting journal bearing case with a convergent-divergent lubricating gap height (section 4.3.2). For completeness, Figure 4.22 is repeated below to define the planes in which the flow field behaviour will be assessed (Figure 4.26).

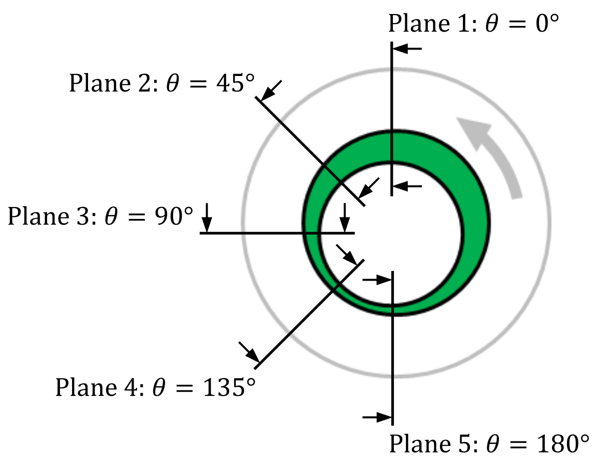

Figure 4.26: Definition of viewing planes for flow field assessment

Table 4.21 shows the air volume fraction contour plot for the planes defined in Figure 4.26 after 1/8 ($t = 0.0046$ s) and 1.0 ($t = 0.0358$ s) planet carrier rotations, respectively.

Table 4.21: CFD model results of an orbiting journal bearing with a convergent-divergent lubricating gap height at maximum load conditions. Contours of air volume fractions.

	$t = 0.0046$ s	$t = 0.0358$ s
Plane 1 $\theta = 0°$ 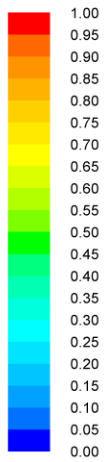	(a) 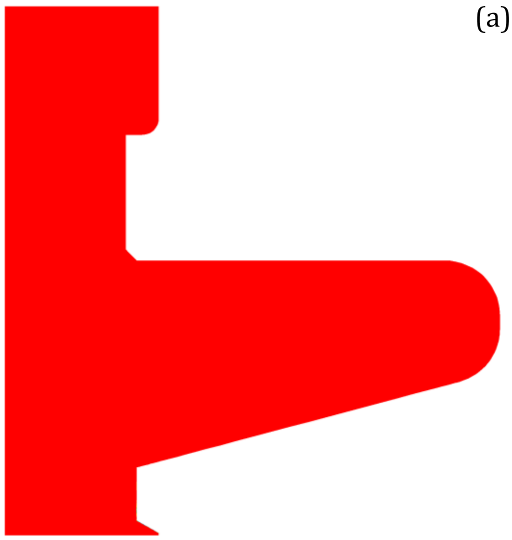	(b) 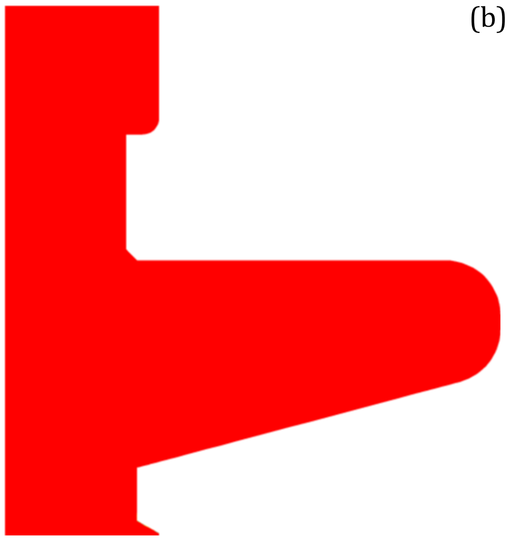

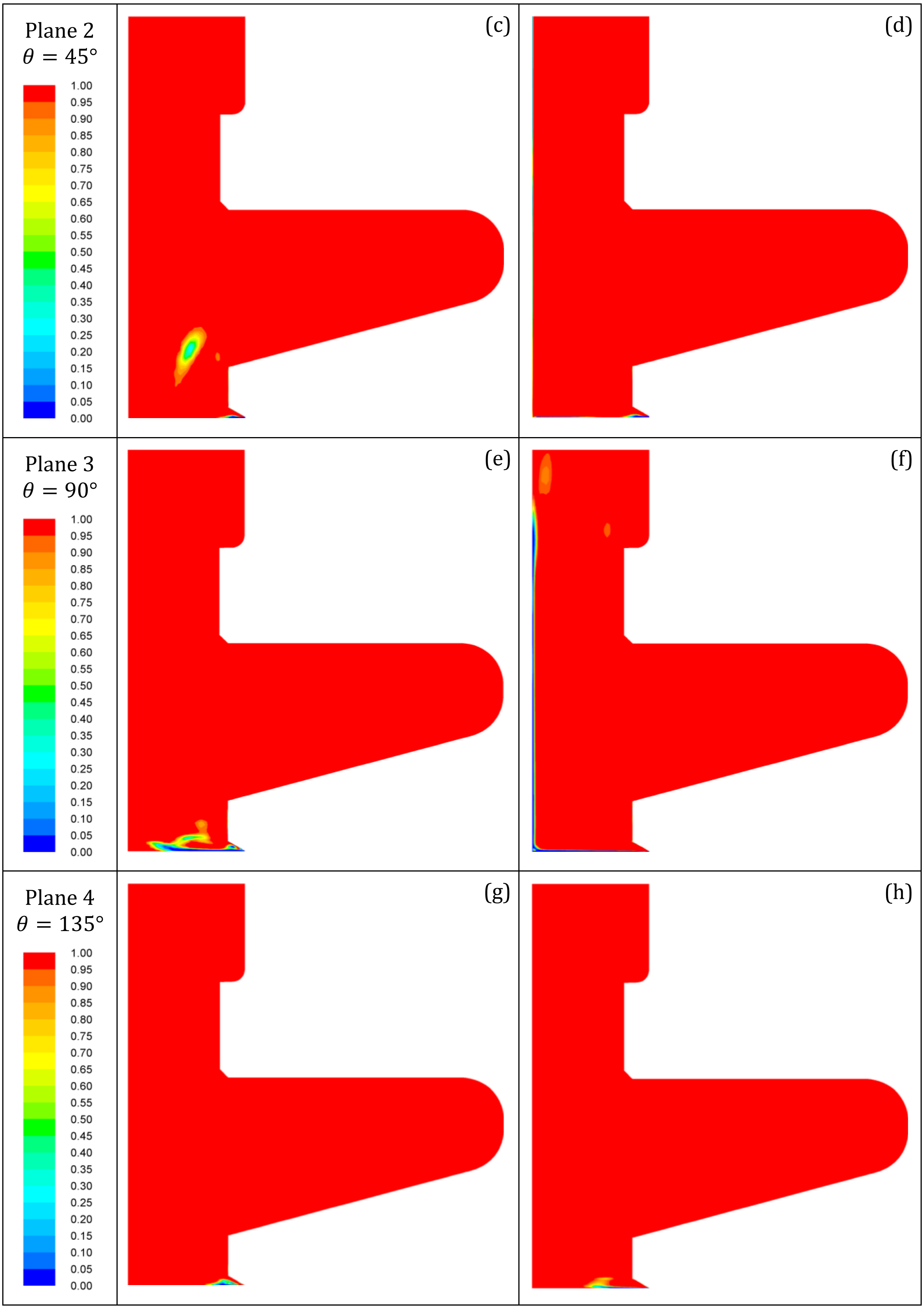
Plane 2
$\theta = 45°$
1.00 0.95 0.90 0.85 0.80 0.75 0.70 0.65 0.60 0.55 0.50 0.45 0.40 0.35 0.30 0.25 0.20 0.15 0.10 0.05 0.00
(c)
(d)
Plane 3
$\theta = 90°$
1.00 0.95 0.90 0.85 0.80 0.75 0.70 0.65 0.60 0.55 0.50 0.45 0.40 0.35 0.30 0.25 0.20 0.15 0.10 0.05 0.00
(e)
(f)
Plane 4
$\theta = 135°$
1.00 0.95 0.90 0.85 0.80 0.75 0.70 0.65 0.60 0.55 0.50 0.45 0.40 0.35 0.30 0.25 0.20 0.15 0.10 0.05 0.00
(g)
(h)

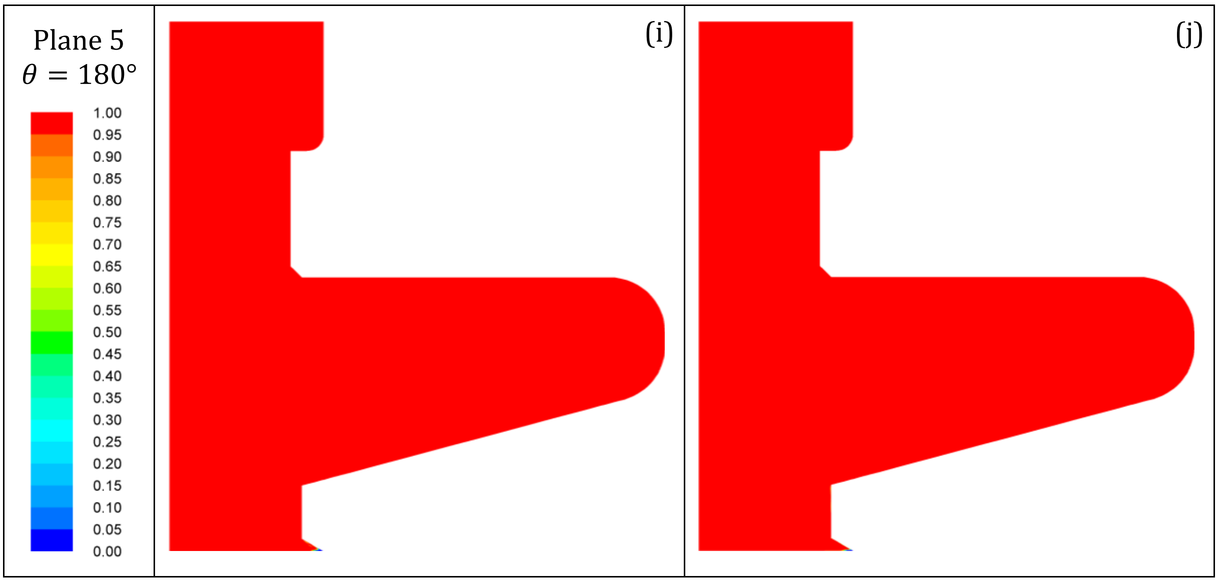

In general, the flow field behaviour observed in view planes 1 to 5, i.e. $0° \leq \theta \leq 180°$, is similar to that of the non-orbiting journal bearing case with a convergent-divergent gap height, h (section 4.3.2). Primarily, axial oil outflow prevails. However, some radial oil outflow occurs due to the following three different mechanisms.

a) Oil entrainment by the rotating planet gear from the oil film covering the pin
b) Temporary oil entrainment by the rotating planet gear from the initially patched oil meniscus between the gear chamfer and the pin surface (Table 4.10 (e))
c) Radial oil outflow at low axial velocities, v (section 4.1.2).

Any differences observed between the case under investigation and the non-orbiting journal bearing case with a convergent-divergent lubricating gap height, h, are caused by the centrifugal force, $F_{c,C}$, which is generated by the planet carrier motion.

In view plane 1, i.e. $\theta = 0°$, at no point in time oil will be entering into the external domain. However, as shown in Table 4.21 (a), a very thin oil film has formed on the vertical face of the planet gear base after 0.4 planet gear rotations. The observed flow behaviour is very similar compared to that previously described for the non-orbiting journal bearing case with a convergent-divergent lubricating gap height, h (section 4.3). The 3D images provided in Table 4.22 show this more clearly. Over time, as shown in Table 4.21 (b), this oil film progresses radially outwards along the vertical face of the planet gear base and separates from the upper edge of the gear base (diameter d_2 in Figure 2.2). As oil is shed from this edge, the film becomes intermittent (Table 4.22 (b)).

In plane 2, i.e. $\theta = 45°$, oil outflow does occur with an axial velocity of $v = 0.22\omega_G r_G$ (Figure 3.7). This is sufficient to cause the oil to enter the external domain in the axial direction at any point in time. Very similar to the observations made for the non-orbiting journal bearing case with a convergent-divergent lubricating gap height, h, over time, the oil film does not significantly progress in the axial direction. This is due to the highly three-dimensional nature of the oil outflow as the circumferential velocity component, u, carries the film out of plane 2 towards plane 3, i.e. $\theta = 90°$, in the direction of the planet gear rotation. After one full planet carrier rotation, i.e. 3.1 planet gear rotations, a thin oil film can be observed on the upper part of the planet carrier and the pin surface. Both films are caused by oil which enters into the external flow domain downstream of plane 2, i.e. at angular locations of $\theta > 45°$. Due to the centrifugal force generated by the planet carrier rotation, $F_{\mathrm{c,C}}$, oil from downstream locations is driven radially outwards with respect to the planet carrier axis and flows along the pin surface against the direction of the planet gear rotation.

In plane 3, i.e. $\theta = 90°$, at any point in time, oil enters into the external domain in the axial direction. The magnitude of the axial oil outflow velocity into the external domain is close to its maximum value of $v = 0.44\omega_{\mathrm{G}}r_{\mathrm{G}}$. After a sufficiently long period of time has elapsed, an oil film has formed on the pin and on the planet carrier. Compared to the flow behaviour previously observed for the non-orbiting journal bearing case with a convergent-divergent gap height, h, the oil inside the external domain appears less dispersed. Instead, the oil film is more continuous and homogeneous.

In plane 4, i.e. $\theta = 135°$, compared to plane 3, the axial outflow velocity is reduced to $v = 0.35\omega_{\mathrm{G}}r_{\mathrm{G}}$. The flow field behaviour compared that observed for the non-orbiting journal bearing case with a convergent-divergent gap height, h, is noticeably different. Although oil enters into the external domain in the axial direction at any point in time, the oil film travelling across the pin surface is unable to reach the planet carrier surface. As previously highlighted when assessing the flow field behaviour in plane 2, i.e. $\theta = 45°$, the swirling motion of the oil as it exits the lubricating gap height, and the additional centrifugal force generated by the planet carrier rotation, $F_{\mathrm{c,C}}$, result in highly three-dimensional effects. When travelling across the pin surface, the oil film loses circumferential momentum due to friction between the liquid and the wall, and due to $F_{\mathrm{c,C}}$ acting on the film. In fact, $F_{\mathrm{c,C}}$ is sufficiently large to reverse the direction of swirl of the oil film on the pin before it reaches the planet carrier surface. In Table 4.21 (h), the oil film front swirls against the direction of the planet gear rotation. Thus, the oil film is carried out of plane 4 towards view plane 3, $\theta = 90°$.

In plane 5, i.e. $\theta = 180°$, oil outflow no longer occurs as the view plane is well inside the cavitation region, which begins at $\theta = 166°$. A very small amount of oil is visible at the exit of the lubricating gap between the planet gear chamfer and the pin surface. This oil originates from the initially patched oil meniscus in this location.

In order to show the three-dimensional nature of the oil outflow behaviour of an orbiting journal bearing with a convergent-divergent gap, h, this paragraph follows the same approach as previously chosen for the assessment of the oil outflow behaviours from a journal bearing with a constant lubricating gap height, h_0 (section 4.2.2) and from a non-orbiting journal bearing with a convergent-divergent gap height, h (section 4.3.2). Table 4.22 shows 3D images of the oil outflow conditions after an elapsed flow time of $t = 0.0046$ s and $t = 0.0358$ s, respectively. At these points in time, the planet carrier completed 1/8 and 1.0 revolutions, respectively. Accordingly, the planet gear rotated about its own axis 0.4 and 3.1 times, respectively. The chosen points in time are consistent with those used for the 2D assessment of the oil outflow behaviour presented in Table 4.21. Figure 4.27 illustrates the view points from which the 3D images shown in Table 4.22 were created.

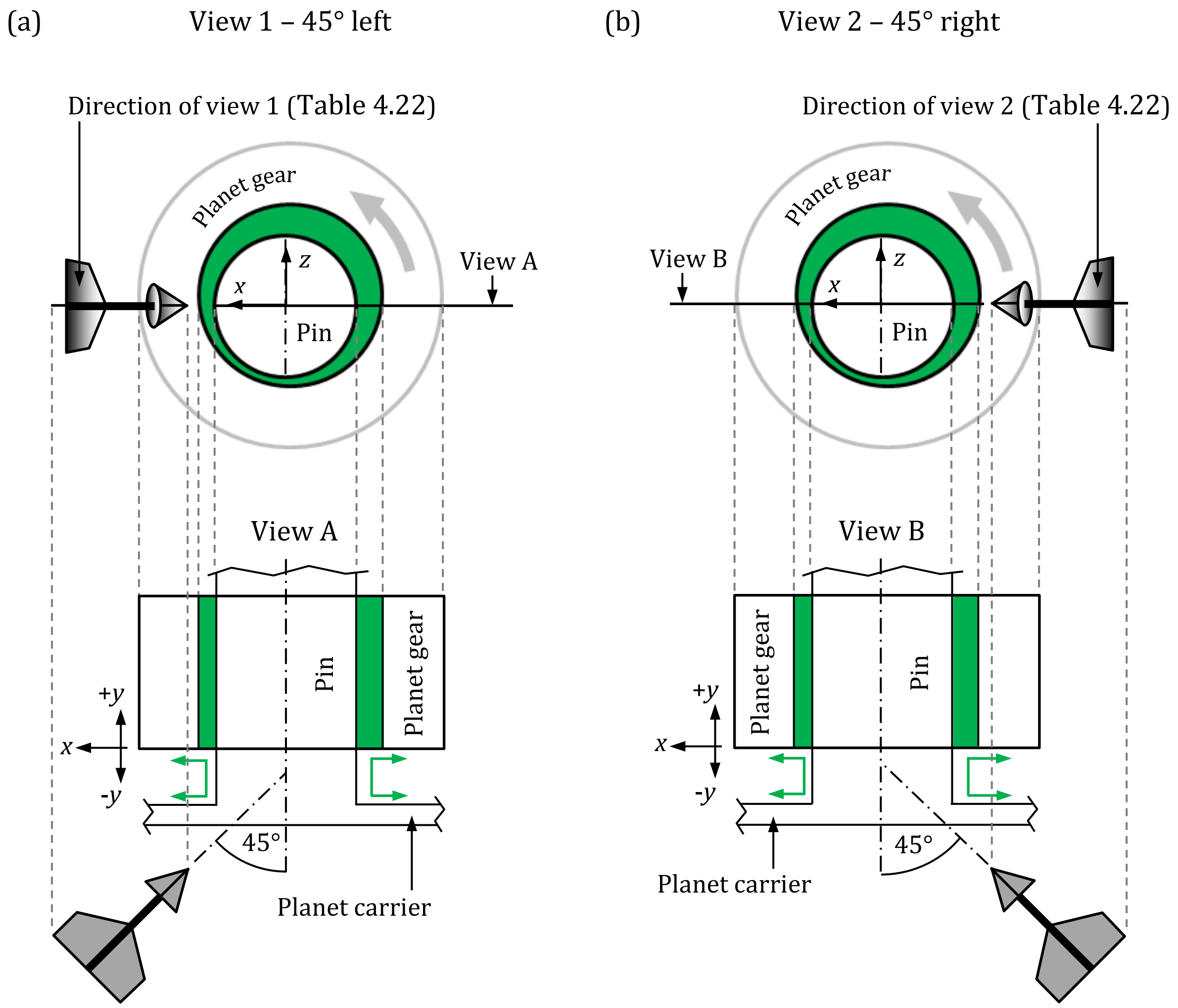

Figure 4.27: View point definition for 3D images shown in Table 4.22

The arrows shown in Figure 4.27 represent the direction of view chosen for the 3D images shown in Table 4.22. The observer's line of sight is in the x-y-plane and at the same level as the pin axis. With respect to the y-z-plane, the line of sight is angled by 45°.

In Table 4.22, the phase interface is visualised by an iso-surface that indicates 50% oil volume fraction. In order to enhance clarity, the iso-surface is coloured by the axial distance from the gear base, y.

Table 4.22: CFD model results for an orbiting journal bearing with a convergent-divergent gap height at maximum load conditions. Contours of 50% oil volume fraction coloured by axial position, y.

View	$t = 0.0046$ s	$t = 0.0358$ s
View 1 45° left 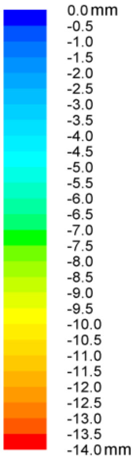	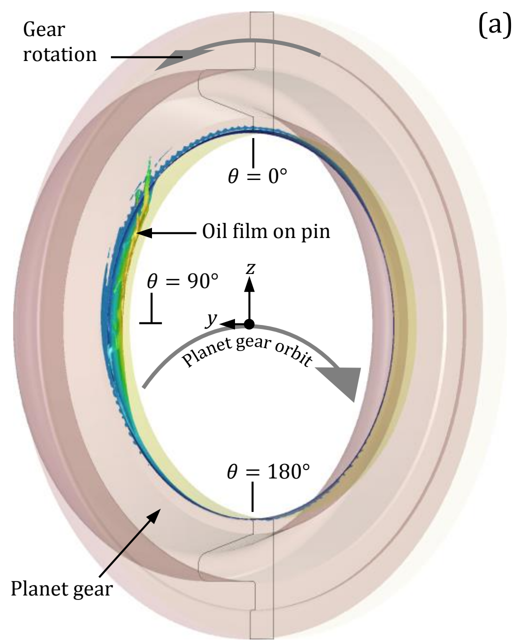	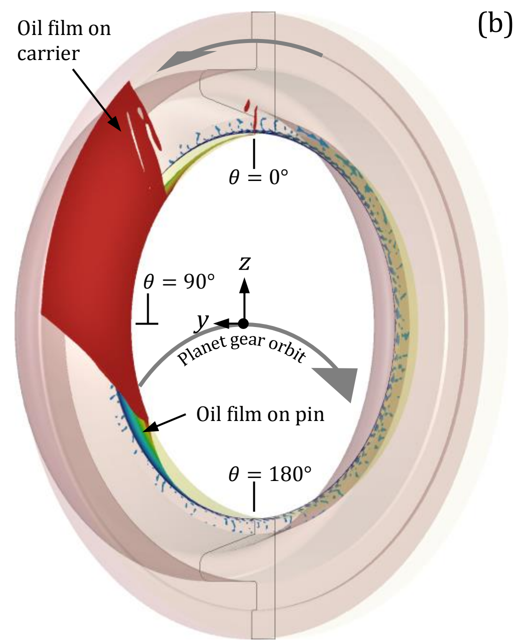
View 2 45° right 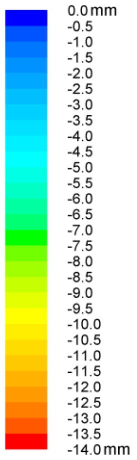	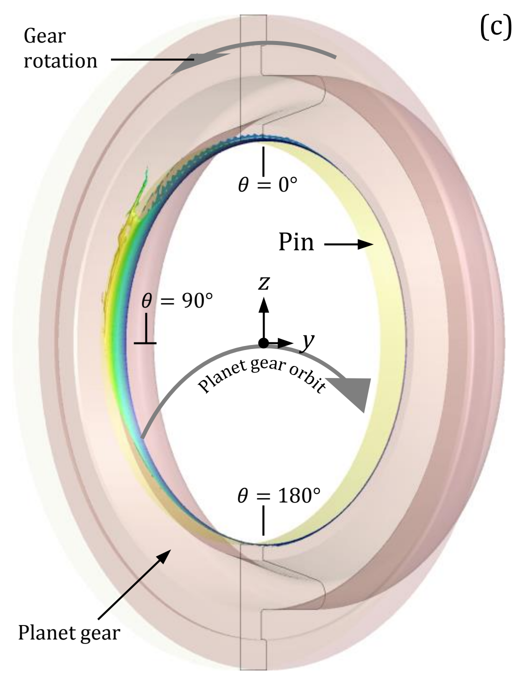	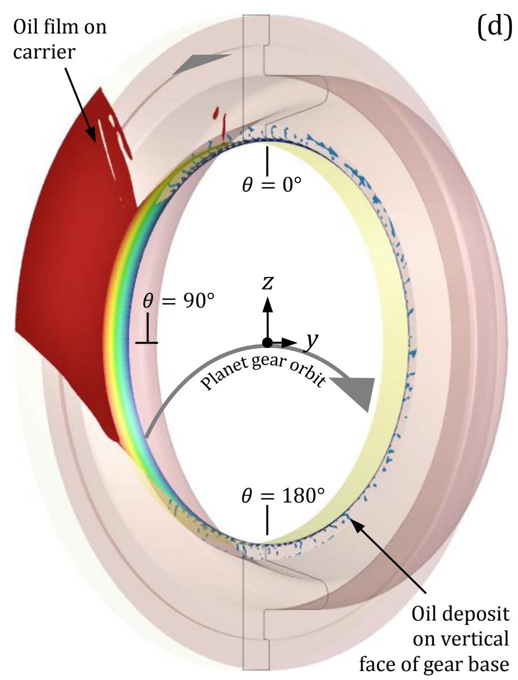

Consistent with the convention introduced in Figure 2.1, the bearing end-face, i.e. the point where the oil enters into the external domain, is located at $y = 0$ mm. The planet carrier surface is located at $y = -14$ mm. Thus, oil that is attached to the gear or in close vicinity to it, is shaded in a blue colour and oil that is attached to the planet carrier or in close vicinity to it, is shaded in a red colour.

The 3D images provided in Table 4.22 show that outflow primarily occurs in the axial direction. This is similar to the flow path direction observed for the non-orbiting journal bearing case with a convergent-divergent gap height, h. In the region where outflow occurs, i.e. between $38° < \theta < 166°$, an oil film is formed on the pin. Once the oil film has reached the planet carrier, the oil is driven radially outwards with respect to the planet carrier axis. Some of the mechanisms which cause this behaviour have previously been discussed in section 4.3.2. Due to the orbiting motion of the planet carrier and the associated additional centrifugal force, $F_{c,C}$, additional mechanisms occur, all of which are summarised below.

a) When impinging on the planet carrier, some axial momentum of the oil is converted into a radial momentum component.
b) The oil momentum in the circumferential direction, which exists due to its swirling motion, creates a centrifugal force which forces the oil radially outwards.
c) The centrifugal force generated by the planet carrier motion drives the oil radially outwards with respect to the planet carrier axis.

In addition, as previously noted when assessing the outflow behaviour of an orbiting journal bearing with a constant lubricating gap height, h_0 (section 4.2.2), a Coriolis effect is present as the outflow behaviour is analysed in the planet carrier fixed frame of reference. The area which is covered by the oil film on the planet carrier surface, after an elapsed flow time of $t = 0.0358$ s, i.e. 3.1 planet gear rotations, is noticeably different compared to that of the non-orbiting journal bearing case with a convergent-divergent gap height, h. This is caused by the centrifugal force generated by the planet carrier motion, $F_{c,C}$. It is sufficiently large to reverse the circumferential velocity component of the oil with respect to the planet gear axis. Whilst the oil swirls in the same direction as the rotation of the planet gear at the point where it enters into the external domain, on the planet carrier, it has a circumferential velocity component, which points in the opposite direction.

The images provided in Table 4.22 (a, c) show that after 0.4 planet gear rotations, i.e. an elapsed flow time of $t = 0.0046$ s, some radial oil outflow can be observed in the vicinity of the top dead centre location, i.e. $\theta \approx 0°$. Thus, a thin oil film is formed on the vertical face of the planet gear base. Some radial oil outflow in the vicinity of the bottom dead centre location was previously observed for the non-orbiting journal bearing case with a convergent-divergent gap height, h (section 4.3.2). The shift of the location of the radial oil outflow from bottom to top dead centre can be explained by the additional centrifugal force, $F_{c,C}$, which is generated by the planet carrier rotation. For a given rotational speed of the planet gear, radial oil outflow is promoted through low axial outflow velocities (section 4.1.2) and high radial forces with respect to the planet carrier axis. Moreover, it should be noted that initially, in transient conditions, radial oil outflow is likely to occur due to the radial acceleration of the patched oil meniscus between the gear chamfer and the pin surface (section 4.3.1). As previously discussed in section 4.3.2, visible oil in the region that does not exhibit oil outflow, i.e. $166° \leq \theta \leq 38°$, must originate from the region that does exhibit oil outflow, i.e. $38° < \theta < 166°$. Oil transport occurs due to the rotating motion of the planet gear and the associated momentum transfer into the oil, and due to the centrifugal forces, $F_{c,G}$ and $F_{c,C}$, respectively.

After 3.1 planet gear rotations, i.e. an elapsed flow time of $t = 0.0358$ s, as shown in Table 4.22 (b, d), the very continuous and homogeneous oil film on the planet carrier has reached the outlet of the domain. Oil that was initially attached to the vertical face of the planet gear base has been shed off. Only small patches of deposited oil remain. In contrast to the non-orbiting journal bearing case with a convergent-divergent gap height, h (section 4.3.2), these oil patches do not extend into the gear undercut. Moreover, there is no evidence of oil impacting on the upper part of the gear undercut.

4.4.3 Conclusions

From the analyses presented in section 4.4.2, the investigated case allows the following conclusions can be drawn.

a) Oil outflow occurs in a relatively small section of the journal bearing's circumference in the range $38° < \theta < 166°$.
b) Oil outflow occurs primarily in the axial direction. Some radial oil outflow can be observed due to natural liquid entrainment by the rotating planet gear.
c) The oil in the external domain appears to be less dispersed compared to the non-orbiting journal bearing case with a convergent-divergent gap height, h (section 4.3.2).
d) There is no evidence of oil deposit in the gear undercut and in the upper part of the gear.

5 Experimental Flow Investigations

In the previous chapter, oil outflow from a journal bearing in an epicyclic gearbox was investigated computationally. In order to create a fundamental understanding about the mechanisms affecting the oil outflow behaviour, a step-wise approach was followed. This included the analyses of four CFD models, namely a non-orbiting journal bearing model with a constant lubricating gap height (section 4.1), an orbiting journal bearing model with a constant lubricating gap height (section 4.2), a non-orbiting journal bearing model with a convergent-divergent lubricating gap height (section 4.3), and an orbiting journal bearing model with a convergent-divergent lubricating gap height (section 4.4). Whilst the first model was a simplified representation, the latter fully resembled the kinematic conditions of an actual journal bearing in an epicyclic gearbox in planetary configuration.

A rig test programme was planned and performed to experimentally investigate the external oil flow behaviour of a full-scale, non-orbiting journal bearing with a constant lubricating gap height, h_0. This simplified set-up was chosen for the following reasons.

a) A simplified set-up allows key fundamental flow physics to be observed and analysed.

b) Experimental investigations on an orbiting journal bearing would require a substantial support structure to bear the loads generated by the orbiting motion. The available budget, resources, timescales and test cell space were insufficient for such a facility to be designed and built.

c) Flow visualisation on an orbiting journal bearing is extremely challenging due to the bearing's kinematics and due to load-bearing structures, which may obstruct camera access.

The objectives of the experimental flow investigations were as follows.

a) Assess the effect of a variation of key geometrical and operational rig parameters, namely the lubricating gap height, h_0, the angular velocity of the gear representation, ω_G, the volumetric oil flow rate, $\dot{V}_{in}$, and the dynamic oil viscosity, μ, on the flow field behaviour.

b) Confirm the occurrence of axial and radial oil outflow depending on the journal bearing's operational parameters.
c) Identify the conditions for which axial and radial oil outflow, respectively, prevail.
d) Assess prevailing flow regimes and compare them to those observed on rotating cups and discs.
e) Qualitatively validate the CFD model results presented in chapter 4 (section 4.1).

Section 5.1 provides details about the facility set-up, including explanations about the different rig subsystems. Section 5.2 describes the test module, which is part of the rig facility, and which contains the actual test article. In section 5.3, an overview of all test parameters and their range of variation is provided. The approaches used to design the experiment, the test schedule and the test procedure are detailed in section 5.4. The experimental results were analysed with respect to the prevailing flow regime, the outflow direction, i.e. radial or axial and radial outflow, and the flow temperatures. A discussion is presented in sections 5.5 to 5.7. Section 5.8 summarises key findings and conclusions from the experimental campaign.

5.1 Facility Set-Up

The rig facility consists of five subsystems, all of which are explained in detail in the following paragraphs. A process flow diagram is shown in Figure 5.1.

a) **Supervisory Control and Data Acquisition (SCADA) System.** The SCADA system monitors and controls all facility systems, e.g. opening and closing of valves, regulating speeds and activating pumps, to ensure the correct and safe operation of the facility.
b) **Facility Drive System (FDS).** The FDS consists of a direct current (DC) electric motor which is connected to a 4:1 step-up gearbox. A short quill shaft provides drive from the gearbox output to the main shaft, which is supported at the rear by a grease-packed angular contact ball bearing and at the front by an oil-lubricated roller bearing. Gearbox output torque and speed are measured by an in-line flange-mounted torque transducer. For the unit under test (UUT), i.e. the journal bearing module, the maximum rotational speed is limited to 6,000 rpm for safety reasons.
c) **Facility Oil System (FOS), including oil supply and oil scavenge.** The FOS supplies the FDS with cooling and lubrication oil. It comprises an oil tank, a variable displacement pump and a feed manifold. The pump is configured to maintain a pressure of 20 bar at the manifold up to a total volumetric flow rate of $\dot{V}_{\mathrm{in}} = 20\ \mathrm{l/min}$. The manifold oil

temperature is regulated to a fixed value of $T_{\mathrm{man}} = 40°\mathrm{C}$. The feed manifold has four independent offtakes, two of which are in use:

- Feed 1: Supply to the facility drive gearbox.
- Feed 2: Supply to the facility drive rear bearing.

The SCADA system monitors the feed pressure on both feed lines. If pressure values reach levels at which the operation of the rig becomes unsafe, the facility is shut down automatically. Note that the FOS is not shown in Figure 5.1, as it is fully system-controlled and no operator inputs are required.

d) **Unit Under Test (UUT) Oil System.** The UUT oil system supplies oil to the journal bearing module. It comprises an oil tank, a variable displacement pump, a feed manifold, a return manifold and a cooler. The feed pump is configured to maintain a pre-set pressure at the feed manifold up to a total pre-set volumetric flow rate, $\dot{V}_{\mathrm{in}}$. Through an oil flow meter and a flow control valve, $\dot{V}_{\mathrm{in}}$ can be varied between one and 160 l/min. The oil temperature of the UUT feed manifold is regulated to a temperature set by the operator. It may be varied between ambient and 80°C.

The UUT oil feed system provides four independently controlled oil feeds to the UUT. Each feed line comprises a flow meter and a pressure transducer, providing feedback to a process controller. Moreover, a pneumatic ball valve is fitted to each feed line for isolation, if required. The controllable volumetric flow rate for each feed line, $\dot{V}_{\mathrm{in}}$, ranges from one to 45 l/min. For the operation of the journal bearing test module, only one of the four feed lines is active.

The UUT oil scavenge system removes the oil from the UUT and comprises a 170 l/min progressive cavity scavenge pump. The volumetric flow rate of this pump, $\dot{V}_{\mathrm{out}}$, is derived automatically from the measured feed flow rate, $\dot{V}_{\mathrm{in}}$, and the requested scavenge ratio. During continuous operation, a scavenge ratio of 1.5 was used. The SCADA system automatically synchronises the operation of the scavenge pump with the UUT oil feed system.

e) **Test module (UUT).** The test module consists of a static cylinder and a rotating planet gear representation contained within a static outer chamber made from Perspex. The chamber is vented to atmosphere via a filter and notionally runs at ambient pressure. The test model is described in detail in section 5.2.

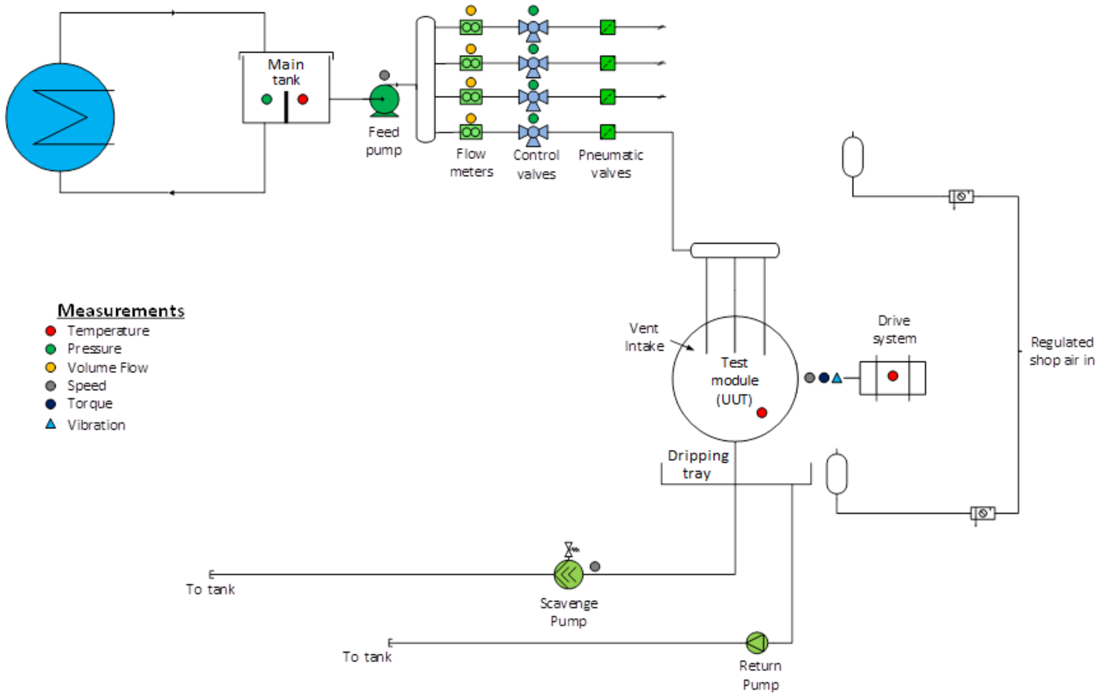

Figure 5.1: Rig process flow diagram

As part of the University of Nottingham's health and safety regulations a safe operating procedure (SOP) [80] was written for the facility and the test module, which captures more technical detail and operational processes.

5.2 Test Module Set-Up

In order to meet the objectives for the experimental test campaign, the rig was designed with best possible visual access to capture photographic and videographic footage of the oil flow behaviour.

Whilst operational parameters, such as the angular velocity of the planet gear representation, ω_{G}, the volumetric oil flow rate, $\dot{V}_{\mathrm{in}}$, and the main tank oil temperature, T_{T}, can easily be adjusted by the operator through the SCADA system, a variation of geometrical parameters, i.e. the lubricating gap height, h_0, requires a hardware change of the planet gear representation (Figure 5.2). The test module design allowed hardware to be changed within one day. Three different planet gear representations were manufactured. Their internal diameters were ground to different nominal dimensions. As the journal representation (Figure 5.2) remained unchanged, this lead to lubricating gap heights of $h_0 = 55.5$ µm, $h_0 = 125.0$ µm and $h_0 = 223.5$ µm.

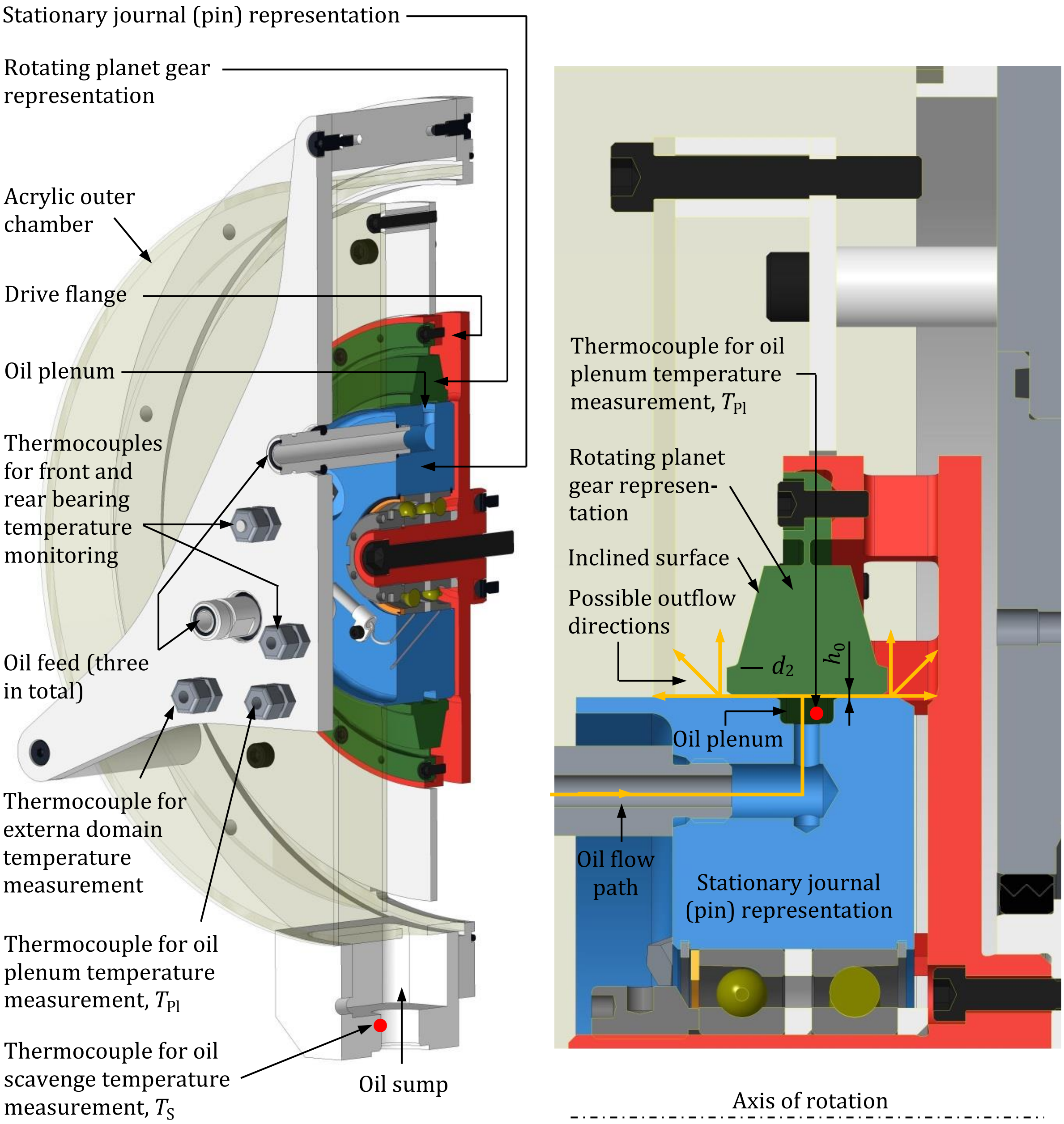

Figure 5.2: General arrangement of test module

As shown in Figure 5.2, the test module is supplied with oil via three feed lines, which are equally spaced around the circumference. The oil fills a circumferential groove, also known as the plenum, which allows the oil to distribute evenly. A temperature measurement, T_{Pl}, is taken at this location. This will later be referred to as the oil inlet temperature of the external flow domain. From the plenum, the oil is squeezed through the lubricating gap into the external domain. In order to balance the forces generated by the oil pressure and the exiting oil, the planet gear representation was designed symmetrical to its vertical axis. The supplied oil splits evenly into a portion exiting towards the front and towards the rear of the test module.

The recess, which forms the transition between the upper edge of the gear base (diameter d_2 in Figure 5.2) and the inclined surface of the planet gear representation (Figure 5.2), was designed to force oil separation at that particular point. Images of the actual test module with and without visualisation equipment are shown in Figure 5.3.

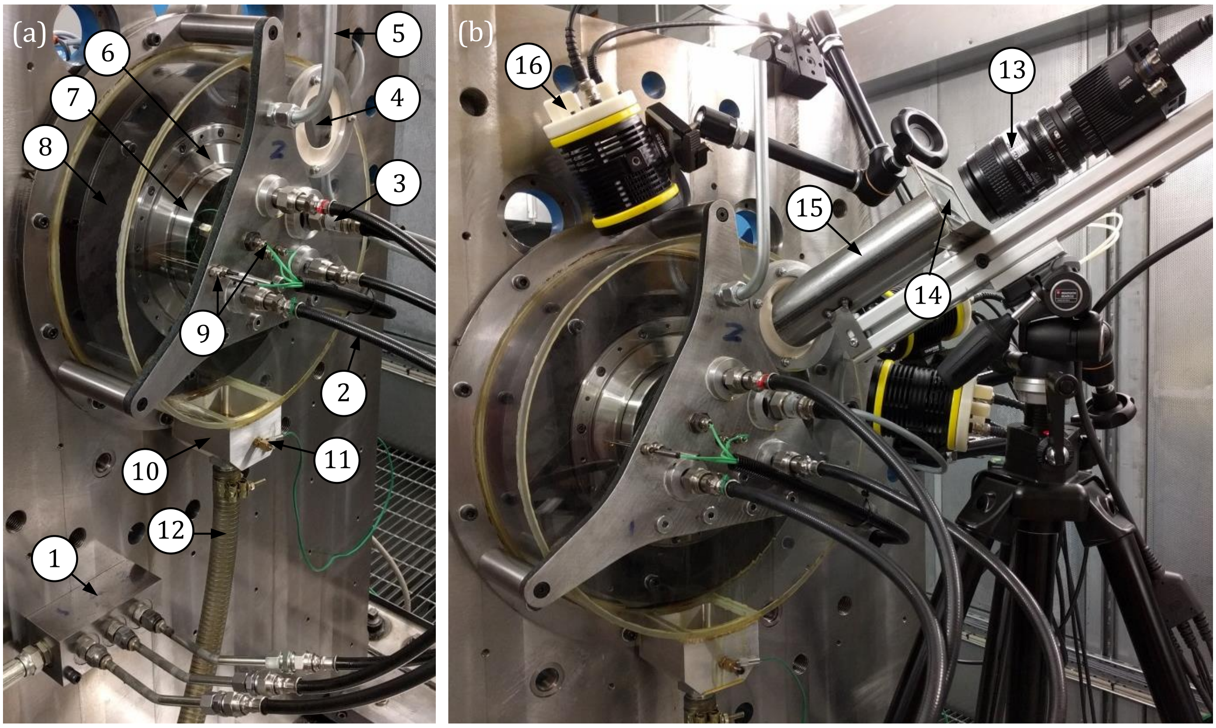

Figure 5.3: Test module without (a) and with (b) visualisation equipment

A high-speed camera was used to capture photographic and videographic footage of the oil as it exits the lubricating gap towards the front of the test module.

The description of the labels is as follows: oil feed manifold (1), test module oil feed pipes (three in total) (2), pressure transducer to measure oil plenum pressure (Figure 5.2) (3), hole with flexible membrane for visualisation equipment access (4), vent pipe (5), rotating planet gear representation (6), stationary journal (pin) representation (7), outer Perspex chamber (8), thermocouples for flow characterisation and health monitoring (9), oil sump (10), thermocouple for oil scavenge temperature measurement (11), oil scavenge pipe (12), high-speed camera (13), protective plastic screen to avoid oil droplets reaching the camera lens (14), tube to contain splashing oil within the test module chamber (15), lights (three in total) (16).

The hole for visualisation equipment access (item (4) in Figure 5.3) was incorporated as a design improvement following initial trials during which photographs and videos were recorded directly through the transparent Perspex chamber wall. Whilst this yielded good results for low flow rates and low rotational speeds of up to 1,000 rpm, oil wetting of the chamber walls at higher rotational speeds prevented a clear line of sight to the exit of the lubricating gap. Using a tube (item (15) in Figure 5.3), which protrudes into the chamber, avoids this problem as the oil that drains down on the chamber walls flows around the tube. This provides significantly better visual access especially at rotational speeds higher than 1,000 rpm.

5.3 Test Parameters and Variations

The rig allowed four independent parameters to be varied (input parameters), namely the lubricating gap height, h_0, the planet gear representation's rotational speed, n_G, the volumetric oil feed flow rate, $\dot{V}_{in}$, and the main tank oil temperature, T_T (Figure 5.1).

Table 5.1: Input parameters and range of variation

Input parameter	Values tested
Lubricating gap height, h_0 [μm]	55.5, 125.0, 223.5
Main tank oil temperature, T_T [°C]	20, 50
Volumetric oil feed flow rate, $\dot{V}_{in}$ [l/min]	2, 4, 6, 8, 10, 15, 20, 40
Planet gear representation's rotational speed, n_G [rpm]	100, 175, 250, 500, 1,000, 2,000, 3,000, 4,000, 5,000, 6,000

Table 5.1 summarises the input parameters, including their range of variation. $\dot{V}_{in}$ refers to the total volumetric oil feed flow rate supplied to the test module. This flow rate is evenly split into a portion exiting towards the front and towards the rear of the test module.

In addition to visualising the air-oil flow behaviour in the external domain, temperature measurements, T_{Pl}, were taken in the oil plenum upstream of the lubricating gap and in the oil sump, T_S, to enable scavenge temperature measurements (output parameters, Figure 5.2).

In order to record a representative temperature of the oil entering into the external domain, it is essential to measure as close as possible to the exit of the lubricating gap. The operator-set main tank oil temperature, T_T, is inappropriate as the oil is subjected to different heat transfer mechanisms on its path to the oil plenum, where T_{Pl} is measured. Two key sources were identified, which significantly affect T_{Pl}.

a) Heat generation by the bearings that locate the journal representation (Figure 5.2).
b) Heat generation inside the oil plenum due to shearing action caused by the rotating planet gear representation. This affect was deduced from the fact that the bearing

temperatures, which were recorded for the purpose of monitoring rig health, were lower than T_{Pl}.

In general, the recorded values for T_{Pl} were always higher than those for T_{T}. The difference, $T_{\mathrm{Pl}} - T_{\mathrm{T}}$, increased with decreasing $\dot{V}_{\mathrm{in}}$ and increasing with n_{G}. The highest difference, $T_{\mathrm{Pl}} - T_{\mathrm{T}} = 40\ \mathrm{K}$ was recorded at the highest value for n_{G} and the lowest value for $\dot{V}_{\mathrm{in}}$.

Due to the shearing action caused by the rotating planet gear representation, heat will be transferred into the oil as it passes through the lubricating gap. The oil temperature increase inside the gap is a function of a number of variables, such as material properties, heat transfer coefficients, the gap height, h_0, the rotational speed of the planet gear representation, n_{G}, and the volumetric feed flow rate, $\dot{V}_{\mathrm{in}}$. As some of these parameters are unknown and very challenging to determine, the oil temperature rise inside the lubricating gap could not be accounted for. In order to minimise viscous heating inside the lubricating gap, the axial length of the gap was designed to be as short as possible, but sufficiently long to guarantee fully developed flow velocity profiles in the axial and the circumferential directions at the entrance to the external flow domain for all operating conditions.

5.4 Design of Experiment, Test Schedule and Test Procedure

The test values presented in Table 5.1 were purposely chosen to have more data points for low flow rates and low rotational speeds. Preliminary experimental work revealed that flow regime changes no longer occurred for higher flow rates and higher rotational speeds.

Based on the available time for conducting the rig tests, a full factorial design was chosen for the experiments. In theory, this resulted in 480 unique test points. However, whilst testing with the largest lubricating gap height, $h_0 = 223.5\ \mu\mathrm{m}$, a seal failure led to the rig being inoperative for four full days. Thus, for $h_0 = 223.5\ \mu\mathrm{m}$, only 30 out of 160 test points are available. As for the remaining gap heights, $h_0 = 55.5\ \mu\mathrm{m}$ and $h_0 = 125.0\ \mu\mathrm{m}$, respectively, the full data set is available, the total number of unique test points recorded is 350.

The following sequence of parameter variations was chosen.

1) Set lubricating gap height to $h_0 = 125.0\ \mu\mathrm{m}$.
2) Set desired main tank oil temperature to $T_{\mathrm{T}} = 20°\mathrm{C}$.
3) Set desired volumetric oil feed flow rate to $\dot{V}_{\mathrm{in}} = 2\ \mathrm{l/min}$.
4) Set desired rotational speed to $n_{\mathrm{G}} = 100\ \mathrm{rpm}$.

5) Increase rotational speed, n_{G}, step-wise to test all values listed in Table 5.1.
6) Increase volumetric oil feed flow rate, $\dot{V}_{\mathrm{in}}$, according to the test values listed in Table 5.1 and repeat points 4) and 5) for every value set for $\dot{V}_{\mathrm{in}}$.
7) Set desired main tank oil temperature to $T_{\mathrm{T}} = 50°\mathrm{C}$ and repeat points 3) to 6).
8) Set lubricating gap height to $h_0 = 223.5$ µm and repeat points 2) to 7).
9) Set lubricating gap height to $h_0 = 55.5$ µm and repeat points 2) to 7).

The reason for testing with $h_0 = 55.5$ µm at the end of the experimental campaign was to minimise the impact of a rig failure on the project as for this particular gap height, pressures and temperatures reached their maximum values.

The oil plenum temperature, T_{Pl}, and the oil scavenge temperature, T_{S} (Figure 5.2), were measured at steady state conditions. Due to the thermal inertia of the system, it can take a very long time for the temperatures to reach that state. For this reason, steady state conditions were defined as being reached when the temperatures changed by less than 0.2°C over a measurement period of one minute. Measurements were taken automatically at a frequency of 1 Hz. For post-processing purposes, all temperatures were averaged over the full measurement period. For cases with a high rotational speed, n_{G}, steady state temperatures were reached after five to 10 minutes, depending on the volumetric oil feed flow rate, $\dot{V}_{\mathrm{in}}$.

A video with a duration of one second was recorded for every test point, with a frame rate of 1,000 frames per second. In order to capture very fast moving droplets, the exposure time was chosen to be as short as possible. Depending on the specific case, it varied between 6 µs and 10 µs.

5.5 Experimental Results – Flow Regime

This section shows the different flow regimes and flow structures that were observed during the experimental test campaign. In order to compare the results to existing literature data, a non-dimensional disintegration map is provided and differences to flow regime transition conditions established by other researchers in the past are explored and discussed. For clarification, Figure 5.4 correlates the CAD image previously shown in Figure 5.2 to an actual image recorded by the high-speed camera.

During the experimental campaign it could be demonstrated that the lubricating gap height, h_0, and the oil plenum temperature, T_{Pl}, do not significantly affect the prevailing flow regimes (Figure 5.6). Both do, however, affect the flow path direction, which is assessed in detail in section 5.6.

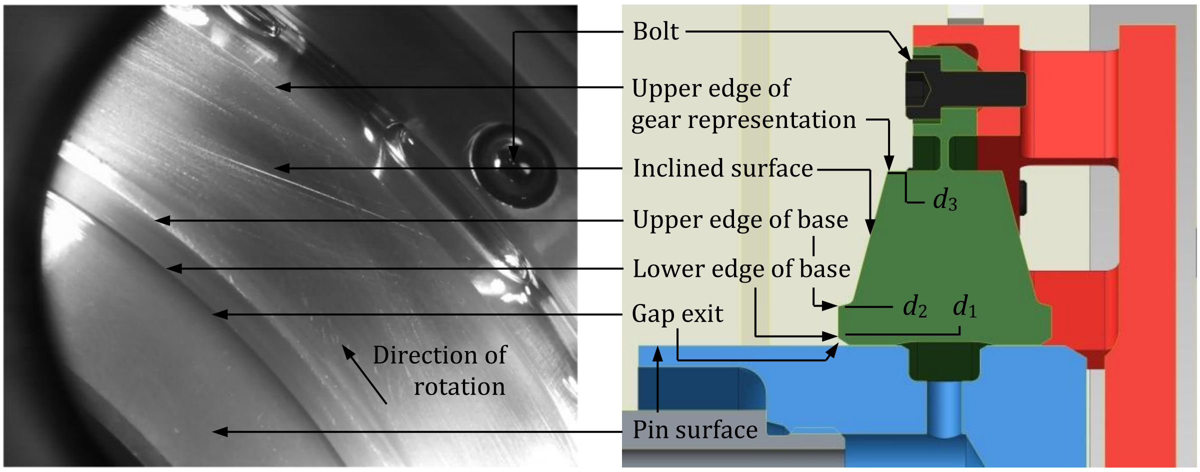

Figure 5.4: Comparison of experimental set-up with CAD model

The following images show how the flow regime changes with increasing rotational speed of the planet gear representation, n_G, and the volumetric oil feed flow rate, $\dot{V}_{in}$.

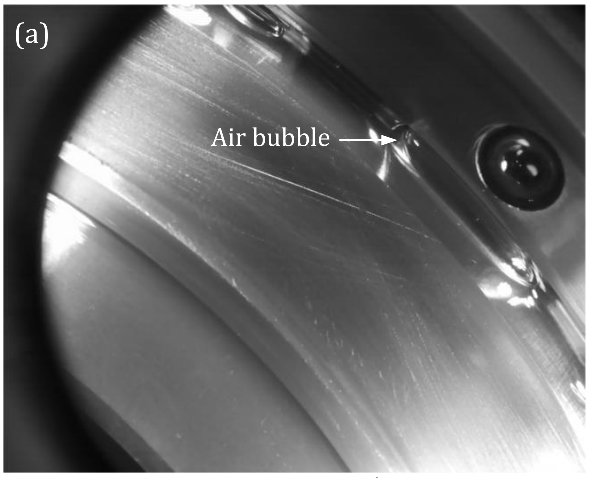

Film formation: $h_0 = 125.0$ µm, $\dot{V}_{in} = 2$ l/min, $n_G = 100$ rpm, $T_{Pl} = 29.7$°C

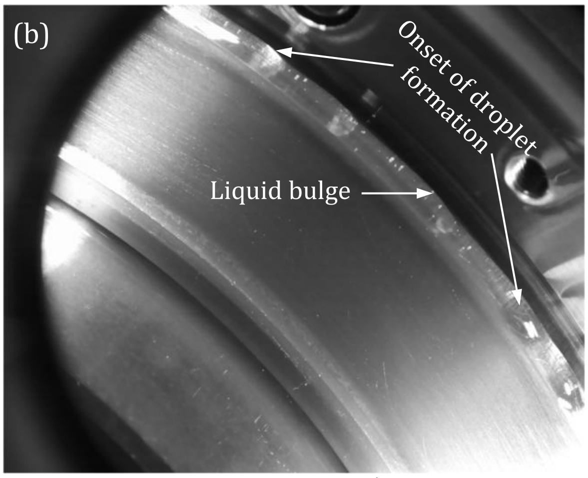

Film formation: $h_0 = 125.0$ µm, $\dot{V}_{in} = 2$ l/min, $n_G = 175$ rpm, $T_{Pl} = 49.4$°C

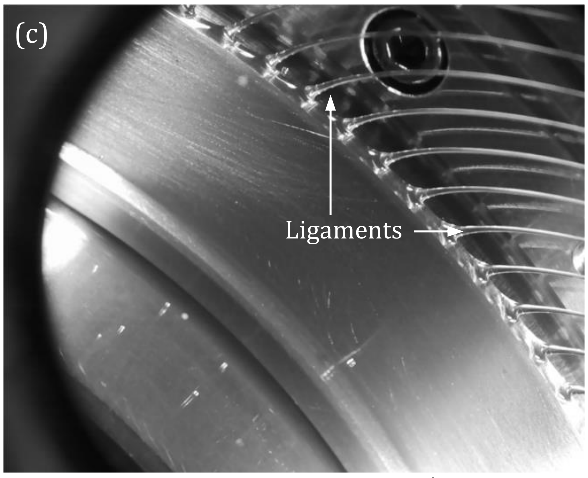

Ligament formation: $h_0 = 125.0$ µm, $\dot{V}_{in} = 4$ l/min, $n_G = 250$ rpm, $T_{Pl} = 30.9$°C

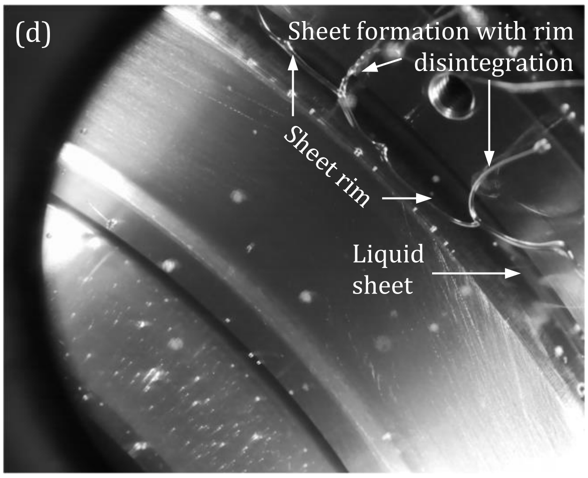

Sheet formation with rim disintegration: $h_0 = 125.0$ µm, $\dot{V}_{in} = 4$ l/min, $n_G = 500$ rpm, $T_{Pl} = 30.1$°C

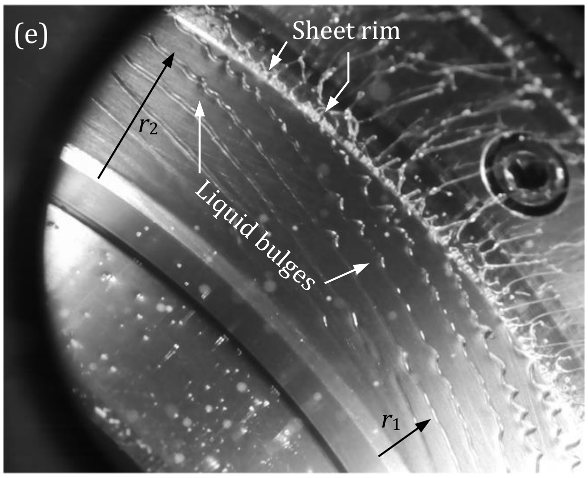

Sheet formation with combined rim and wave disintegration: $h_0 = 125.0$ µm, $\dot{V}_{\mathrm{in}} = 6$ l/min, $n_{\mathrm{G}} = 1{,}000$ rpm, $T_{\mathrm{Pl}} = 53.3$°C

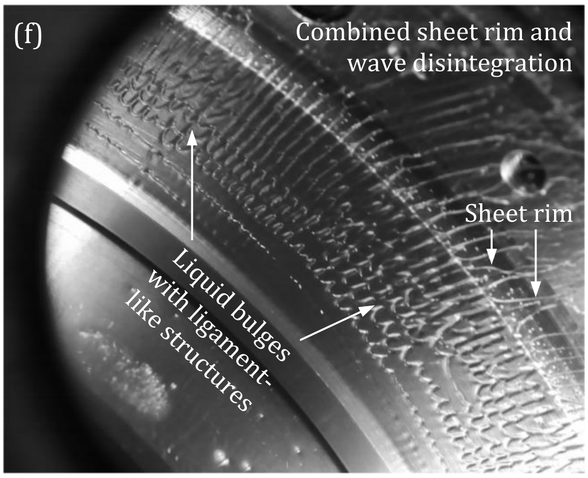

Sheet formation with combined rim and wave disintegration: $h_0 = 125.0$ µm, $\dot{V}_{\mathrm{in}} = 8$ l/min, $n_{\mathrm{G}} = 2{,}000$ rpm, $T_{\mathrm{Pl}} = 34.3$°C

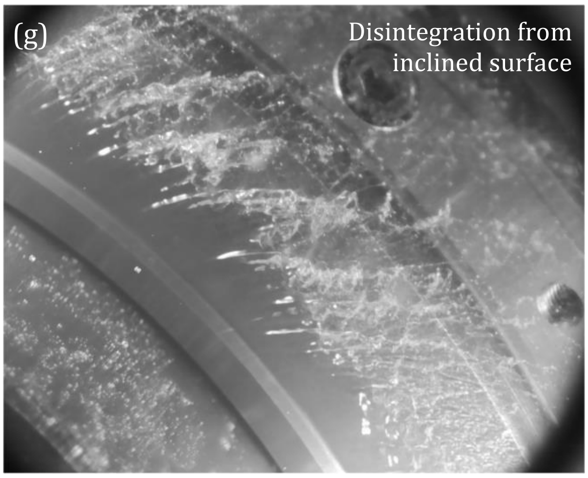

Sheet formation with wave disintegration: $h_0 = 55.5$ µm, $\dot{V}_{\mathrm{in}} = 15$ l/min, $n_{\mathrm{G}} = 4{,}000$ rpm, $T_{\mathrm{Pl}} = 62.0$°C

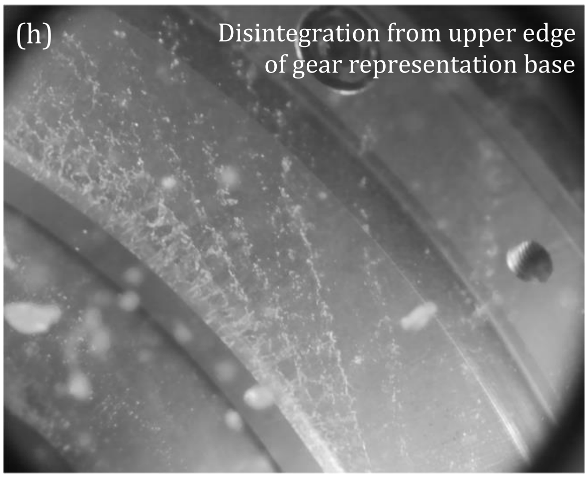

Sheet formation with wave disintegration: $h_0 = 55.5$ µm, $\dot{V}_{\mathrm{in}} = 15$ l/min, $n_{\mathrm{G}} = 6{,}000$ rpm, $T_{\mathrm{Pl}} = 68.8$°C

Figure 5.5: Key flow regimes observed during experimental testing

For low rotational speeds, n_{G}, and low flow rates, $\dot{V}_{\mathrm{in}}$, as shown in Figure 5.5 (a), oil entering into the external flow domain attaches to the chamfer of the rotating planet gear representation. It follows the gear contour in a radially outward direction. The recess on the upper edge of the gear base (diameter d_2 in Figure 5.4) is insufficient to cause oil separation from that point. Instead, the oil flow negotiates this corner and follows the inclined surface towards the upper edge of the gear representation (diameter d_3 in Figure 5.4). From there, the oil film jumps to the surface which contains the bolts to connect the planet gear representation to the drive flange. In Figure 5.5 (a), this is indicated by air bubbles, which are trapped between the two features. This flow regime is defined as film formation. Film separation and disintegration occur at a point which is beyond the field of view captured by the camera.

When n_G is increased, as shown in Figure 5.5 (b), the centrifugal force becomes large enough to prevent the oil film from jumping across the gap between the upper edge of the gear representation (diameter d_3 in Figure 5.4) and the surface containing the bolts. Instead, a liquid bulge forms at diameter d_3. Small irregularities in the bulge indicate the onset of direct droplet formation. At this stage, the centrifugal force generated by the rotation of the planet gear representation is balanced by the liquid's surface tension [41].

When increasing both $\dot{V}_{in}$ and n_G further, as shown in Figure 5.5 (c), ligaments are formed which separate from the upper edge of the gear representation (diameter d_3 in Figure 5.4). The number of ligaments depends on the Weber number, We, and Ohnesorge number, Oh. As the ligaments extend into the atmosphere, they are stretched and become thinner.

Figure 5.5 (d) shows the prevailing flow regime when doubling n_G from 250 rpm to 500 rpm. The liquid throughput can longer be accommodated by ligaments and a liquid sheet is formed. As n_G is still relatively low, this sheet is undisturbed and the sheet rim, which is thicker than the sheet itself, can clearly be identified. Similar to the liquid bulge, which is formed during direct droplet formation (Figure 5.5 (b)), at this point, surface tension forces are balanced by centrifugal forces. As the rim has no controlling solid surface, it breaks down into threads in an irregular fashion.

In Figure 5.5 (e), the centrifugal force becomes large enough to produce wave-like structures which travel radially outwards across the inclined surface of the planet gear representation. The physical mechanism causing this behaviour is identical the one described in the previous case (Figure 5.5 (d)). The peak of the wave is essentially a liquid bulge, similar to that shown in Figure 5.5 (b), which forms as the centrifugal force becomes more significant than the surface tension force. In the direction of rotation, the radial distance from the liquid bulge to the upper edge of the gear representation base (diameter d_2 in Figure 5.4) increases from r_1 to r_2 (Figure 5.5 (e)). If the liquid's radial velocity component can be neglected, the liquid bulge follows an involute curve. At the upper edge of the gear representation, an irregular sheet is produced. As n_G is higher compared to that in Figure 5.5 (d), the radial extent of the liquid sheet is shorter and interactions between the liquid and the atmosphere become more significant, i.e. the sheet is more wavy and irregular.

When increasing both $\dot{V}_{in}$ and n_G further, as shown in Figure 5.5 (f), the liquid bulges observed at lower values of $\dot{V}_{in}$ and n_G develop ligament-like structures, which are formed perpendicular to the involute curves described by the liquid bulges. At this stage, the centrifugal force is large enough to overcome the surface tension force. The result, i.e. the formation of ligament-type structures, is similar to what was previously observed at the transition from direct droplet formation to ligament formation (Figure 5.5 (b) and Figure 5.5 (c)). Liquid disintegration at the upper edge of the gear representation (diameter d_3 in Figure 5.4) appears to be more regular compared to the lower flow rate and lower speed case shown in Figure 5.5 (e). This trend does not seem to be consistent with the observations made so far, which showed that, in general, irregularities and disorder in flow structures increase for higher values of $\dot{V}_{\mathrm{in}}$ and n_{G}. However, this can be explained by the fact that the ligament-type flow structures are removing liquid from the film that travels across the inclined surface. Consequently, the liquid flow rate reaching the upper edge of the gear representation is reduced. Thin and more regular ligaments separate from the edge.

Figure 5.5 (g) shows how the prevailing flow regime changes when $\dot{V}_{\mathrm{in}}$ and n_{G} are approximately doubled compared to the previous case (Figure 5.5 (f)). Regular flow structures do no longer exist. Instead, the oil film separates from the inclined surface of the planet gear representation and atomises into small droplets via sheet wave disintegration. Turbulent flow structures can be observed which are caused by the strong interaction between the liquid sheet and the surrounding air.

Figure 5.5 (h) shows a similar flow field behaviour as previously described in Figure 5.5 (g). Whilst $\dot{V}_{\mathrm{in}}$ remained unchanged, n_{G} was increased to 6,000 rpm. Sheet formation with wave disintegration prevails. In contrast to lower rotational speeds, the sheet separates from the upper edge of the gear representation's base (diameter d_2 in Figure 5.4). Due to very strong interactions between the liquid sheet and the surrounding air, droplet sizes are even smaller than those generated in the previous case.

No further flow regime changes were observed beyond the conditions shown in Figure 5.5 (h). A change in flow path direction was recorded for very high values of $\dot{V}_{\mathrm{in}}$ and T_{Pl}. These scenarios are separately investigated in section 5.6.

In order to enable a comparison to the work carried out by Fraser et al [40], Liu et al [41] and Glahn et al [42], it is practicable to analyse the flow field transitions in a non-dimensional fashion.

The test points investigated during the experimental campaign were chosen to cover a very wide range of flow rates and rotational speeds (Table 5.1). However, the transition from direct droplet formation to ligament formation only occurs at low flow rates and rotational speeds. The test point density for this transition type is therefore very low. As the transition from ligament formation to sheet formation occurs at higher flow rates and rotational speeds, more test points are available and the conditions for the transition can be established with higher accuracy. The data gathered during the experimental campaign was categorised according to the following flow regimes:

a) Ligament formation

b) Sheet formation with rim disintegration

c) Sheet formation with wave disintegration

In order to demonstrate the potential effect of the lubricating gap height, h_0, on the prevailing flow regime, this parameter was included in the plot shown in Figure 5.6.

Figure 5.6 shows a distinct separation between ligament formation, sheet formation with rim disintegration and sheet formation with wave disintegration. Whilst the transition from ligament formation to sheet formation with rim disintegration is marked by a straight line which is a function of the term $\dot{V}^{+1/2}\mathrm{Oh}^{1/6}$, the transition from sheet formation with rim disintegration to sheet formation with wave disintegration is marked by a straight line which is independent of this term.

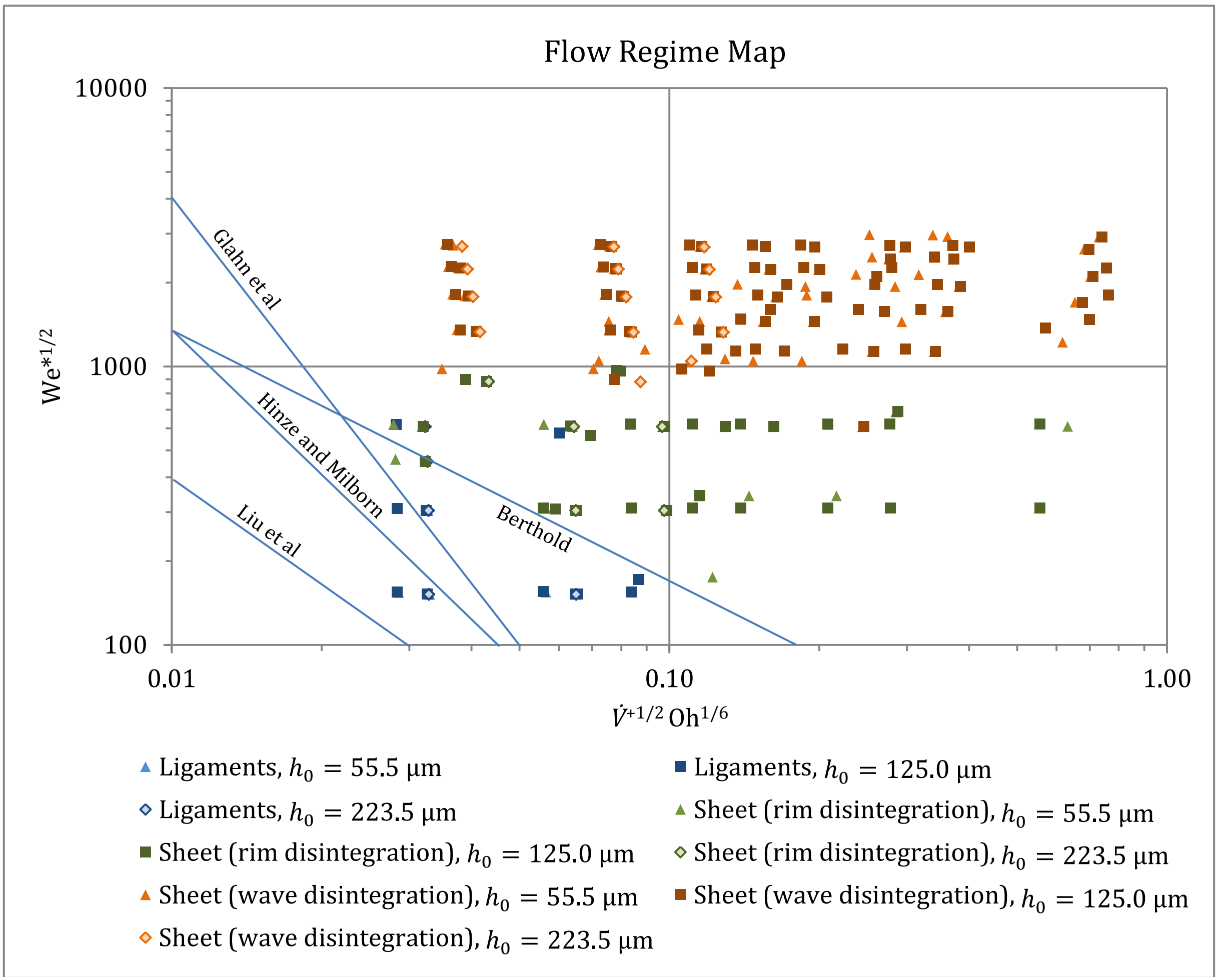

Figure 5.6: Flow regime and disintegration map

The conditions for a flow regime change from ligament formation to sheet formation are broadly consistent with those identified by other researchers in the past, e.g. Liu et al [41], Glahn et al [42], and Hinze and Milborn [44]. The transition conditions identified by Fraser et al [40] are outside the limits of the graph shown in Figure 5.6. They occur for values of $\dot{V}^{+1/2}\mathrm{Oh}^{1/6}$ that are approximately one order of magnitude lower than those obtained by the experimental tests presented in this section. As previously discussed in section 2.3.2, in contrast to a rotating cup, a rotating disc exhibits significant slip between the bulk flow of the liquid and the rotating surface. Thus, the angular bulk velocity of the liquid is lower than that of the rotating disc. Hence, the transition from one disintegration mode to another occurs at higher Weber numbers. The transition conditions established from the experimental test data is most consistent with the transition conditions observed on rotating discs [42]. For radial oil outflow, this behaviour was already anticipated and discussed in section 2.3.2. However, compared to the transition conditions established by Glahn et al [42], the experimental data follows a straight line with a smaller gradient. For higher flow rates, the transition occurs at higher Weber numbers. There are a number of possible explanations for that:

a) The bulk flow velocity of the liquid over the rotating planet gear representation may not be representative of that over a rotating disc, as investigated by Glahn et al [42]. The key differences in the experimental set-up are:

   - The rotating planet gear representation is equivalent to an incomplete disc, whereas Glahn et al [42] carried out research on a complete disc.
   - Liquid is fed with a pre-swirl to the rotating planet gear representation. As a Couette flow velocity profile prevails inside the lubricating gap, the swirl ratio of the bulk flow is $S_R = 0.5$. In Glahn's et al [42] experiments, no pre-swirl was present as the liquid was supplied at the centre of the disc.

b) The discrepancy between the transition conditions established by Glahn et al [42] is greatest for low rotational speeds and high flow rates. At these conditions, both axial and radial outflow occur. Due to the rotation of the planet gear representation, some liquid is entrained naturally. If the amount of liquid supplied through the lubricating gap exceeds that amount, it will enter the external domain in the axial direction. Consequently, the actual amount of liquid, which is driven radially outwards along the planet gear representation's contour, is less than the amount of liquid supplied through the lubricating gap. The chosen rig set-up did not allow the mass flow rates for radial and axial oil outflow to be determined individually when both occurred simultaneously. If the flow split had been measured, it would have shifted the transition conditions towards lower values of $\dot{V}^{+1/2}\mathrm{Oh}^{1/6}$, and hence closer to those established by Glahn et al [42].

Figure 5.6 also shows that the effect of the lubricating gap height, h_0, on the prevailing flow regime is negligible.

The separation of sheet formation with rim disintegration and sheet formation with wave disintegration by a constant modified Weber number, We*, indicates that the mechanism for the transition is independent of the liquid's viscosity, μ, and the flow rate, $\dot{V}_{\mathrm{in}}$. This is consistent with the findings reported by Fraser et al [40]. Ignoring single outliers in the available data set, the transition between the two sheet disintegration modes occurs at $800 \leq \mathrm{We}^{*1/2} \leq 1{,}000$, which is equivalent to peripheral speeds between $15\ \mathrm{m/s} \leq u \leq 18\ \mathrm{m/s}$. Fraser et al [40] reported this value to be 8 m/s. However, the researchers used a cup geometry which enabled the liquid to rapidly attain the peripheral speed of the cup. In contrast to liquid flow over a rotating disc, slip between the bulk flow and the rotating surface is significantly smaller or not present at all. For this reason, when using a rotating cup, the transition from sheet formation with rim disintegration to sheet formation with wave disintegration occurs at lower Weber numbers, We.

From the experimental investigations of the flow regimes observed on a non-orbiting journal bearing with a constant lubricating gap height, h_0, the following conclusions can be drawn:

a) The experiments showed the same flow regimes, namely direct droplet formation, ligament formation and sheet formation, which had previously been observed by other researchers in the past.

b) The transition characteristics are broadly consistent with those observed on rotating discs. Due to the unique set-up of the experimental rig, the transition from ligament to sheet formation at low rotational speeds is shifted towards higher flow rates.

c) The existence of two difference sheet disintegration mechanisms, namely rim and wave disintegration, could be confirmed. However, due to using a different type of geometry, the transition characteristics are shifted.

5.6 Experimental Results – Flow Path

During the experimental campaign, for certain operating conditions, both radial and axial oil outflow were observed at the same time. This section explores the conditions for which axial outflow occurs. Based on the available test data, a flow map is provided which enables the prediction of axial outflow for arbitrary, user-defined operating conditions.

As previously discussed in section 4.1, whether axial oil outflow occurs or not depends on the combination of the fluid's viscosity, μ, the outflow velocity, v_0, and the rotational speed, n_{G}. As soon as the gear representation rotates, it will naturally entrain some oil, which is transported outwards in the radial direction. If the amount of oil supplied to the lubricating gap exceeds the amount entrained by the gear representation, axial will occur in addition to remove the excess oil. The following images show a direct comparison between two similar operating points with different oil plenum temperatures, T_{Pl}.

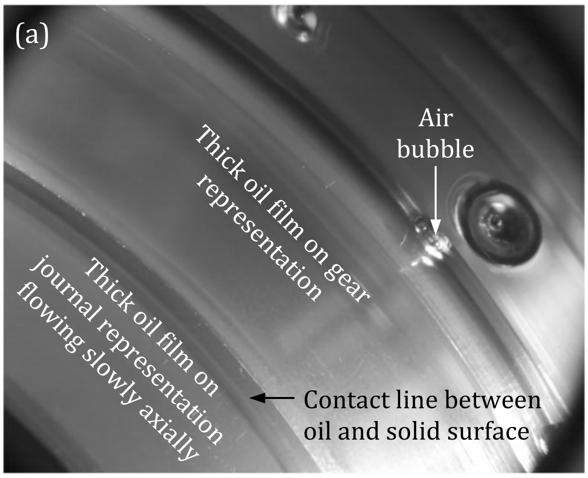

Radial and axial outflow: $h_0 = 55.5\ \mu\mathrm{m}$, $\dot{V}_{\mathrm{in}} = 40\ \mathrm{l/min}$, $n_{\mathrm{G}} = 100\ \mathrm{rpm}$, $T_{\mathrm{Pl}} = 33.1°\mathrm{C}$

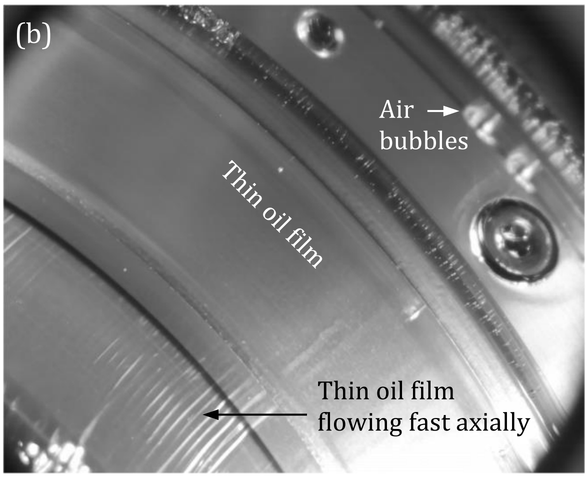

Radial and axial outflow: $h_0 = 55.5\ \mu m$, $\dot{V}_{\mathrm{in}} = 40\ \mathrm{l/min}$, $n_{\mathrm{G}} = 100\ \mathrm{rpm}$, $T_{\mathrm{Pl}} = 55.4°\mathrm{C}$

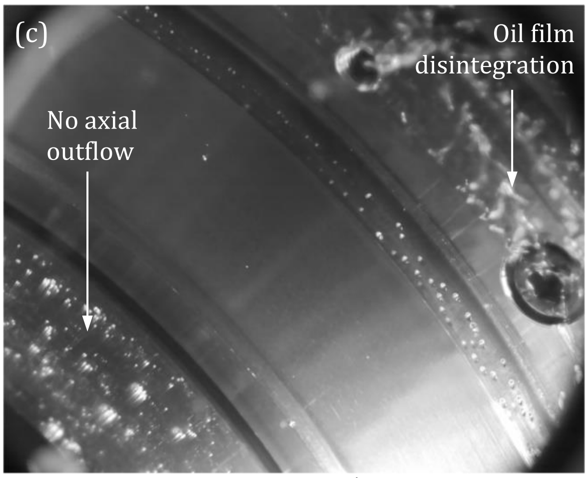

Radial outflow: $h_0 = 55.5\ \mu\mathrm{m}$, $\dot{V}_{\mathrm{in}} = 20\ \mathrm{l/min}$, $n_{\mathrm{G}} = 1{,}000\ \mathrm{rpm}$, $T_{\mathrm{Pl}} = 30.5°\mathrm{C}$

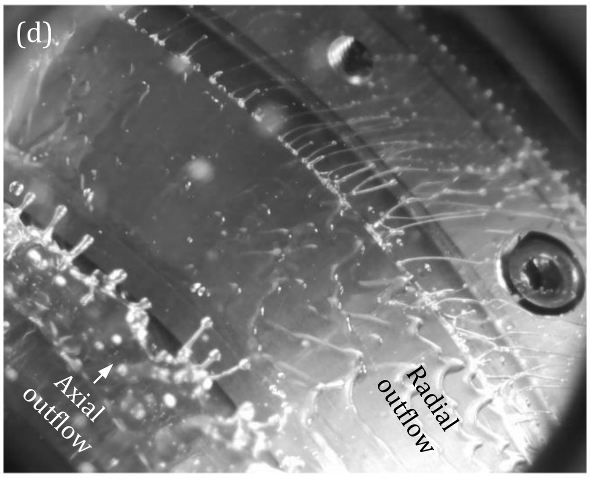

Radial and axial outflow: $h_0 = 55.5\ \mu m$, $\dot{V}_{\mathrm{in}} = 20\ \mathrm{l/min}$, $n_{\mathrm{G}} = 1{,}000\ \mathrm{rpm}$, $T_{\mathrm{Pl}} = 54.9°\mathrm{C}$

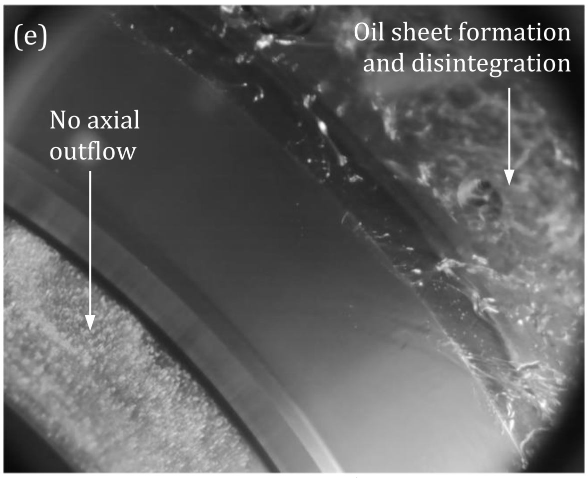

Radial outflow: $h_0 = 55.5\ \mu m$, $\dot{V}_{\mathrm{in}} = 40\ \mathrm{l/min}$, $n_{\mathrm{G}} = 2{,}000\ \mathrm{rpm}$, $T_{\mathrm{Pl}} = 36.7°\mathrm{C}$

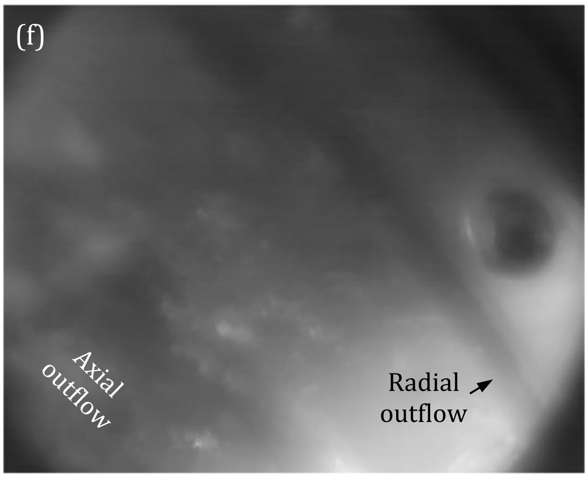

Radial and axial outflow: $h_0 = 55.5\ \mu m$, $\dot{V}_{\mathrm{in}} = 40\ \mathrm{l/min}$, $n_{\mathrm{G}} = 2{,}000\ \mathrm{rpm}$, $T_{\mathrm{Pl}} = 56.5°\mathrm{C}$

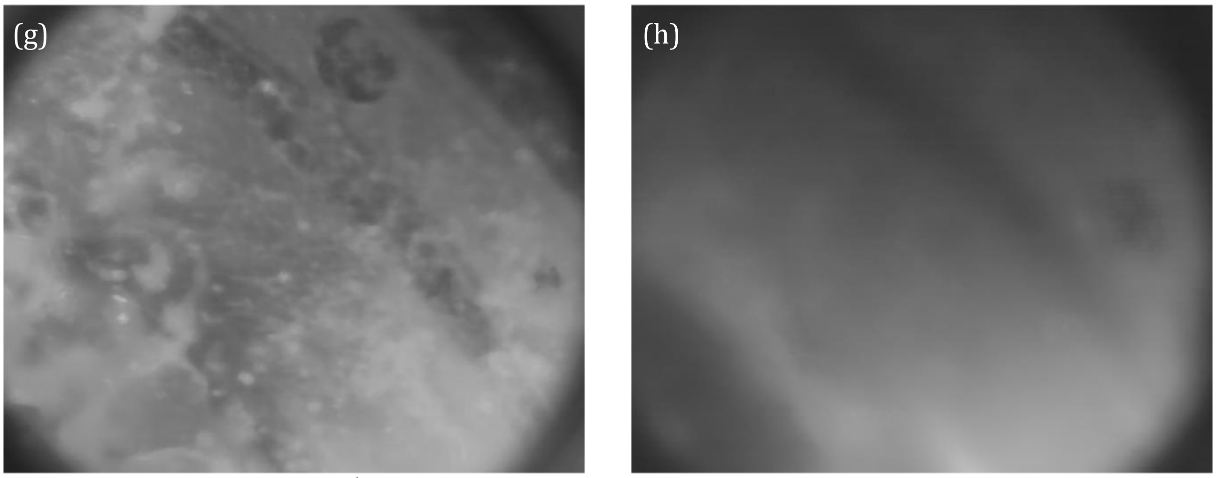

Radial outflow: $h_0 = 55.5\ \mu$m, $\dot{V}_{\mathrm{in}} = 40$ l/min, $n_{\mathrm{G}} = 6{,}000$ rpm, $T_{\mathrm{Pl}} = 40.0$°C

Radial and axial outflow: $h_0 = 55.5\ \mu$m, $\dot{V}_{\mathrm{in}} = 40$ l/min, $n_{\mathrm{G}} = 6{,}000$ rpm, $T_{\mathrm{Pl}} = 65.2$°C

Figure 5.7: Radial vs radial and axial oil outflow

Figure 5.7 (a, b) show the outflow behaviour for a low rotational speed of the planet gear representation, n_{G}, and a high volumetric flow rate, $\dot{V}_{\mathrm{in}}$, for different dynamic oil viscosities, μ, i.e. for different oil plenum temperatures, T_{Pl}. For high values of μ, the axial velocity, v_0, of the oil entering into the external flow domain reduces rapidly. Due to mass conservation, the oil film thickness is relatively large. The contact line between the oil and the solid surface of the gear representation is visible, indicating the thickness of the oil film. The flow drains into the sump region under gravity. For similar conditions, but with a lower value of μ, v_0 is visibly higher, as indicated by the flow structures in the axial direction. Reflections in the bottom left corner of Figure 5.7 (b) show how the oil film separates from the journal surface. Due to the planet gear representation's rotation, in both cases, some radial oil outflow occurs simultaneously. This is indicated by trapped air bubbles.

For higher values of n_{G}, the different outflow behaviours become more apparent. For high values of μ (Figure 5.7 (c)), only radial outflow occurs. This is indicated by the oil film which covers the gear representation and which disintegrates approximately at the pitch circle diameter (PCD) of the bolts. White spots on the journal representation are created by aerated droplets that drip from the upper housing wall. In contrast, Figure 5.7 (d) shows a significant amount of axial outflow. Due to the swirling motion of the flow, centrifugal forces lift the film off the journal representation's surface after travelling approximately half the distance to the planet carrier. Additionally, radial outflow occurs. This is indicated by the formation of liquid bulges on the inclined surface of the gear representation and by the formation of ligaments and sheets on the upper edge of the gear representation (diameter d_3 in Figure 5.4).

When increasing n_{G} by a factor of two compared to the previous case, for otherwise similar operating conditions, the same types of outflow behaviours can be observed. For high values of

μ, as shown in Figure 5.7 (e), radial oil outflow continues to prevail. The journal representation is now covered in a thin aerated oil film, which is created by oil dripping from the upper housing wall. For low values of μ, as shown in Figure 5.7 (f), a combination of axial and radial oil outflow occurs. Oil splashing towards the camera lens made it challenging to achieve good visualisation results of this operating point. This indicates that, as seen in the previous case (Figure 5.7 (d)), swirling oil travelling across the journal representation's surface lifts off the surface.

Figure 5.7 (g, h) show the oil flow path for high and low values of μ, respectively, at $\dot{V}_{\mathrm{in,\,max}} = 40$ l/min and $n_{\mathrm{G,\,max}} = 6{,}000$ rpm. As both parameters are at their respective maximum values at the same time, the flow is generally very turbulent. A large amount of very small droplets, moving at very high speeds, are generated. This makes the visualisation of the flow field behaviour, even through direct observation into the chamber, difficult. Figure 5.7 (g) shows the outflow behaviour for a high value of μ. Compared to the flow field behaviour shown in Figure 5.7 (e), the only significant change is the increase from $n_{\mathrm{G}} = 2{,}000$ rpm to $n_{\mathrm{G}} = 6{,}000$ rpm. As an increase of n_{G} promotes radial oil outflow due to higher centrifugal forces, there are supported reasons to believe that radial outflow continues to prevail for these extreme conditions, even though the image of Figure 5.7 (g) is inconclusive with respect to the prevailing flow path direction. In Figure 5.7 (h), image blur indicates that for low values of μ, a significant amount of oil is directed towards the camera lens, i.e. the oil enters into the external domain in the axial direction and lifts off the journal representation's surface due to the centrifugal force generated by the swirling motion of the oil.

The experimental investigations into the flow path direction revealed two different types of outflow behaviours.

a) No axial outflow, i.e. radial outflow only
b) Axial outflow with some radial outflow

For all test points of the experimental campaign, the prevailing flow path was classified into the two types of outflow behaviours mentioned above. As the flow path direction depends on the rotational speed of the planet gear representation, n_{G}, the outflow velocity, v_0, and the dynamic oil viscosity, μ, it is practicable to plot the data for representative terms of these three parameters. The rotational speed, n_{G}, directly affects the radial acceleration, ${\omega_{\mathrm{G}}}^2 r_{\mathrm{G}}$, and the y-axis was chosen to represent this term. In order to best show the dependencies of all three parameters on the outflow direction in a single 2D plot, v_0 was weighted with μ. Thus, the x-axis was chosen to represent the term v_0/μ. It should be noted that the flow rates, $\dot{m}_{\mathrm{in}}$ or $\dot{V}_{\mathrm{in}}$, do not need to be represented in the terms chosen for the graph axes. This is due to the fact that v_0 already contains the combined dependencies of the oil flow path direction on $\dot{m}_{\mathrm{in}}$ and h_0 (equation (4.1)). Figure 5.8 shows the graph of the terms discussed in this paragraph.

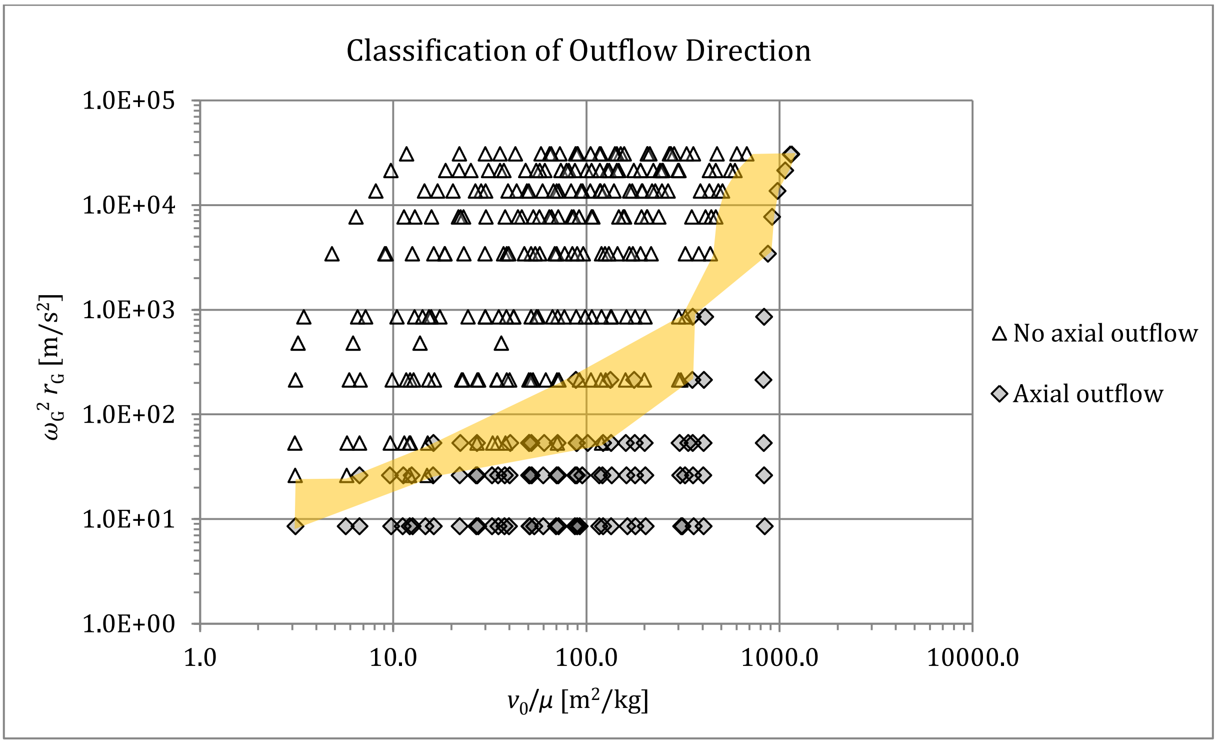

Figure 5.8: Classification of outflow direction depending on radial acceleration and viscosity-weighted axial outflow velocity

Figure 5.8 shows a clear distinction between test points showing axial and no axial outflow, respectively. Both regions are separated by a band in which axial or no axial outflow can occur, depending on the specific operating conditions. Identical values of the term v_0/μ can be obtained for multiples of v_0 and μ, respectively. The outflow direction, however, can change due to the highly non-linear dependency of μ on the oil temperature, T.

As previously discussed in Chapter 1 section 1.2.4, during the design phase of an epicyclic gearbox, it is beneficial to know whether for certain values of v_0, μ, and $\omega_G{}^2 r_G$, axial outflow occurs or not. Figure 5.8 allows the flow path direction to be determined based on the gathered experimental data.

The presented problem of classifying the outflow direction is ideally suited for MATLAB's [81] supervised machine learning capabilities. The aim of supervised machine learning is to build a model that is able to make predictions based on available evidence, i.e. given data points, in the presence of uncertainty. The most accurate classifier for the data set in question can predict the occurrence of axial oil outflow for an arbitrary combination of v_0, μ, and $\omega_G{}^2 r_G$ with an accuracy of over 96%. One of the advantages of using the MATLAB [81] classifier is that it is not limited to a two-dimensional representation of the problem, but can process the data based on the number of given input parameters, i.e. three for the specific case under investigation.

From the experimental investigations into the flow path direction, the following key conclusions can be drawn:

a) The numerically predicted occurrence of axial oil outflow for certain operating conditions could be confirmed experimentally.

b) Two different types of flow path behaviours were observed

- No axial outflow, i.e. radial outflow only
- Axial outflow with some radial outflow

c) The oil's axial outflow velocity, v_0, its dynamic viscosity, μ, and centrifugal acceleration, ${\omega_G}^2 r_G$, are adequate parameters to classify and predict the flow path direction.

5.7 Experimental Results – Flow Temperatures

Detailed investigations into the behaviour of the flow temperatures were conducted to investigate a potential correlation between the flow temperatures, the flow regimes and the outflow directions, respectively. As previously shown in Figure 5.2, as part of the rig instrumentation, thermocouples were installed to measure the oil plenum temperature, T_{Pl}, which indicates the temperature of the oil entering into the external domain, and the oil scavenge temperature, T_{S}. After measuring T_{Pl}, the oil passes through the lubricating gap where its temperature is affected by viscous heating due to the shearing action caused by the rotating gear representation and by heat transfer between the oil and the components bounding the lubricating gap. Whilst viscous heating will always tend to increase the oil's temperature, heat transfer between the liquid and the components bounding the lubricating gap can either increase or decrease the temperature of the oil, depending on whether the metal temperatures are higher or lower than the oil temperature itself. The lubricating gap was purposely designed to be as short as possible. Thus, even for the lowest volumetric flow rate, $\dot{V}_{\mathrm{in}} = 2\ \mathrm{l/min}$, it takes just over 0.02 s for the oil to pass through the gap. This short duration is not deemed sufficient to significantly change the temperature of the oil. Based on these considerations, the only mechanism to affect the oil temperature as it passes through the lubricating gap is viscous heating.

In order to assess the oil scavenge temperature behaviour, the following normalised formulation, is introduced.

$$T_{\mathrm{S}}^{+} = \frac{T_{\mathrm{S}} - T_{\mathrm{Pl}}}{T_{\mathrm{Pl}}} \tag{5.1}$$

In the equation above, T_{S} is the scavenge temperature and T_{Pl} is the oil plenum temperature (Figure 5.2).

The following paragraphs show how T_S^+ is affected by the rotational speed, n_G, the volumetric oil feed flow rate, $\dot{V}_{in}$. Moreover, the effect of two different gap heights, namely $h_0 = 55.5$ μm and $h_0 = 125.0$ μm, and two different oil tank temperatures, namely $T_T = 20°C$ and $T_T = 50°C$, on T_S^+ is investigated.

Figure 5.9 shows how T_S^+ changes depending on n_G and $\dot{V}_{in}$ for $h_0 = 125.0$ μm and $T_T = 20°C$, and Figure 5.10 shows how T_S^+ changes depending on the same parameters, but with $T_T = 50°C$.

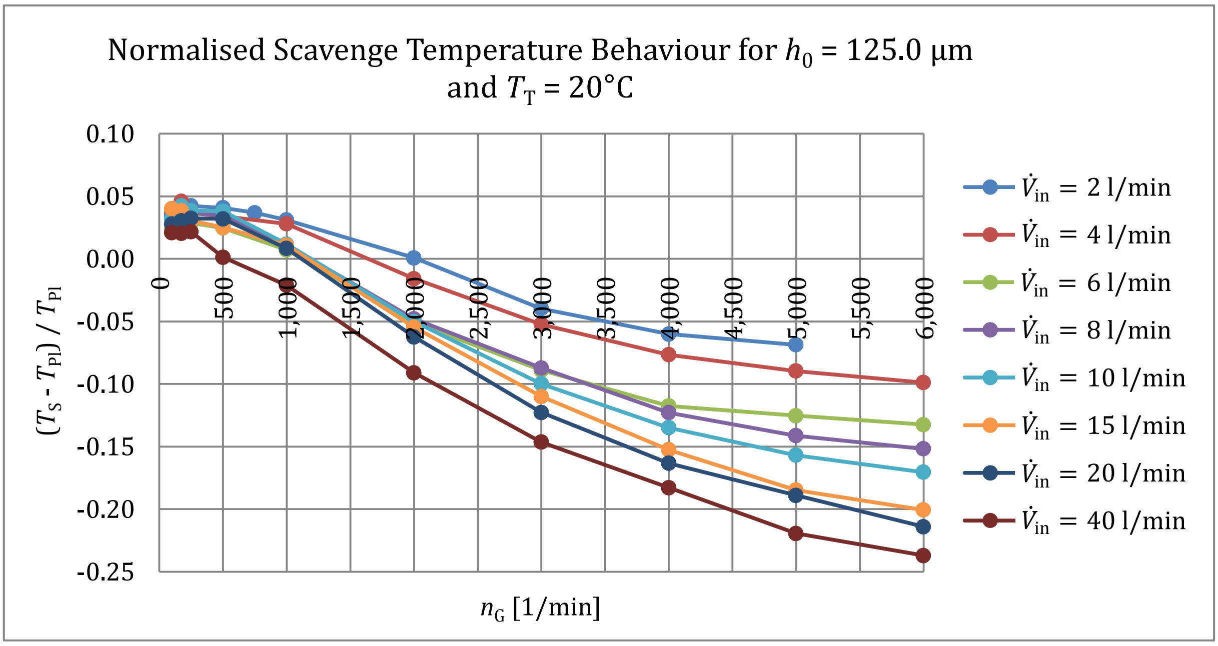

Figure 5.9: Normalised oil scavenge temperature behaviour for h_0=125.0 μm and T_T=20°C

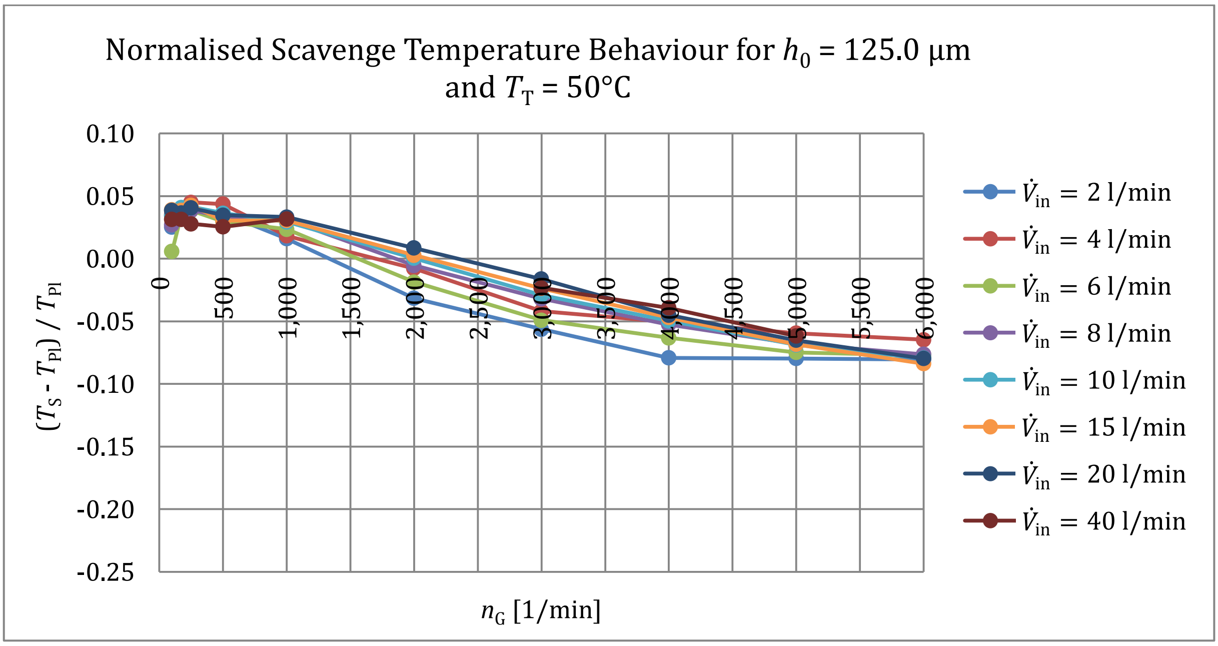

Figure 5.10: Normalised oil scavenge temperature behaviour for h_0=125.0 μm and T_T=50°C

According to Figure 5.9 and Figure 5.10, two different regions can be identified for T_S^+.

a) $T_S^+ > 0$, i.e. $T_S > T_{Pl}$, for low rotational speeds and

b) $T_S^+ < 0$, i.e. $T_S < T_{Pl}$, for high rotational speeds.

For a given lubricating gap height, h_0, the cross-over point, $T_S^+ = 0.00$, depends on T_{Pl} and $\dot{V}_{in}$. As shown in Figure 5.9, at low values of n_G the oil picks up more heat at low values of $\dot{V}_{in}$ compared to high values of $\dot{V}_{in}$. This is due to the fact that, at low volumetric flow rates, the axial velocity, v_0, of the oil through the lubricating gap is lower than for high volumetric flow rates. As a result, more viscous heating takes place. Moreover, for $n_G < 1{,}200$ rpm, the gravitational force, F_g, dominates over the centrifugal force, F_c. For these conditions, after entering into the external flow domain, oil drains immediately into the sump region. There is no or very little interaction with the chamber walls. Heat exchange between the oil and its surroundings as it passes from the exit of the lubricating gap into the sump is negligible. T_S is therefore most affected by T_{Pl}, and by the amount of viscous heating taking place.

For $n_G > 1{,}200$ rpm, F_c dominates over F_g. As a result, swirling oil is driven towards the chamber walls, where a film is formed. At very high values of n_G, this film is not only driven by its own momentum, but also through windage effects. Due to the interaction between the oil and the chamber walls, heat transfer takes place. As the ambient temperature, T_{amb}, was always lower than T_{Pl}, the temperature of the oil decreases.

Figure 5.9 shows that the graphs for different values of $\dot{V}_{in}$ diverge as n_G increases. As this behaviour could not be confirmed for a higher value of T_T, as shown in Figure 5.10, it can be concluded that the cause for this characteristic is related to the dynamic oil viscosity, μ. The diverging behaviour of the graphs shown in Figure 5.9 can be explained as follows. In general, as previously discussed in section 5.3, T_{Pl} is always greater than T_T. The highest differences, $T_{Pl} - T_S$, were recorded for low values of $\dot{V}_{in}$ and high values of n_G. For a given operating point, T_{Pl} is higher for $\dot{V}_{in} = 2$ l/min than it is for $\dot{V}_{in} = 40$ l/min. Thus, μ is much lower at low values of $\dot{V}_{in}$ at a given rotational speed, n_G. A lower value of μ, in turn, results in lower internal fluid friction. This enables the oil to drain more quickly and more effectively. The residence time of the oil inside the chamber is expected to be short and heat transfer leading to a reduction of the oil temperature is limited. In contrast, at high values of $\dot{V}_{in}$, T_{Pl} is lower than at low values of $\dot{V}_{in}$. Thus, μ is much higher and increased fluid friction prevents the oil from being drained quickly and effectively. The oil residence time inside the chamber is expected to be longer for high values of $\dot{V}_{in}$ compared to that for low values of $\dot{V}_{in}$. Heat transfer mechanisms take place over a longer period of time, which leads to a greater reduction of the oil scavenge temperature, T_S.

Figure 5.9 and Figure 5.10 show that the cross-over points, $T_S^+ = 0.00$, occur over a wider range of rotational speeds for a lower value of T_T than for a higher one. The fact that this range is smaller for a higher value of T_T, suggests that the location of $T_S^+ = 0.00$ does not just depend on $\dot{V}_{in}$, but also on μ. Moreover, for a given value of $\dot{V}_{in}$, but a higher value of T_T, $T_S^+ = 0.00$ is shifted towards higher rotational speeds, n_G. For example, at $\dot{V}_{in} = 20\,\mathrm{l/min}$, $T_S^+ = 0.00$ occurs at approximately $n_G = 1{,}100\,\mathrm{rpm}$ for $T_T = 20°\mathrm{C}$, and at approximately $n_G = 2{,}300\,\mathrm{rpm}$ for $T_T = 50°\mathrm{C}$. The reason for this shift is that the lower value of μ at higher temperatures, T_T, promotes axial oil outflow as the viscosity weighted axial outflow velocity, v_0/μ, increases (Figure 5.8). By nature, axial outflow interacts very little with the chamber walls. Hence, the cooling effect on the oil is negligible even at higher values of n_G .

When analysing the normalised oil scavenge temperature behaviour for a lubricating gap height of $h_0 = 55.5\,\mu\mathrm{m}$, in principle, the same trends can be observed as previously described for $h_0 = 125.0\,\mu\mathrm{m}$. With a smaller gap height, more viscous heating takes place at a given rotational speed, n_G. As a result, T_S shifts towards higher values. Moreover, for a given value of $\dot{V}_{in}$, the axial outflow velocity, v_0, is larger compared to set-ups with bigger gap heights, h_0. This promotes axial oil outflow also for higher values of μ and n_G, respectively. Both effects result in the cross-over points, $T_S^+ = 0.00$, to shift towards higher values of n_G. These theoretical considerations are confirmed by the data presented in Figure 5.11.

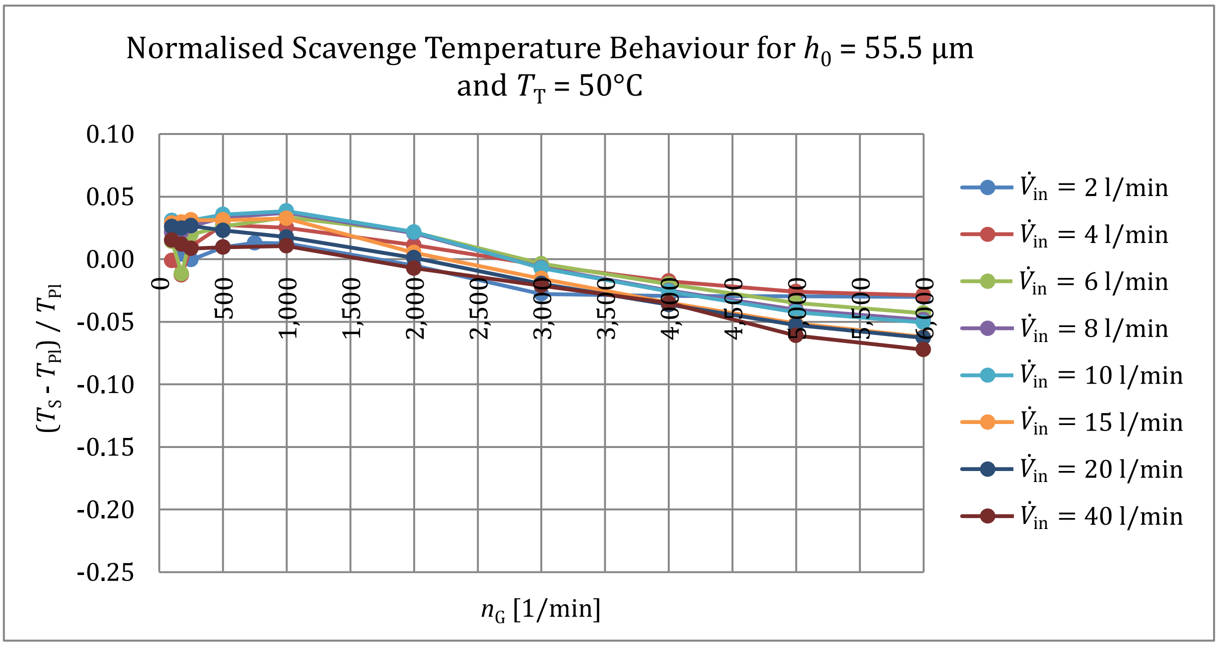

Figure 5.11: Normalised oil scavenge temperature behaviour for h_0=55.5 µm and T_T=50°C

5.8 Conclusions of Experimental Test Campaign

The experimental investigations of the flow temperatures allow the following key conclusions to be drawn:

a) When analysing the normalised oil scavenge temperature, T_S^+, two regions can be identified, namely $T_S^+ > 0.00$ and $T_S^+ < 0.00$.

b) The region for $T_S^+ > 0.00$ is characterised by very little interaction between the oil and the chamber walls. The oil scavenge temperature, T_S, is primarily affected by the oil plenum temperature, T_{Pl}, and by viscous heating effects inside the lubricating gap.

c) The region for $T_S^+ < 0.00$ is characterised by strong interactions between the oil and the chamber walls. The oil scavenge temperature, T_S, is primarily affected by the chamber wall temperature.

6 CFD Model Validation

In the previous chapter, the oil outflow behaviour from a simplified non-orbiting journal bearing with a constant lubricating gap height was investigated experimentally. This included investigations with respect to the flow regime (section 5.5), the flow path (section 5.6) and the oil scavenge temperature behaviour (section 5.7).

Due to the complex kinematics of an orbiting journal bearing with a convergent-divergent lubricating gap height, h, the validation of key characteristics, such as the outflow direction, the outflow velocity, the flow regime, and the liquid disintegration regime, for this particular case, is very challenging and only achievable with a complex test facility (chapter 5) with highly specialised visualisation and measurement equipment. Based on the high associated costs and the time required to perform such work, and the limited additional benefit the results can provide, CFD model validation was conducted using a simplified set-up, namely a non-orbiting journal bearing with a constant lubricating gap height, h_0 (section 4.1).

A number of different approaches are available. Based on the theoretical flow path and flow regime considerations presented in sections 2.3.2 and 2.3.3, and section 3.6, respectively, a comparison to analytically obtained data can be performed (section 6.1). In addition, the data presented in chapter 5 allows the CFD model predictions to be qualitatively validated to the experimental results (section 6.2).

6.1 Analytical Validation

A comparison of analytically obtained data and the CFD model predictions for a non-orbiting journal bearing with a constant lubricating gap height, h_0 (section 4.1), was carried out with respect to the predicted oil flow path direction (section 6.1.1), the flow regime (section 6.1.2), and the oil film thickness on the planet gear chamfer in case of radial oil outflow (section 6.1.3). The purpose of the following sections is to show how different flow characteristics can be validated if experimental data is unavailable.

The analytical models used to validate the flow regime (section 6.1.2) and the oil film thickness (section 6.1.3) were validated by the respective authors, namely Fraser et al [40], and Hinze and Milborn [44]. The modified force balance model (section 3.6) used to compare the analytically predicted flow path direction with the CFD model results (section 6.1.1), however, is unvalidated. Additional details are provided in section 6.1.1.

6.1.1 Flow Path Validation

The analytical data for the flow path direction was obtained from the modified force balance model developed in section 3.6. Whilst the original model established by Friedrich et al [45] was validated by the authors, the modified force balance model presented in section 3.6 is unvalidated, since there was no possibility to confirm the analytical model's validity as part of the work presented in this thesis. A comparison with the CFD model predictions is still valuable as the CFD model is additionally validated by means of other methods. This allows insights into the performance of the analytical model to be gained.

For completeness, the modified force balance equation from section 3.6 is repeated below.

$$\rho|\boldsymbol{u}_1^*|^2 t_F \sin\lambda = \sigma\sin\lambda + \sigma + \rho\, t_S\, a \left(1 - F_{slip}\right)^2 \omega_{\mathrm{G}}{}^2\, \frac{d_1}{2}\cos(\lambda + \xi). \tag{6.1}$$

In the equation above, ρ is the liquid density, $\boldsymbol{u}_1^*$ is the resultant velocity vector of the liquid's axial and radial velocity component, v and w, respectively, t_F is the film thickness, λ is the flow deflection angle, σ is the surface tension, t_S is the sheet thickness, a is the radial extent of the sheet, F_{slip} is the slip factor between the liquid and the rotating planet gear, ω_{G} is the angular velocity of the gear, d_1 is the diameter at which oil separation occurs and ξ is the gear chamfer angle.

Equation (6.1) allows the flow deflection angle, λ, to be determined. For the specific case under investigation, the slip factor, F_{slip}, has to be determined. Different options are available to obtain an estimated value. Based on the considerations discussed in section 3.6, F_{slip} can assumed to be approximately 0.23. Moreover, F_{slip} can be obtained by determining the circumferential oil bulk flow velocity component, u, in the CFD model and comparing it to the circumferential planet gear velocity, u_{G} (equation (3.19)). Doing so yields $F_{slip} = 0.32$. CFD cases 1 (d) and 3 (d), respectively (section 4.1.2), were chosen to compare the calculated values for λ (equation (6.1)) with the ones obtained from the CFD models. For reference, key operating parameters are repeated below. Table 6.1 provides an overview of the results. For the calculated values of λ (equation (6.1)), three different slip factors, namely $F_{slip} = 0.32$, $F_{slip} = 0.23$ and $F_{slip} = 0.00$, respectively, were used to assess sensitivities.

Table 6.1: Comparison of calculated and numerically determined flow deflection angles, λ, for Case 1 (d) and Case 3 (d)

	Case 1 (d)	Case 3 (d)
Angular gear velocity, ω_G	$\omega_{G,\text{ max load}}$	$\omega_{G,\text{ max load}}$
Outflow velocity, v_0 [m/s]	$0.14\omega_G r_G$	$0.14\omega_G r_G$
Oil temperature, T [°C]	20	$T_{\text{max load}}$
Phase interface reconstruction scheme	Compressive	Compressive
Steady state flow field conditions (t = 0.03 s). Contours of 50% oil volume fraction iso-surface.	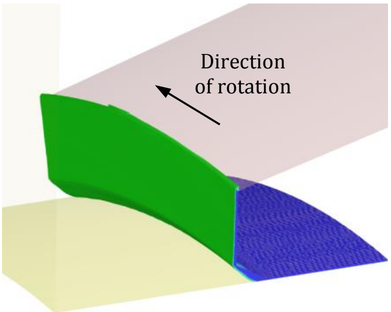	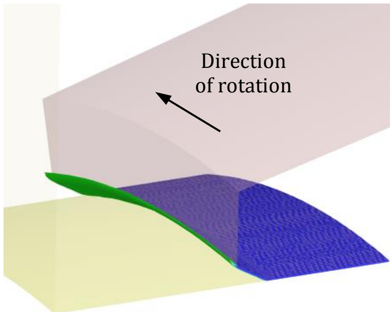
Steady state flow field conditions (t = 0.03 s). Air volume fraction contour plot at mid-plane.	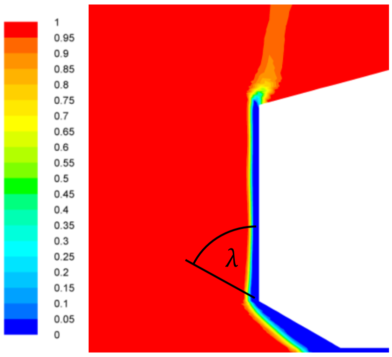	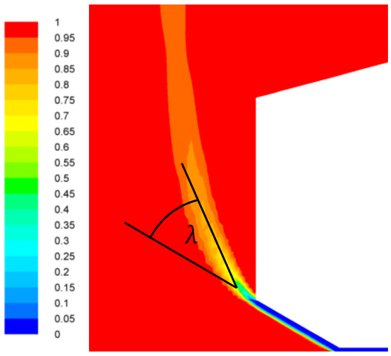
Flow path direction	(b_2)	(b_1)
λ determined in CFD model [°]	60.0	36.0
λ calculated, $F_{slip} = 0.32$ (equation (6.1)) [°]	59.4	45.7
λ calculated, $F_{slip} = 0.23$ (equation (6.1)) [°]	59.6	48.4
λ calculated, $F_{slip} = 0.00$ (equation (6.1)) [°]	59.8	52.8

As shown in Table 6.1, for Case 1 (d) there is a good agreement between the numerically determined values of λ and the calculated ones. A variation of the slip factor, F_{slip}, has only a very minor effect on λ, indicating a low sensitivity.

In contrast, for Case 3 (d), the deviations between the numerically determined values of λ and the calculated ones are much larger. The difference, $\Delta\lambda$, is 9.7° for $F_{slip} = 0.32$, 12.4° for $F_{slip} = 0.23$ and 16.8° for $F_{slip} = 0.32$. Compared to Case 1 (d), a variation of F_{slip} affects the calculated value of λ to a much larger extent, indicating a higher sensitivity. As the only difference between Case 1 (d) and Case 3 (d) is the oil viscosity, μ, it can be concluded that this parameter must be a major contributor to this behaviour. Whilst the deviations between the numerically determined values of λ and the calculated ones are larger for Case 3 (d) compared to those observed for Case 1 (d), the flow path directions predicted by the CFD simulations are consistent with the predictions made by the force balance model. For Case 1 (d), both tools predict no flow separation from the lower edge of the gear base (diameter d_1 in Figure 2.2). In contrast, for case 3 (d), flow separation is predicted at that diameter.

There are multiple possible reasons why the numerically determined values of λ and the calculated ones agree better for high oil viscosities than they do for low oil viscosities. Sources of inaccuracy can originate from both the CFD model predictions and the force balance model itself.

Due to its formulation, the compressive phase interface reconstruction scheme is more diffusive than the more accurate geometric reconstruction scheme (section 3.1.5). Moreover, particularly for low oil viscosities, the oil film is very thin. This, combined with growing calculational cell sizes away from the wall, leads to very high cell air volume fraction values, α. Table 6.1 shows that, at some distance to the wall, α can be as high as 0.90 to 0.95. Due to the high diffusivity in these regions, the oil film is more strongly affected by the air field as this would be the case for a highly resolved oil film. The oil sheet trajectory after separation from the lower edge of the gear base (diameter d_1 in Figure 2.2) can therefore not expected to be accurate. Moreover, due to the oil sheet following a curved trajectory, an accurate representation, and hence determination, of λ is challenging.

In addition to the inaccuracies originating from the CFD model, the uncertainties of some assumptions made when establishing the force balance model can also contribute to inaccurate calculations of λ. The slip factor, F_{slip}, for instance represents an average value for the bulk flow. However, the circumferential velocity component of the liquid, u, varies across the film thickness. Due to the no-slip condition, at the wall, u takes the value of the circumferential gear velocity, u_G, i.e. $F_{slip} = 0.00$. With increasing distance from the wall, u will decrease; hence $F_{slip} \neq 0.00$. The calculation of λ is affected by the variation of F_{slip} (equation (6.1)).

In order to calculate λ, the sheet thickness, t_S, is required (equation (6.1)). The determination of t_S can introduce additional uncertainties for the calculation of λ. Fraser et al [40] have shown that t_S decreases with increasing radial distance from the edge of liquid separation. However, particularly for high flow rates and high rotational speeds, t_S diminishes quickly to a near-constant value. For this reason, the force balance model proposed in section 3.6 assumes a constant value of t_S based on the maximum radial extent, a, of the sheet (equation (3.21)). Whilst the chosen approach is a good approximation, it does introduce additional uncertainty in the calculation of λ.

In summary, it can be concluded that the calculated deflection angle, λ, provides a good indication on whether the flow will separate from the lower edge of the gear base (diameter d_1 in Figure 2.2) or not. However, actual quantitative data for λ must be carefully assessed. Due to the complexity of the flow field, accurate values for λ are challenging to obtain.

6.1.2 Flow Regime Validation

As previously discussed in section 2.3, there are significant similarities between the prevailing flow regimes observed on a simplified journal bearing with a constant lubricating gap height, h_0, and those observed on rotating cups and discs. Liquid flow over the latter components has been investigated on a number of occasions in the past (section 2.3.3). Research carried out by Fraser et al [40], Liu et al [41], Hinze and Milborn [44], and Glahn et al [42] and Matsumoto et al [43], respectively, yielded equations for the calculation of the transition flow rates from direct droplet formation to ligament formation, $\dot{V}_1^+$, and from ligament formation to sheet formation, $\dot{V}_2^+$, respectively.

The expected flow regime can be determined by calculating and comparing the non-dimensional flow rate, $\dot{V}^+$, for a particular operating point with the non-dimensional transition flow rates, $\dot{V}_1^+$ and $\dot{V}_2^+$. The following scenarios are possible:

a) $\dot{V}_1^+ > \dot{V}^+$: direct droplet formation
b) $\dot{V}_1^+ < \dot{V}^+ < \dot{V}_2^+$: ligament formation
c) $\dot{V}_2^+ < \dot{V}^+$: sheet formation

Table 6.2 provides an overview of the non-dimensional volumetric transition flow rates, $\dot{V}_1^+$ and $\dot{V}_2^+$, and the actual non-dimensional flow rate, $\dot{V}^+$, for maximum load conditions. The operational parameters of Case 3 (section 4.1.2) were used to determine $\dot{V}_1^+$, $\dot{V}_2^+$ and $\dot{V}^+$.

Table 6.2: Prediction of prevailing flow regime for Case 3 (d)

Reference	$\dot{V}_1^+$	$\dot{V}_2^+$	$\dot{V}^+$	Comparison
Fraser et al [40]	N/A	0.363 equation (2.23)	51 equation (2.33)	$\dot{V}_2^+ < \dot{V}^+$
Liu et al [41]	2.35×10^{-7} equation (2.31)	1.65×10^{-5} equation (2.32)	6.32×10^{-4} equation (2.28)	$\dot{V}_2^+ < \dot{V}^+$
Hinze and Milborn [44]	N/A	3.85×10^{-4} equation (2.39)	2.65×10^{-1} equation (2.33)	$\dot{V}_2^+ < \dot{V}^+$
Glahn et al [42]	4.86×10^{-5} equation (2.36)	1.32×10^{-3} equation (2.37)	2.65×10^{-1} equation (2.33)	$\dot{V}_2^+ < \dot{V}^+$
Matsumoto et al [43]	1.90×10^{-5} equation (2.38)	N/A	2.65×10^{-1} equation (2.33)	$\dot{V}_2^+ < \dot{V}^+$

Table 6.2 shows that all relevant correlations available in the literature predict the flow regime at maximum load conditions (Case 3, section 4.1.2) to be sheet formation by some margin. This conclusion is consistent with the observations made by Glahn et al [42]. As a result of their work, it was highlighted that, due to the generally high volumetric oil flow rates and the high rotational shaft speeds in aero-engine bearing chambers, sheet formation predominantly prevails when liquid separates from a rotating disc. The experimental investigations presented in section 5.5 proved that Glahn's et al [42] observations and conclusions also apply for a non-orbiting journal bearing case with a constant lubricating gap height, h_0, with radial oil outflow, as the transition characteristics of a rotating disc are most similar to those observed during the experimental test campaign (Figure 5.6). Using Glahn's et al [42] correlations, and assuming that radial oil outflow prevails, sheet formation is predicted not just for maximum load conditions, but over the entire operating range of the journal bearing.

Due to the generally high rotational shaft speeds involved, the oil sheet will interact with the surrounding air and, according to Fraser et al [40], disintegrate by a mechanism called sheet wave disintegration (section 2.3). Table 6.3 shows a comparison between the sheet formation with wave disintegration by liquid flow over a rotating cup and the modelled sheet formation with subsequent liquid disintegration by CFD analysis of Case 3 (d). Key operating parameters and liquid properties are summarised below.

Table 6.3: Comparison of sheet formation with wave disintegration by Fraser et al [40] and by CFD analysis of Case 3 (d)

	Fraser et al [40]	Case 3 (d)
Flow regime: photographic footage (left) and contours of 50% oil volume fraction iso-surface (right)	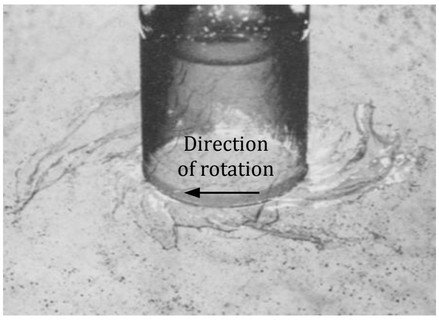	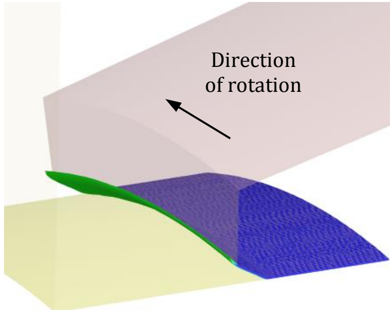
Flow regime: Air volume fraction contour plot at mid-plane	N/A	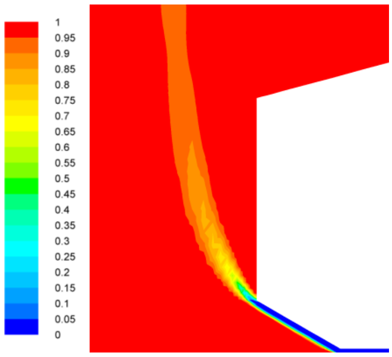
Angular velocity	ω_{Fraser}	$1.23\omega_{\text{Fraser}}$
Diameter of separation	d_{Fraser}	$3.09d_{\text{Fraser}}$
Volumetric flow rate	$\dot{V}_{\text{Fraser}}$	$4.29\dot{V}_{\text{Fraser}}$
Liquid density	ρ_{Fraser}	$1.13\rho_{\text{Fraser}}$
Liquid dynamic viscosity	μ_{Fraser}	$0.84\mu_{\text{Fraser}}$
Liquid surface tension	σ_{Fraser}	$0.86\sigma_{\text{Fraser}}$

Table 6.3 shows that the CFD model predicts the correct flow regime. As the oil separates from the rotating component, a liquid sheet is formed. The radial extent of the sheet, a, predicted by the CFD simulation is noticeably shorter compared to that observed by Fraser et al [40] for the case presented in Table 6.3. This is mainly due to two reasons. Firstly, the angular velocity, ω, used in the CFD analysis is 23% higher compared to that of the cup used by Fraser et al [40]. According to equations (2.26) and (2.27), respectively, a, decreases with increasing values of ω. Secondly, and more importantly, due to using a compressive phase interface reconstruction

scheme (section 3.1.5) in combination with growing calculational cell sizes away from the wall, details of the sheet structure and the radial extent of the sheet, a, cannot be resolved accurately in the CFD simulation. The primary goal of the CFD investigations, however, was to accurately predict the oil flow path direction. Details about the liquid disintegration phenomena after separating from the rotating component are of secondary importance for the work presented in this thesis. If the focus, however, had been on investigating detailed sheet properties, such as the sheet thickness, t_S, the radial extent of the sheet, a, and wave-like structures travelling across the sheet, a geometric phase interface reconstruction scheme in combination with a much finer computational mesh would have had to be adopted.

6.1.3 Film Thickness Validation

As previously discussed in section 2.3.3, Hinze and Milborn [44] established a formula (equation (2.21)) to calculate the fluid film thickness, t_F, on the wall of a rotating cup. Equation (2.21) is repeated below for completeness.

$$t_F = \left(\frac{3\,\dot{V}\,\nu}{2\,\pi^3\,d^2\,n^2 \sin\xi} \right)^{\frac{1}{3}} \tag{6.2}$$

In the equation above, $\dot{V}$ is the volumetric flow rate, n is the rotational speed, ξ is the opening angle of the cup (Figure 2.13), d is the cup diameter and ν is the kinematic viscosity.

With known operational parameters and liquid properties, equation (6.2) allows an expected film thickness to be calculated. This value can then be compared to the simulated film thickness in the CFD model. For a valid comparison, it must be ensured that the oil film on the gear chamfer is fully developed. Figure 6.1 shows the direction and the location of the film thickness determination in the CFD model for Case 3 (d).

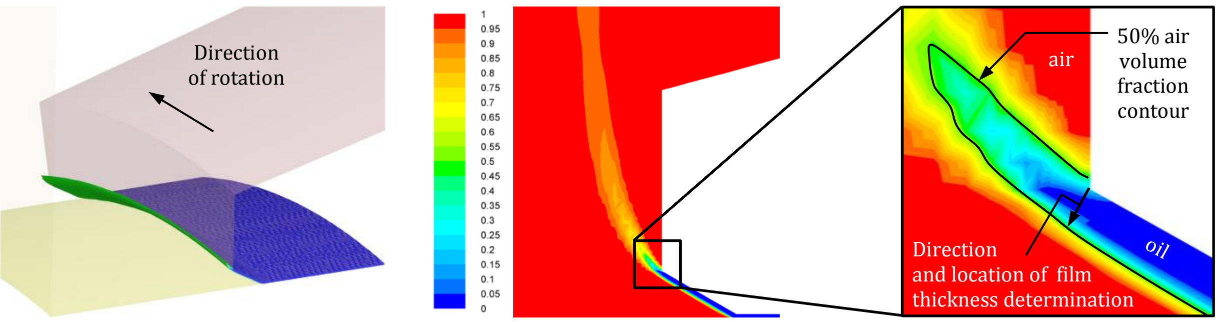

(a) Contours of 50% oil volume fraction iso-surface (b) Air volume fraction contour plot at mid-plane

Figure 6.1: Direction and location of film thickness determination

Due to numerical diffusion (section 3.1.5), the transition between the regions of 100% oil volume fraction and 100% air volume fraction is gradual. The film thickness was determined perpendicular to the wall up to an oil volume fraction value of 50%.

Table 6.4 provides a summary of the results of the film thickness determination for a number of different CFD cases. The film thickness on the planet gear chamfer was determined as shown in Figure 6.1. The data presented in Table 6.4 includes a comparison to the calculated expected film thickness values using equation (6.2) and key operating conditions for each case.

Table 6.4: Comparison of calculated (equation (6.2)) and simulated film thicknesses (CFD model) on gear chamfer

	Case 1 (d)	Case 3 (d)	Case 7	Case 8	Case 9
Angular gear velocity, ω_{G}	$\omega_{\mathrm{G,\,max\,load}}$	$\omega_{\mathrm{G,\,max\,load}}$	$\omega_{\mathrm{G,\,max\,load}}$	0.66 $\omega_{\mathrm{G,\,max\,load}}$	$\omega_{\mathrm{G,\,max\,load}}$
Outflow velocity, v_0 [m/s]	$0.140\omega_{\mathrm{G}} r_{\mathrm{G}}$	$0.140\omega_{\mathrm{G}} r_{\mathrm{G}}$	$0.140\omega_{\mathrm{G}} r_{\mathrm{G}}$	$0.047\omega_{\mathrm{G}} r_{\mathrm{G}}$	$0.047\omega_{\mathrm{G}} r_{\mathrm{G}}$
Oil temperature, T [°C]	20	$T_{\mathrm{max\,load}}$	31	31	31
Phase interface reconstruction	Compressive	Compressive	Geo-reconstruct	Geo-reconstruct	Geo-reconstruct
t_F calculated (equation (6.2)) [mm]	0.260	0.086	0.202	0.184	0.140
t_F predicted (CFD model) [mm]	0.253	0.135	0.209	0.181	0.144
Δt_F	-2.7%	+56.6%	+3.4%	-1.4%	+2.8%

A comparison between the calculated film thickness values and the ones simulated with the CFD models shows generally a very good agreement. With exception of Case 3 (d), the difference between the two values is within ±3.4% relative to the calculated value with equation (6.2). For Case 3 (d), the CFD model significantly overpredicts the film thickness (+56.6%). The following paragraph provides an explanation for this behaviour.

The derivation of the film thickness equation (equation (6.2)) established by Hinze and Milborn [44] is based on a number of assumptions, one of which is that the difference between the circumferential velocity component of the rotating cup and the liquid flowing over the cup is very small, i.e. no slip occurs between the rotating cup surface and the circumferential velocity component of the bulk flow ($F_{slip} \approx 0$). For the specific cases under investigation (Table 6.4), this assumption was verified by assessing the circumferential bulk flow velocity of the oil at the location of the film thickness measurement (Figure 6.1). The analysis revealed that for low oil temperatures ($T = 20°C$ and $T = 31°C$), i.e. high oil viscosities, there is less slip between the circumferential bulk flow velocity of the liquid and the rotating cup surface than for high oil temperatures ($T = T_{\text{max load}}$), i.e. low oil viscosities. Whilst the low oil temperature cases, namely Case 1 (d), Case 7, Case 8 and Case 9 in Table 6.4, exhibited a slip of $F_{slip} \approx 0.10 \ldots 0.14$, the high temperature case, namely Case 3 (d) in Table 6.4, exhibited a much higher slip of $F_{slip} \approx 0.30$. Thus, equation (6.2), which is used to calculate the film thickness on the gear chamfer, will produce more accurate results for cases with low oil temperatures, i.e. high oil viscosities, as the slip between the circumferential bulk flow velocity of the liquid and the surface of the rotating cup is more similar to the assumption made by Hinze and Milborn [44].

In summary, it can be concluded that for the case under investigation the oil film thickness, t_F, on the gear chamfer is a suitable parameter for validating the CFD model, providing the assumptions used for establishing the film thickness equation (equation (6.2)) are valid.

6.2 Experimental Validation

The experimental campaign described in chapter 5 allows the CFD models to be qualitatively validated by comparing the simulated oil outflow behaviour with that observed in the test rig. Validation of the CFD models of non-orbiting journal bearings with constant lubricating gap heights, h_0, is beneficial as sector models with rotationally periodic boundary conditions can be used. Being able to use a sector model has a number of advantages.

a) For a given mesh density, the calculational cell count to discretise the external flow domain is significantly smaller compared to that of a full 360° model and proportional to the size of the sector.
b) Multiple operating points can be assessed as the computational time required to reach steady state flow field conditions is drastically reduced.
c) Reasonably short computational times to reach steady state flow field conditions can still be achieved with a much denser mesh.

In section 4.1.5, a sensitivity study with respect to the computational grid density in the y-z-plane (section 4.1.5.1) and the θ-direction (section 4.1.5.2) was presented. The key conclusion from this study was that the predicted oil flow path directions are independent of the chosen computational grid density within the investigated ranges. Moreover, section 4.1.3 showed that the predicted oil flow path direction is independent of the chosen phase interface reconstruction scheme. It is therefore valid to conduct the CFD model validation with a computational grid that is denser than the baseline grid used in chapter 4 and with the most accurate phase interface reconstruction scheme available, i.e. the geometric reconstruction scheme. This combination will provide a higher resolution of the flow field and the flow structures.

6.2.1 CFD Model Set-Up

In this section, the CFD model set-up for the validation of the predicted oil outflow behaviour against selected experimental test conditions will be discussed. The general approach of generating the computational mesh for the domain under investigation has previously been described in section 3.3. Figure 6.2 shows a 2D plane of the mesh used for the CFD validation cases investigated in this section. The geometry of the domain is identical to the nominal dimensions of the test rig (chapter 5).

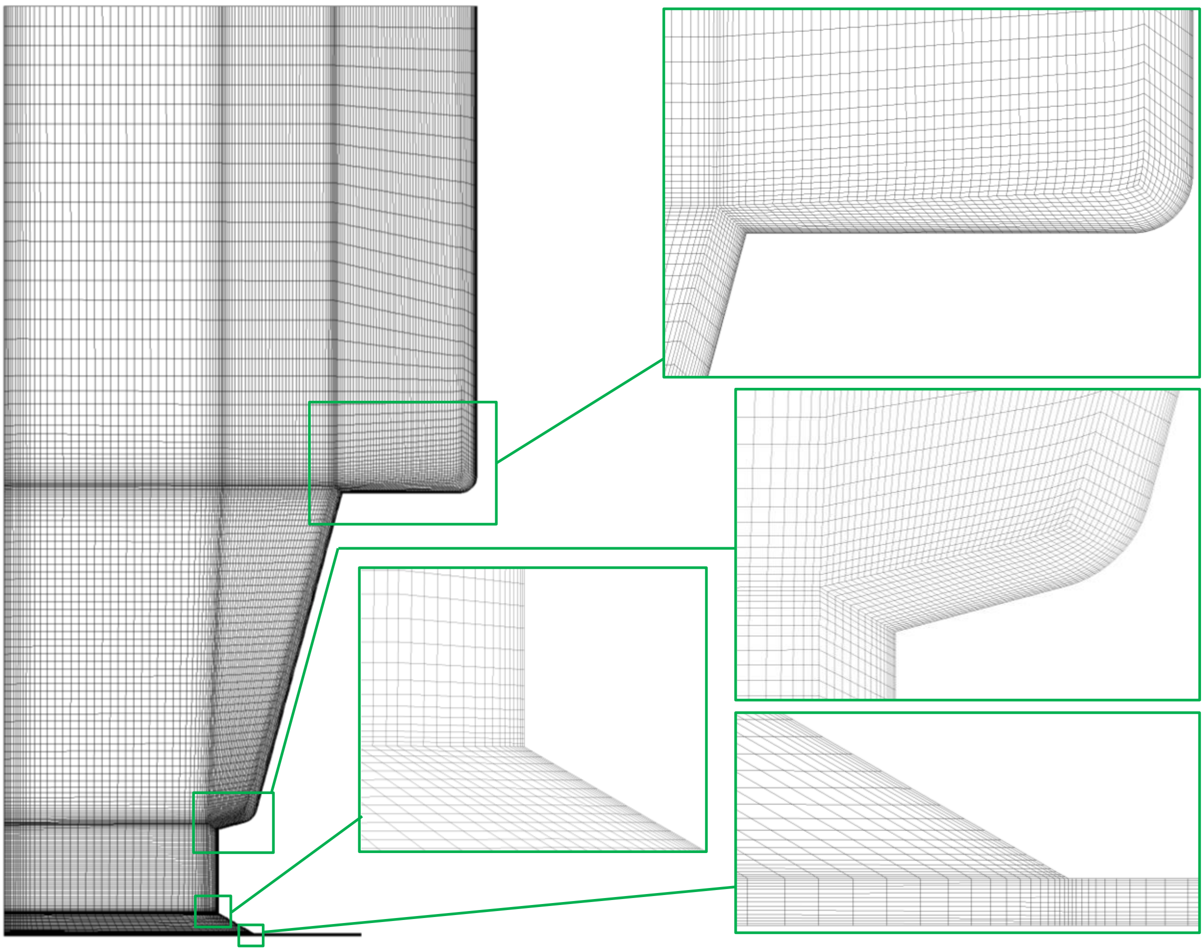

Figure 6.2: 2D computational grid for CFD validation cases

The 2D mesh was subsequently rotated about gear's axis to create a 20° sector model, as shown in Figure 6.3. Key mesh parameters are summarised in Table 6.5

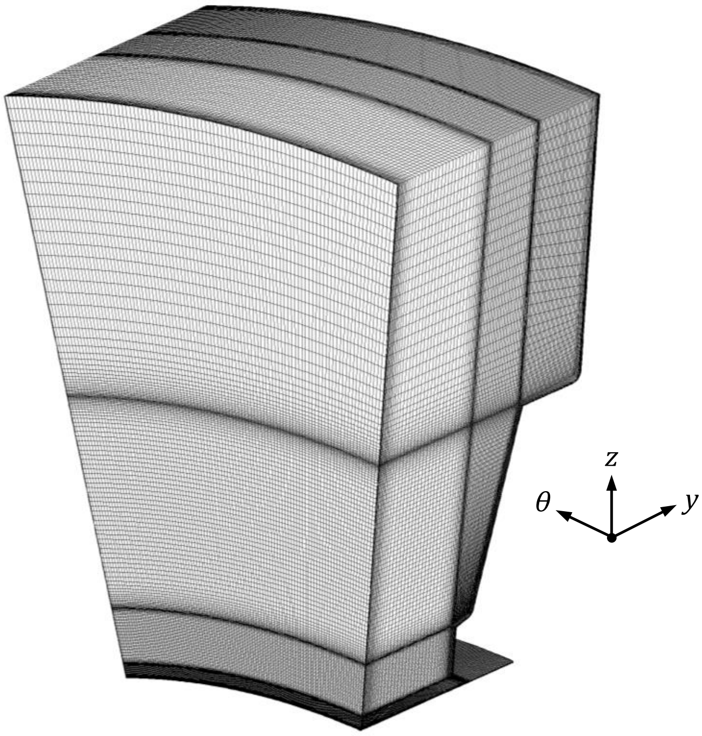

Figure 6.3: 3D computational grid for CFD validation cases

Table 6.5: Mesh properties for CFD validation cases

Mesh parameter	Value
Cell count in each 2D plane	19,002
Cell count in circumferential direction	99 (100 node points)
Total cell count in 20° sector	1,881,198
Lubricating gap height, h_0	125 μm
Number of cells across h_0	14 (15 node points)
Height of first cell perpendicular to wall	0.01 mm
Cell growth factor	1.0…1.2

The boundary condition types applied to the domain are identical to those used for the CFD sector analyses presented in section 4.1. Figure 6.4 shows the domain boundaries and the applied boundary condition types. For illustration purposes, dimensions are not to scale.

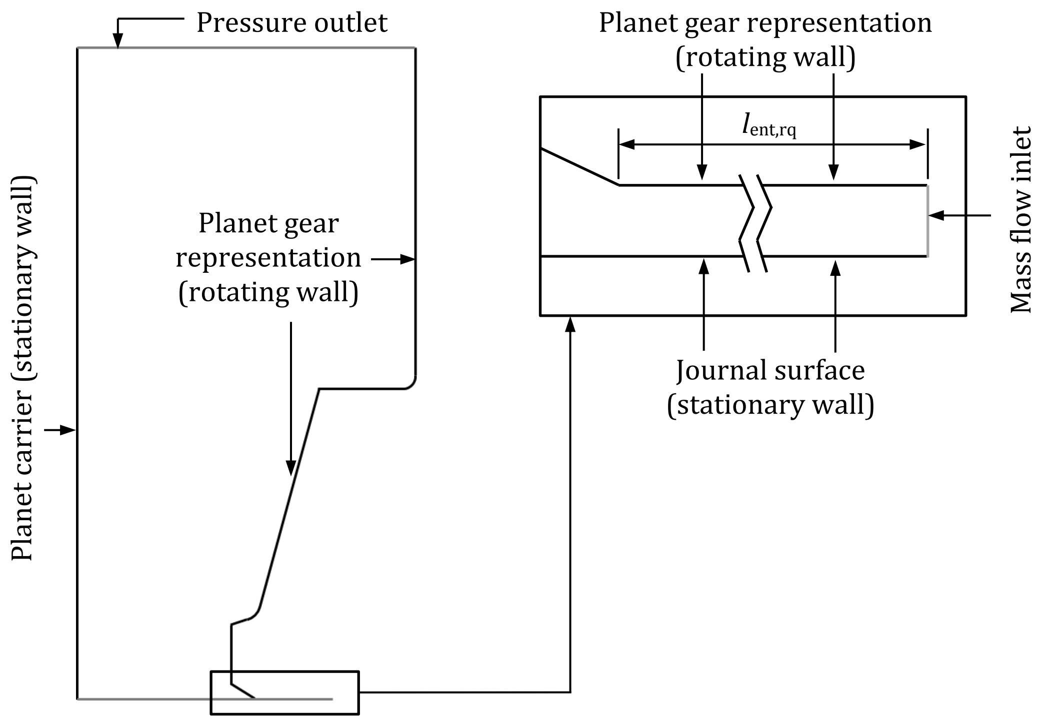

Figure 6.4: Boundary condition types applied to domain under investigation

In section 4.1.7, it was concluded that patching an oil meniscus between the gear chamfer and the pin surface, as shown in Table 4.10 (e), provides the preferred initial wall condition. Thus, the CFD models used to simulate key experimental test conditions were set up to include a patched oil meniscus at the exit of the lubricating gap. The liquid properties required to run the CFD models were determined based on the oil plenum temperature, T_{Pl}, of the associated experimental test case. Case specific boundary conditions, such as the angular velocity of the planet gear representation, ω_{G}, the volumetric feed flow rate, $\dot{V}_{\mathrm{in}}$, and the liquid temperature, $T = T_{\mathrm{Pl}}$, which determines the values for the liquid density, ρ, the dynamic viscosity, μ, and the surface tension, σ, are mentioned in the appropriate paragraphs in section 6.2.2. A complete list of all numerical settings for the CFD validation cases is included in Appendix 8.

6.2.2 CFD Model Validation Results

This section shows a qualitative comparison between the key flow regimes observed during experimental rig testing and the outflow behaviour predicted by a CFD model with identical operational parameters. Similar to the approach used when presenting the experimental results in section 5.5, the following figures show the flow regimes with increasing rotational speed, n_{G}, and/or volumetric flow rate, $\dot{V}_{\mathrm{in}}$. The stated values for $\dot{V}_{\mathrm{in}}$ refer to the total volumetric oil feed flow rate supplied to the test module. This flow rate is evenly split into a portion exiting towards the front and towards the rear of the test module. This approach is consistent with that used in chapter 5.

In Table 6.6, the phase interface is visualised by an iso-surface (green) that indicates 50% oil volume fraction. Areas shaded in blue indicate that the oil is in full contact with the appropriate surface of the planet gear representation, the pin or the planet carrier.

Table 6.6: Qualitative comparison between key experimental operating conditions and CFD model results

<table>
<tr><td>Experimental test case</td><td>CFD model prediction</td></tr>
<tr><td>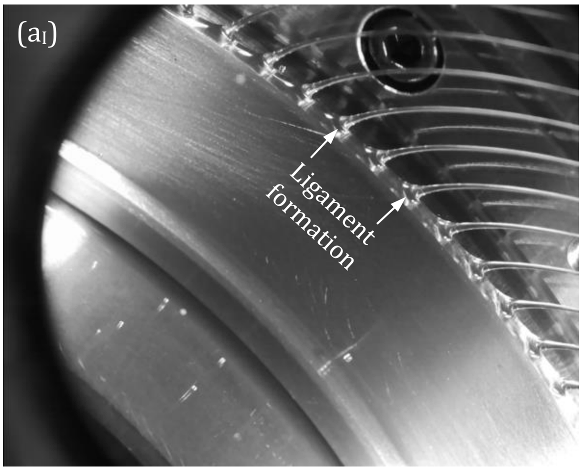
</td><td>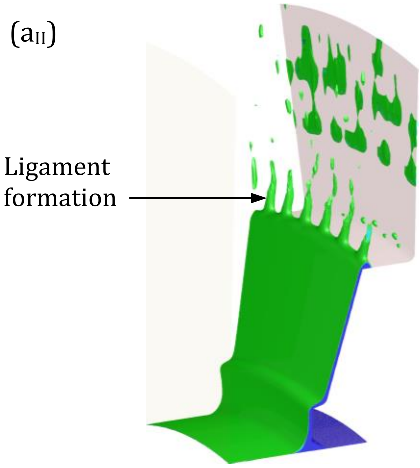
</td></tr>
<tr><td colspan="2">CFD validation Case a): $\dot{V}_{\mathrm{in}} = 4$ l/min, $n_{\mathrm{G}} = 250$ rpm, $T_{\mathrm{Pl}} = 30.9$°C</td></tr>
<tr><td>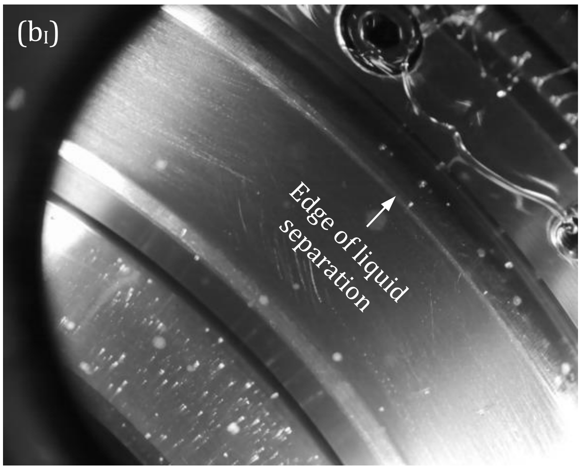
</td><td>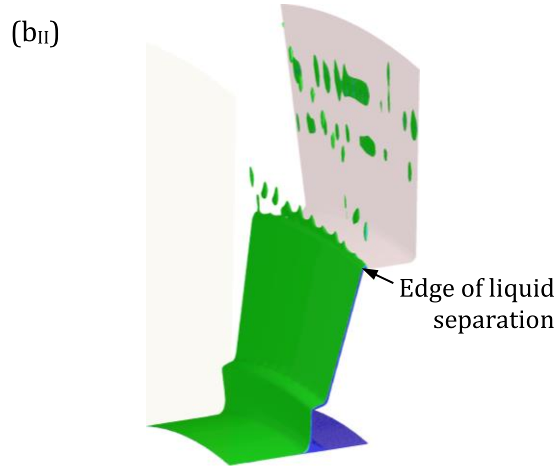
</td></tr>
<tr><td colspan="2">CFD validation Case b): $\dot{V}_{\mathrm{in}} = 4$ l/min, $n_{\mathrm{G}} = 500$ rpm, $T_{\mathrm{Pl}} = 30.9$°C</td></tr>
</table>

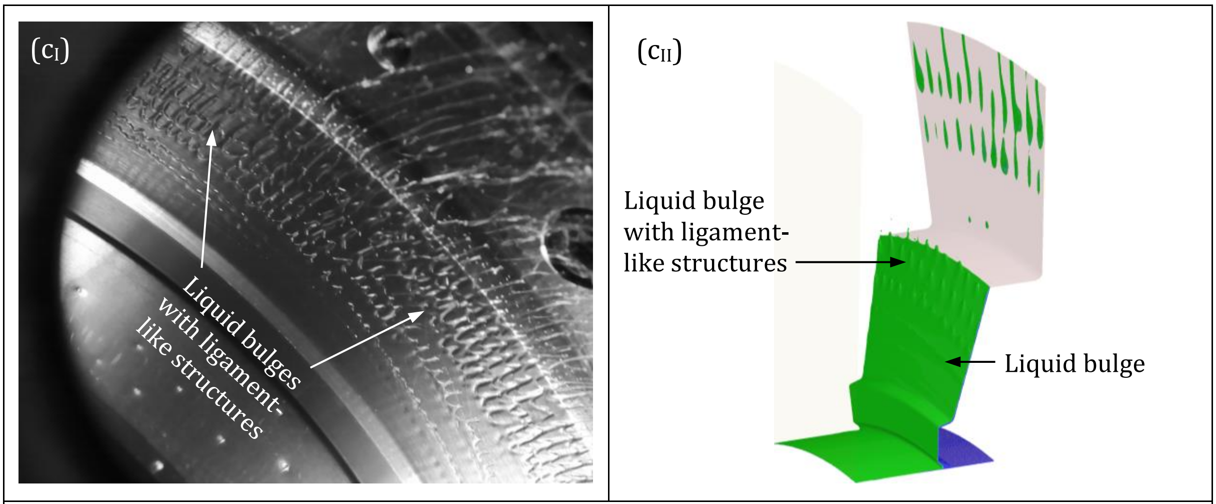

CFD validation Case c): $\dot{V}_{\text{in}} = 10$ l/min, $n_{\text{G}} = 2{,}000$ rpm, $T_{\text{Pl}} = 34.2$°C

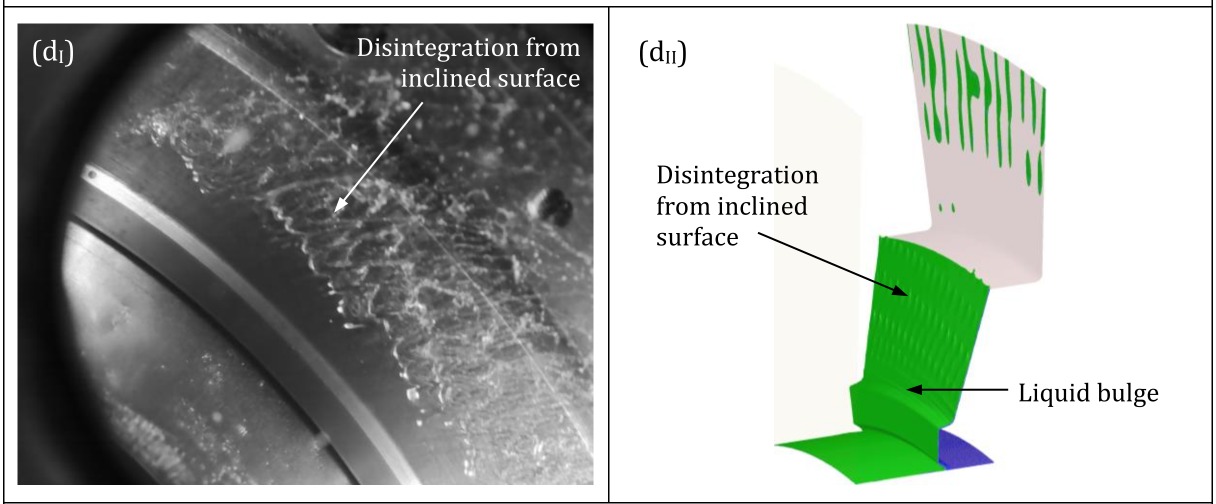

CFD validation Case d): $\dot{V}_{\text{in}} = 20$ l/min, $n_{\text{G}} = 4{,}000$ rpm, $T_{\text{Pl}} = 41.0$°C

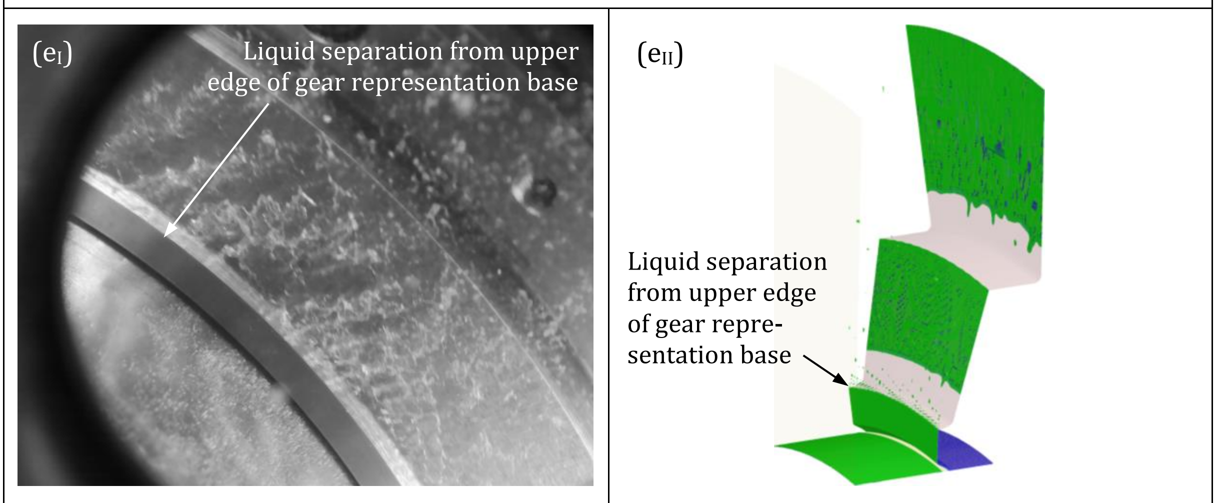

CFD validation Case e): $\dot{V}_{\text{in}} = 20$ l/min, $n_{\text{G}} = 6{,}000$ rpm, $T_{\text{Pl}} = 49.6$°C

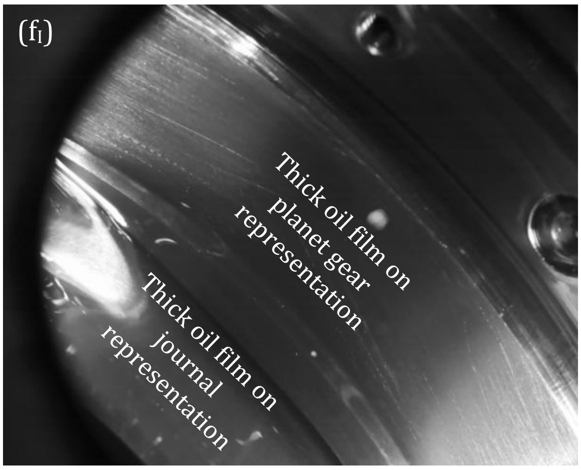

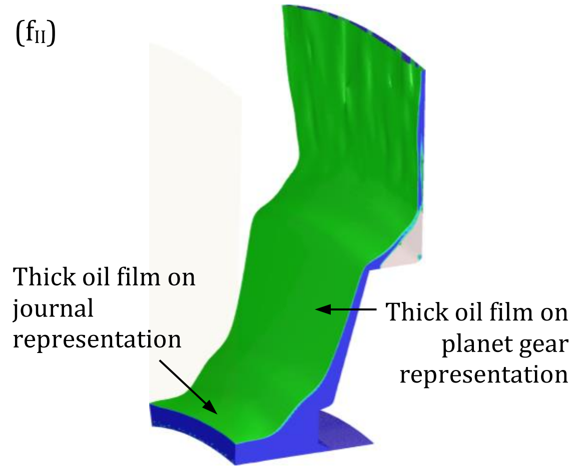

CFD validation Case f): $\dot{V}_{\mathrm{in}} = 40$ l/min, $n_{\mathrm{G}} = 250$ rpm, $T_{\mathrm{Pl}} = 28.0$°C

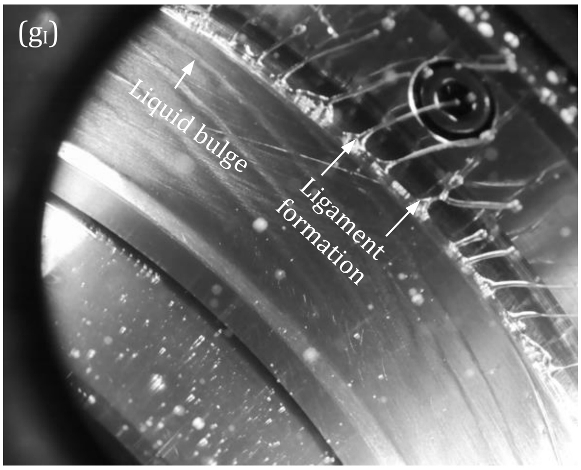

(g_{II}) – transient

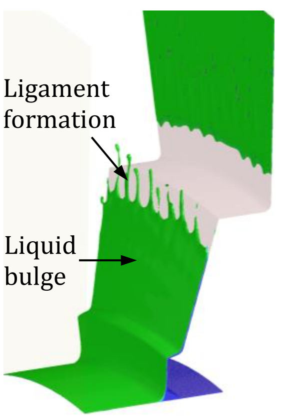

(g_{III}) – steady state

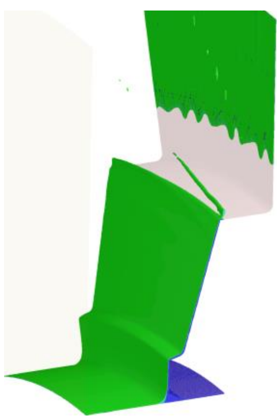

CFD validation Case g): $\dot{V}_{\mathrm{in}} = 4$ l/min, $n_{\mathrm{G}} = 500$ rpm, $T_{\mathrm{Pl}} = 53.2$°C

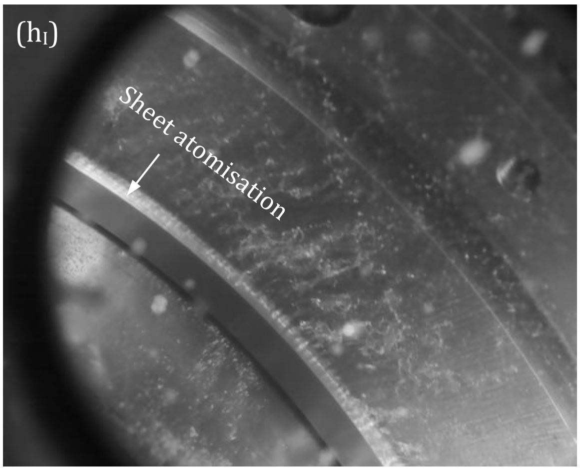

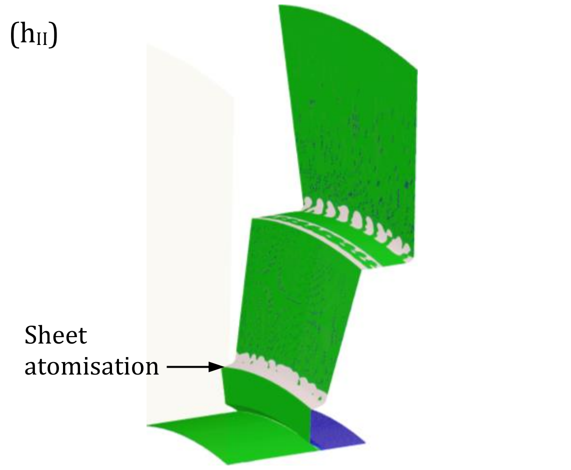

CFD validation Case h): $\dot{V}_{\mathrm{in}} = 20$ l/min, $n_{\mathrm{G}} = 5{,}000$ rpm, $T_{\mathrm{Pl}} = 64.6$°C

Table 6.6 (a) shows an operating point at which ligaments are generated from the upper edge of the planet gear representation (diameter d_3 in Figure 5.4). These ligaments are spaced nearly equally around the planet gear representation's circumference. The CFD model is able to accurately predict the flow path direction observed during the experiment. This includes the correct prediction of the point of liquid separation from the planet gear representation's geometry, the correct prediction of the liquid disintegration regime (ligament formation) and the correct number of ligaments within a 20° sector. Whilst the experiments showed the number of ligaments to be between six and seven within a 20° sector, the CFD model predicts six ligaments. However, previously published studies demonstrated that the number of ligaments predicted by a CFD model with geometric phase interface reconstruction is dependent on the number of cells in the circumferential direction [82]. The correct prediction of the number of ligaments in a sector can therefore not be relied on. Moreover, the length of the ligaments is underpredicted. This is mainly due to two reasons. Firstly, the size of the calculational cells increases with increasing distance from the walls. Thus, the resolution of the domain core is lower compared to that in the vicinity of the domain boundaries. Secondly, as the ligaments stretch into the atmosphere, they become thinner and a larger number of calculational cells is required to accurately model the phase interface. This combination results in an underprediction of the length of the ligaments.

When doubling the rotational speed from $n_{\mathrm{G}} = 250$ rpm to $n_{\mathrm{G}} = 500$ rpm, with otherwise identical operational conditions (Table 6.6 (b)), the liquid disintegration regime transitions from ligament formation to sheet formation. Similar to CFD validation Case a), liquid separation occurs at the upper edge of the planet gear representation (diameter d_3 in Figure 5.4). The CFD model is able to accurately predict the flow path direction and the point of liquid separation from the planet gear representation's geometry. Unlike the observations made in the experiment, the CFD model predicts the liquid to disintegrate into ligament-like structures. Compared to CFD validation Case a), these are, however, much less pronounced and have a much closer spacing in the circumferential direction. This makes the predicted disintegration regime to appear more similar to sheet formation. The CFD model is unable to accurately resolve the sheet and the rim of the sheet. The radial extent of the sheet, a, is underpredicted by some margin. The two main reasons for this were discussed during the assessment of CFD validation Case a) in the first paragraph of this section.

When increasing the volumetric oil flow rate to $\dot{V}_{\mathrm{in}} = 10$ l/min and the rotational speed to $n_{\mathrm{G}} = 2{,}000$ rpm (Table 6.6 (c)), liquid separation occurs from the inclined surface between the upper edge of the planet gear representation's base (diameter d_2 in Figure 5.4) and the upper edge of the planet gear representation (diameter d_3 in Figure 5.4). This flow regime was described in detail in section 5.5, Figure 5.5 (f). Due to the centrifugal force acting on the oil film, radially outwards travelling liquid bulges develop ligament-like structures which are formed perpendicular to the involute curves described by the liquid bulges. The CFD model is able to accurately predict the flow path direction and the locations of liquid separation from the planet gear representation's geometry. In the vicinity of the domain boundaries, where the size of the calculational cells is small, and thus the resolution of the phase interface is high, detailed flow structures are accurately resolved. At lower radii, i.e. radii close to diameter d_2 (Figure 5.4), this includes the wave-like liquid bulges which travel radially outwards and describe an involute curve. At higher radii, i.e. radii close to diameter d_3 (Figure 5.4), this includes the ligament-type disintegration of the liquid bulges. However, the very thin ligaments and small droplets separating from the upper edge of the planet gear representation (diameter d_3 in Figure 5.4) are not resolved by the CFD model. The two main reasons for this were discussed during the assessment of CFD validation Case a) in the first paragraph of this section.

When doubling the volumetric flow rate to $\dot{V}_{\mathrm{in}} = 20\,\mathrm{l/min}$ and the rotational speed to $n_{\mathrm{G}} = 4{,}000$, respectively, liquid separation continues to occur from the inclined surface between the upper edge of the planet gear representation's base (diameter d_2 in Figure 5.4) and the upper edge of the planet gear representation (diameter d_3 in Figure 5.4) (Table 6.6 (d)). Compared to CFD validation Case c), the flow disintegration is much more turbulent. The CFD model is able to accurately predict the flow path direction and the locations of liquid separation from the planet gear representation's geometry. As the rotational speed for this case is higher compared to that of CFD validation Case c), liquid separation from the planet gear representation's geometry starts at lower radii, i.e. radii closer to diameter d_2 (Figure 5.4). This fact is represented by the CFD model. However, the model is unable to resolve small turbulent structures and thin ligaments due to the limitations imposed by the topology of the calculational mesh, which were discussed when assessing CFD validation Case a) in the first paragraph of this section.

When further increasing the rotational speed from $n_{\mathrm{G}} = 4{,}000$ rpm to $n_{\mathrm{G}} = 6{,}000$ rpm, whilst maintaining a volumetric flow rate of $\dot{V}_{\mathrm{in}} = 20\,\mathrm{l/min}$ (Table 6.6 (e)), liquid separation occurs from the upper edge of the planet gear representation's base (diameter d_2 in Figure 5.4). A very thin sheet with a very small radial extent, a, develops and disintegrates into small droplets. The CFD model is able to accurately predict the flow path direction and the location of liquid separation from the planet gear representation's geometry. Larger droplets can be resolved by the calculational mesh. However, smaller ones cannot be captured with the chosen mesh density. Compared to the experiment, the CFD model underpredicts the amount of generated small droplets by some margin. This is due to the limitations imposed by the chosen mesh topology, which were discussed when assessing CFD validation Case a) in the first paragraph of this section.

Table 6.6 (f) shows the oil outflow behaviour for a very high volumetric flow rate of $\dot{V}_{\mathrm{in}} = 40\,\mathrm{l/min}$ in combination with a low rotational speed of $n_{\mathrm{G}} = 250$ rpm. For these conditions, axial and radial oil outflow prevail. Oil which exits the lubricating gap in the axial direction drains almost immediately into the oil sump under gravity. The rotating motion of the planet gear representation causes some oil to be entrained by this component. As a result, radial oil outflow occurs. The experiment, as shown in Table 6.6 ($\mathrm{f_I}$), indicates that the pin is fully covered by a thick film of oil. The image was captured as a droplet impacts on the oil film on the pin. This causes a local change in the film thickness, leading to an apparent distortion of the edges of the gear representation's base. Under these conditions, i.e. $\dot{V}_{\mathrm{in}} = 40\,\mathrm{l/min}$, $n_{\mathrm{G}} = 250\,\mathrm{rpm}$ and $T_{\mathrm{Pl}} = 28.0$°C, it is difficult to observe radial outflow by visual inspection of a stationary image, as shown in Table 6.6 ($\mathrm{f_I}$). Radial oil outflow, however, could be reliably identified when assessing the video for the case under investigation. Moreover, Figure 5.7 (a) in section 5.6, which showed the oil outflow behaviour for very similar operational conditions, i.e. $\dot{V}_{\mathrm{in}} = 40$ l/min, $n_{\mathrm{G}} = 100$ rpm and $T_{\mathrm{Pl}} = 33.1$°C, allowed radial oil outflow to be detected through the observation of air bubbles in the vicinity of the upper edge of the planet gear representation (diameter d_3 in Figure 5.4). The CFD model is able to accurately predict the flow path both in the axial and the radial directions. In the CFD simulation, the oil film separates from the upper edge of the planet gear representation (diameter d_3 in Figure 5.4) and reattaches to the vertical surface containing the bolts which connect the planet gear representation to the drive flange. This creates an air pocket which was experimentally observed for $\dot{V}_{\mathrm{in}} = 40$ l/min, $n_{\mathrm{G}} = 100$ rpm and $T_{\mathrm{Pl}} = 33.1$°C (Figure 5.7 (a) in section 5.6). However, the experimental test conditions for the case under investigation, i.e. $\dot{V}_{\mathrm{in}} = 40\,\mathrm{l/min}$, $n_{\mathrm{G}} = 250$ rpm, $T_{\mathrm{Pl}} = 28.0$°C could not conclusively confirm this flow path behaviour in this area of the domain under investigation

Table 6.6 (g) shows the oil outflow behaviour for a volumetric flow rate of $\dot{V}_{\mathrm{in}} = 4$ l/min and a rotational speed of $n_{\mathrm{G}} = 500$ rpm, respectively, which were previously discussed in Table 6.6 (b). The oil plenum temperature, T_{Pl}, however, was increased from $T_{\mathrm{Pl}} = 30.9$°C to $T_{\mathrm{Pl}} = 53.2$°C. Thus, the liquid's dynamic viscosity, μ, is significantly reduced by a factor of approximately three. This alters the liquid disintegration regime from the planet gear representation's upper edge (diameter d_3 in Figure 5.4) from sheet formation to ligament formation (Table 6.6 ($\mathrm{g_I}$)). As previously reported for CFD validation Cases c) and d), respectively, wave-like liquid bulges, which describe involute curves, travel radially outwards across the planet gear representation's inclined surface. The CFD model is able to accurately predict the oil flow path direction and the point of liquid separation from the planet gear representation's geometry. In transient conditions (Table 6.6 ($\mathrm{g_{II}}$)), the ligaments developing from the radially outwards progressing oil front are accurately resolved. This is due to the high computational mesh density in the vicinity of the domain boundaries. Wave-like liquid bulges traveling across the planet gear representation's inclined surface can also be observed in the associated CFD simulation (Table 6.6 (g_{II})), even though they are much more faint compared to those captured in the experiment (Table 6.6 (g_{I})). In steady state conditions, the CFD model is unable to resolve the ligaments separating from the upper edge of the planet gear representation (diameter d_3 in Figure 5.4) (Table 6.6 (g_{III})). Due to the lower dynamic oil viscosity, μ, compared to CFD validation Case b), the oil film thickness for the case under investigation is smaller and associated flow structures, such as ligaments, are thinner and shorter. Thus, the CFD model is unable to resolve these flow structures as they separate from the upper edge of the planet gear representation (diameter d_3 in Figure 5.4) with the chosen computational mesh density.

Table 6.6 (h) shows the oil outflow behaviour for a volumetric flow rate of $\dot{V}_{\mathrm{in}} = 20\,\mathrm{l/min}$, a rotational speed of $n_{\mathrm{G}} = 5{,}000\,\mathrm{rpm}$ and an oil plenum temperature of $T_{\mathrm{Pl}} = 64.6°\mathrm{C}$. Similar to CFD validation Case e), liquid separation occurs from the upper edge of the planet gear representation's base (diameter d_2 in Figure 5.4). A very thin sheet with a very small radial extent, a, develops and disintegrates into small droplets. The CFD model is able to accurately predict the flow path direction and the location of liquid separation from the planet gear representation's geometry. The limitations with respect to resolving single droplets, which have been previously discussed when assessing CFD validation Case e), are also valid for this case. Thus, compared to the experiment, the CFD model underpredicts the amount of generated small droplets by some margin.

Based on the assessments of the CFD validation cases presented in this section, the following conclusions can be drawn:

a) The CFD models accurately predict the flow path direction and the point of liquid separation from the planet gear representation's geometry.

b) In the vicinity of the domain boundaries, where the density of the computational mesh is high, detailed flow features, such as wave-like liquid bulges on the inclined surface of the planet gear representation, and ligament-like flow structures, are well resolved. They qualitatively compare well to the experiments.

c) In areas where the computational mesh is less dense, detailed flow structures as described in point b) above cannot be accurately resolved. This is especially true for operating conditions with high rotational speeds, n_{G}, and low dynamic liquid viscosities, μ, when the prevailing flow structures are very small. It is not practicable to resolve these structures as the required computational mesh density would not allow the steady state flow field behaviour in the domain under investigation to be simulated with the available computational resources in the given time-scales. Moreover, in order to meet the objectives of the work presented in this thesis (section 1.3), the accurate resolution of these flow structures is not necessary.

As highlighted in the introduction to this chapter, the primary purpose of the performed validation work was to confirm the validity of the computational flow investigations of a non-orbiting journal bearing with a constant lubricating gap height, h_0, presented in section 4.1. Based on the comparisons between the numerical results and analytically obtained data (section 6.1) and experimental validation work (section 6.2), the CFD models results presented in section 4.1 are considered valid.

The gained knowledge from these investigations can be directly applied to provide information on the preferred oil outflow direction, and thus guidance and methods to control the flow path of the oil as it enters into the external flow domain (section 6.3).

6.3 Implementation and Application of Created Knowledge in Chapter 4

The combined results presented in sections 6.1 and 6.2 concluded the validity of the CFD model results of a non-orbiting journal bearing with a constant lubricating gap height, h_0, presented in section 4.1. This allows the preferred oil outflow direction to be determined (section 6.3.1) and guidance on flow control mechanisms in the external domain to be provided.

6.3.1 Preferred Oil Outflow Direction

The combination of the theoretical considerations presented in section 2.3 and the analysis of the full steady-state flow field conditions presented in section 4.1.4 allow the preferred oil outflow direction to be determined. Axial oil outflow is preferred over radial oil outflow for the following reasons.

- **Lower load-independent power losses:** Axial outflow exhibits fewer interactions with the rotating planet gear. Thus, less momentum is transferred from the gear into the oil and less heat is being generated. Moreover, particularly for high rotational speeds, radial oil outflow is atomised when separating from the upper edge of the gear base (diameter d_2 in Figure 2.2). Consequently, the mean density inside the gearbox chamber will increase, leading to higher windage losses. With radial oil outflow, an intermittent oil film is formed on the end-face of the gear teeth (Figure 4.8). If hot oil, which has already been worked inside the lubricating gap of the journal bearing, is being entrained into the gear tooth contacts, the risk of tooth contact over-lubrication increases. All these mechanisms are detrimental to the efficiency of the gearbox as load-independent power losses increase. For axial oil outflow these mechanisms are either not present or much less severe.

- **Potentially longer lubricant lifetime:** If hot oil, which has already been worked inside the lubricating gap of the journal bearing, is being entrained into the gear tooth contacts, the risk of oil over-heating increases. This may accelerate the aging of the lubricant.
- **Potentially lower oil consumption:** Axial oil outflow produces a relatively homogeneous film instead of highly dispersed droplets, as seen with radial oil outflow. As part of the oil scavenging process in an aero-engine, the oil typically passes through an air-oil-separator. This separation is more efficient for continuous, homogeneous films with small amounts of residual air. The air-oil-separation is less efficient for highly dispersed flows with small droplets and large amounts of air. Therefore, for radial outflow, the oil consumption is potentially higher than for axial oil outflow.
- **Reduced risk of oil interaction with the sun gear when operating in a planetary configuration (Figure 1.1):** When axial oil outflow occurs, the oil entering into the external flow domain travels across the pin until it reaches the planet carrier. From there, the oil is driven radially outwards with respect to the planet carrier axis (Figure 4.9). Hence, the risk of oil interacting with the sun gear can expected to be low. In contrast, when radial oil outflow occurs, oil attached to the rotating gear will attain a circumferential velocity component with respect to the gear axis. Depending on the magnitude of the centrifugal forces generated by the rotating gear, $F_{\mathrm{c,G}}$, and by the planet carrier rotation, $F_{\mathrm{c,C}}$, compared to axial oil outflow, there is an increased risk of oil being flung towards the sun gear and the other planet gears. As discussed above, interactions between the oil and a rotating gear may have an adverse effect on the load-independent power losses, lubricant life and oil consumption.

6.3.2 Suggested Design Improvements

In order to avoid the potential risks associated with radial oil outflow and to optimise axial oil outflow, the following design changes are proposed for the planet gear, the pin and the planet carrier, respectively. The proposed design changes aim to minimise the power losses caused by the interaction between the oil and the components bounding the domain under investigation. Figure 6.5 schematically shows the initial, i.e. unchanged geometry of the planet gear, the pin and the planet carrier. Figure 6.6 shows a detailed view on the proposed design changes.

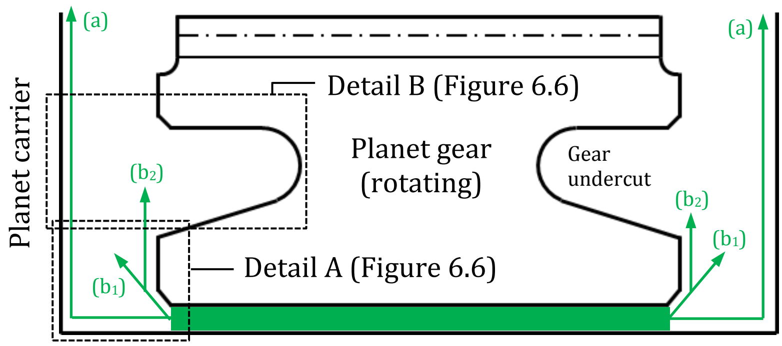

Figure 6.5: Concepts for design changes applied to domain under investigation

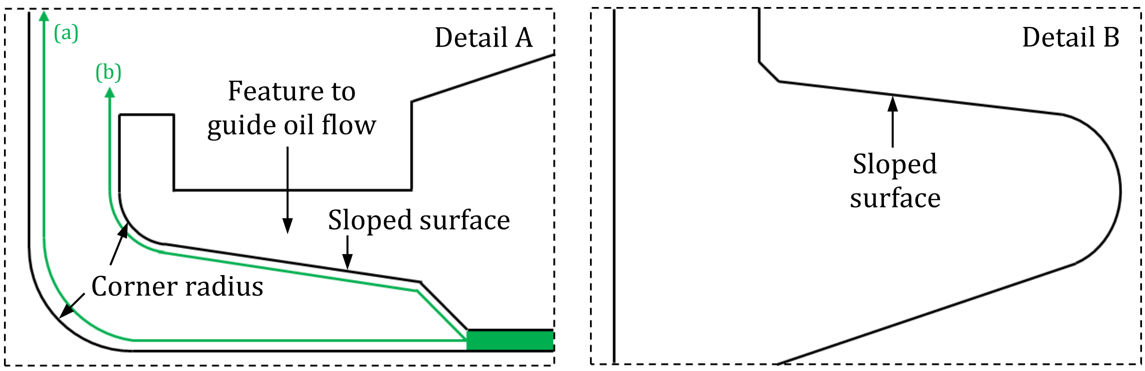

Figure 6.6: Detail A and Detail B (Figure 6.5)

The intent of the design feature shown in Figure 6.6 Detail A is to guide the oil in the axial direction if radial oil outflow occurs. In this case, oil, which emerges from the lubricating gap into the external domain, attaches to the chamfer of the planet gear base and follows the gear contour. The sloped surface of the design feature in this area ensures that the oil film remains thin. This mitigates the risk of imbalance forces generated by an uneven distribution of the oil film thickness. The corner radius allows the oil film to turn smoothly and to separate from a defined point. As the design feature protrudes significantly into the space between the planet carrier and the planet gear, the risk of oil deposition in the undercut of the gear (Figure 6.5) is greatly reduced.

However, there is still a risk of an oil film being formed in the gear undercut due to secondary droplet deposition, i.e. through droplets that are not created by direct droplet formation, ligament or sheet disintegration, but through liquid-solid interaction, e.g. oil interaction with the domain walls, liquid-gas interaction, e.g. oil interaction with the air, and liquid-liquid interaction, e.g. oil droplet impingement on films. It is imperative to mitigate the potential imbalance forces originating from an uneven distribution of the oil film thickness. This can be achieved by a design change to the initially horizontal surface of the gear undercut (Figure 6.5). Applying a slope to the surface in question, as shown in Figure 6.6 Detail B, helps to reduce the oil film thickness in this area and all associated detrimental effects on the gear's performance.

Even though the proposed design changes are likely to yield improvements related to the fluid flow behaviour within the domain under investigation, they are likely to have an adverse effect on the journal bearing's weight and cost of manufacturing. For this reason, a holistic assessment of the proposed design changes with respect to other key system parameters is strictly necessary.

7 Conclusions and Recommendations

In the previous chapter, the CFD model results of a non-orbiting journal bearing with a constant lubricating gap height, h_0, were validated by comparison to qualitative and quantitative data obtained from analytical and empirical models, and rig test results.

The aim of this chapter is to present the overall conclusions of the work performed as part of this project. Newly created knowledge will be highlighted and key achievements, and their impact, will be discussed. Points 1) to 5) mentioned below are linked to the appropriate objective with the same number set out in section 1.3.

1) Validated CFD analysis capabilities for the evaluation of external oil flow from a journal bearing were developed. The CFD analysis capabilities developed as part of this work include:

   a) The choice of a suitable multiphase model in junction with the selection of appropriate numerical sub-models and settings, which is capable of accurately predicting the flow path of the oil as it emerges from the lubricating gap into the external flow domain (section 3.1), in time scales that are acceptable for industrial applications.
   b) A computational grid generation approach which enables the spatial discretisation of the domain under investigation that meets the requirements of the chosen multiphase model (section 3.3).
   c) Representative velocity inlet boundary conditions for the external oil flow from a journal bearing with a constant lubricating gap height, h_0 (section 3.4), and with a convergent-divergent lubricating gap height, h (section 3.5).

   The choices made for the set-up of the CFD models are justified by the good qualitative and quantitative agreement between the CFD simulation results and the analysis and experimental investigations presented as part of the CFD model validation work (chapter 6).

2) Novel insights into external oil flow from a journal were gained through both numerical simulations and experimental rig testing. This enabled the knowledge gaps identified in

section 1.2.5 to be addressed. Points a) to h) mentioned below are linked to the appropriate knowledge gap with the same letter identified in section 1.2.5.

a) The preferred outflow direction of the oil as it enters into the external flow domain, i.e. axial oil outflow, was identified through a combination of the theoretical considerations presented in section 2.3 and the analysis of the full steady state flow field conditions presented in section 4.1.4. The reasons as to why axial oil outflow is preferred compared to radial oil outflow are summarised in section 6.3.1.

b) Based on the knowledge for the preferred oil outflow direction, i.e. axial oil outflow, new design concepts were developed to control and guide the oil flow after exiting the lubricating gap (section 6.3.2). The aim of all flow control mechanisms is to encourage axial oil outflow and to minimise oil film disintegration or atomisation through excessive interactions with the components bounding the domain under investigation.

c) The oil flow path direction, i.e. axial or radial oil outflow, can be reliably determined through CFD analysis or by using empirical data presented in section 5.6. The flow path direction depends on the specific operating conditions and fluid properties. The oil outflow velocities at the inlet to the external domain can be determined through the analytical considerations presented in sections 3.4 and 3.5. At any other location within the domain under investigation, the air and oil flow velocities can be determined by CFD analysis.

   The development of predictive capabilities to determine the oil flow path direction of the liquid as it enters into the external flow domain is a novel contribution to knowledge.

d) The combination of CFD analysis and experimental flow investigations enabled the oil interactions with the air surrounding the bearing, and the components bounding the domain under investigation, namely the planet gear, the planet carrier and the pin, to be identified.

   For representative aero-engine operating conditions, axial oil outflow produces a homogeneous film, whilst radial oil outflow leads to liquid atomisation. The investigations revealed the air-oil flow field behaviour after the oil entered into the external flow domain, which is a novel contribution to knowledge

e) Through the experimental flow investigations presented in section 5.5, the oil flow regimes, namely direct droplet formation, ligament formation and sheet formation, were determined. Moreover, the sheet disintegration mechanisms, namely rim disintegration and wave disintegration, for liquid flow over a non-orbiting journal bearing with a constant lubricating gap height, h_0, were identified based on the journal bearing's operating conditions and fluid properties.

f) Through both CFD analysis and experimental flow investigations, knowledge could be created with respect to how the oil interacts with the components bounding the domain under investigation.

g) Parameters affecting the oil outflow behaviour were determined through CFD analysis (section 4.1) and confirmed by the experimental flow investigations (sections 5.5 and 5.6). Primarily, these were identified to be the axial outflow velocity, v, the liquid's dynamic viscosity, μ, and the planet gear's angular velocity, ω_G.

h) For the assessment of different or future journal bearing designs, it is recommended to follow the methodology presented in chapter 3. The suitability of the presented methods was confirmed and justified through analytical considerations and by the good qualitative and quantitative agreement between the CFD simulation results and the analysis and experimental investigations presented as part of the CFD model validation work (chapter 6).

3) Capabilities for the evaluation of external oil flow from a journal bearing were developed based on analytical and empirical investigations. This includes the creation of a flow regime map (section 5.5) and a flow path map (section 5.6). In combination with the extension to Friedrich's et al [45] force balance model (section 3.6), this allows the flow path, the point of liquid separation from the planet gear geometry and the flow regime to be determined without conducting any numerical modelling.

4) Knowledge created from the CFD simulations and experimental flow investigations highlighted potential risks associated with radial oil outflow. These are summarised in section 6.3.1.

5) Accurate boundary conditions for other CFD models used for modelling the air-oil flow field behaviour inside gearboxes and bearing chambers can be derived from the knowledge created by the work presented in this thesis.

a) In order to avoid the explicit modelling of the journal bearing oil outflow behaviour, quantitative data, such as fluid film thicknesses and flow velocities, can be extracted from a CFD model. The flow conditions at the outlet of the external journal bearing domain can be used as representative inlet boundary conditions for larger gearbox models. For operating conditions that lead to radial oil outflow, additional post-processing of the experimental flow investigations can provide droplet size distributions, which can be incorporated into CFD models of larger gearboxes.

b) A more generic conclusion with regard to the conditions of gearbox or bearing chamber CFD model domain walls could be drawn from the investigations presented in section 4.1.7. In regions where the geometrical length scales of domain boundary features are of the same order of magnitude as the expected oil film thickness on the walls, the condition of the domain boundary, i.e. dry or oil-wetted, can significantly affect the flow path prediction. This fact should be carefully considered when modelling the oil flow behaviour in generic gearboxes or bearing chambers.

The work presented in this thesis allows the following recommendations to be made:

1) Journal bearing oil outflow should be analysed using the methodology presented in this thesis. In summary, this includes the following steps:

   a) Determination of the fluid pressure distribution within the lubricating film of the journal bearing under investigation, using a software tool capable of solving the Reynolds equation. From the results, the fluid pressure gradients in the axial direction, $\partial p/\partial y$, at the bearing end face ($y = 0$), and the values of the fluid's dynamic viscosity, μ, can be extracted at multiple locations around the bearing's circumference. It is recommended to use one degree increments.
   b) Calculation of the mean axial velocity across the lubricating gap height, v_{mean}, at the same circumferential locations as in a), using equation (3.10).
   c) Determination of the outflow direction, i.e. axial or radial oil outflow, using Figure 5.8. If radial oil outflow prevails, the flow regime can be determined by using Figure 5.6, and the point of liquid separation from the planet gear's base can be determined with the force balance model established in section 3.6.
   d) If more detailed information about the outflow behaviour is required, a CFD model should be set up in accordance with the methodology described in chapters 3 and 4.

2) Based on the created knowledge for the preferred outflow direction, i.e. axial oil outflow, guidance on flow control mechanisms was provided. Recommendations of design improvements are summarised in section 6.3.2.

8 Future Research

Based on the results of the work presented in this thesis, further research is proposed to be carried out both numerically and experimentally.

From a CFD modelling point of view, external oil outflow from an orbiting journal bearing with a convergent-divergent gap height, h, should be assessed for additional key flight cycle phases, such as minimum and typical load conditions. Whilst maximum load conditions were assessed as part of the work presented in this thesis, simulations at minimum load conditions will help to assess the lower bound of the operating envelope. Particularly for long haul flights, the cruise segment can account for up to 90% of the flight cycle duration. It is therefore suggested to simulate the external oil outflow behaviour also for this condition (typical load condition). For every operating point to be assessed, the step-by-step guide reported in recommendation 1 a) in chapter 7 should be followed. In order to make the set-up of future CFD simulations more efficient, it should be considered to automate this process by using a process integration software tool, such as Isight [83], for instance.

It is recommended to improve the fidelity of the CFD models for highly-loaded journal bearings with a convergent-divergent gap height, h, by including the effects of an elastic deformation of the bearing surfaces due to the fluid film pressure (section 1.2.1). The non-orbiting and orbiting journal bearings with convergent-divergent lubricating gap heights, h, which were investigated in sections 4.3 and 4.4, respectively, are characterised by perfectly cylindrical bearing surface shapes. Thus, the effects caused by an elastic deformation of these surfaces have not been accounted for. Journal bearing analysis tools, such as COMSOL [28] and COMBROS [29], are capable of fully coupled fluid film pressure calculations that account for these effects. Comparing a calculation with undeformed bearing surfaces to a calculation with elastically deformed bearing surfaces, the minimum gap height, h_0, will be larger for the latter case. Consequently, the peak pressure value will drop. This will reduce the pressure gradients in the axial direction at the bearing end-face ($y = 0$). As the peak pressure value drops, the peak temperature value will decrease accordingly. Both phenomena will have an effect on the magnitude of the axial outflow velocity, v, and its distribution around the bearing's circumference.

The modelling of external journal bearing outflow with a full 360° model, using the methodology presented in chapter 3, generally still requires large computational efforts, which make the simulations very time-consuming. A significant reduction of the computational time required to reach steady state flow field conditions may be achievable by using an alternative flow simulation method. The review of relevant numerical modelling techniques for multiphase flows provided in section 2.8 concluded that the Lattice Boltzmann Method (LBM) presents an attractive alternative approach to modelling this class of flows. More work is proposed to be carried out to gain a better understanding of the capabilities and the limitations of LBM. This does not just apply to modelling external oil flow from a journal bearing, but to modelling gearbox and bearing chamber flows in general.

From an experimental flow investigation point of view, it is suggested to carry out tests with a set-up that includes a non-orbiting journal bearing with a convergent-divergent gap height, h. This will allow the oil outflow behaviour predicted by the appropriate CFD models discussed in section 4.3 to be qualitatively and quantitatively validated. A rig test with a non-orbiting journal bearing model will ensure that the requirements with respect to visual access to all areas of interest can be met. As previously discussed in chapter 5, this will be very challenging to achieve with an orbiting arrangement due to the much more complex rig design.

Furthermore, it is recommended to quantify the improvements suggested by the design recommendations made in section 6.3.2. Additional CFD simulations are proposed to be conducted to confirm that the suggested changes to the planet gear, the pin and the planet carrier meet the design intent. A quantification of the improvements can be achieved by comparing the oil film thickness values and the values of the dimensionless moment coefficient, c_m, between the proposed and the baseline geometry.

Publications

During the course of the research work presented in the thesis, two papers were published, both of which were submitted to the American Society of Mechanical Engineers (ASME). After incorporation of minor changes, both papers were accepted for journal publication.

[1] Berthold, M; Morvan, H; Young, C and Jefferson-Loveday, R (2017) "Towards Investigation of External Oil Flow From a Journal Bearing in an Epicyclic Gearbox", Proceedings of the ASME Turbo Expo 2017: Turbomachinery Technical Conference and Exposition, Vol. 7A: Structures and Dynamics, Charlotte, North Carolina, USA, June 26–30, 2017, V07AT34A010. ASME. https://doi.org/10.1115/GT2017-63451.

[2] Berthold, M; Morvan, H; Young, C and Jefferson-Loveday, R (2018). "Toward Investigation of External Oil Flow From a Journal Bearing in an Epicyclic Gearbox." ASME Journal of Engineering for Gas Turbines and Power, June 2018, Vol. 140, Issue 6: 062501, https://doi.org/10.1115/1.4038284.

[3] Berthold, M; Morvan, H; Jefferson-Loveday, R; Rothwell, B C and Young, C (2018) "Multiphase CFD Modeling of External Oil Flow From a Journal Bearing", Proceedings of the ASME Turbo Expo 2018: Turbomachinery Technical Conference and Exposition, Vol. 1: Aircraft Engine; Fans and Blowers; Marine, Oslo, Norway, June 11–15, 2018, V001T01A039. ASME. https://doi.org/10.1115/GT2018-77130.

[4] Berthold, M; Morvan, H; Jefferson-Loveday, R; Young, C; Rothwell, B C and Ambrose, S (2018) "Multiphase Computational Fluid Dynamics Modeling of External Oil Flow From a Journal Bearing", ASME Journal of Engineering for Gas Turbines and Power, May 2019, Vol. 141, Issue 5: 051002, https://doi.org/10.1115/1.4041517.

References

[1] Advisory Council for Aviation Research and Innovation in Europe (2017) "Strategic Research and Innovation Agenda – 2017 Update | Volume 1", ACARE, Brussels, Belgium.

[2] Cumpsty, N (2003) "Jet Propulsion – A simple guide to the aerodynamic and thermodynamic design and performance of jet engines", 2nd edition, Cambridge University Press, Cambridge, United Kingdom.

[3] August, R; Kasuba, R; Frater, J L; Pintz, A (1984) "Dynamics of Planetary Gear Trains", NASA Contractor Report 3793, Cleveland State University, Cleveland, Ohio, USA.

[4] Townsend, D P (1991) "Dudley's Gear Handbook", 2nd edition, McGraw-Hill, New York, New York, USA.

[5] Adeniyi, A A; Morvan H P; Simmons, K A (2015) "A Multiphase Computational Study of Oil-Air Flow Within the Bearing Sector of Aeroengines", Proceedings of ASME Turbo Expo 2015: Turbine Technical Conference and Exposition, Paper No. GT2015-43496, Montreal, Canada.

[6] Ambrose, S (2017) "Oil Flow in an Epicyclic Gearbox – CFD Model Recommendations", unpublished report no. FF159/SA/024/Issue 03, Gas Turbine and Transmissions Research Centre, University of Nottingham, Nottingham, United Kingdom.

[7] Welsh, R J (1984) "Plain Bearing Design Handbook", Butterworth, United Kingdom.

[8] Dowson, D; Higginson, G R (1977) "Elasto-hydrodynamic Lubrication", International Series in Materials Science and Technology, Vol. 23, Pergamon Press Ltd, Oxford, United Kingdom.

[9] Krantz, T L; Handschuh, R F (1990) "Efficiency Study Comparing Two Helicopter Planetary Reduction Stages", NASA Technical Memorandum 103106, Lewis Research Center, Cleveland, Ohio, USA.

[10] Butsch, M (1989) "Untersuchungen der hydraulischen Leerlaufverluste an schnellaufenden Stirnradgetrieben mit Umfangsgeschwindigkeiten bis 200 m/s und Radbreiten bis 125 mm", Forschungsvereinigung Antriebstechnik E.V., Forschungsvorhaben Nr. 44/V, Frankfurt am Main, Germany.

[11] Maurer, J (1994) "Lastunabhängige Verzahnungsverluste schnellaufender Stirnradgetriebe", Berichte des Institutes für Maschinenkonstruktion und Getriebebau, University of Stuttgart, Stuttgart, Germany.

[12] Rolls-Royce plc Press Release "Rolls-Royce sets new aerospace record with UltraFan® Power Gearbox", Monday 4 September 2017, Rolls-Royce plc, Derby, United Kingdom, accessible via http://www.rolls-royce.com/media/press-releases/yr-2017/04-09-2017-rr-sets-new-aerospace-record-with-ultrafan-power-gearbox.aspx.

[13] Air BP (2002) "BP Turbo Oil 2380 – Turbine Engine & Accessory", Manufacturer Specification, BP, Parsnippany, New Jersey, USA.

[14] Smith, P J (2004) "Cooling and Lubrication of High-Speed Helical Gears", Proceedings of the 33rd Turbomachinery Symposium, page 41 to page 48, The Texas A&M University, College Station, Texas, USA.

[15] Akin, L S; Townsend D P; Mross, J J (1974) "Study of Lubricant Jet Flow Phenomena in Spur Gears", NASA Technical Memorandum, NASA TM X-71572, Lewis Research Center, Cleveland, Ohio, USA.

[16] Townsend D P (1985) "Lubrication and Cooling for High Speed Gears", NASA Technical Memorandum, NASA-TM-87096, Lewis Research Centre, Cleveland, Ohio, USA.

[17] Arisawa, H; Nishimura, M; Imai, H; Goi, T (2009) "CFD Simulation for Reduction of Oil Churning Loss and Windage Loss on Aeroengine Transmission Gears", Proceedings of ASME Turbo Expo 2009: Turbomachinery Technical Conference and Exposition, Paper No. GT2009-59226, Orlando, Florida, USA.

[18] Arisawa, H; Nishimura, M; Imai, H; Goi, T (2011) "Oil Scavenging CFD Simulation and Experiments in the Accessory Gearbox of an Aircraft Engine", International Gas Turbine Congress, Paper No. IGTC2011-0214, Osaka, Japan.

[19] Arisawa, H; Nishimura, M; Imai, H; Goi, T (2014) "Computational Fluid Dynamics Simulations and Experiments for Reduction of Oil Churning Loss and Windage Loss in Aeroengine Transmission Gears", ASME Journal of Engineering for Gas Turbines and Power, Vol. 136, Issue 9, Article No. 092604, New York, New York, USA.

[20] Fondelli, T; Andreini, A; Da Soghe, R; Facchini, B, Cipolla, L (2015) "Numerical Simulation of Oil Jet Lubrication for High Speed Gears", International Journal of Aerospace Engineering, Vol. 2015, Article No. 752457, Hindawi, London, United Kingdom.

[21] Fondelli, T; Andreini, A; Da Soghe, R; Facchini, B, Cipolla, L (2015) "Volume of Fluid (VOF) Analysis of Oil-Jet Lubrication for High-Speed Spur Gears Using an Adaptive Meshing Approach", Proceedings of ASME Turbo Expo 2015: Turbomachinery Technical Conference and Exposition, Paper No. GT2015-42461, Montreal, Canada.

[22] Massini, D; Fondelli, T; Facchini, B; Tarchi, L; Leonardi, F (2017) “Experimental Investigation on Power Losses due to Oil Jet Lubrication in High Speed Gearing Systems”, Proceedings of ASME Turbo Expo 2017: Turbomachinery Technical Conference and Exposition, Paper No. GT2017-64703, Charlotte, North Carolina, USA.

[23] Keller, M; Braun, S; Wieth, L; Chaussonnet, G; Dauch, T F; Koch, R; Schwitzke, C; Bauer, H J (2017) “Smoothed Particle Hydrodynamics Simulation of Oil-Jet Gear Interaction”, Proceedings of ASME Turbo Expo 2017: Turbomachinery Technical Conference and Exposition, Paper No. GT2017-63594, Charlotte, North Carolina, USA.

[24] Ambrose, S; Morvan H; Simmons, K A (2018) “Investigation of Oil Jet Impingement on a Rotating Gear Using Lattice Boltzmann Method (LBM)”, Proceedings of ASME Turbo Expo 2018: Turbomachinery Technical Conference and Exposition, Paper No. GT2018-76371, Oslo, Norway.

[25] Khonsari, M M; Booser, R E (2008) “Applied Tribology – Bearing Design and Lubrication”, 2nd edition, John Wiley & Sons Ltd, Chichester, United Kingdom.

[26] Hamrock, B (1991) “Fundamentals of Fluid Film Lubrication”, NASA Office of Management, Scientific and Technical Information Program, Reference Publication 1255, Lewis Research Center, Cleveland, Ohio, USA.

[27] Szeri, A. Z. (1980) “Tribology: Friction, Lubrication and Wear”, Hemisphere Publishing Corporation, London, United Kingdom.

[28] COMSOL Inc. (2016) “COMSOL Multiphysics 5.3 User’s Guide”, COMSL Inc., Burlington, Massachusetts, USA.

[29] Hagemann, T (2013) “Documentation – COMBROS Radial Journal Bearing Calculation Program”, Institute of Tribology and Energy Conversion Machinery, Technical University of Clausthal, Clausthal, Germany.

[30] Guo, Z; Hirano, T; Kirk, R G (2005) “Application of CFD Analysis for Rotating Machinery: Part I – Hydrodynamic, Hydrostatic Bearings and Squeeze Film Damper”, ASME Journal of Engineering for Gas Turbines and Power, Vol. 127, Issue 2, page 445 to page 451, New York, New York, USA.

[31] Chen, W J (2002) “DyRoBeS BePerf Version 7.0’’, Eigen Technologies, Davidson, North Carolina, USA.

[32] Uhkötter, S (2016) “Untersuchung der Strömungs- und Vermischungsphänomene in schnelllaufenden hydrodynamischen Turbinengleitlagern”, Dissertation, Helmut Schmidt University/University of the Federal Armed Forces Hamburg, Hamburg, Germany

[33] Taylor, G I (1923) “Stability of a Viscous Liquid Contained between Two Rotating Cylinders”, Series A, Containing Papers of a Mathematical or Physical Character, Vol. 223, Issue 605-615, page 289 to page 343, The Royal Society, London, United Kingdom.

[34] Schlichting, H; Gersten, K (2006) “Grenzschicht-Theorie”, 10th edition, Springer, Berlin, Germany.

[35] Kármán, T (1921) “Über Laminare und Turbulente Reibung”, Zeitschrift für angewandte Mathematik und Mechanik, Vol. 1, No. 4, Wiley-VCH, Weinheim, Germany.

[36] Theodorsen, T; Regier, A (1944) “Experiments on Drag of Revolving Discs, Cylinders and Streamline Rods at High Speeds”, NACA Technical Memorandum 793, NACA, Hampton, Virginia, USA.

[37] Daily, J; Nece R (1958) “Roughness and Chamber Dimension Effects on Induced Flow and Frictional Resistance of Enclosed Rotating Disks”, Massachusetts Institute of Technology, Cambridge, Massachusetts, USA.

[38] Dorfman, L A (1963) “Hydrodynamic Resistance and Heat Loss of Rotating Solids”, Oliver & Boyd, Edinburgh, United Kingdom.

[39] Owen, J M; Rogers, R H (1989) “Flow and Heat Transfer in Rotating-Disc-Systems – Volume 1: Rotor-Stator Systems”, Research Studies Press Ltd, Taunton, United Kingdom.

[40] Fraser, R P; Dombrowski, N; Routley, J H (1963) “The Filming of Liquids by Spinning Cups”, Chemical Engineering Science, Vol. 18, page 323 to page 337, Pergamon Press Ltd, Oxford, United Kingdom.

[41] Liu, J; Yu, Q; Guo, Q (2012) “Experimental Investigation of Liquid Disintegration by Rotary Cups”, Chemical Engineering Science, Vol. 73, page 44 to page 50, Elsevier B.V., Amsterdam, The Netherlands.

[42] Glahn, A; Busam, S; Blair, M F; Allard, K L; Wittig, S (2002) “Droplet Generation by Disintegration of Oil Films at the Rim of a Rotating Disk”, ASME Journal of Engineering for Gas Turbines and Power, Vol. 124, Issue 1, page 117 to page 124, New York, New York, USA.

[43] Matsumoto, S; Belcher, D W; Crosby, E J (1985) “Rotary Atomizers: Performance, Understanding and Prediction”, Proceedings of the 3rd International Conference on Liquid Atomization and Spray Systems (ICLASS-85), Institute of Energy, London, United Kingdom.

[44] Hinze, J O; Milborn, H (1950) “Atomization of Liquids by Means of a Rotating Cup”, ASME Journal of Applied Mechanics, Vol. 17, page 145 to page 153, New York, New York, USA.

[45] Friedrich, M A; Lan, H; Wegener, J L; Drallmeier, J A; Armaly, B F (2008) “ A Separation Criterion With Experimental Validation for Shear-Driven Films in Separated Flows”, ASME Journal of Fluids Engineering, Vol. 130, Issue 5, Article No. 051301, New York, New York, USA.

[46] Arai, T; Hishimoto, H (1985) “Disintegration of a Thin Liquid Sheet in a Concurrent Gas Stream”, Proceedings of the 3rd International Conference on Liquid Atomization and Spray Systems (ICLASS-85), Institute of Energy , London, United Kingdom.

[47] Khonsari, M; Beaman J (1996) "Thermohydrodynamic Analysis of Laminar Incompressible Journal Bearings", ASLE Transactions, Vol. 29, Issue 2, page 141 to page 150, London, United Kingdom.

[48] ANSYS Inc. (2013) "ANSYS Fluent User's Guide", ANSYS Inc., Canonsburg, Pennsylvania, USA.

[49] ANSYS Inc. (2013) "ANSYS Fluent Theory Guide", ANSYS Inc., Canonsburg, Pennsylvania, USA.

[50] Versteeg, H K; Malalasekera, W (2007) "An Introduction to Computational Fluid Dynamics – The Finite Volume Method", 2nd edition, Pearson Education Limited, Harlow, United Kingdom.

[51] Boussinesq, J (1877) "Essai sur la théorie des eaux courantes", Mémoires résentés par divers savants à l'Académie des Sciences, Vol. 23, Issue 1, page 1 to page 659, Imprimerie Nationale, Paris, France.

[52] Spalart, P R; Allmaras, S R (1992) "A one-equation turbulence model for aerodynamic flows", AIAA 30th Aerospace Sciences Meeting and Exhibit, Paper No. 1992-0439, Reno, Nevada, USA.

[53] Launder, B E; Spalding, D B (1974) "The numerical computation of turbulent flows", Computer Methods in Applied Mechanics and Engineering, Vol. 39, Issue 2, page 269 to page 289, North-Holland Publishing Company, Amsterdam, The Netherlands.

[54] Wilcox, D C (1988) "Re-Assessment of the Scale-Determining Equation for Advanced Turbulence Models", AIAA Journal, Vol. 26, Issue 11, page 1299 to page 1310, Reston, Virginia, USA.

[55] Menter, F R (1992) "Performance of Popular Turbulence Models for Attached and Separated Adverse Pressure Gradient Flow", AIAA Journal, Vol. 30, Issue 8, page 2066 to page 2072, Reston, Virginia, USA.

[56] Menter, F R (1994) "Two-Equation Eddy-Viscosity Turbulence Models for Engineering Applications", AIAA Journal, Vol. 32, Issue 8, page 1598 to page 1605, Reston, Virginia, USA.

[57] Bristot, A (2017) "Application of the Volume of Fluid Method with Heat Transfer to a Two-Shaft Aero-engine Bearing Chamber", PhD Thesis, University of Nottingham, Nottingham, United Kingdom.

[58] Tkaczyk, P; Morvan, H (2012) "SILOET: CFD Modelling Guidelines for Engine Sumps", Internal Report Number JF82/PT/06, University of Nottingham, Nottingham, United Kingdom.

[59] Hirt, C W; Nichols, B D (1979) "Volume of Fluid (VOF) Method for the Dynamics of Free Boundaries, Journal of Computational Physics, Vol. 39, Issue 1, page 201 to page 225, Elsevier B.V., Amsterdam, The Netherlands.

[60] Seo, J (2014) "Multiphase Flow Modeling with Free Surface Flows", ANSYS Inc., Canonsburg, Pennsylvania, USA, accessible via https://www.ansys.com/en-gb/resource-library/presentation/multiphase-flow-modeling-with-free-surfaces-flow.

[61] Williams, J (2008) "Thin Film Rimming Flow Subject to Droplet Impact at the Surface", PhD Thesis, University of Nottingham, Nottingham, United Kingdom.

[62] Kay, E; Hibberd, S; Power, H (2014) "A Depth-Averaged Model for Non-Isothermal Thin-Film Rimming Flow", International Journal of Heat and Mass Transfer, Vol. 70, page 1003 to page 1015, Elsevier B.V., Amsterdam, The Netherlands.

[63] Kakimpa, B; Morvan, H; Hibberd, S (2016) "The Depth-Averaged Numerical Simulation of Laminar Thin-Film Flows with Capillary Waves", ASME Journal of Engineering for Gas Turbines and Power, Vol. 138, Issue 11, Article No. 112501, New York, New York, USA.

[64] Chen, S; Doolen, G D (1998) "Lattice Boltzmann Method for Fluid Flows", Annual Review of Fluid Mechanics, Vol. 30, page 329 to page 364, Palo Alto, California, USA.

[65] Dassault Systèmes SE (2019) "XFlow User Guide", Dassault Systèmes SE, Vélizy-Villacoublay Cedex, France.

[66] Gingold, R A; Monaghan, J J (1977) "Smoothed Particle Hydrodynamics: Theory and Application to Non-Spherical Stars", Monthly Notices of the Royal Astronomical Society, Vol. 181, page 375 to page 389, London, United Kingdom.

[67] Kruisbrink, A; Pearce, F; Yue, T; Cliffe, A; Morvan, H (2011) "SPH Concepts for Continuous Wall and Pressure Boundaries," Proceedings of the 6th International SPHERIC workshop, page 298 to page 304, Hamburg, Germany.

[68] Kruisbrink, A; Morvan, H; Pearce, F (2014) "Progress in Smoothed Particle Hydrodynamics to Simulate Bearing Chambers", Proceedings of the ASME Turbo Expo 2014: Turbine Technical Conference and Exposition, Paper No. GT2014-26403, Düsseldorf, Germany.

[69] Korzilius, S; Kruisbrink, A; Schilders, W; Anthonissen, M; Yue, T (2014) "Momentum Conserving Methods that Reduce Particle Clustering in SPH", Report CASA, Vol. 1415, Technische Universiteit Eindhoven, Eindhoven, The Netherlands.

[70] Violeau, D; Issa, R (2007) "Numerical Modelling of Complex Turbulent Free-Surface Flows with the SPH Method: An Overview", International Journal for Numerical Methods in Fluids, Vol. 53, page 277 to page 304, John Wiley & Sons Inc., Hoboken, New Jersey, USA.

[71] Jacobs, A P (2012) "ELUBSYS D1.6: Real Engine TBH and KIT Bearing Housing Simulation Results", Rolls-Royce plc Internal Report FSG 90660, Rolls-Royce plc, Derby, United Kingdom.

[72] Tkaczyk, P; Morvan H P (2012) “Methodology for Modelling Two-Phase Flow in Bearing Chambers using CFD (Volume of Fluid)”, SILOET Report UTC JF82/PT/06, The University of Nottingham, Nottingham, United Kingdom.

[73] Adeniyi, A A; Morvan, H P; Simmons, K A (2013) “Droplet-Film Impact Modelling Using a Coupled DPM-VoF Approach”, Proceedings of the 21st International Symposium on Air-Breathing Engines, Paper Number ISABE-2013-1419, Busan, South Korea.

[74] Adeniyi, A A (2014) “A Coupled Lagrangian-Eulerian Framework to Model Droplet to Film Interaction with Heat Transfer”, PhD Thesis, The University of Nottingham, Nottingham, United Kingdom.

[75] Adeniyi, A A; Morvan, H P; Simmons, K A (2014) “A Transient CFD Simulation of the Flow in a Test Rig of an Aeroengine Bearing Chamber”, Proceedings of ASME Turbo Expo 2014: Turbine Technical Conference and Exposition, Paper No. GT2014-26399, Düsseldorf, Germany.

[76] Incropera, F P; DeWitt, D P (2002) “Fundamentals of Heat and Mass Transfer”, 5th edition, John Wiley & Sons Inc., Hoboken, New Jersey, USA.

[77] Press, W H; Teukolsky, S A; Vetterling, W T; Flannery, B P (1992) “Numerical Recipes in FORTRAN: The Art of Scientific Computing”, 2nd edition, Cambridge University Press, Cambridge, United Kingdom.

[78] Curzons, S (2001) “Chebyfit – FORTRAN Code for Chebyshev Approximation”, Rolls-Royce plc, Derby, United Kingdom.

[79] Kalin, M; Polajnar, M (2013) “The Wetting of Steel, DLC Coatings, Ceramics and Polymers with Oils and Water: The Importance and Correlations of Surface Energy, Surface Tension, Contact Angle and Spreading”, Journal of Applied Surface Science, Vol. 293, page 97 to page 108, Elsevier B.V., Amsterdam, The Netherlands.

[80] Berthold, M (2019) “Operation of Single Shaft Test Rig with Journal Bearing Oil Outflow Module”, Gas Turbines and Transmissions Research Centre, The University of Nottingham, Nottingham, United Kingdom.

[81] The MathWorks Inc. (2019) “Statistics and Machine Learning Toolbox™ User’s Guide”, The MathWorks Inc., Natick, Massachusetts, USA.

[82] Berthold, M; Morvan, H; Young, C; Jefferson-Loveday, R (2018) "Toward Investigation of External Oil Flow From a Journal Bearing in an Epicyclic Gearbox", ASME Journal of Engineering for Gas Turbines and Power, Vol. 140, Issue 6, Article No. 062501, New York, New York, USA.

[83] Dassault Systèmes SE (2014) “Isight – Automate Design Exploration and Optimization”, Dassault Systèmes SE, Vélizy-Villacoublay Cedex, France, accessible via

https://www.3ds.com/fileadmin/PRODUCTS-SERVICES/SIMULIA/RESOURCES/simulia-isight-brochure.pdf.

Appendix

Appendix 1: Summary of 6th order polynomial coefficients to approximate $v_{\mathbf{flux}}$-distribution of journal bearing under investigation at maximum load conditions

Interval	C_6	C_5	C_4	C_3	C_2	C_1	C_0
$38° < \theta < 41°$	-1.10×10^{3}	1.05×10^{5}	-2.60×10^{6}	0.00	0.00	0.00	4.25×10^{11}
$41° \leq \theta < 60°$	-1.88×10^{2}	5.93×10^{4}	-7.82×10^{6}	5.48×10^{8}	-2.16×10^{10}	4.55×10^{11}	-3.99×10^{12}
$60° \leq \theta < 80°$	2.68×10^{-1}	-7.96×10^{1}	9.97×10^{3}	-6.00×10^{5}	1.64×10^{7}	0.00	-4.69×10^{9}
$80° \leq \theta < 100°$	1.31	-4.92×10^{2}	7.42×10^{4}	-5.35×10^{6}	1.65×10^{8}	0.00	-7.41×10^{10}
$100° \leq \theta < 120°$	9.49	-4.54×10^{3}	8.58×10^{5}	-7.74×10^{7}	2.97×10^{9}	0.00	-2.08×10^{12}
$120° \leq \theta < 140°$	-1.22×10^{2}	7.60×10^{4}	-1.84×10^{7}	2.11×10^{9}	-1.02×10^{11}	0.00	1.11×10^{14}
$140° \leq \theta < 150°$	-2.67×10^{2}	1.33×10^{5}	-2.32×10^{7}	1.44×10^{9}	0.00	0.00	-1.97×10^{14}
$150° \leq \theta < 160°$	1.12×10^{3}	-6.23×10^{5}	1.20×10^{8}	-8.20×10^{9}	0.00	0.00	1.49×10^{15}
$160° \leq \theta < 163°$	1.29×10^{2}	-4.96×10^{4}	4.95×10^{6}	0.00	0.00	0.00	-2.11×10^{14}
$163° \leq \theta < 166°$	-2.71×10^{2}	1.08×10^{5}	-1.12×10^{7}	0.00	0.00	0.00	5.68×10^{14}

Appendix 2: Summary of 44th order Chebyshev polynomial coefficients to approximate $v_{\mathbf{flux}}$-distribution of journal bearing under investigation at maximum load conditions

Interval	$38° < \theta < 166°$				
C_0	1.56×10^{11}	C_{15}	-5.42×10^{9}	C_{30}	-2.75×10^{8}
C_1	2.14×10^{11}	C_{16}	-3.27×10^{9}	C_{31}	-2.31×10^{8}
C_2	1.81×10^{10}	C_{17}	-1.50×10^{9}	C_{32}	-1.98×10^{8}
C_3	-1.35×10^{11}	C_{18}	-5.16×10^{8}	C_{33}	-1.61×10^{8}
C_4	-1.84×10^{11}	C_{19}	-2.40×10^{8}	C_{34}	-1.35×10^{8}
C_5	-1.42×10^{11}	C_{20}	-3.15×10^{8}	C_{35}	-1.04×10^{8}

C_6	-6.40×10^{10}	C_{21}	-5.23×10^{8}	C_{36}	-8.57×10^{7}
C_7	5.16×10^{9}	C_{22}	-6.60×10^{8}	C_{37}	-6.17×10^{7}
C_8	4.19×10^{10}	C_{23}	-7.19×10^{8}	C_{38}	-4.97×10^{7}
C_9	4.79×10^{10}	C_{24}	-6.82×10^{8}	C_{39}	-3.26×10^{7}
C_{10}	3.49×10^{10}	C_{25}	-6.13×10^{8}	C_{40}	-2.57×10^{7}
C_{11}	1.72×10^{10}	C_{26}	-5.22×10^{8}	C_{41}	-1.46×10^{7}
C_{12}	2.94×10^{9}	C_{27}	-4.43×10^{8}	C_{42}	-1.12×10^{7}
C_{13}	-4.64×10^{9}	C_{28}	-3.75×10^{8}	C_{43}	-4.64×10^{6}
C_{14}	-6.62×10^{9}	C_{29}	-3.19×10^{8}	C_{44}	-3.46×10^{6}

Appendix 3: Source code for UDF to model inlet velocity profiles (orbiting journal bearing with constant lubricating gap height)

```
#include "udf.h"
#include "math.h"

DEFINE_PROFILE(v_ax_inlet, t, i) /*Definition of axial velocity profile*/
{
double x[ND_ND]; /*Position vector*/
double pi = 3.14159265358979; /*Definition of Pi*/
double G = 0.0774997;  /*Definition of gear radius in [m]. The original radius of 0.0775 m had to be
                       adjusted in order to account for geometry translation errors from ICEM to
                       Fluent. Adjustment is required to guarantee a fully symmetrical axial
                       velocity profile across the gap height.*/
double theta; /*Definition of circumferential coordinate*/
double v_flux; /*Definition of velocity flux*/
double r; /*Definition of global radial coordinate*/
double k; /*Definition of local radial coordinate across gap height*/
double h; /*Definition of gap height*/

face_t f;
begin_f_loop(f, t)
{
F_CENTROID(x, f, t);

if (x[2]<0 && x[1]>0) /*Definition of theta in [deg] based on node coordinates x[1] and x[2]*/
        theta = (atan(x[2] / x[1])*(-1.0))*180.0 / pi;
if (x[2]<0 && x[1]<0)
        theta = (atan(x[1] / x[2]) + pi / 2.0)*180.0 / pi;
if (x[2]>0 && x[1]<0)
        theta = (atan(x[2] / x[1])*(-1.0) + pi)*180.0 / pi;
if (x[2]>0 && x[1]>0)
        theta = (atan(x[1] / x[2]) + pi + pi / 2.0)*180.0 / pi;

v_flux = 2633295513;  /*Definition of v_flux, which is constant for a journal bearing with a constant
                      lubricating gap height*/
r = pow(((x[2] * x[2]) + (x[1] * x[1])), 0.5);
h = 0.000116;
k = G - r;

F_PROFILE(f, t, i) = v_flux*(pow(k, 2.0) - k*h); /*Definition of axial velocity profile*/
}
end_f_loop(f, t)
}
```

```
DEFINE_PROFILE(v_tan_inlet, t, i) /*Definition of tangential velocity profile*/
{
double x[ND_ND]; /*Position vector*/
double pi = 3.14159265358979; /*Definition of Pi*/
double G = 0.0774997;  /*Definition of gear radius in [m]*/
double theta; /*Definition of circumferential coordinate*/
double rl; /*Definition of local radial coordinate*/
double rg; /*Definition of global radial coordinate*/
double k; /*Definition of local radial coordinate across gap height*/
double h = 0.000116; /*Definition of gap height in [m]*/
double omega_g = -547.6800000; /*Definition of angular velocity of gear*/
double cd = 0.2588200000; /*Definition of gear centre distance in [m]*/
double yg; /*Definition of global y coordinate*/
double ugeartan; /*Definition of tangential speed of gear*/

face_t f;
begin_f_loop(f, t)
{
F_CENTROID(x, f, t);

if (x[2]<0 && x[1]>0) /*Definition of theta in [deg] based on node coordinates x[1] and x[2]*/
        theta = (atan(x[2] / x[1])*(-1.0))*180.0 / pi;
if (x[2]<0 && x[1]<0)
        theta = (atan(x[1] / x[2]) + pi / 2.0)*180.0 / pi;
if (x[2]>0 && x[1]<0)
        theta = (atan(x[2] / x[1])*(-1.0) + pi)*180.0 / pi;
if (x[2]>0 && x[1]>0)
        theta = (atan(x[1] / x[2]) + pi + pi / 2.0)*180.0 / pi;

rl = pow(((x[2] * x[2]) + (x[1] * x[1])), 0.5);
yg = cd + x[1];
rg = pow((pow(x[2], 2.0) + pow(yg, 2.0)), 0.5);
k = G - rl;

ugeartan = omega_g * G * ((pow(rl, 2.0) + pow(rg, 2.0) - pow(cd, 2.0)) / (2.0*rl*rg)); /*Calculation
of ugeartan relative to orbit centre*/

F_PROFILE(f, t, i) = (-k / h * ugeartan + ugeartan); /*Definition of tangential velocity profile*/
}
end_f_loop(f, t)
}

DEFINE_PROFILE(v_rad_inlet, t, i) /*Definition of radial velocity profile.*/
{
double x[ND_ND]; /*Position vector*/
double pi = 3.14159265358979; /*Definition of Pi*/
double G = 0.0774997; /*Definition of gear radius in [m]*/
double theta; /*Definition of circumferential coordinate*/
double rl; /*Definition of local radial coordinate*/
double rg; /*Definition of global radial coordinate*/
double k; /*Definition of local radial coordinate across gap height*/
double h = 0.000116; /* Definition of gap height in [m]*/
double omega_g = -547.6800000; /*Definition of angular velocity of gear*/
double cd = 0.2588200000; /*Definition of gear centre distance in [m]*/
double yg; /* Definition of global y coordinate*/
double ugearrad; /* Definition of radial speed of gear*/

face_t f;
begin_f_loop(f, t)
{
F_CENTROID(x, f, t);

if (x[2]<0 && x[1]>0) /*Definition of theta in [deg] based on node coordinates x[1] and x[2]*/
        theta = (atan(x[2] / x[1])*(-1.0))*180.0 / pi;
if (x[2]<0 && x[1]<0)
        theta = (atan(x[1] / x[2]) + pi / 2.0)*180.0 / pi;
if (x[2]>0 && x[1]<0)
        theta = (atan(x[2] / x[1])*(-1.0) + pi)*180.0 / pi;
if (x[2]>0 && x[1]>0)
        theta = (atan(x[1] / x[2]) + pi + pi / 2.0)*180.0 / pi;

rl = pow(((x[2] * x[2]) + (x[1] * x[1])), 0.5);
yg = cd + x[1];
```

```
rg = pow((pow(x[2], 2.0) + pow(yg, 2.0)), 0.5);
k = G - rl;

if (theta > 0 && theta < 180) /*Calculation of ugearrad relative to orbit centre*/
        ugearrad = omega_g * G * sin(acos((pow(rl, 2.0) + pow(rg, 2.0) - pow(cd, 2.0)) /
        (2.0*rl*rg)));
if (theta > 180 && theta < 360) /*Calculation of ugearrad relative to orbit centre*/
        ugearrad = omega_g * G * -sin(acos((pow(rl, 2.0) + pow(rg, 2.0) - pow(cd, 2.0)) /
        (2.0*rl*rg)));

F_PROFILE(f, t, i) = (-k / h * ugearrad + ugearrad); /*Definition of tangential velocity profile*/
}
end_f_loop(f, t)
}
```

Appendix 4: Source code for UDF to model inlet velocity profiles (non-orbiting and orbiting journal bearing with convergent-divergent lubricating gap height)

```
#include "udf.h"
#include "math.h"

DEFINE_PROFILE(v_ax_inlet, t, i) /*Definition of axial velocity profile*/
{
double x[ND_ND]; /*Position vector*/
double pi = 3.14159265358979; /*Definition of Pi*/
double C = 0.00011582; /*Definiton of nominal radial clearance between gear and pin in [m]*/
double e = 0.00010963; /*Definition of eccentricity between gear and pin axis in [m]*/
double G = 0.0774997; /*Definition of gear radius in [m]. The original radius of 0.0775 m had to be
                        adjusted in order to account for geometry translation errors from ICEM to
                        Fluent. Adjustment is required to guarantee a fully symmetrical axial
                        velocity profile across the gap height.*/
double J = 0.07738417; /*Definition of pin radius in [m]*/
double theta; /*Definition of circumferential coordinate*/
double thetamin = 38.0; /*Definition of circumferential coordinate where outlow begins*/
double thetamax = 166.0; /*Definition of circumferential coordinate where outflow ends*/
double thetan; /*Definition of circumferential coordinate*/
double v_flux; /*Definition of velocity flux*/
double r; /*Definition of global radial coordinate*/
double k; /*Definition of local radial coordinate across gap height*/
double h; /*Definition of gap height*/

/*Definition of coefficients for Chebyshev polynomials, defining the velocity flux distribution
around the bearing's circumference*/
int j;
double a[45], T[45];
        a[0] = 155606800000.0;
        a[1] = 214350100000.0;
        a[2] = 18101710000.0;
        a[3] = -134758400000.0;
        a[4] = -183524100000.0;
        a[5] = -141917600000.0;
        a[6] = -63952570000.0;
        a[7] = 5162919000.0;
        a[8] = 41892300000.0;
        a[9] = 47855560000.0;
        a[10] = 34949080000.0;
        a[11] = 17182570000.0;
        a[12] = 2940773000.0;
        a[13] = -4639431000.0;
        a[14] = -6622597000.0;
        a[15] = -5420370000.0;
        a[16] = -3265186000.0;
        a[17] = -1503216000.0;
        a[18] = -515905500.0;
        a[19] = -239902700.0;
        a[20] = -315175300.0;
        a[21] = -522790300.0;
        a[22] = -659540000.0;
        a[23] = -719148900.0;
        a[24] = -682101400.0;
        a[25] = -612583400.0;
```

```
        a[26] = -522135800.0;
        a[27] = -443357000.0;
        a[28] = -375279300.0;
        a[29] = -319073700.0;
        a[30] = -274613000.0;
        a[31] = -231332800.0;
        a[32] = -198336800.0;
        a[33] = -161079200.0;
        a[34] = -135387300.0;
        a[35] = -104226700.0;
        a[36] = -85690780.0;
        a[37] = -61679100.0;
        a[38] = -49685070.0;
        a[39] = -32619150.0;
        a[40] = -25739550.0;
        a[41] = -14575780.0;
        a[42] = -11206430.0;
        a[43] = -4647729.0;
        a[44] = -3456132.0;

face_t f;
begin_f_loop(f, t)
{
F_CENTROID(x, f, t);

if (x[2]<0 && x[1]>0) /*Definition of theta in [deg] based on node coordinates x[1] and x[2]*/
        theta = (atan(x[2] / x[1])*(-1.0))*180.0 / pi;
if (x[2]<0 && x[1]<0)
        theta = (atan(x[1] / x[2]) + pi / 2.0)*180.0 / pi;
if (x[2]>0 && x[1]<0)
        theta = (atan(x[2] / x[1])*(-1.0) + pi)*180.0 / pi;
if (x[2]>0 && x[1]>0)
        theta = (atan(x[1] / x[2]) + pi + pi / 2.0)*180.0 / pi;

/*Reconstruction of Chebyshev polynomials using Clenshaw recurrence in the region between thetamin
and thetamax*/
if (theta >= 0.0 && theta < thetamin)
        v_flux = 0.0;
else
        if (theta >= 0.0 && theta <= thetamax)
        {
                thetan = 2 * (theta - thetamin) / (thetamax - thetamin) - 1;
                for (j = 0, v_flux = 0.0; j <= 44; j++)
                {
                        if (j == 0)
                                T[j] = 1;
                        else
                                if (j == 1)
                                        T[j] = thetan;
                                else
                                        T[j] = 2 * thetan * T[j - 1] - T[j - 2];
                        v_flux = v_flux + a[j] * T[j];
                }
        }
if (theta > thetamax && theta < 360.0) /*Define v_flux = 0 in the cavitated region*/
        v_flux = 0.0;
if (v_flux > 0.0) /*Define v_flux as positive at all times*/
        v_flux = v_flux;
else
        v_flux = 0.0;

r = pow(((x[2] * x[2]) + (x[1] * x[1])), 0.5);
h = C + J + e*cos((theta + 19.0)*pi / 180.0) - J*pow((1 - pow(e / J, 2.0)*sin((theta + 19.0)*pi /
180.0)*sin((theta + 19.0)*pi / 180.0)), 0.5);
k = G - r;

F_PROFILE(f, t, i) = v_flux*(pow(k, 2.0) - k*h); /*Definition of axial velocity profile*/
}
end_f_loop(f, t)
}
```

```
DEFINE_PROFILE(v_tan_inlet, t, i) /*Definition of tangential velocity profile*/
{
double x[ND_ND]; /*Position vector*/
double pi = 3.14159265358979; /*Definition of Pi*/
double C = 0.00011582; /*Definiton of nominal radial clearance between gear and pin in [m]*/
double e = 0.00010963; /*Definition of eccentricity between gear and pin axis in [m]*/
double G = 0.0774997; /*Definition of gear radius in [m]*/
double J = 0.07738417; /*Definition of pin radius in [m]*/
double theta; /*Definition of circumferential coordinate*/
double rl; /*Definition of local radial coordinate*/
double rg; /*Definition of global radial coordinate*/
double k; /*Definition of local radial coordinate across gap height*/
double h; /*Definition of gap height*/
double omega_g = -547.6800000; /*Definition of angular velocity of gear*/
double cd = 0.2588200000; /*Definition of gear centre distance in [m]*/
double yg; /*Definition of global y coordinate*/
double ugeartan; /*Definition of tangential speed of gear*/

face_t f;
begin_f_loop(f, t)
{
F_CENTROID(x, f, t);

if (x[2]<0 && x[1]>0) /*Definition of theta in [deg] based on node coordinates x[1] and x[2]*/
        theta = (atan(x[2] / x[1])*(-1.0))*180.0 / pi;
if (x[2]<0 && x[1]<0)
        theta = (atan(x[1] / x[2]) + pi / 2.0)*180.0 / pi;
if (x[2]>0 && x[1]<0)
        theta = (atan(x[2] / x[1])*(-1.0) + pi)*180.0 / pi;
if (x[2]>0 && x[1]>0)
        theta = (atan(x[1] / x[2]) + pi + pi / 2.0)*180.0 / pi;

rl = pow(((x[2] * x[2]) + (x[1] * x[1])), 0.5);
yg = cd + x[1];
rg = pow((pow(x[2], 2.0) + pow(yg, 2.0)), 0.5);
h = C + J + e*cos((theta + 19.0)*pi / 180.0) - J*pow((1 - pow(e / J, 2.0)*sin((theta + 19.0)*pi /
180.0)*sin((theta + 19.0)*pi / 180.0)), 0.5);
k = G - rl;

ugeartan = omega_g * G * ((pow(rl, 2.0) + pow(rg, 2.0) - pow(cd, 2.0)) / (2.0*rl*rg));

F_PROFILE(f, t, i) = (-k / h * ugeartan + ugeartan); /*Definition of tangential velocity profile*/
}
end_f_loop(f, t)
}

DEFINE_PROFILE(v_rad_inlet, t, i) /*Definition of radial velocity profile*/
{
double x[ND_ND]; /*Position vector*/
double pi = 3.14159265358979; /*Definition of Pi*/
double C = 0.00011582; /*Definiton of nominal radial clearance between gear and pin in [m]*/
double e = 0.00010963; /*Definition of eccentricity between gear and pin axis in [m]*/
double G = 0.0774997; /*Definition of gear radius in [m]*/
double J = 0.07738417; /*Definition of pin radius in [m]*/
double theta; /*Definition of circumferential coordinate*/
double rl; /*Definition of local radial coordinate*/
double rg; /*Definition of global radial coordinate*/
double k; /*Definition of local radial coordinate across gap height*/
double h; /*Definition of gap height*/
double omega_g = -547.6800000; /*Definition of angular velocity of gear*/
double cd = 0.2588200000; /*Definition of gear centre distance in [m]*/
double yg; /*Definition of global y coordinate*/
double ugearrad; /*Definition of radial speed of gear*/

face_t f;
begin_f_loop(f, t)
{
F_CENTROID(x, f, t);

if (x[2]<0 && x[1]>0) /*Definition of theta in [deg] based on node coordinates x[1] and x[2]*/
        theta = (atan(x[2] / x[1])*(-1.0))*180.0 / pi;
if (x[2]<0 && x[1]<0)
        theta = (atan(x[1] / x[2]) + pi / 2.0)*180.0 / pi;
```

```
if (x[2]>0 && x[1]<0)
        theta = (atan(x[2] / x[1])*(-1.0) + pi)*180.0 / pi;
if (x[2]>0 && x[1]>0)
        theta = (atan(x[1] / x[2]) + pi + pi / 2.0)*180.0 / pi;

rl = pow(((x[2] * x[2]) + (x[1] * x[1])), 0.5);
yg = cd + x[1];
rg = pow((pow(x[2], 2.0) + pow(yg, 2.0)), 0.5);
h = C + J + e*cos((theta + 19.0)*pi / 180.0) - J*pow((1 - pow(e / J, 2.0)*sin((theta + 19.0)*pi /
180.0)*sin((theta + 19.0)*pi / 180.0)), 0.5);
k = G - rl;

if (theta > 0 && theta < 180)
        ugearrad = omega_g * G * sin(acos((pow(rl, 2.0) + pow(rg, 2.0) - pow(cd, 2.0)) /
        (2.0*rl*rg)));
if (theta > 180 && theta < 360)
        ugearrad = omega_g * G * -sin(acos((pow(rl, 2.0) + pow(rg, 2.0) - pow(cd, 2.0)) /
        (2.0*rl*rg)));

F_PROFILE(f, t, i) = (-k / h * ugearrad + ugearrad); /*Definition of radial velocity profile*/
}
end_f_loop(f, t)
}
```

Appendix 5: Boundary conditions and numerical settings for CFD sector analysis of a non-orbiting journal bearing model with a constant lubricating gap height

Parameter	Value/setting
Numerical solver	ANSYS Fluent 16.2
Multiphase model	VOF
Suface tension model	Enabled
Wall adhesion model	Disabled
Engergy model	Isothermal
Turbulence model	SST k–ω
Spatial flow discretisation scheme	Second order
Temporal discretisation scheme	First order for geometric phase interface reconstruction, Second order for compressive phase interface reconstruction
Time-step, Δt	Fixed, 2×10^{-7} s $\leq \Delta t \leq 1 \times 10^{-5}$ s, depending on operating conditions
Volume fraction discretisation scheme	Geometric reconstruction scheme, compressive scheme
Pressure-velocity coupling	Pressure-based coupled solver

Courant number	$C \leq 1$ for explicit temporal discretisation, $C \leq 12.5$ for implicit temporal discretisation
Rotational speed of planet gear, ω_{G}	Fixed, case specific
Rotational speed of planet carrier, ω_{C}	$0\ \mathrm{s}^{-1}$
Inlet boundary condition type	Mass flow inlet
Air inlet mass flow rate, $\dot{m}_{\mathrm{air}}$	0 kg/s
Oil inlet mass flow rate, $\dot{m}_{\mathrm{oil}}$	fixed, case specific
Outlet boundary condtion type	Pressure outlet
Material properties	
Air density, ρ_{air} ($T = 20°\mathrm{C}$)	$1.19\ \mathrm{kg/m^3}$
Air density, ρ_{air} ($T = 31°\mathrm{C}$)	$1.15\ \mathrm{kg/m^3}$
Air density, ρ_{air} ($T = T_{\mathrm{max\,load}}$)	$0.89\ \mathrm{kg/m^3}$
Air dynamic viscosity, μ_{air} ($T = 20°\mathrm{C}$)	$18.23 \times 10^{-6}\ \mathrm{kg/(ms)}$
Air dynamic viscosity, μ_{air} ($T = 31°\mathrm{C}$)	$18.77 \times 10^{-6}\ \mathrm{kg/(ms)}$
Air dynamic viscosity, μ_{air} ($T = T_{\mathrm{max\,load}}$)	$22.71 \times 10^{-6}\ \mathrm{kg/(ms)}$
Oil density, ρ_{oil} ($T = 20°\mathrm{C}$)	$0.991\ \mathrm{kg/m^3}$
Oil density, ρ_{oil} ($T = 31°\mathrm{C}$)	$0.983\ \mathrm{kg/m^3}$
Oil density, ρ_{oil} ($T = T_{\mathrm{max\,load}}$)	$0.919\ \mathrm{kg/m^3}$
Oil dynamic viscosity, μ_{oil} ($T = 20°\mathrm{C}$)	0.101 kg/(ms)
Oil dynamic viscosity, μ_{oil} ($T = 31°\mathrm{C}$)	0.044 kg/(ms)
Oil dynamic viscosity, μ_{oil} ($T = T_{\mathrm{max\,load}}$)	0.003 kg/(ms)
Surface tension, σ ($T = 20°\mathrm{C}$)	0.0323 N/m
Surface tension, σ ($T = 31°\mathrm{C}$)	0.0315 N/m
Surface tension, σ ($T = T_{\mathrm{max\,load}}$)	0.0250 N/m

Appendix 6: Boundary conditions and numerical seetings for CFD analysis of a full 360° orbiting journal bearing model with a constant lubricating gap height

Parameter	Value/setting
Numerical solver	ANSYS Fluent 16.2
Multiphase model	VOF
Suface tension model	Enabled
Wall adhesion model	Disabled
Engergy model	Isothermal
Turbulence model	SST k–ω
Spatial flow discretisation scheme	Second order
Temporal discretisation scheme	Second order
Time-step, Δt	Fixed, $\Delta t = 2 \times 10^{-6}$ s
Volume fraction discretisation scheme	Compressive scheme
Pressure-velocity coupling	Pressure-based coupled solver
Flow courant number	$C \approx 2.5$
Rotational speed of planet gear, ω_{G}	$\omega_{\mathrm{G,\,max\,load}}$
Rotational speed of planet carrier, ω_{C}	$\omega_{\mathrm{C,\,max\,load}}$
Inlet boundary condition type	Velocity inlet
Air inlet mass flow rate, $\dot{m}_{\mathrm{air}}$	0 kg/s
Oil inlet mass flow rate, $\dot{m}_{\mathrm{oil}}$	$\dot{m}_{\mathrm{oil,\,max\,load}}$
Outlet boundary condtion type	Pressure outlet
Material properties	
Air density, ρ_{air} ($T = T_{\mathrm{max\,load}}$)	0.89 kg/m^3
Air dynamic viscosity, μ_{air} ($T = T_{\mathrm{max\,load}}$)	22.71×10^{-6} kg/(ms)
Oil density, ρ_{oil} ($T = T_{\mathrm{max\,load}}$	0.919 kg/m^3
Oil dynamic viscosity, μ_{oil} ($T = T_{\mathrm{max\,load}}$)	0.003 kg/(ms)
Surface tension, σ ($T = T_{\mathrm{max\,load}}$)	0.0250 N/m

Appendix 7: Boundary conditions and numerical seetings for CFD analysis of a full 360° non-orbiting and orbiting journal bearing model with a convergent-divergent lubricating gap height

Parameter	Value/setting
Numerical solver	ANSYS Fluent 16.2
Multiphase model	VOF
Suface tension model	Enabled
Wall adhesion model	Disabled
Engergy model	Isothermal
Turbulence model	SST k–ω
Spatial flow discretisation scheme	Second order
Temporal discretisation scheme	Second order
Time-step, Δt	Fixed, $\Delta t = 2 \times 10^{-6}$ s
Volume fraction discretisation scheme	Compressive scheme
Pressure-velocity coupling	Pressure-based coupled solver
Flow courant number	$C \approx 2.5$
Rotational speed of planet gear, ω_{G}	$\omega_{\mathrm{G,\,max\,load}}$
Rotational speed of planet carrier, ω_{C}	$\omega_{\mathrm{C}} = 0\ \mathrm{s}^{-1}$
Inlet boundary condition type	Velocity inlet
Air inlet mass flow rate, $\dot{m}_{\mathrm{air}}$	0 kg/s
Oil inlet mass flow rate, $\dot{m}_{\mathrm{oil}}$	$\dot{m}_{\mathrm{oil,\,max\,load}}$
Outlet boundary condtion type	Pressure outlet
Material properties	
Air density, ρ_{air} $(T = T_{\mathrm{max\,load}})$	0.89 kg/m^3
Air dynamic viscosity, μ_{air} $(T = T_{\mathrm{max\,load}})$	22.71×10^{-6} kg/(ms)
Oil density, ρ_{oil} $(T = T_{\mathrm{max\,load}})$	0.919 kg/m^3
Oil dynamic viscosity, μ_{oil} $(T = T_{\mathrm{max\,load}})$	0.003 kg/(ms)
Surface tension, σ $(T = T_{\mathrm{max\,load}})$	0.0250 N/m

Appendix 8: Boundary conditions and numerical seetings for CFD validation cases

Parameter	Value/setting
Numerical solver	ANSYS Fluent 16.2
Multiphase model	VOF
Suface tension model	Enabled
Wall adhesion model	Disabled
Engergy model	Isothermal
Turbulence model	SST k–ω
Spatial flow discretisation scheme	Second order
Temporal discretisation scheme	First order
Time-step, Δt	Fixed, depending on operating conditions
Volume fraction discretisation scheme	Geometric reconstruction scheme
Pressure-velocity coupling	Pressure-based coupled solver
Flow courant number	$C \leq 1$
Rotational speed of planet gear, ω_{G}	Fixed, case specific
Rotational speed of planet carrier, ω_{C}	$0\ \mathrm{s}^{-1}$
Inlet boundary condition type	Mass flow inlet
Air inlet mass flow rate, $\dot{m}_{\mathrm{air}}$	0 kg/s
Oil inlet mass flow rate, $\dot{m}_{\mathrm{oil}}$	Fixed, depending on operating conditions
Outlet boundary condtion type	Pressure outlet
Material properties	
Air density, ρ_{air}	Fixed, based on operating temperature
Air dynamic viscosity, μ_{air}	Fixed, based on operating temperature
Oil density, ρ_{oil}	Fixed, based on operating temperature
Oil dynamic viscosity, μ_{oil}	Fixed, based on operating temperature
Surface tension, σ	Fixed, based on operating temperature